

**Simulation and Analysis of  
Stimulus Evoked and Seizure-like  
Activity in an Acute Rat  
Neocortical Brain Slice Preparation**

Christopher Brian Thornton

**Newcastle University  
Faculty of Science, Agriculture, and Engineering  
School of Computing Science**

This thesis is submitted in partial fulfilment of the requirements for the degree of  
Doctor of Philosophy

Submitted: March 2020



## Acknowledgements

This thesis has built on the work of Richard Tomsett, who created the original VERTEX simulator. I am very grateful to him for his thoughtful program design, well commented code, and very informative thesis. I would also like to acknowledge my collaborators, Anupam Hazra and Frances Hutchings, they have both been brilliant to work with, very helpful, thoughtful, hard working, and knowledgeable. Thanks to Anupam for all the hard work involved in preparing and looking after the rats, designing the experiments, performing experiments, and teaching me the tricks of the electrophysiology trade. Thanks to Frances for her input on the theory and practise of non-invasive brain stimulation, as well as her contributions to the VERTEX code base - particularly the multi-region simulation framework, and the time dependent electric fields. Thanks to Joachen Spanke for his help and contributions to the seizure detection and analysis code (both theory and code) - in particular the detection of events by entropy, and the identification of seizure troughs. Thanks to Georgia Rentesi and Felix Chan for their company and help in the lab. Thanks to Yujiang Wang for her tutorials on dynamical systems theory. Special thanks to my supervisors, Marcus Kaiser, for his many contributions, support, and advice and also to Mark Cunningham for his ideas for experiments, and help with practical issues in the lab. All members of the labs of Marcus Kaiser and Mark Cunningham have been of great help, thanks to them all. Thank you to Connie Mackenzie-Gray Scott for reading through my thesis and giving lots of great feedback. Finally, I'm really grateful to all the people in Newcastle (and those no longer in Newcastle) who have provided support, encouragement, and company over these last few years.



## Abstract

This thesis aims to provide tools for the simulation and analysis of acute brain slice experiments that have recorded spontaneous seizure-like activity and activity evoked using electric field stimulation. The Virtual Electrode Recording Tool for Extracellular Potentials (VERTEX) (Tomsett et al., 2015) is a simulation framework that can act as a scaffold for anatomical and physiological knowledge and can be used to test how interventions affect the dynamics observed in the extracellular potentials. We extend VERTEX so that one can model a greater range of experimental setups, in particular those that involve electric field stimulation. We also devise a software pipeline for the identification and analysis of epileptiform neuronal activity, which we apply to *in vitro* recordings from acute neocortical slices from a chronic model of epilepsy in rat.

In Chapter 1 we look at the intersection of electric field stimulation, synaptic plasticity and epilepsy.

In Chapter 2 we look at the implementation of electric field stimulation that we have added to the VERTEX simulator. We show that our simulation compares well with simulations using detailed neuron models, and with previously published *in vitro* data. We also describe our implementations of short term plasticity and spike-timing dependent plasticity.

In Chapter 3 we describe some example simulations of focal electric field stimulation in neocortex, investigating a single pulse of stimulation, a paired pulse of stimulation and the role of short term plasticity in the response. We also use theta burst stimulation to provoke a potentiation of the response when we apply spike-timing dependent plasticity to the synapses of the network.

We then look to the experimental context of our framework. Chapter 4 describes an analysis tool for identifying and evaluating epileptiform activity recorded *in vitro* and outlines a method devised to measure the abruptness of seizure build up.

Chapter 5 uses this analysis pipeline to analyse seizure-like events recorded *in vitro* from slices of motor cortex prepared from rats with chronic seizures induced by injection of tetanus toxin. In this chapter we also describe two VERTEX simulations; one that uses short term plasticity as the vehicle for the breakdown in inhibition and the build up of activity during a seizure-like event, and another of stimulus evoked activity in a

seizure-prone neocortical slice. We compare the latter with stimulus evoked potential in an example *in vitro* multi-electrode array recording from the chronic epilepsy model.

In Chapter 6 we discuss the future uses of VERTEX in modelling stimulus evoked activity and epileptiform activity.

# Contents

List of Figures	vii
List of Tables	xiii
Chapter 1. Introduction	1
1.1. Synapses and synaptic plasticity	1
1.1.1. Synaptic efficacy and short term synaptic plasticity	3
1.1.2. Electric field stimulation and plasticity	4
1.1.3. spike-timing dependent plasticity	5
1.1.4. Brain stimulation as a treatment for neurological disorders	6
1.2. Epilepsy	6
1.2.1. Electric field stimulation and <i>in vitro</i> epilepsy models	7
1.2.2. Clinical applications	10
1.3. Simulating local field potentials in neocortex	10
1.3.1. Simulating neuron dynamics	12
1.3.2. Types of neocortical neuron	14
1.4. Simulations of electric field stimulation	16
1.5. Thesis structure	18
Chapter 2. Adding Electric Field Stimulation and Synaptic Plasticity to the VERTEX Simulator	21
2.1. Introduction	21
2.2. Simulating the effect of electric fields on neuronal fibers:	22
2.3. Evaluating the accuracy of the reduced compartment model	23
2.3.1. The fidelity of the model	23
2.3.2. Comparing the reduced model with a detailed reconstruction	27
2.3.3. Uniform field stimulation	31
2.3.4. Including stimulation in a VERTEX simulation	35
2.4. Adding synaptic plasticity to VERTEX	36
2.4.1. Short term plasticity	36
2.4.2. Spike-timing dependent plasticity	39
2.5. Discussion	42
Chapter 3. A Model Of stimulus-evoked Activity In Rat Somatosensory Cortex	45
3.1. Introduction	45
3.1.1. Long term potentiation and theta burst stimulation	45
3.1.2. Paired pulse stimulation and ambiguities in the paired pulse ratio	46
3.2. Rat Neocortical Microcircuit	47
3.2.1. Parameterising the model	48
3.3. Creating a finite element model of a bipolar electrode and brain slice	51
3.3.1. Creating the 3D model:	51
3.3.2. The volume conductor equation:	52
3.3.3. The boundary conditions:	54
3.4. Response To Stimulation	55
3.4.1. Single Pulse Stimulation	55
3.4.2. Theta burst stimulation	67
3.4.3. Paired Pulse Stimulation	74

3.5. Discussion	79
Chapter 4. Analysis of Epileptiform Activity Recorded <i>in vitro</i>	83
4.1. Introduction	83
4.1.1. Experimental models of epilepsy	83
4.2. Event Isolation	85
4.2.1. Isolating events:	86
4.2.2. Isolating late recurrent discharges	87
4.2.3. Altering and saving event times	87
4.2.4. The accuracy of the tool	88
4.3. Event Analysis	88
4.3.1. Automatic annotation	89
4.3.2. Seizure-like events	90
4.3.3. Correlations between SLE measures	94
4.3.4. Quantifying Repetitive Short Events	95
4.4. Discussion	97
Chapter 5. An Analysis of <i>Ex Vivo</i> Recordings From A Chronic Model of Epilepsy In Rats	101
5.1. Introduction	101
5.2. The Tetanus Toxin Model of Chronic Epilepsy	102
5.2.1. Mechanism of action	102
5.2.2. Resected neocortical slices from rats injected with tetanus toxin.	103
5.3. Experimental Setup	103
5.4. Experimental Results	104
5.4.1. Interhemispheric differences in seizure-like events	104
5.4.2. Response to stimulation	110
5.4.3. Discussion and summary of experimental results	114
5.5. Simulating evoked potentials and epileptiform discharges in rat neocortex	119
5.5.1. A simulation of the response to bipolar stimulation in rat neocortex bathed in magnesium-free ACSF	119
5.5.2. A model of epileptiform activity	124
5.5.3. Discussion of simulations	130
Chapter 6. Discussion and Outlook	133
6.1. Contributions	133
6.1.1. Interpreting field potential responses to electric field stimulation	133
6.1.2. Predicting the effects of electric field stimulation on large scale dynamic networks	134
6.1.3. Validating maps of neocortical microcircuits:	135
6.2. Current limitations and avenues for future research	135
6.2.1. The effect of electric fields on axons	135
6.2.2. More accurate models of plasticity	136
6.2.3. Extending to model human or mouse tissue	137
6.2.4. Modifying neuronal circuits with brain stimulation	138
6.2.5. A full biophysical model of ictal activity	138
6.2.6. Controlling epileptiform activity with stimulation	139
6.2.7. Measuring the properties of epileptic networks with stimulation	139
Appendix A. Adding Electric Field Stimulation to a VERTEX Simulation	141
A.1. Creating the 3D model in Blender	141
A.2. Calculating the electric field	143
A.3. Running the simulation	144
Appendix B. Adding Synaptic Plasticity to a VERTEX Simulation	147

B.1. Adding short term plasticity	147
B.2. Adding spike-timing dependent plasticity	148
Appendix C. Simulating the effect of an electric field	149
Appendix D. The Adaptive Exponential Integrate And Fire Model	151
Appendix E. Implementation of the Synapse Models and Spike Processing	155
E.1. Class hierarchy:	155
E.2. Data structures for synapse variables:	157
Appendix F. Inhibitory Synapse Location and the Propagation of Activity	159
F.1. Introduction	159
F.2. Methods	159
F.3. The Firing Rate Of A Single Neuron	160
F.4. Somatic Inhibition Provides a More Powerful Restraint	160
References	163



## List of Figures

1.1	Shows a cartoon of a typical neuron.	2
1.2	Shows a cartoon of a synapse.	3
1.3	Illustrates spike-timing dependent plasticity.	5
1.4	Shows electrically evoked epileptiform activity.	8
1.5	A typical VERTEX workflow.	11
1.6	Illustration of a compartmental model neuron.	13
1.7	Shows a cartoon pyramidal cells and interneurons.	15
1.8	In networks with somatic inhibition, far higher excitatory synapse strength to inhibitory synapse strength is required to propagate activity. Further details of these simulations are provided in appendix F.	16
2.1	The steady state membrane potential of the detailed and reduced neuron models as a result of a monopolar stimulation at 500 uA.	25
2.2	Randomly generated electrode locations.	26
2.3	The effect of compartment size on the response to stimulation in the Layer 2/3 pyramidal cell model.	27
2.4	The effect of compartment size on the response to stimulation in the interneuron model.	28
2.5	The effect of compartment size on the response to stimulation in the Layer 5 pyramidal cell model.	29
2.6	Comparing the response to stimulation in detailed reconstructions of the morphology to our reduced models	30
2.7	Shows the relationship between the mean dendrite width and the soma polarisation for the L5 pyramidal cell.	31
2.8	Reducing the mean diameter of the dendrites brings the response of the reduced model closer to that of the detailed model when presented with dendritic stimulation.	32
2.9	The extent of polarisation at the soma with increasing electric field strength in cortical pyramidal cells and interneurons.	32
2.10	Shows the polarisation rate, a measure of the increase in steady state soma membrane polarisation with an increase in field strength.	33
2.11	Compares the polarisation rates of our reduced models compared with the <i>in vitro</i> results of Radman et al. (2009).	34
2.12	Illustrates how one would include a stimulating field into a VERTEX simulation.	36
2.13	The data structure for processing synaptic delays.	43
3.1	The structure of the neocortical slice model.	48
3.2	The response of a selection of neuron types to current injection.	49

3.3	The expected number of connections from the population of presynaptic neurons in the presynaptic group to a single neuron in the postsynaptic group.	50
3.4	The time constant for facilitation of synapses between the cell types of rat somatosensory cortex.	51
3.5	The time constant for depression of synapses between the cell types of rat somatosensory cortex.	52
3.6	Modelling the field potential generated by a bipolar electrode.	53
3.7	The tissue placed within the electric field.	53
3.8	Shows the cells recruited directly by bipolar stimulation.	57
3.9	Increasing the stimulus amplitude and pulse width increases the recruitment of cell in layers 2-5.	58
3.10	Shows the LFP recorded by an electrode in layer 2 and generated by the 5 cell types that contribute the most.	59
3.11	The synaptic currents arriving at and local field potential generated by layer 5 pyramidal cells.	62
3.12	The amplitude of the response increases with increasing stimulus amplitude.	63
3.13	The response amplitude increases as the pulse width increases.	64
3.14	Increasing the number of synapses from layer 4 spiny stellate cells to layer 2/3 pyramidal cells causes significant increase in the number of spikes seen in layer 2/3.	65
3.15	Peri-stimulus time histogram for a range of stimulus amplitudes and pulse widths.	66
3.16	The strength of spiking response for each of the neuron types.	68
3.17	Shows the neural activity of the network during the theta burst stimulation.	69
3.18	Peri-stimulus time histogram during theta burst stimulation.	70
3.19	The extent of the synaptic weight change for each neuron in a single network	71
3.20	The extent of the synaptic weight change on the connection between each neuron group.	72
3.21	The change in synapse strength on the L4SS to L23PC connection as a result of TBS in the default, modified, and reduced inhibition networks.	73
3.22	The proportion of cells recruited by the second stimulus increases and the mean inhibitory currents arriving at these cells decreases as we increase the interval from 50 ms to 300 ms.	75
3.23	The relative synapse strength on synapses during paired pulse stimulation.	76
3.24	The paired pulse ratio with increasing pulse intervals.	76
3.25	Shows the error and 95% confidence interval between our estimate of the PPR using the recruitment and synapse ratios and the PPR measured via the LFP.	77
3.26	The paired pulse ratio of the recruitment, the synapse strength, and the LFP.	77
3.27	Estimating the paired pulse ratio.	78
4.1	Schematic showing the workflow of the event isolation tool and the associated analysis scripts.	85
4.2	The graphical interface to the event isolation tool showing seizure-like events automatically isolated from the rest of the trace using the power of the low frequency component of the signal.	87

4.3	Measuring the accuracy of the tool.	89
4.4	The analysis tool.	90
4.5	Shows an example SLE with troughs identified using the method outlined in this chapter.	92
4.6	An example SLE with the cumulative maximum of its trough amplitudes shown.	95
4.7	The cumulative maximum of the multi unit activity from the example.	96
4.8	The correlation between the major features of the events.	97
4.9	A late recurrent discharge, with an after hyperpolarisation oscillation.	98
5.1	A comparison of the trough characteristics of events contralateral and ipsilateral to the TeNT injection site.	105
5.2	A comparison of the duration, multi-unit activity peak amplitude, coastline, and intermittancy of events contralateral and ipsilateral to the TeNT injection site.	105
5.3	A comparison of the abruptness measurements applied to events recorded from slices contralateral and ipsilateral to the injection site.	107
5.4	The rate at which the event LFP and MUA approaches its maximum.	108
5.5	Shows the relative power of the various frequency bands.	109
5.6	The inter-event interval and amplitude of LRDs recorded in slices either contralateral or ipsilateral to the injection site.	109
5.7	Shows the two setups used for stimulating and recording the rat motor cortex slices.	111
5.8	The averaged waveforms of responses in layer 2/3 to stimulation in layer 2/3.	114
5.9	The amplitude of the averaged response potential decays as we move away from the stimulating electrode.	114
5.10	the spatial decay constant of the response potential in slices contralateral and ipsilateral to the injection site.	115
5.11	Shows an example of a spontaneous events, and an evoked event.	116
5.12	The number of events evoked per stimulus applied.	117
5.13	Comparing the response in the experiment to the response in the simulation.	121
5.14	Shows the amplitude of the simulated and experiment response against the distance from the stimulating electrode.	122
5.15	Shows the difference in amplitude and decay space constant between the simulated response and the experiment.	122
5.16	Shows the neuronal response of the tissue to stimulation.	123
5.17	<b>Top:</b> Shows the LFP recorded in layer 2/3 (blue trace) and the peri-stimulus time histogram of layer 2/3 pyramidal cells. The spikes that occur while the stimulus is applied have not been included to emphasise the spiking activity seen in immediately after the stimulus. <b>Bottom:</b> Shows the currents arriving at layer 2/3 pyramidal cells (the average of the 100 cells nearest to the stimulating electrode). We can see that the net current becomes excitatory at around 200 ms, just as the secondary spiking response begins in the top panel.	124

5.18	Shows a response to stimulation that includes a second deflection. Five out of the 10 control slices show a second deflection in at least one response. When considering only those slices that do show a second deflection, the proportion of responses showing a second deflection is 14 % with a standard deviation of 5 %. The average delay between stimulus applied and the second deflection is 1467 ms with a standard deviation of 702 ms.	125
5.19	Seizure-like events are induced by increasing the excitatory synaptic strength and increasing the rate of inhibitory synaptic depression.	126
5.20	Shows the relative synapse strengths (fraction of full synapse strength) of layer 5 pyramidal cells, basket cells, and Martinotti cells, during a simulated epileptiform discharge.	127
5.21	Comparing simulated epileptiform discharges with those recorded in experiments.	129
5.22	Shows the local field potential (blue trace) during a simulated epileptiform discharge, along with the excitatory and inhibitory currents arriving at layer 5 pyramidal cells (the mean recorded from 100 cells). We can see that the main excitatory barrage coincides with the initial peak in the LFP. The inhibitory current briefly becomes positive (and so excitatory), this is possible because synapses are conductance based, and so if the membrane potential of the compartment onto which they synapse polarises beyond their reversal potential they will provide an depolarising current.	130
5.23	Shows an example epileptiform discharge recorded <i>in vitro</i> which shows an initial peak before the main trough. (A) Shows a sequence of discharges. (B) Shows a single discharge.	131
6.1	Depolarisation block induced by injection of a large excitatory current into a pyramidal cell.	140
A.1	Shows the Blender environment. The location of the tools required at each step are circled in green and numbered.	141
A.2	Shows the electrode placed into the slice.	142
A.3		142
A.4	Exporting the STL file.	143
A.5	The mesh and electric potential calculated.	143
A.6	The above code will import the geometry and plot it, the specific face numbers may need to be altered for the specific geometry. Then apply the boundary conditions and coefficients to produce the electric field.	144
A.7	Code for calling the first script to load the geometry and create the electric field model. Then we assign the stimulation on and off times. Then we call the tutorial 2 file. This is a typical tutorial to run a simple network simulation in VERTEX.	145
A.8	The result of stimulation on the tutorial 2 output.	145
B.1	Shows the code required to specify a synaptic connection between two neuron groups (here connections from one group to itself) with short term synaptic plasticity.	147
B.2	Shows the code required to add spike-timing dependent plasticity to a synaptic connection.	148
C.1	Code for incorporating external potentials.	150

- D.1 Shows the neuronal dynamics of a VERTEX AdEx neuron with the parameters described in table D.1. 153
- E.1 Using multiple inheritance to represent multiple types of synapse. 156
- F.1 Spatially arranged spike raster after stimulation of subset of neurons. Magenta dots indicate an excitatory neuron firing, blue dots represent an inhibitory neuron firing. This figure illustrates the simulations we performed, a seizure focus is created in the centre of network by applying current injection. If this, and recurrent excitatory connections, are strong enough then activity will begin to spread. Depending on the network this activity may or may not be restrained by inhibition. In this case it is restrained by strong somatic inhibition. 160
- F.2 The firing rate of the neuron increases most rapidly without inhibition, less rapidly with dendritic inhibition and less rapidly still when somatic inhibition is present. With dendritic inhibition the same maximum firing rate is still achievable, but somatic inhibition reduces this by a half. 161
- F.3 In networks with somatic inhibition, far higher excitatory synapse strength to inhibitory synapse strength is required to propagate activity. 161



## List of Tables

3.1	The 29 neuron types present in the model, along with their layer, their synaptic reversal potential (RP) indicating whether they are excitatory or inhibitory, and the proportion of the model they compose.	54
3.2	Response potential parameters in simulation and experimental literature.	63
3.3	The STDP parameters and VERTEX synapse model used during the theta burst stimulation simulation.	68
4.1	The parameters used to generate the artificial traces. Shows the mean and standard deviation in parenthesis. Duration and interval were sampled from normal distribution, the frequency was constant.	88
4.2	Description of the main features currently extracted from the seizure-like event signal	91
4.3	Shows the results of applying the three techniques used to measure the abruptness to 124 SLEs. Shows the abruptness value ( $\log(k)$ , where $k$ is the coefficient of the logistic function), the median fitting error ( $R^2$ ), and the percentage of events that have an $R^2$ greater than 0.95. The standard deviation (SD) is shown for the mean value, and inter quartile range (IQR) shown for the fitting error.	94
5.1	Shows the p values of measures with a statistically significant difference before multiple comparisons correction and after.	110
5.2	Contralateral slices are more likely to show spontaneous events during the hour of stimulation and recording in layer 5.	113
5.3	The number of evoked events in each hemisphere.	113
5.4	The proportion of spontaneous SLEs found in slices from rats with TeNT injection and rats with saline injection.	115
5.5	The proportion of evoked SLEs found in slices from rats with TeNT injection and rats with saline injection.	115
D.1	Show the parameters used to generate a range of neuronal dynamics with the AdEx model.	152



## CHAPTER 1

### Introduction

In this chapter we review the motivations and context of the work in this thesis. We begin by describing the biology of the synapse, and the role played by electrical stimulation in the discovery of various forms of synaptic plasticity. We then review recent work on the therapeutic use of stimulation to modulate the connectivity of human brain networks, and its use as a therapy more generally. This leads us to epilepsy; we first discuss its physiology and the role that electric field stimulation has played and continues to play in its study, before looking at the role it plays in treatment. This motivates the contribution of this thesis, which is primarily a modelling framework to aid in the studying of electrically evoked neural activity. This may be to probe the properties of a network in diseases such as epilepsy but also as a means to modify networks through the pathways of synaptic plasticity.

#### 1.1. Synapses and synaptic plasticity

The synapse is the primary means by which neurons communicate. Its role can be seen as to convey to other neurons that the presynaptic neuron has generated an action potential. An action potential (also known as a spike, or described as firing) is produced when the potential difference across the cell membrane (membrane potential) around the axon hillock (the start of the axon near to the neuron cell body) reaches a threshold, this results in a sharp increase in the membrane potential propagating down the axon of the cell. A cartoon of the morphology of a neuron is shown in figure 1.1. When an action potential reaches the synapse, it causes the release of neurotransmitter across the synaptic cleft (the gap between the axon and the postsynaptic cell membrane), this binds to the receptors on the postsynaptic cell, which then causes the opening of ion channels, resulting in current flowing across the postsynaptic cell membrane. This current may generate an excitatory postsynaptic potential (EPSP) or inhibitory postsynaptic potential (IPSP) depending on the synapse type. This is illustrated in figure 1.2.

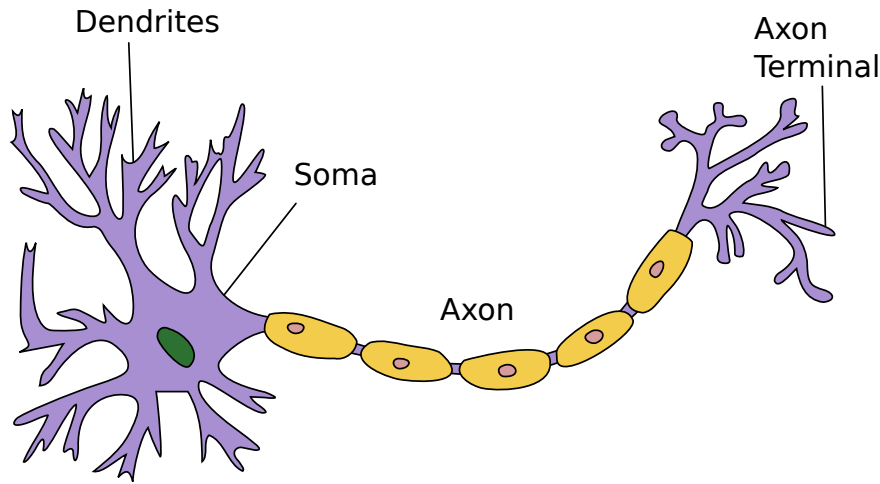


FIGURE 1.1. A cartoon of the structure of a typical neuron. Shows the soma, dendrites, and axon. (Image by Quasar Jarosz, licensed under: CC BY-SA 4.0)

Functionally, the axon can be seen as the main output of the neuron, conveying to the cells it synapses on to that the neuron has reached its threshold input. The dendrites of the neuron (where most excitatory synapses are made) form the input to the neuron, with the machinery involved in the generation of the action potential integrating the input over time (EPSPs and IPSPs decay and are only present for a short time) and space (inputs on dendrites nearer to the soma arrive quicker).

The computational capabilities of a network of neurons connected in this manner are utilised by artificial neural networks (ANNs), used in machine learning algorithms. These networks use a simple description of the neuron such as the Threshold Logic Unit (TLU) introduced by McCulloch and Pitts (1943). Here the input to each unit is summed and if it passes a threshold, the unit is activated and all units that it connects to receive a signal, weighted by the strength of their particular connection. The weights of the connections define the computation. Single units can be constructed to replicate logic gates, and many can be connected together in multiple layers to perform pattern recognition or classification of noisy data. The use of a threshold and an all or none response makes them quite robust - small fluctuations in input will not affect the output unless they push it beyond or below threshold (Gurney, 1997). In simple networks the weights can be set manually, but for the large networks used in applications such as classification, they must be set automatically. Often, a training set of data is used, where the correct output given an input is known. The network is trained on this data

set using an algorithm (such as the backpropagation of errors (Hecht-nielsen, 1989)) to alter the weights of the network until a suitable accuracy has been found. This is known as supervised learning. If the training data well represents the wider dataset then the network should be able to generalise and accurately classify unseen data.

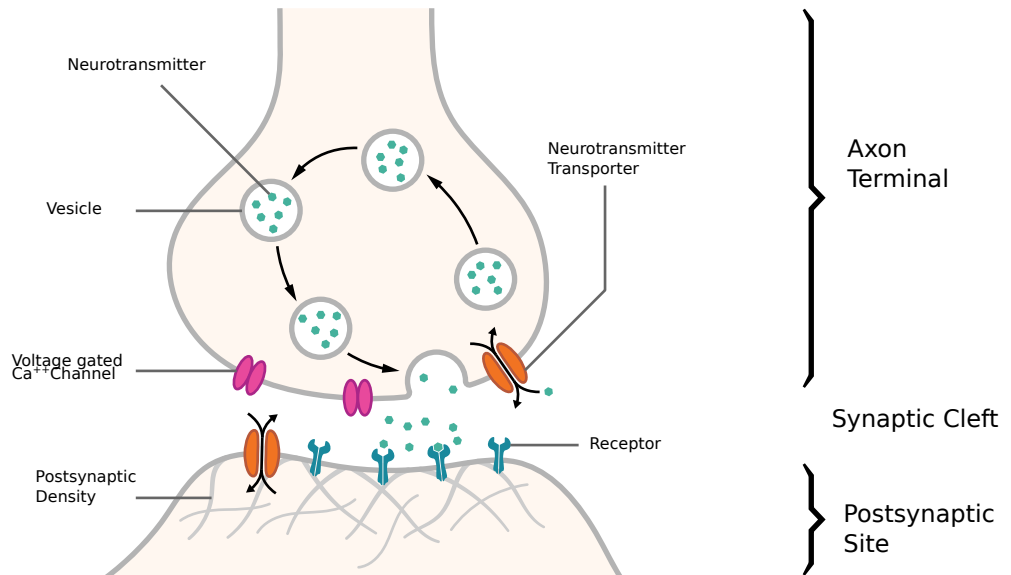


FIGURE 1.2. Shows a cartoon of a synapse and the various components involved in synaptic transmission. When an action potential arrives at the synapse, the elevated membrane potential opens the voltage gated  $Ca^{2+}$  channels. This increases the concentration of  $Ca^{2+}$  in the axon terminal which increases the rate of neurotransmitter release into the synaptic cleft. (Image by Thomas Spletstoesser, licensed under: CC BY-SA 4.0)

**1.1.1. Synaptic efficacy and short term synaptic plasticity.** In biological neural networks the weights of synapses also change over time - synaptic plasticity - but here a vast array of processes modify the weight or *efficacy* of the synapse. The efficacy is also less clearly defined for biological neurons. Functionally, the efficacy means the effect of the presynaptic neuron firing on the likelihood of the postsynaptic neuron firing (as captured by the Mcculloch and Pitts (1943) model). In computational neuroscience, various abstractions of the synapse are used. If we are using a current based synapse model then the efficacy may refer to the current input to the postsynaptic neuron, if we are using a conductance based model it may refer to the magnitude of the conductance of postsynaptic ion channels. Efficacy may also refer to the release probability of a synapse, or to the average number of transmitter quanta released after a presynaptic action potential (London et al., 2002). Changes to these properties would also be seen as changes in the average conductance or postsynaptic

potential. More detailed physiological models (e.g those discussed by Hennig (2013)) model the release probability and number of quanta available for release explicitly. The release probability is a function of calcium concentration in the presynaptic activation zone (Lou et al., 2005), the number of quanta available is dependent on the rate of vesicle replenishment as well as the rate of release. The amount of transmitter released is then a function of the release probability and the quanta available, and the conductance applied to the postsynaptic neuron a function of this and the peak conductance of the synapse. Fluctuations in the number of available quanta and in the calcium concentration in the presynaptic activation zone cause a short term plasticity of the synaptic efficacy (Hennig, 2013). However, this does not facilitate long term changes in synaptic weight, analogous to those seen in the training of ANNs.

**1.1.2. Electric field stimulation and plasticity.** Experimental neuroscientists began to explore the biological correlates of synaptic plasticity in the 19th century, and their primary tool was extracellular electrical stimulation and extracellular recording of the local field potential (Markram et al., 2011). Unlike most pharmacological manipulations, electric field stimulation provides a spatially restricted and time dependent modulation of neural activity. This specificity allows experimenters to invoke activity in a localised population of cells, and measure the effect of this on a neighbouring population. This effect, measured as a response in the local field potential (LFP), can be interpreted as the synchronised action of synapses from the stimulated population. Any modulation of the response can therefore be seen as a modulation of the synapses of the underlying network.

As well as measuring the modulation, stimulation is also used to induce it. The long term potentiation of synapse efficacy (LTP) was first described using this technique by Bliss and Lomo (1973). They applied rapid tetanic (repetitive) stimulation to a bundle of axons connecting to the hippocampus of the rabbit. The amplitude of the response after the tetanic stimulation was 50% larger than before, with this effect persisting for many hours. Ito et al. (1982) applied a slower repetitive stimulation in a similar setup, they found that after this stimulation protocol, the response decreased - long term depression (LTD). These experiments, and others, contributed to the understanding that strong postsynaptic depolarisation combined with presynaptic spiking resulted in

a potentiation of the synapse, while weak postsynaptic depolarisation and presynaptic spiking produced depression.

**1.1.3. spike-timing dependent plasticity.** The early LTP and LTD experiments used repetitive stimulation to induced a depolarisation at the postsynaptic site. Markram et al. (1997) showed that the more subtle depolarisation caused by a single action potential in the postsynaptic cell propagating back into the dendrites can produce long term potentiation or depression depending on the precise timing of the presynaptic action potential. Presynaptic firing before postsynaptic firing produced a larger depolarisation and so potentiated the synapse, postsynaptic followed by presynaptic produced a smaller depolarisation and so depressed the synapse. The crucial role played by the precise timing of spikes has led this to be called spike-timing dependent plasticity (STDP) (Song et al., 2000). Figure 1.3 illustrates this relationship between relative spike timing and the magnitude of synaptic change.

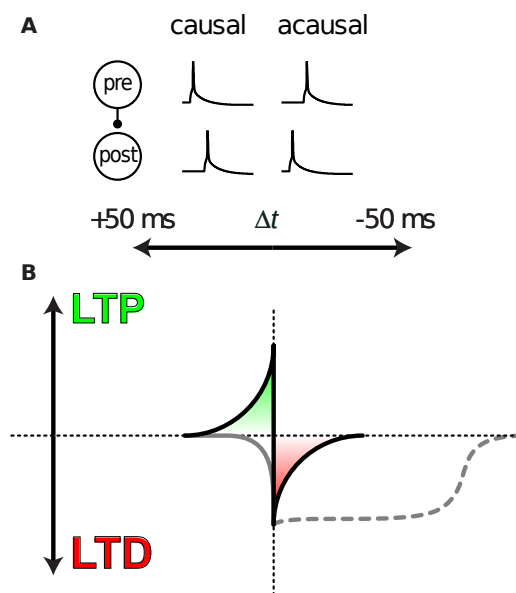


FIGURE 1.3. Illustrates spike-timing dependent plasticity. (A) Shows a presynaptic cell connected to a postsynaptic cell. In the causal scenario, the presynaptic cell fires just before the postsynaptic cell (a positive delay), contributing to its firing. This leads to a potentiation of the synapse. In the acausal scenario the presynaptic cell fires after the postsynaptic cell (a negative delay), this leads to depression of the synapse. (B) Shows the magnitude of synapse change given a positive delay (green area), and a negative delay (red area). These are the temporal windows for LTP and LTD, respectively. Some synapses have an extended LTD window (dashed line), and during low frequency activity LTP may not occur (gray line). Adapted from Markram et al. (2011)

This can be described as a form of Hebbian plasticity, because inputs to the neuron that lead to it producing an action potential will be strengthened, while those that

do not will be weakened (Feldman, 2012). Hebbian plasticity can be summarised as follows: when the firing of cell A contributes to the firing of cell B then the strength of connection from A to B increases (Hebb, 1949). This forms the basis of many unsupervised learning algorithms for artificial neural networks (Sanger, 1989) and STDP has since been shown to allow the training of simple networks to do tasks such as digit recognition (Diehl and Cook, 2015).

**1.1.4. Brain stimulation as a treatment for neurological disorders.** Many modern studies of the low level mechanisms of plasticity employ single cell recordings and stimulate cells using techniques that can target specific cell types such as optogenetics (Sciamanna et al., 2015). However, electric field stimulation remains popular for studying the functional consequences of plasticity at the network level, particularly in *in vivo* studies (Fritsch et al., 2010). Clinically, non-invasive electric field stimulation is hoped to provide a way to alter synaptic connections that may be causing a pathological state (Huerta and Volpe, 2009; Bliss and Cooke, 2011). For example, an over-excitability of the prefrontal cortex is thought to contribute to the symptoms of major depressive disorder in some cases (Nitsche et al., 2009). Repetitive Transcranial Magnetic Stimulation (rTMS) at low frequencies, applied to the prefrontal cortex, has been shown to have a beneficial effect on major depressive disorder symptoms (Fitzgerald et al., 2006). A possible mechanism for this could be an LTD like reduction in connectivity strength between regions of the prefrontal cortex. Schizophrenia is associated with a hyperexcitable sensory cortex. rTMS applied to auditory cortex has been shown to reduce auditory hallucinations in patients with schizophrenia (Kahn, 2007). Again, a suggested mechanism for this in an LTD like reduction in synaptic strength within auditory cortex. Computational models that relate the cellular level processes of synaptic modification, realistic models of the electric field stimulation and realistic brain connectivity models, with experimentally measurable signals or cognitive effects offer the potential for better informed stimulation paradigms.

## 1.2. Epilepsy

One clinical application of electric field stimulation is in the treatment of epilepsy. Epilepsy is a neurological disorder characterised by recurrent interruptions of normal brain function, typically caused by periods of excessive and highly synchronous neural

activity known as seizures (Beghi et al., 2005). An imbalance in the contributions of excitatory and inhibitory neurons forms the basis of most theoretical and experimental models of seizures and epilepsy. The precise nature of this imbalance is known for some experimental models and acute seizure caused by toxicity. However, with regards to clinical manifestations there are many factors involved and significant variations between aetiologies of different forms of epilepsy - epilepsy refers more to the symptoms (excessive synchronous activity) than the causes (Staley, 2015). In the experimental setting activity resembling that of a seizure (epileptiform activity) can be induced by blocking inhibitory synapses (Chagnac-Amitai and Connors, 1989), or by inducing excessive excitatory activity (Perreault and Avoli, 1991). Focal epilepsy is characterised by a seizure-generating region of tissue known as the focus. This tissue shows excessive excitability often as a result of an imbalance of excitatory and inhibitory synaptic currents. It generates waves of hypersynchronous activity that propagate into other regions, causing seizures. Low frequency rTMS has been shown to reduce the frequency of seizures when applied at the seizure focus (Rotenberg et al., 2009). The long term nature of this suppression (several weeks) suggests that synaptic depression may form part of the physiology of the effect (Tergau et al., 1999). While non-invasive electric field stimulation is showing new promise in epilepsy treatment, electrical stimulation has been used in epilepsy research for some time.

**1.2.1. Electric field stimulation and *in vitro* epilepsy models.** Extracellular electrical stimulation has been used to investigate various aspects of epileptiform activity in animal models *in vivo* and *in vitro* as well as in the screening of potential anti epileptic drugs (Castel-Branco et al., 2009). As for investigating synaptic plasticity, it is useful because it allows researchers to probe the network in a way that is temporally precise and spatially localised. In hyperexcitable tissue, it can be used to provoke waves of activity that spread across the network. This allows researchers to study the initiation and propagation of epileptiform events because they know where and when the events will initiate. This method was used by Chagnac-Amitai and Connors (1989) to show that in neocortical slices bathed in very low concentrations of GABA<sub>A</sub> (gamma-Aminobutyric acid) antagonists, propagating waves of activity could be evoked by focal electric stimulation to layer 4, even when spontaneous epileptiform activity was not observed. This provided further evidence that GABAergic inhibition

constrains the horizontal propagation of activity. Building on the same model, Pinto et al. (2005) looked at the layer specific initiation of events. Again in a partially disinhibited slice they stimulated in layer 4 of rat neocortex while recording in layers 5 and 2/3. They found that 7/18 of the layer 5 cells recorded from spiked during the delay between stimulus and wave onset, while the none of the 20 layer 2/3 cells recorded from spiked at all before wave onset. From this they propose that the epileptiform activity evoked by the stimulation in layer 4, is initiated in layer 5. Figure 1.4 illustrates this finding.

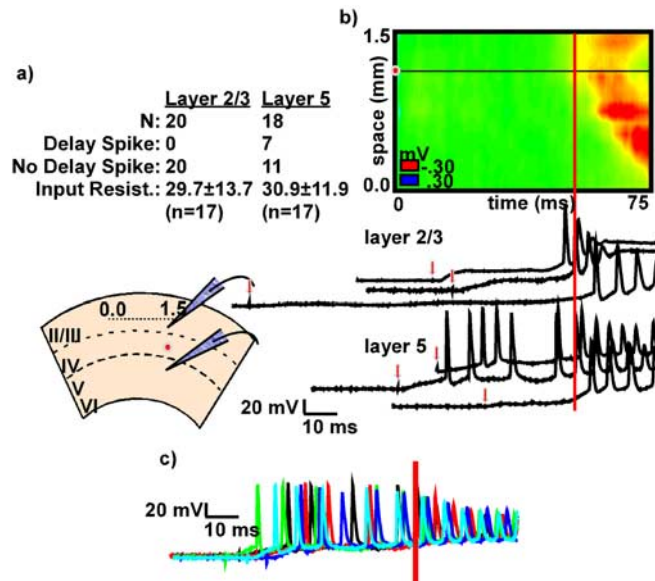


FIGURE 1.4. Reproduced from Pinto et al. (2005). Rat neocortex was made hyper-excitable through the application of low doses of picrotoxin ( $10\mu\text{M}$ ), stimulation was then applied to layer 4, and the resulting activity measured using a multi-electrode array in layer 2/3 and single cell recordings in layer 2/3 and 5. (a) A table summarising the results of the single cell recordings. Only layer 5 cells spike during the delay to wave onset (7/18), layer 2/3 and layer 5 spike during the wave itself. (b) Shows the propagation of a single wave across the multi electrode array. The red dot shows the time and location of the electric stimulus. The red line shows the time recorded as the wave onset time. Below are some example traces from single cells in layer 2/3 and layer 5, small red arrows show the stimulus time, the red line shows the wave onset time, based on the multi-electrode array recording. Beside this we can see a schematic of the protocol used, with the red dot showing stimulating electrode location. (c) Shows 5 overlain traces from a single layer 5 cell during build up to wave onset. The time of wave onset is shown by the red line.

Focal stimulation has also been used to investigate the properties of synapses in slices of epileptic tissue, taken from rodent models (Hagemann et al., 1999), and resected from humans during surgery (Koch et al., 2005). As the function of inhibitory

synapses is thought to play an important role in the generation of seizures, their short term dynamics in seizure generating tissue are of interest. Hagemann et al. (1999) use paired pulses of stimulation to assess the function of inhibitory synapses in various areas of neocortex from rats injected with tetanus toxin. This toxin is thought to impair the function of inhibitory synapses, they show that the effect is stronger in motor cortex than in somatosensory cortex. They rely on the inhibitory currents evoked by the first stimulation to dampen the response to the second and take the ratio as a measure of the impairment of inhibition. This allows them to use the spatial accuracy of electric field stimulation to map out the topography of inhibition impairment around the injection site. Koch et al. (2005) use paired pulse stimulation to measure the properties of inhibition in human epileptic neocortex and rat non-epileptic neocortex. They find the paired pulse ratio to be similar in their control slices and epileptic slices for short inter-stimulus intervals, however for an interval of 100 ms they find the response to the second stimulus to have recovered in the human epileptic tissue but not the rat non-epileptic tissue, indicating a more excitable network in the human tissue.

In addition to the work on slices of tissue, electric field stimulation has been used extensively to explore intact epileptic tissue, again in rodent models and human patients. The response to stimulation varies during a seizure. Wilson et al. (1998) use paired pulse stimulation to assess the excitability of the hippocampus in patients with focal epilepsy. They compared the response in the hemisphere identified as containing the focus with the contralateral hemisphere. They found that in the focus containing hemisphere, the paired pulse depression was increased. This has been shown by Queiroz et al. (2009) who applied paired pulse stimulation to the dentate gyrus of rats with spontaneous seizures induced by kainate. They find that paired pulse depression gradually reduces during a seizure and takes some time to recover after its termination. This can be interpreted as a loss of inhibition during the event, however there are a complex array of changes to the function of inhibition during seizures, including short term plasticity, depolarisation block of the interneurons themselves, and even changes to the reversal potential of GABA, all of which could drastically alter the response to stimulation (Ellender et al., 2014; Staley, 2015; Trevelyan, 2016).

The specific differences in the networks causing these differences in response are not clear. This ambiguity comes from the many processes that may contribute to the short

term dynamics seen through the evoked local field potentials. Both the short term dynamics of the excitatory and inhibitory synapses, as well as the residual inhibition from the first stimulation may play a role. Detailed modelling of these processes as well as explicitly modelling the stimulation and local field potential may help to resolve the ambiguity in interpreting responses to paired pulse stimulation measured by the local field potential.

**1.2.2. Clinical applications.** Despite these ambiguities in interpretation, focal electric field stimulation does appear to be able to distinguish more excitable tissue from healthy tissue. This has given it a role in the identification of the seizure onset zone (SOZ), in patients with focal epilepsies. As well as the paired pulse protocol outlined by Wilson et al. (1998), single pulse stimulation has also been used to assist in the identification of more excitable tissue (Valentín et al., 2002, 2005). Valentín et al. (2002) identified a delayed but more complex spike and sharp wave response in the EEG (electroencephalogram) near the stimulating electrode which associated with the location of the seizure onset zone. This was in contrast to a single immediate response seen in healthy tissue. These delayed responses resemble interictal epileptiform events and have been shown to almost always match with the morphology of interictal epileptiform discharges in observed on electrodes near or in the SOZ in the same patient (Nayak et al., 2014).

### 1.3. Simulating local field potentials in neocortex

To inform the interpretation of local field potentials (LFPs) recorded *in vitro* or *in vivo* we can simulate the LFP generated by the activity we would expect to see. The Virtual Electrode Recording Tool for EXtracellular potentials (VERTEX) is a MATLAB tool for the simulation of neocortical dynamics and extracellular potentials (Tomsett et al., 2015). This process of constructing, running, and analysing a VERTEX simulation is shown in figure 1.5. VERTEX simulates each neuron in the network, using a series of differential equations to calculate the evolution of each membrane potential, synaptic conductance and external currents, among other values. Other approaches to the simulation of neocortical dynamics represent the activity of populations of neurons with a single set of variables. The choice of model often reflects the mechanisms under investigation and the biological measurements available for comparison. Neural

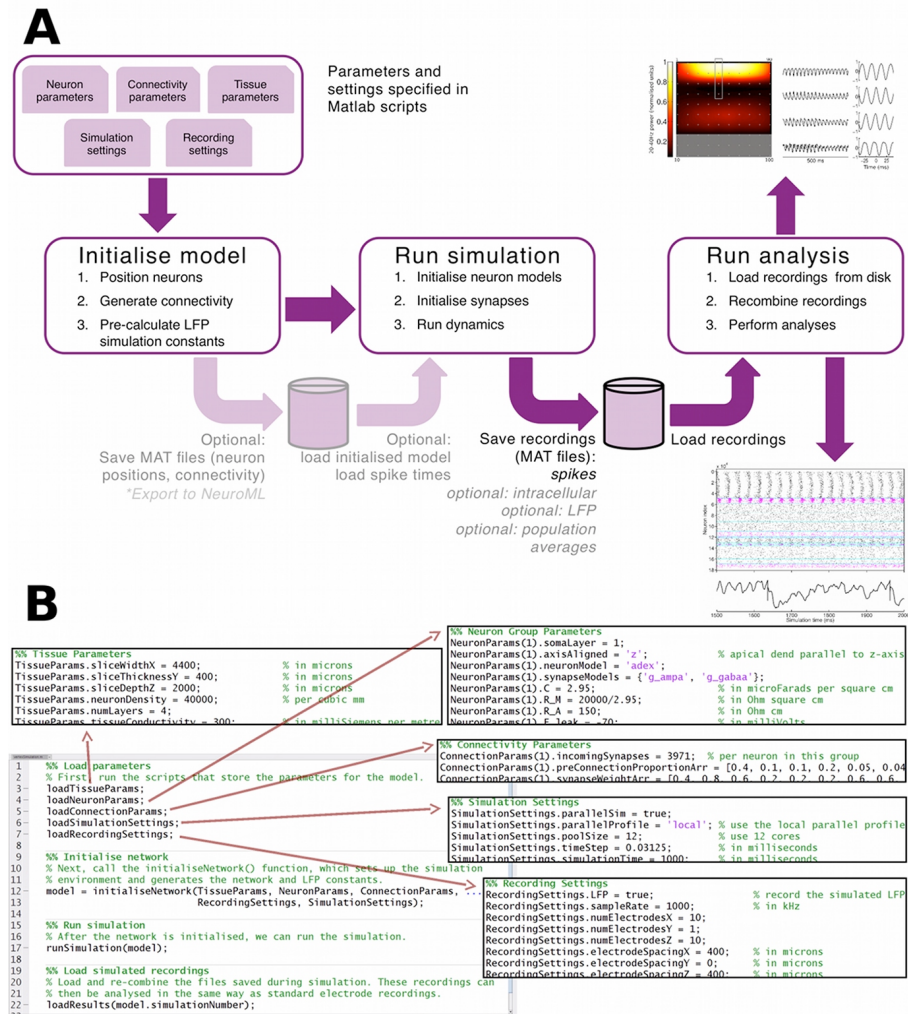


FIGURE 1.5. Reproduced from Tomsett et al. (2015). (A) Shows the workflow of the VERTEX simulator, from model initialisation to analysis of output. (B) Shows example scripts for parameterisation, initialisation, and running of simulations in VERTEX.

mass models lump the membrane potentials of large ensembles of neurons together into a single variable representing the mean membrane potential, and replace spiking dynamics with a firing rate, calculated as a function of the mean membrane potential. They are particularly suited for studying the dynamics of circuits comprising large areas of the brain, where signals recorded non-invasively are used for comparison such as EEG (Costa et al., 2016). Neural field models such as the the Wilson-Cowan model (Wilson and Cowan, 1973; Coombes, 2006) are similar but introduce a spatial component by coupling multiple volumes of tissue into a sheet, where the activity in each volume is modelled by values representing the mean activity of each of the populations present. This allows simulations of propagating activity, particularly useful in the modelling of focal seizures (Goodfellow et al., 2012). An advantage of models such as these is that the number of parameters is significantly reduced, making parameterisation and

interpretation of results more tractable. Computation is also more tractable and whole brain simulation becomes feasible. On the other hand, in the more detailed approach the parameters often more closely match biologically measurable entities, and low level processes are described. This approach is often more suited to modelling *in vitro* experiments, where the local field potential, multi-unit activity, and recordings of the membrane potentials of individual cells may be available for comparison. VERTEX allows direct comparison with all of these measures. In particular at this scale the local field potential can be quite distinct from the multi unit activity.

**1.3.1. Simulating neuron dynamics.** Simulating the dynamics of a single neuron involves estimating the processes involved in the generation of the action potential. In the Mcculloch and Pitts (1943) model this involves summing the inputs then the application of a function such as a step function if there is a hard threshold or a sigmoid for softer thresholds. When simulating neural tissue as VERTEX does, spiking neuron models are more commonly used. The integrate and fire model (Burkitt, 2006) is a simple example of a spiking neuron model. Here the cell is represented by an electronic circuit consisting of a resistor and capacitor in parallel, reflecting the cell membrane acting as a capacitor but also allowing current to leak out (illustrated by one of the compartments in figure 1.6). This represents the passive properties of the cell, the active properties are represented by a threshold membrane potential, when this is reached the neuron can be said to fire and its membrane potential is reset. More detailed models simulate the action potential itself. The action potential is generated by the opening of voltage gated ion channels, when the threshold voltage is reached, they open, allowing positively charged ions (mostly  $\text{Na}^+$ ) into the cell. The time course of the conductances of these channels can be simulated using coupled differential equations. The most well known model of this kind is that described by Hodgkin and Huxley (1952). However, these models (known as point neuron models) only describe the membrane potential of the soma or axon, ignoring the dendrites of the neuron.

Multi-compartment neuron models allow a description of the propagation of membrane potential fluctuations through the dendrites of the neuron. By modelling a branch of dendrite as a passive cable (a spatially extended version of the capacitor and resistor circuit) Rall (1962) produced equations for neurons with dendritic trees. He proposed a partial differential equation - the membrane potential varies in space and

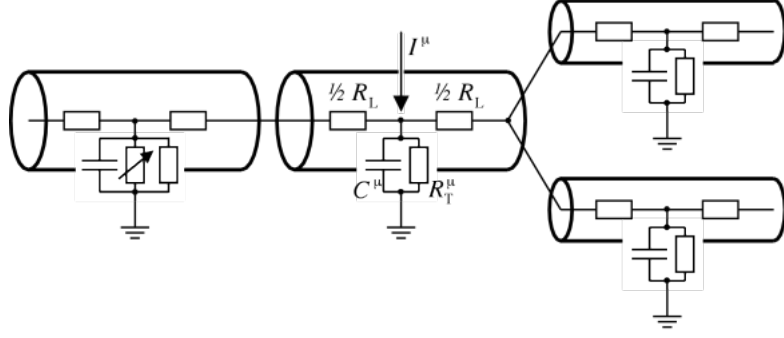


FIGURE 1.6. Illustration of the compartmental model. Four resistor-capacitor circuits connected together. (Reproduced from Gerstner et al. (2014))

time - which can then be discretised over space and solved numerically. This results in a series of compartments each modelled as the capacitor and resistor circuit, tied together with an axial conductance (or resistance) that allows current flow between them, shown in figure 1.6.

$$C \frac{dV}{dt} = -g_L(V - E_L) + g_L \Delta_T \exp\left(\frac{V - V_T}{\Delta_T}\right) - w + I \quad (1)$$

$$\tau_w \frac{dw}{dt} = a(V - E_L) - w \quad (2)$$

VERTEX uses the adaptive exponential integrate and fire model (AdEx), an extension of the integrate and fire model (Brette and Gerstner, 2005), to model the spike generation at the soma. It couples this with dendritic compartments modelled with the passive dynamics described above. Equations 1 and 2 describe the AdEx model. Equation 1 describes the dynamics of the membrane potential. Like the integrate and fire model it uses the resistor-capacitor circuit as its base and it has a leak current ( $g_L(V - E_L)$ , where  $g_L$  is the leak conductance,  $V$  is the membrane potential and  $E_L$  is the leak reversal potential) proportional to the difference between its membrane potential and leak reversal potential. It also has a current (described using an exponential term dependent on the membrane potential) that represents initiation of the spike before it reaches threshold ( $g_L \Delta_T \exp(\frac{V - V_T}{\Delta_T})$ , where  $\Delta_T$  is the slope factor parameter,  $V_T$  is the threshold).  $I$  represents external currents - synaptic currents or currents artificially applied.  $w$  is an adaptation current and is an additional variable. It is updated by an amount  $b$  on spike generation, and otherwise described by equation 2. This allows the AdEx model to describe many different firing patterns in response to

a given input. It has been shown to be able to reproduce a large repertoire of electrophysiological features including spike-frequency adaptation, regular and fast spiking, phasic and tonic bursting, post-inhibitory spiking and bursting, delayed spike initiation and delayed burst initiation (Gerstner and Brette, 2009; Naud et al., 2008). The parameters can be fit to a specific neuronal recording, by seeking a set of parameters that minimise the difference between the recorded trace and simulated trace. As a measurement of error, differences in spike timing may be used, simulated annealing or evolutionary algorithms may be used to select parameters that minimise the error (Friedrich et al., 2014). We reproduce some of the electrophysiological profiles captures using the AdEx model by Naud et al. (2008) in the appendix D.

In VERTEX, this allows users to specify an electrophysiological profile for each neuron type, by selecting the appropriate parameters.

**1.3.2. Types of neocortical neuron.** Cortical neurons can be differentiated in a number of ways. Functionally, one of the most important distinctions between neurons is whether they are excitatory (have depolarising synapses) or inhibitory (have hyperpolarising synapses). In neocortex, this distinction often amounts to the neurotransmitter excreted - glutamate (excitatory) or gamma-aminobutyric acid (GABA, inhibitory). Morphology is often used to further sub-categorise neuron types (Kriegstein and Dichter, 1983). The majority of excitatory neurons in neocortex are also pyramidal cells, these are characterised by a large apical dendrite that reaches towards the cortical surface and a pyramidal soma shape. Inhibitory neurons tend to be smaller and project over a shorter distance (Moore et al., 2010). Neurons can also be classified according to their electrophysiological profile by injecting current into the cells and measuring the firing response. Basket cells are a morphologically defined type of inhibitory neuron found in the neocortex. They also tend to have a fast spiking electrophysiological profile, and strongly express parvalbumin, a calcium binding protein. The expression of various calcium binding proteins often overlaps with particular morphological or electrophysiological subtypes - chemical markers a further means of classifying cell types. In figure 1.7 we can see a cartoon of a pyramidal cell, with synapses made onto it from two different inhibitory interneurons. The red cell is a parvalbumin positive, fast spiking, basket cell. It forms synapses on to the soma of the pyramidal cell. The blue cell is a Martinotti cell, expressing the calcium binding protein

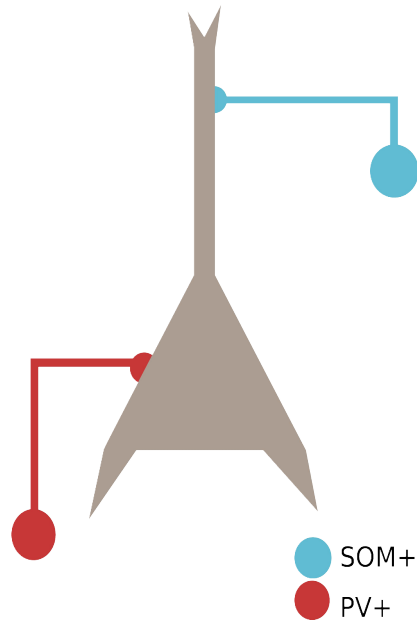


FIGURE 1.7. A cartoon pyramidal cell, with synapses onto its soma from parvalbumin positive basket cells (red), and synapses on to its dendrites from somatostatin positive Martinotti cells(blue).

somatostatin. It synapses onto the dendrites of the pyramidal cell. When simulating the neocortex we wish to include the electrophysiological profiles of as many neuron types as possible, in VERTEX we can do this by finding AdEx parameter regimes that match the most common profiles. The location of synapses is another factor in categorising neuron types, and has important functional consequences (Moore et al., 2010; Pouille et al., 2013). Dendritic inhibition is less effective at reducing the firing rate of a cell receiving strong excitatory drive (Pouille et al., 2013). In the context of epilepsy, this has important consequences. In figure 1.8, I show the seizure restraining properties of two simple networks generated using VERTEX. They both contain a population of pyramidal cells and of inhibitory interneurons. The same number of interneurons are in each but in one there is only dendritic inhibition, in the other only somatic. The balance of excitation and inhibition in the network is evaluated by injecting current into a small cluster of pyramidal cell and measuring if it propagates or is restrained. As the excitatory and inhibitory synapse strength is varied, the network with somatic inhibition can restrain propagation in networks with a much greater ratio of excitatory synapse strength to inhibitory synapse strength. VERTEX is set up to simulate a population of neurons positioned in three dimensional space, with simplified morphologies containing around 10 compartments. This allows users to specify the synapse location

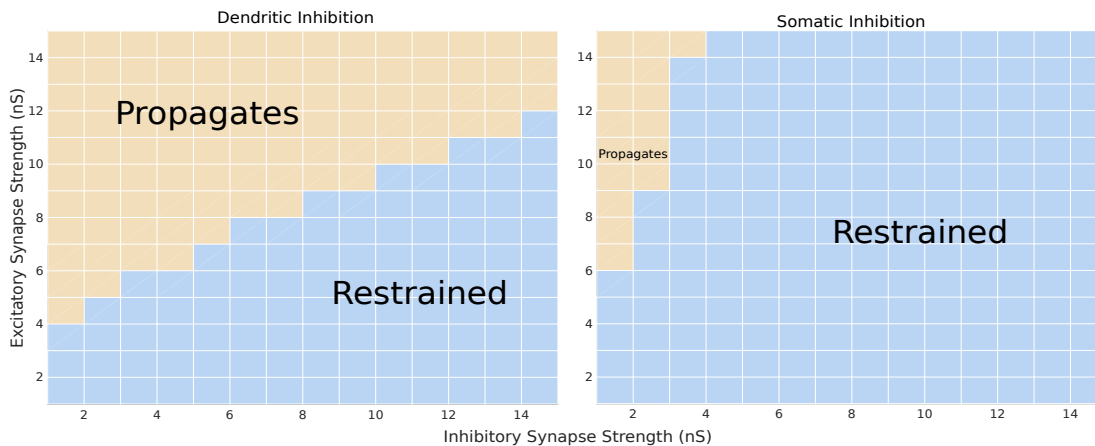


FIGURE 1.8. In networks with somatic inhibition, far higher excitatory synapse strength to inhibitory synapse strength is required to propagate activity. Further details of these simulations are provided in appendix F.

when constructing the synapses for a cell type. The number and weight of synapses between cell types is also needed to construct the simulation. Comprehensive data sets of this nature are rare. Tomsett et al. (2015) use VERTEX to simulate a gamma oscillation in macaque neocortex. They use the cell-type specific connectivity provided by Binzegger et al. (2004). We wished to use VERTEX to simulate stimulus evoked activity and seizure-like activity in rat neocortex. The Neocortical collaborative portal provides a detailed map of rat somatosensory cortex (Ramaswamy et al., 2015). As part of the human brain project, they have used it to produce incredibly detailed simulations of the cortical column (Markram et al., 2015). While we have not sought to replicate the level of detail of this project, we have used the data they provide on neuron types, neuron numbers, cell type and layer specific connectivity and synaptic efficacy, as well as time constants for synaptic facilitation and depression, to construct our model of rat somatosensory cortex.

We sought to build upon the VERTEX simulator by adding functionality for incorporating a stimulating extracellular electric field and synaptic plasticity, so that it could be used to inform the interpretation of electrophysiology experiments that involve electric field stimulation and/or synaptic plasticity.

#### 1.4. Simulations of electric field stimulation

The theory regarding the extracellular stimulation of neurons is very well established. It was touched upon by Rall (1962) when he was outlining his cable equations to describe the biophysics of the neuronal dendrites. It was further built upon by

Frank Rattay (Rattay, 1986, 1989, 1998, 1999) who more explicitly described the theory along with strategies to simulate the effects of arbitrary fields on neuron membrane potentials. A method for finding the steady state membrane potential produced by an electric field on a neuron of complex morphology was outlined by Joucla and Yvert (2009). Much of the current work on electric field stimulation focusses on the accurate estimation of electric potentials produced by more complex electrode-tissue configurations using finite element models (Joucla et al., 2014) or how various aspects of neuron morphology affect its response to stimulation (Yi et al., 2017). Accurately predicting the immediate effect of electric field stimulation at the cellular level requires detailed knowledge and modelling of the cellular properties of the target tissue. This requires a suitable simulation environment that models the morphology of neurons using multi compartment models (Joucla et al., 2014; Yi et al., 2017). This can be computationally costly for large networks and so most simulations focus either on simulations of single neurons using a detailed morphology and compartmental modelling approach, small networks of detailed neurons, or investigate the stimulation applied to large scale networks using an approximation of the stimulation effect and point neuron models or neural fields. The choice of model reflects the studied phenomenon; morphological models tend to be used when studying solely the patterns of polarisation produced by particular stimulation setups on particular cells, while more abstract models are used to study the effect of stimulation on the ongoing intrinsic dynamics of a network of neurons. The scale of the phenomena measured also plays a role, as does the data used for comparison. For example, studies of whole brain networks using electroencephalogram (EEG) or functional magnetic resonance imaging (fMRI) data will likely use a neural field or mass model, while studies that measure single cell dynamics using patch clamp, or intracellular recording techniques would use a morphological model. The tools available for simulation also reflect these two approaches. The NEURON simulator is the only widely available neural simulation tool that provides an extracellular stimulation mechanism that accurately reflects the biology (Hines and Carnevale, 1997, 2000). Its use is mainly in simulating single cells or small networks of neurons (Markram et al., 2015). While NEURON provides an efficient simulation environment that can capture most paradigms and neuronal mechanisms, it is a complex program, and creating simulations of large neocortical networks with many neuron types may

take a long time for someone new to the tool. In spiking neural network simulation tools that specialise in point neuron models (Goodman et al., 2009; Gewaltig and Diesmann, 2007) the effects of stimulation is often approximated by current injection (Brody and Korngreen, 2013; Hall and Kuhlmann, 2013). This does not capture the morphology specific effects of electric field stimulation, or allow one to predict the spatial effects of a specific electrode setup.

### 1.5. Thesis structure

Electric field stimulation is used extensively in the study and treatment of epilepsy, experimentally in *in vitro* slice preparations and *in vivo* models, clinically to identify seizure onset zones, and as a treatment using non-invasive techniques. It is also used extensively in the study of synaptic plasticity, in particular in evaluating the short term dynamics of synaptic efficacy or in provoking long term changes in networks. However predicting its effects, both short term effects (the immediate changes in neuronal dynamics) and long term effects (long term changes in synaptic efficacy) are difficult. So too is interpreting the field potential response to stimulation. We propose simulations at the cellular and microcircuit level as a partial solution to these challenges.

This thesis contributes an extension to the VERTEX simulator, creating a framework suited to simulating the effects of an applied electric field on the activity of neocortical tissue. In particular we look at focal electric field stimulation in the acute rat neocortical brain slice preparation, in physiological conditions to provoke network changes through synaptic plasticity, and in epileptogenic conditions.

In chapter 2 we present the incorporation of electric field stimulation, short term plasticity, and spike-timing dependent plasticity into VERTEX. This provides a framework for the simulation of the field potentials evoked by electric field stimulation, as well as a framework for simulating networks with dynamic synapses. Chapter 3 presents example simulations of electric field stimulation inducing network changes via short term plasticity and spike-timing dependent plasticity, as well as describing our virtual rat neocortical brain slice.

Placing this in the context of epilepsy, we look to the identification, analysis, and simulation of epileptiform events recorded extracellularly in the *in vitro* brain slice preparation. Chapter 4 describes an analysis tool for identifying and quantifying epileptiform events. Chapter 5 applies this analysis to epileptiform events recorded from slices

taken from rats with chronic epilepsy induced by tetanus toxin injection. We consider the effect of tetanus toxin on events that occur spontaneously after applying an altered bathing solution, and those that are evoked by electric field stimulation.

We then present a VERTEX simulation of the response to stimulation in the epileptogenic conditions, as well as a simulation of epileptiform events mediated by short term synaptic plasticity.

We hope this framework will be found useful by those studying seizure-like activity and stimulus evoked activity *in vitro*, as well as those evaluating various brain stimulation protocols as a treatment for neurological and psychiatric disorders.



# Adding Electric Field Stimulation and Synaptic Plasticity to the VERTEX Simulator

## 2.1. Introduction

As an investigatory tool, electric field stimulation has facilitated many important experiments in neurophysiology and is still widely used. This makes it a valuable addition to a simulation framework such as VERTEX (Tomsett et al., 2015). Electric fields applied to the scalp - such as transcranial direct current stimulation (tDCS) and transcranial alternating current stimulation (tACS) - are growing in popularity. Making full use of them will be aided by accurate simulation of the effect of their electric fields on dynamic neural networks incorporating the morphology and physiology of a variety of neuron types.

As discussed in chapter 1 the theory describing the effect of extracellular electric fields on the membrane potential of the neuron is well established (Rattay, 1986, 1989; Joucla and Yvert, 2012). However, due to the large computational resources it would require this is rarely translated into large scale simulations of hundreds of thousands of neurons (Seo et al., 2016). Often simulations of large networks reduce the morphological neurons to a point neuron model (such as the integrate and fire model) in order to make the computation tractable. However, the effect of the electric field is heavily influenced by the morphology, orientation and location of the neuron (Yi et al., 2017). By simulating neurons with a defined morphology, all be it one reduced in complexity, we provide a compromise solution. This allows simulations of tens of thousands of neurons (e.g. a cortical column) on modest hardware or hundreds of thousands (e.g. an *in vitro* brain slice preparation) on a high performance computer, while still capturing the morphology specific effects of the electric fields. However, reducing the detail of the model (simplifying the structure) and reducing the fidelity (reducing the number of compartments) is likely to introduce some discrepancies. In this chapter we seek to quantify these discrepancies by comparing the response to stimulation in our reduced

model with that in higher fidelity versions, detailed reconstructions of the morphology, and *in vitro* results.

We will also detail the methods used to incorporate electric field stimulation into VERTEX and describe the two phenomenological models of synaptic plasticity that have also been added.

## 2.2. Simulating the effect of electric fields on neuronal fibers:

Simulating electric field stimulation involves two steps: the first is to calculate the electric potential caused by the field we are interested in modelling, the second is to calculate how this affects the neuronal activity. The first step can be done analytically for simple electrode-tissue geometries but for more complicated geometries must be solved numerically. We have provided an interface to models constructed using the MATLAB Partial Differential Equation toolbox (The MathWorks, Inc., Natick, Massachusetts, 2016). These can be built to model a wide range of electrode-tissue setups, from bipolar penetrating electrodes used *in vitro* (illustrated in section 3.3) to non-invasive setups that include the skull and cerebrospinal fluid. VERTEX allows users to easily link to a model created using the PDE toolbox or to define an electrode setup analytically, by specifying an electrode location and equation to use. From these, an electric potential is calculated at the mid point of each neuron compartment which is then used in the second step of the process. When modelling neurons using the multicompartmental approach first outlined by Rall (1962), the second step involves considering this extracellular electric potential when calculating the neuron membrane potential change of each compartment using the cable equation shown in Equation 2.2.1.

$$\frac{d(V_{i,n} - V_{e,n})}{dt} \cdot C_{m,n} + I_{ion,n} + \frac{V_{i,n} - V_{i,n-1}}{R_n/2 + R_{n-1}/2} + \frac{V_{i,n} - V_{i,n+1}}{R_n/2 + R_{n+1}/2} = 0 \quad (2.2.1)$$

Where  $V_{i,n}$  is the intracellular potential at compartment  $n$ ,  $V_{e,n}$  is the extracellular potential caused by the stimulating electrode at the midpoint compartment  $n$  (this can be calculated using an analytic approach such as in equation 2.3.2 or by a finite element approach as we describe in the next chapter).  $R_n$  is the resistance between compartment  $n$  and its neighbour,  $C_{m,n}$  is the membrane capacitance at  $n$ , and  $I_{ion,n}$  is the synaptic currents or other ion channel currents. The cable equation describes the flow of charge from one compartment to the other when their membrane potential

differs. It is derived from Kirchoff's current law which states that current flowing in to a particular node in a circuit must equal the current flowing out of that node.

Normally when solving this we consider the extracellular potential to be constant across all compartments allowing us to ignore it. When it is not constant, it can be considered to contribute to the change in membrane potential. To do this we follow previous work (Rattay, 1999) by introducing a reduced membrane potential  $V = V_i - V_e - V_{rest}$ , to take into consideration the non-zero extracellular potential. Substituting this into equation 2.2.1 and rearranging, we get equation 2.2.2.

$$\frac{dV_n}{dt} = [I_{ion} + \frac{V_{n-1} - V_n}{R_{n-1}/2 + R_n/2} + \frac{V_{n+1} - V_n}{R_{n+1}/2 + R_n/2} + \frac{V_{e,n-1} - V_{e,n}}{R_{n-1}/2 + R_n/2} + \frac{V_{e,n+1} - V_{e,n}}{R_{n+1}/2 + R_n/2}] / C_{m,n} \quad (2.2.2)$$

Equations 2.2.1 and 2.2.2 are taken from Rattay (1999). In VERTEX we incorporate equation 2.2.2 as an additional step during the calculation of the axial currents when stimulation is turned on.

### 2.3. Evaluating the accuracy of the reduced compartment model

**2.3.1. The fidelity of the model.** When modelling neurons using compartments and the cable equation, the size of compartments must be considered. VERTEX uses simple neuron geometries, caricatures of the structure of each neuron type that capture synapse location dependent effects (Bush and Sejnowski, 1993) and produce accurate local field potentials (LFPs) (Tomsett et al., 2015), without the detail of a specific neuron reconstruction. However, because we are representing the membrane potential and extracellular potential across the whole compartment by a single value, larger compartment sizes will introduce more error. The acceptable size of the compartment depends on the intracellular properties and the extent to which the field varies in space. Rattay (1999) calculates a space constant ( $\lambda$ , SC) for each of the compartments, equation 2.3.1, where  $d$  is the diameter  $\rho_i$  is the intracellular resistivity, and  $g_m$  the membrane conductance. They show that if the compartment length is less than  $\frac{\lambda}{4}$  then the error compared to the solution to the continuous equation should be of the order of 1%.

$$\lambda = \sqrt{\frac{d}{4\rho_i g_m}} \quad (2.3.1)$$

In VERTEX, when specifying the simulation parameters the user may request that compartment sizes are readjusted so that they are of length less than a specified fraction of the space constant. To investigate the effect of fidelity on our reduced compartmental models we constructed a model with a maximum compartment size of less than  $\frac{\lambda}{4}$  and took this as our baseline model. We then incrementally increased the fraction of  $\lambda$  that compartment lengths were required to be below and measured the discrepancy in their response to stimulation with respect to the baseline model.

We first sought to quantify the accuracy of our models when it comes to capturing stimulation by a focal monopolar electrode. We modelled the electric potential generated by the electrode using equation 2.3.2.

$$V_{e,n} = \frac{\rho I}{4\pi r} \quad (2.3.2)$$

Where  $\rho$  is the conductivity,  $I$  is the stimulus amplitude, and  $r$  is the distance from the electrode.

Figure 2.1 shows a comparison of three neuron types: the pyramidal cell from layers 2 and 3 (L23 PY), the Martinotti cell from layer 4 (L4 MC), and a thick tufted pyramidal cell from layer 5 (L5 TTPC). These are a representative sample of the neuron types in the model described in section 3.2. For each neuron type we show the steady state membrane potential after stimulation with a monopolar electrode in the reduced model (with 3 different compartment sizes) compared with that in the detailed one. We can see a qualitative similarity in between the membrane polarisation in the reduced models and the detailed model both in terms of the locations of depolarisation and hyperpolarisation, as well as in the magnitude. However, it can also be seen that as the compartment size of the reduced model increases, its accuracy decreases. To investigate whether the error introduced by increasing the compartment size (relative to the space constant) is merely a reduction in fidelity or a qualitative error we took the high fidelity reduced model (0.25 x SC) as our baseline and compared the membrane potential with that of the lower fidelity models. We used the compartments of the lowest fidelity model as the sites of comparison, calculating an average membrane potential across the equivalent compartments of the higher fidelity models. Compartments in the higher fidelity models are mapped to the lowest fidelity model by location.

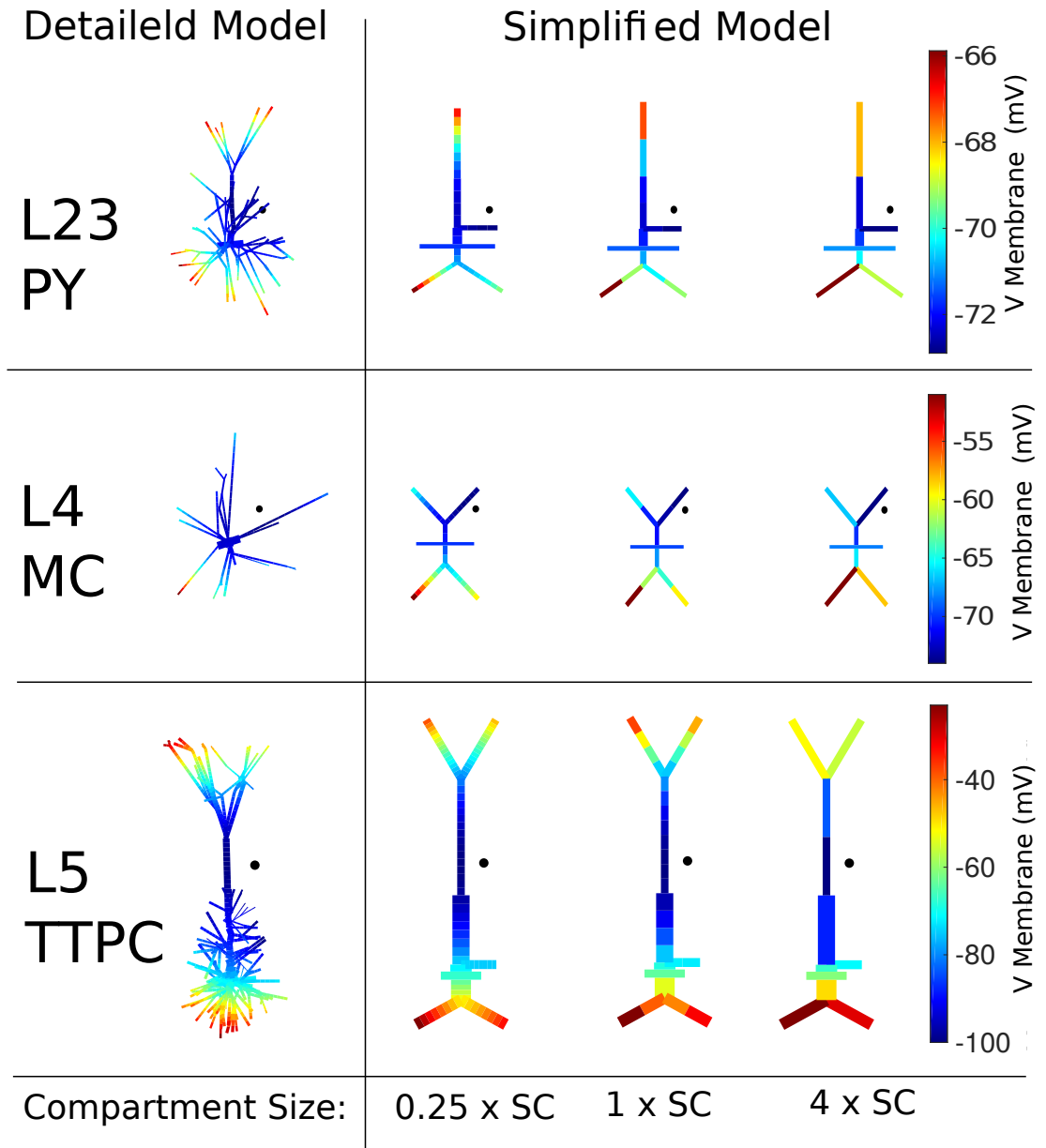


FIGURE 2.1. The steady state membrane potential of the detailed and reduced neuron models as a result of a monopolar stimulation at 500  $\mu\text{A}$  (calculated using equation 2.3.2 with  $I = 500\mu\text{A}$  and  $\rho = 0.3\text{S/m}$ ). The location of the stimulating electrode is shown as the black dot. Three reduced models are shown with increasing compartment sizes. Compartment sizes are factors of the space constant (SC), calculated individually for each model. The reduced models show qualitatively similar patterns of polarisation to the detailed ones, with the overall similarity increasing as the compartment size decreases.

This can be done because the process used to increase the fidelity of the models involves dividing each compartment that is larger than the space constant in half, into two smaller compartments (the children of the initial compartments). This means that each compartment of a higher fidelity model will have a compartment in the lowest fidelity model onto which it can be mapped directly without having to consider whether

it lies on the boundary between two of the larger compartments. So for the higher fidelity models the values used for comparison are the averaged membrane polarisations of the children of each of the initial compartments. At each time point of interest, we calculated a Mean Absolute Percentage Error (MAPE) across the cell (equation 2.3.3), where  $n$  is the number of compartments being compared,  $V$  is the membrane potential of the high fidelity model at that compartment, and  $\hat{V}$  is the membrane potential of the lower fidelity model at that compartment.

$$\text{MAPE} = 100 \frac{\sum_{c=1}^n |V_c - \hat{V}_c|}{\sum_{c=1}^n |V_c|} \quad (2.3.3)$$

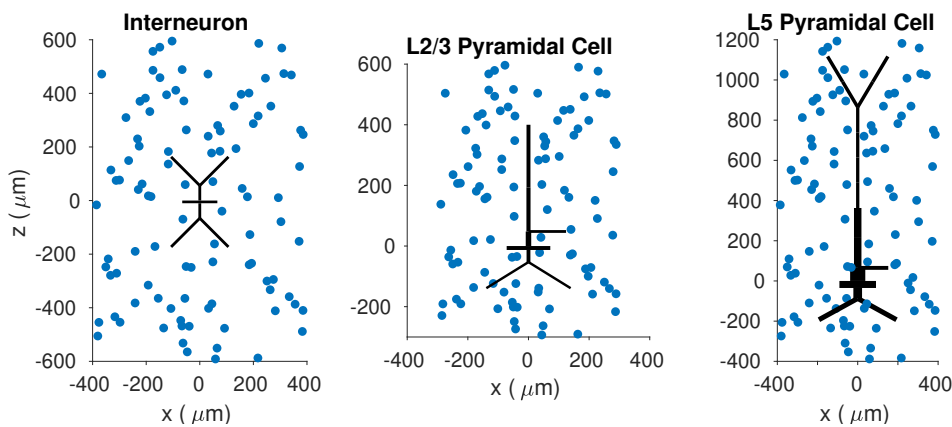


FIGURE 2.2. Shows the locations of the 100 electrode locations randomly sampled from the area around the neuron. The bounds of the sampling space were: Interneuron -  $z=(-600,600)$ ,  $x=(-400,400)$ ; Layer 2/3 Pyramidal Cell -  $z=(-300, 600)$ ,  $x=(-300,300)$ ; Layer 5 Pyramidal Cell -  $z=(-400,1200)$ ,  $x=(-400, 400)$ . The bounds in the  $y$  plane were  $(-40, 40)$  for neuron types.

We use a measure of relative error because with each repeat we are stimulating in a different location, resulting in a different magnitude of response. The stimulus amplitude is  $100 \mu A$  in all cases. We repeat the simulation for 100 electrode locations (shown in figure 2.2) running the simulation with stimulation applied until the membrane polarisation reaches a steady state. We take a snapshot of the error at a range of time points (0.25ms, 0.5ms, 0.75ms, 1ms, 1.25ms, 1.5ms, 1.75ms) to capture the error observed for a range of stimulus durations. We plot the median and interquartile range of errors for the layer 2/3 pyramidal cell, interneuron, and layer 5 thick tufted pyramidal cell in figures 2.3, 2.4, and 2.5 respectively. Increasing the size of compartments introduces an error in all morphologies and at all time points. Errors are most pronounced during the short stimulus durations (50-100% error), while at the steady

state we find errors of 10-15% for the larger compartment sizes. From this, we can conclude that increasing the size of compartments in our model introduces qualitative errors above those that can be removed by averaging over the compartments of the higher fidelity model, particularly for shorter stimulus durations. Of note are the discontinuities present in all three figures. These occur as a result of the process used to reduce the compartment sizes which splits in two all compartments that are larger than the required size until all are below the required size. As this guarantees that all compartments will be of size smaller than the space constant, rather than of the exact size of the space constant, a model altered to be below 2 SC for example may also be below 1.5 SC.

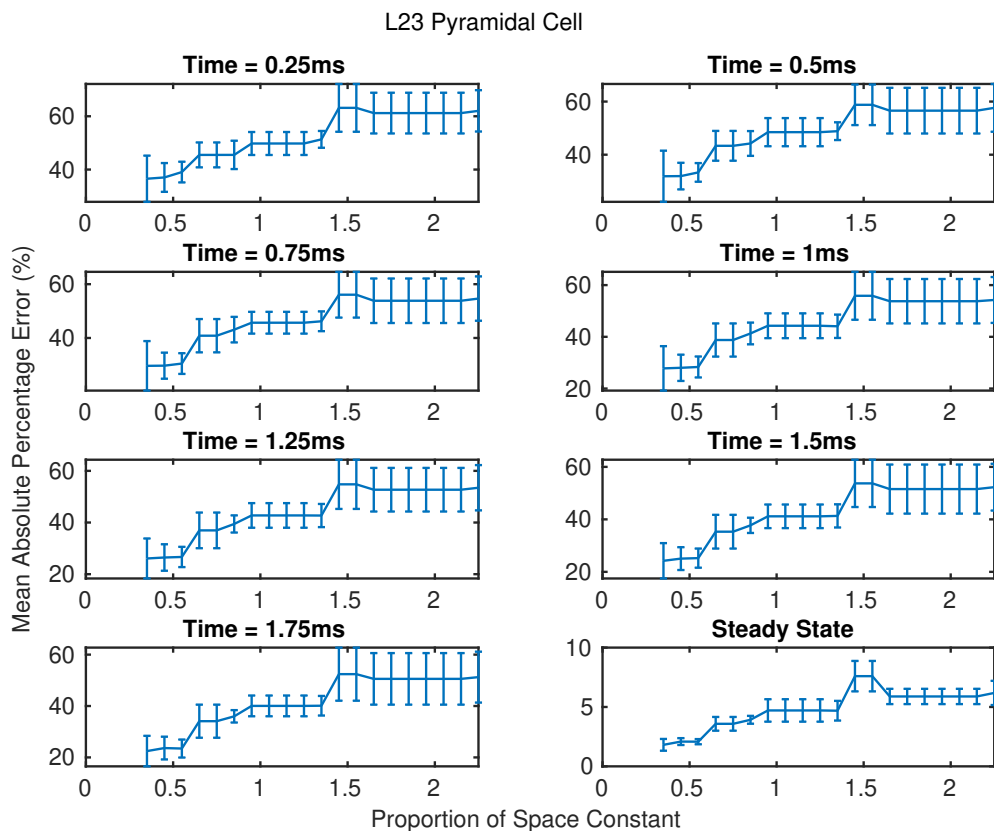


FIGURE 2.3. The effect of compartment size on the response to stimulation in the Layer 2/3 pyramidal cell model. Shows the median and interquartile range of the Mean Absolute Percentage Error (MAPE) calculated on the difference between the membrane potential of the high fidelity reduced model ( $0.25 \times SC$ ) and a range of lower fidelity models. We calculate an error at a range of stimulus durations, each plot shows the MAPE (y axis) for the range of lower fidelity models (x axis) for a given stimulus duration as well as at the steady state.

**2.3.2. Comparing the reduced model with a detailed reconstruction.** As well as the reduction in fidelity, the reduction in the complexity of the morphology,

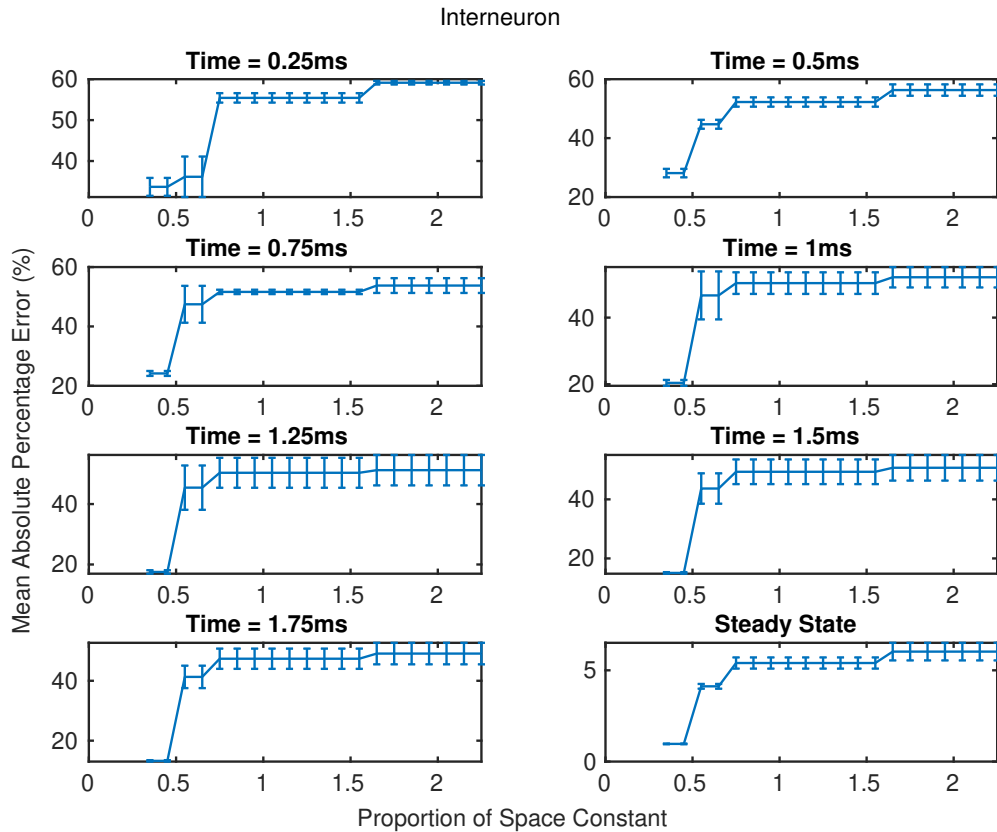


FIGURE 2.4. The effect of compartment size on the response to stimulation in the interneuron model. Shows the median and interquartile range of the Mean Absolute Percentage Error (MAPE) calculated on the difference between the membrane potential of the high fidelity reduced model ( $0.25 \times SC$ ) and a range of lower fidelity models. We calculate an error at a range of stimulus durations, each plot shows the MAPE (y axis) for the range of lower fidelity models (x axis) for a given stimulus duration as well as at the steady state.

may also introduce errors. To quantify how well our reduced neuron morphologies capture the response of real neurons to stimulation, we simulated stimulation of detailed reconstructions of the equivalent cells. We again compare our layer 2/3 pyramidal cell, interneuron, and layer 5 pyramidal cell (the morphologies of these cells are shown in figure 2.1). As there is not a direct mapping between the compartments of the detailed reconstruction and the reduced model, comparing the membrane potential at each compartment is not possible. We have therefore used the membrane potential at the soma to calculate our error, calculating the MAPE across the whole timecourse of stimulation until reaching the steady state. We use equation 2.3.3 to calculate the MAPE, but this time  $n$  is the number of time points being compared,  $y$  is the soma membrane potential of the detailed model at that time point, and  $\hat{y}$  is the soma membrane potential of the reduced model at that time point. The MAPE for each neuron type at a range of

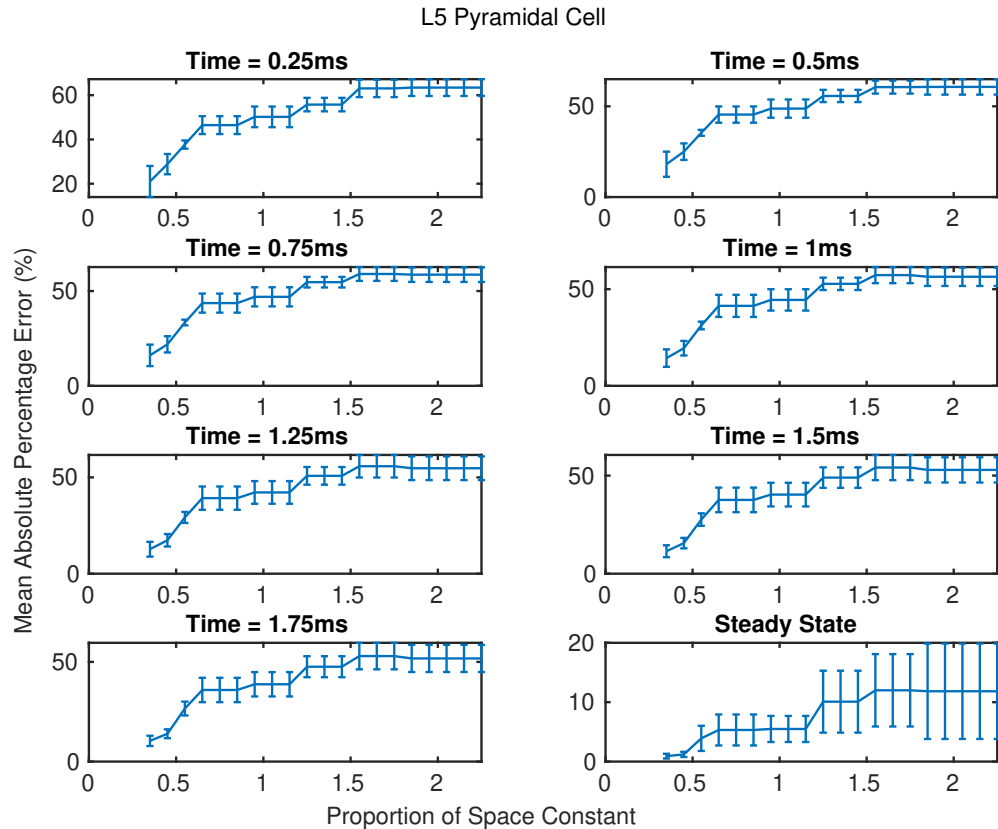


FIGURE 2.5. The effect of compartment size on the response to stimulation in the Layer 5 pyramidal cell model. Shows the median and interquartile range of the Mean Absolute Percentage Error (MAPE) calculated on the difference between the membrane potential of the high fidelity reduced model ( $0.25 \times SC$ ) and a range of lower fidelity models. We calculate an error at a range of stimulus durations, each plot shows the MAPE (y axis) for the range of lower fidelity models (x axis) for a given stimulus duration as well as at the steady state.

compartment sizes is shown in figure 2.6 (right), we can see that all neuron types show a poor fit to their detailed equivalents and that improving the fidelity of the model does not reduce the error. In figure 2.6 (left) we see that a large overestimation of the response polarisation in the two pyramidal cell models is responsible for much of the error. As increasing the fidelity of the models did not reduce the error we considered that simplified morphologies were a possible source of the error. The reduced models were constructed to reproduce the response to synaptic input and current injection, and so the process used to generate them does not preserve the spatial profile of the neuron or aspects such as dendrite diameter (Bush and Sejnowski, 1993). The dendrite diameter is scaled up in the reduced model so that each compartment has an axial resistance to match that of all those it is representing. Unlike the response to synaptic stimulation or current injection, the response to focal electrical stimulation is very

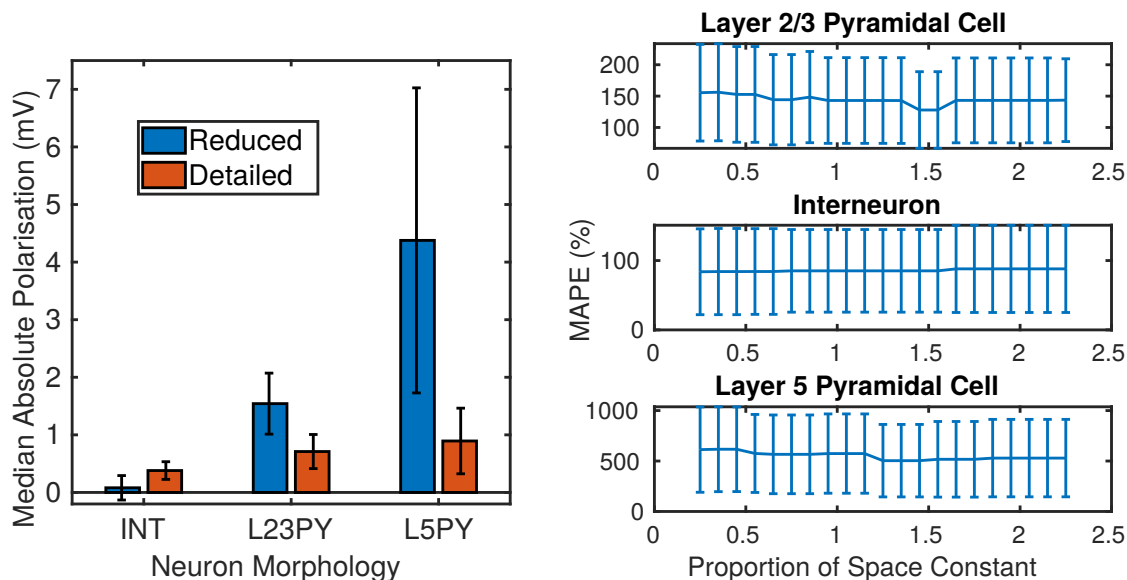


FIGURE 2.6. Comparing the response to stimulation in detailed reconstructions of the morphology to our reduced models. Both plots show median values and interquartile range for all 100 stimulating electrode locations shown in figure 2.2. (Right) Shows the Mean Absolute Percentage Error (MAPE) calculated on the membrane potential at the soma of each cell, for the duration of stimulation. On the x axis is the proportion of the space constant for which the compartment sizes are smaller. The error bars indicate the interquartile range. (Left) Shows the absolute polarisation at the soma for the reduced (blue) and detailed (red) models. For the two pyramidal cells there is a significant overestimation, for the interneuron there is an underestimation.

sensitive to the angle of the compartments. Lumping together the axial conductances of many compartments with various angles (many of which are likely to have counteracting responses to the stimulus) into a single large conductance could introduce an overestimation of the response. We investigated the effect of dendrite size on the response of the layer 5 pyramidal cell (the one with the greatest error), by constructing neuron models with a range of average dendrite diameters. These were built by scaling the dendrite diameters of the original model by a range of factors (0.05 in steps of 0.05 to 1). Again, 100 electrode locations were selected, this time from the area around the apical dendrite (shown in figure 2.8), and stimulus applied ( $100 \mu A$  monopolar). The polarisation of the soma (the difference between the resting membrane potential and that reached as a result of stimulation -  $V_{rest} - V$ ) was measured at several time points, including at the steady state. Figure 2.7 shows the polarisation of the soma at the range of dendrite diameters, and a range of time points. As we increase the diameter of the dendrite we see an increase in the polarisation at all time points. The detailed reconstruction of the layer 5 pyramidal cell that we have used has a average

dendrite compartment length of  $0.89 \mu m$ , while our reduced model has a average dendrite compartment length of  $4.22 \mu m$ . Reducing the dendrite diameter of the reduced model to that of the detailed model reduces the median error, as can be seen in figure 2.8. While further reduction in the diameter past that of the detailed model further reduces the error, the error climbs again when the dendrite diameter reaches  $0.21 \mu m$ . This indicates that while fitting the dendrite diameter exactly to that of the detailed model may not be the best approach, it is an important factor and can in part account for the large overestimation seen in our reduced model of the layer 5 pyramidal cell.

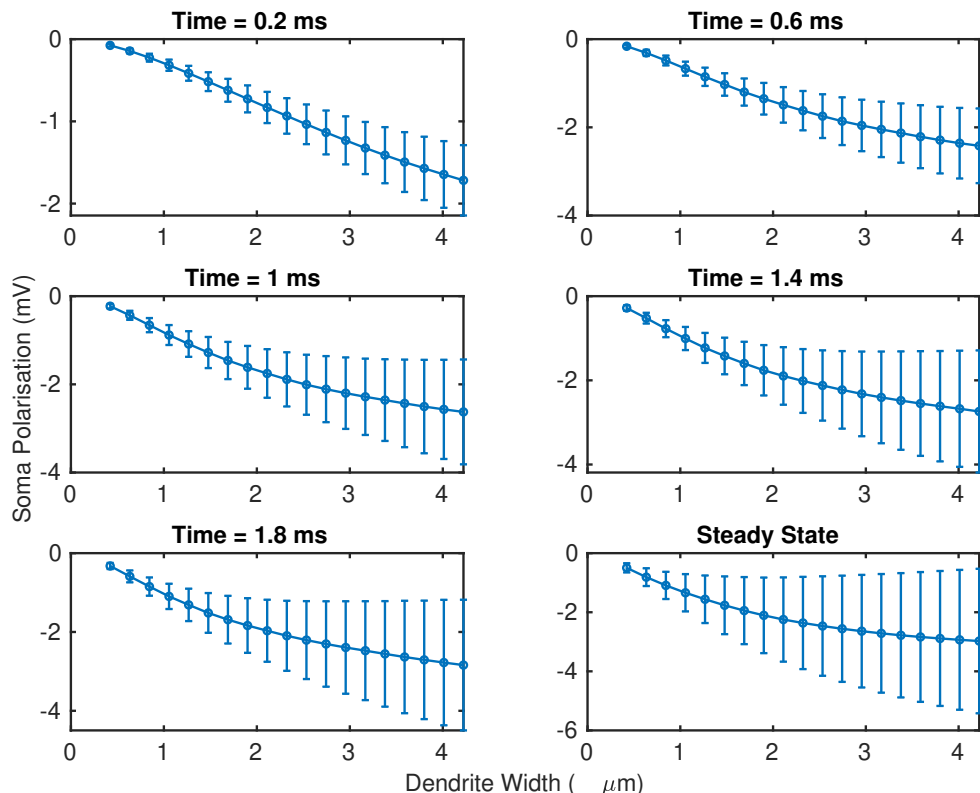


FIGURE 2.7. Shows the relationship between the mean dendrite width and the soma polarisation for the L5 pyramidal cell. The polarisation at 5 time points and the steady state is shown. Points indicate the median and interquartile range of the soma polarisation produced by a monopolar electrode placed at 100 locations randomly sampled from a uniform distribution bounded by the vicinity of the apical dendrite (shown in figure 2.8).

**2.3.3. Uniform field stimulation.** For focal electric field stimulation, comparison with *in vitro* experimental studies is difficult due to the variability caused by slight changes to electrode position. However, for uniform fields the systematic study of the effect of morphology and orientation on the extent of polarisation is possible. Radman

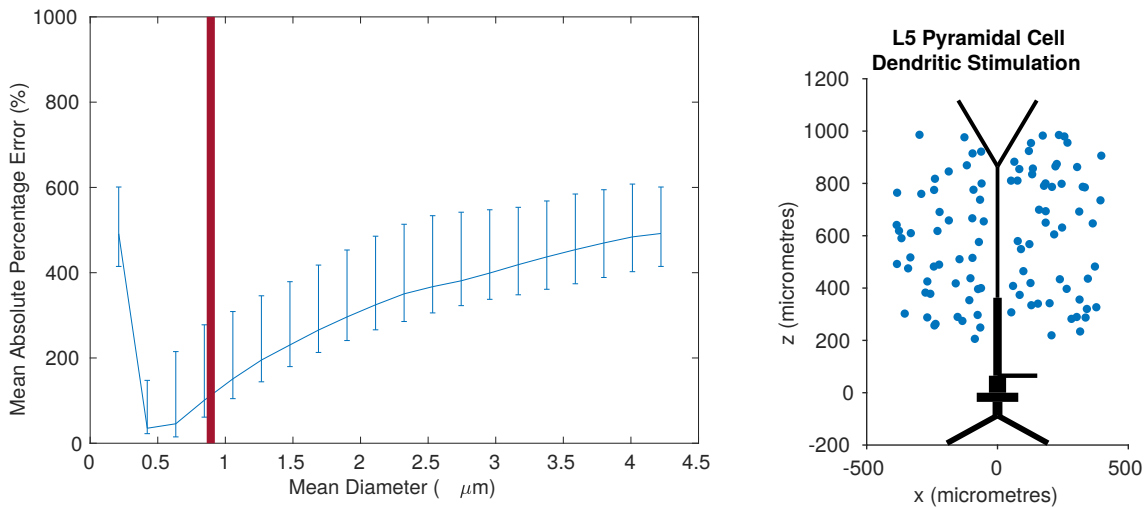


FIGURE 2.8. Reducing the mean diameter of the dendrites brings the response of the reduced model closer to that of the detailed model when presented with dendritic stimulation. On the right we can see the randomly selected locations of the stimulating electrode relative to the reduced model. On the left we can see the Mean Absolute Percentage Error (MAPE) of the response soma polarisation of the reduced model compared to the detailed model. Each data point shows the median error of all stimulus locations, and error bars show the interquartile range. The red line indicates the mean diameter of the detailed model.

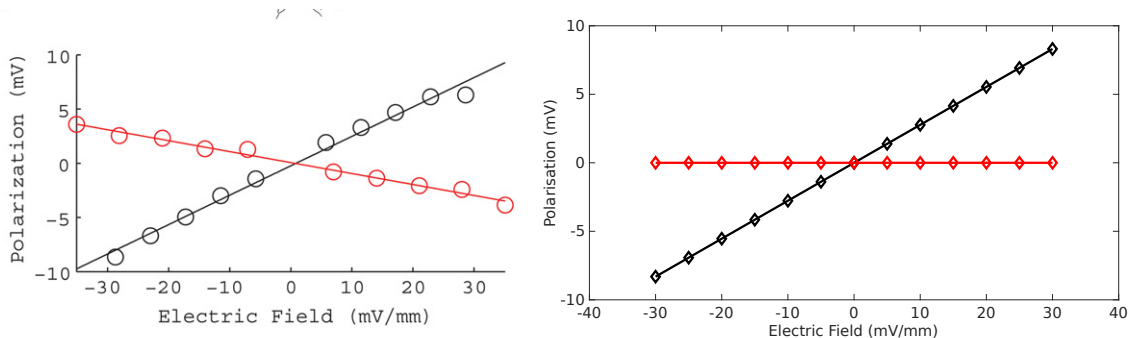


FIGURE 2.9. The extent of polarisation at the soma with increasing electric field strength in cortical pyramidal cells (black) and interneurons (red). (Left) Shows the polarisation found by Radman et al. (2009) in a layer 5 pyramidal cell and interneuron in rat neocortex. (Right) Shows the polarisation of a layer 5 pyramidal cell and interneuron in our rat neocortex model.

et al. (2009) have described the effect of uniform fields on a variety of cortical neuron morphologies. We reproduce some of their key findings with our *in silico* equivalent. Following their procedure we applied a uniform field, positive at the cortical surface and negative towards the white matter, at strengths ranging from -30 mV/mm to 30 mV/mm at steps of 5 mV/mm. We applied the field to the models illustrated in figure 2.1, an interneuron, a layer 2/3 pyramidal cell, and a thick tufted layer 5 pyramidal cell. All cells had compartment sizes smaller than 2 SC. Figure 2.9 shows how the

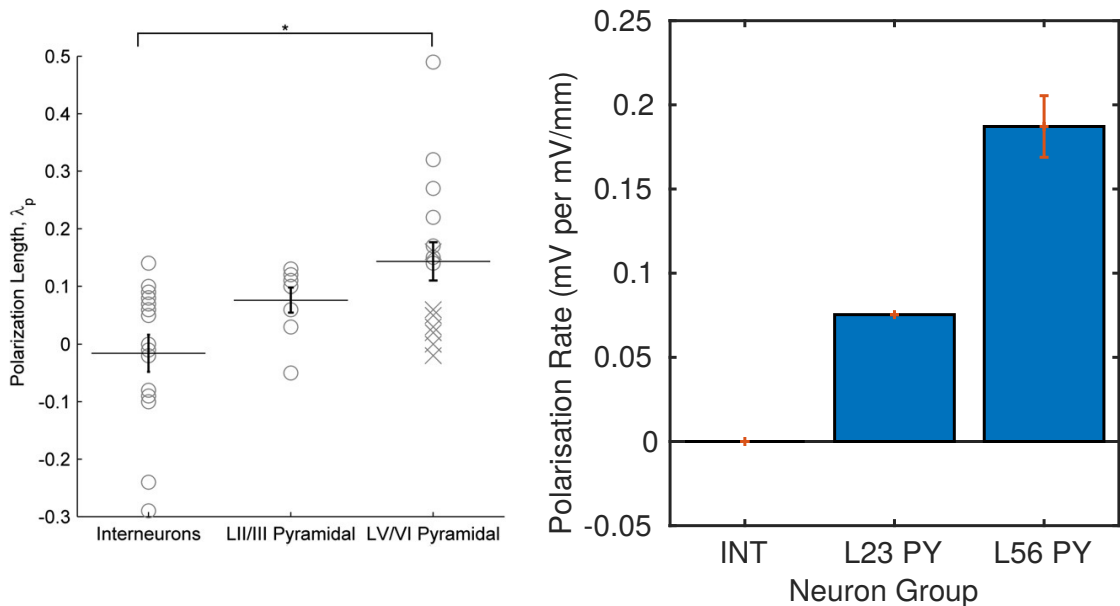


FIGURE 2.10. Shows the polarisation rate (or polarisation length as described by Radman et al. (2009)), a measure of the increase in steady state soma membrane polarisation with an increase in field strength. This is calculated as  $pr = \frac{cellpolarisation(mV)}{fieldstrength(mV/mm)}$ . (Left) Reproduced from Radman et al. (2009), shows the mean plus standard error of polarisation rates of interneurons, layer 2/3 pyramidal cells, and layer 5 or 6 pyramidal cells. Circles indicate the value found for individual cells, crosses show cells that had a severed dendritic tree. There is a significant difference between the interneurons and deep layer pyramidal cells (t test,  $p=0.06$ ) (Right) Shows the polarisation rate of interneurons, layer 2/3 pyramidal cells, and layer 5 thick tufted pyramidal cells in our model.

steady state polarisation of a single pyramidal cell and interneuron changes as the field strength varies. We can see that in the experimental results and in the simulated results that the polarisation increases or decreases linearly with the field strength, the gradient of this line can be used to summarise the sensitivity of the cell to the electric field as it indicates the cell polarisation achieved for every mV per mm increase in strength of the electric field. Here, we use the term polarisation rate and the units mV per mV/mm, however Radman et al. (2009) have reduced this to polarisation length (in mm). The field has negligible effects on the interneuron in our model, some of the interneurons measured by Radman et al. (2009) were sensitive to the field, including the one used to create the figure we reproduce in figure 2.9. The orientation of our model leads it to be exactly symmetrical to the field, resulting in the field having little effect on the membrane potential of the soma. As the interneurons measured by Radman et al. (2009) will not have this exact symmetry they will be affected by the field to some extent, however, we can see from figure 2.10 that on average they undergo very little

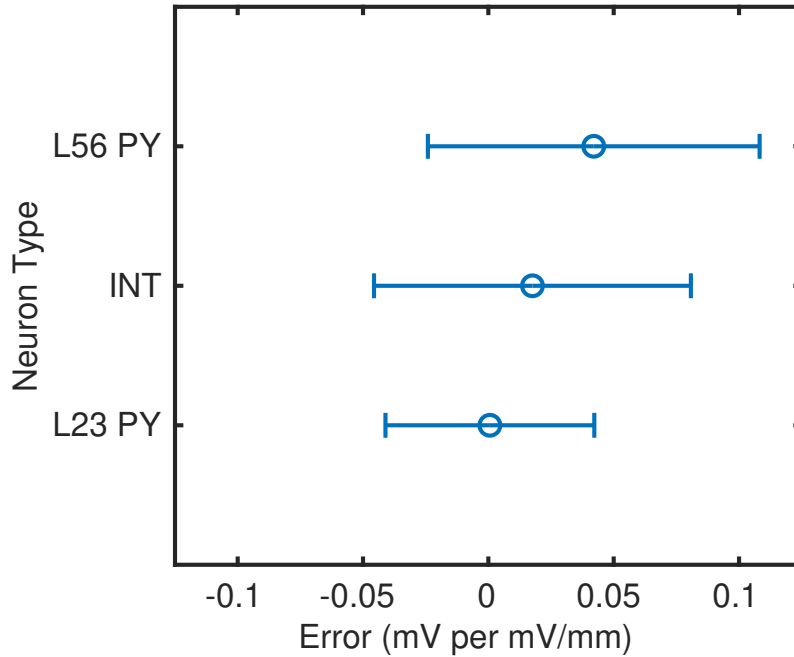


FIGURE 2.11. Shows the error (simulated - experimental) and 95% confidence interval of the polarisation rates of our reduced models compared with the *in vitro* results of Radman et al. (2009). The mean and standard deviation of the experimental results were derived from the chart. The confidence interval was calculated as  $C_i = 1.645 \sqrt{\frac{\sigma_e^2}{N_e} + \frac{\sigma_s^2}{N_s}}$ , where  $\sigma_e$  and  $N_e$  are the variance and number of samples of the experimental result and  $\sigma_s$  and  $N_s$  are the variance and number of samples of the simulated result.

polarisation in comparison to the other neuron types sampled. To compare our models to the results of Radman et al. (2009) we calculated a polarisation length for 100 samples of each cell type. The orientation of the cell relative to the field was selected at random from a uniform distribution between  $-\frac{\pi}{4}$  rad and  $\frac{\pi}{4}$  rad for the pyramidal cells and between  $-2\pi$  rad and  $2\pi$  rad for the interneuron. We show the polarisation rates of our reduced models compared with that of the experiments in figure 2.10. As can be seen our results compare well with the results of Radman et al. (2009) in terms of the magnitude of response and the relative effects on each cell type. We can see that on average the interneurons they measured have a polarisation rate of just below zero, of 0.08 mV per mV/mm for layer 2/3 pyramidal cells and of around 0.14 mV per mV/mm for the layer 5 pyramidal cell. We show the 90% confidence interval on the discrepancy between our models and the experimental results in figure 2.11. We can see that we are 90% confident that the error on the layer 2/3 pyramidal cell is between -0.05 and 0.05, indicating a good match. The interneuron is overestimated slightly, as they found a slightly negative polarisation rate, while our model has a polarisation rate

of zero. The layer 5 pyramidal cell is also over estimated, this could be because they have included neurons with severed dendritic trees in their analysis. Nevertheless, the polarisation rates of all three of our models fall within the range of values found by Radman et al. (2009) for their *in vitro* equivalents.

**2.3.4. Including stimulation in a VERTEX simulation.** We have described how electric field stimulation affects the neuron models used in VERTEX, comparing this to what we would expect from more detailed models, and from the effects recorded *in vitro*. To include electric field stimulation in a VERTEX simulation, one must provide a model of the electric field. Essentially this must be able to describe the electric potential at the compartments of each neuron in the model. This can be achieved for fields which can be described analytically by passing the name of a function. This user defined function should be able to take a set of 3D coordinates and return a value for each of them describing the electric potential at that point. The suggested option is to use 3D modelling software such as Blender to build a 3D model of the tissue and electrode. This can then be imported into MATLAB as an STL (STereoLithography) file. The MATLAB PDE toolbox can then be used to calculate the electric field and potential across the tissue using geometry provided, and user input regarding the boundary conditions and volume conductor equation. We describe how to do this for a bipolar electrode in chapter 3. The solution provided can then be passed to VERTEX as a StationarySolution object for static electric fields or a TimeDependentSolution object for time varying fields. This requires MATLAB 2016b or later and the PDE Toolbox, both are typically available at most universities. However, other more powerful and flexible software solutions for constructing finite element models of electric fields exist, such as ANSYS (2017) or COMSOL (Pryor, 2009). Interface to these can be achieved by the user defined function described above, or by providing a grid of pre-calculated electric potentials at sufficient resolution so that MATLAB can interpolate from this to the midpoints of each neuron compartment. Ideally, users wishing to import from external tools should investigate the possibility of interfacing between their tool and MATLAB to allow their tool to calculate the values precisely at the compartment midpoints. Figure 2.12 shows the workflow involved in creating a VERTEX simulation with electric field stimulation. When the field has been calculated, VERTEX will calculate the electric potential at the midpoint of the compartment of each neuron. Users must

also specify when the stimulation field is turned on and off. For stationary fields, they will be applied for the duration of their on time. Time-varying fields will be applied by looping through their time series at the same rate as the rest of the simulation, so that if they reach the end of their timecourse before they have been turned off they will continue again. This may save users time and memory as oscillating fields only need to be calculated for one full cycle.

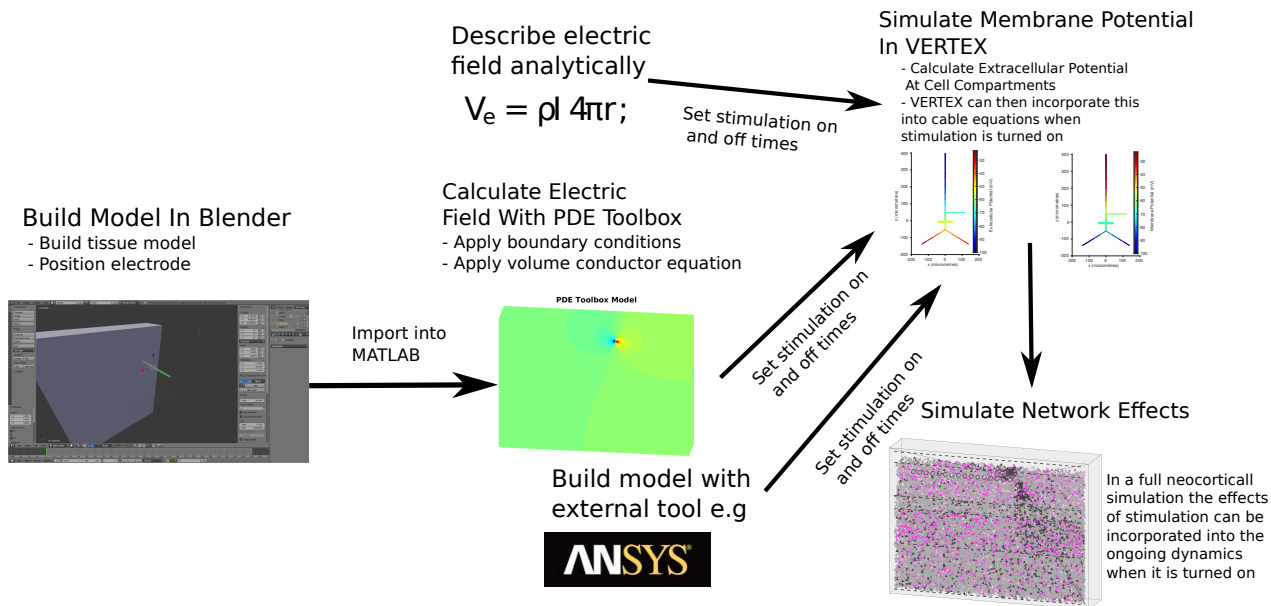


FIGURE 2.12. Illustrates how one would include a stimulating field into a VERTEX simulation. We show the three possible routes: a model described analytically by passing a MATLAB function with the equation, a model build with Blender and the MATLAB PDE toolbox, or a model built with external finite element modelling software such as ANSYS.

## 2.4. Adding synaptic plasticity to VERTEX

The efficacy of synaptic connections varies over time. Often these changes can be attributed to use-dependent plasticity - where the activity of the synapse and its constituent neurons determines the change. In VERTEX we take the synaptic efficacy to be the magnitude of the conductance or current depending on the synapse model type. So synaptic plasticity concerns the activity dependent changes in the conductance or current applied by a synapse. We have added phenomenological models of short term plasticity (STP) and spike-timing dependent plasticity (STDP) to the VERTEX simulator, and describe their implementation here.

### 2.4.1. Short term plasticity.

2.4.1.1. *Biology.* Short term plasticity has two components, facilitation (a short term increase in the efficacy of the synapse) and depression (a short term decrease). Both components are often present on the same synapse but the strength of one may mask the other (Wang et al., 2006). Short term depression occurs when the rate of replenishment of transmitter quanta is less than the rate of release; when a neuron endures sustained activation the replenishment of the transmitter-containing vesicles cannot keep up with their release, there is then less transmitter released and the post-synaptic response decreases (Hennig, 2013). Short term facilitation has been attributed to a facilitation of the release probability caused by a build up of calcium ions in the presynaptic terminal (Zucker and Regehr, 2002), which then positively modulates local calcium channels (Mochida et al., 2008). We have included two commonly used models of short term plasticity in the VERTEX simulator.

2.4.1.2. *The Abbott Model.* The first, which we refer to as the Abbott model, has been previously described and extensively used (Varela et al., 1997; Abbott and Regehr, 2004; Brody and Korngreen, 2013). It is a phenomenological model and unlike more detailed models of STP, such as those described by Hennig (2013), it does not directly follow any biological mechanisms. However, it does reproduce key aspects of STP observed in neocortex, can be parametrized by widely available measures, and implemented to run efficiently. It models feedforward (Abbott and Regehr, 2004) short term plasticity and so does not take in to account postsynaptic activity. The model contains two variables:  $F$  (the facilitation effect) and  $D$  (the depression effect) and four parameters:  $f$  the facilitation rate,  $d$  the depression rate,  $t_F$  the facilitation decay rate, and  $t_D$  the depression decay rate.  $F$  and  $D$  are both initially set to one,  $f$  should be greater than zero, and  $d$  should be between zero and one. When the presynaptic neuron generates an action potential each variable is updated according to the following rules:

$$F \rightarrow F + f \tag{2.4.1}$$

$$D \rightarrow D \cdot d \tag{2.4.2}$$

The facilitation effect is increased by the facilitation rate (equation 2.4.1), and the depression effect is multiplied by the depression rate (equation 2.4.2). Like Brody and Korngreen (2013) we add rather than multiply the facilitation rate to avoid unrealistic facilitation during high frequency activity. At each time step,  $F$  and  $D$  are both subject

to exponential decay (equations 2.4.3 and 2.4.4).

$$F \rightarrow F + \frac{(1 - F)}{t_F} \cdot dt \quad (2.4.3)$$

$$D \rightarrow D + \frac{(1 - D)}{t_D} \cdot dt \quad (2.4.4)$$

The facilitation and depression effects multiply the synaptic weight as it is applied (equation 2.4.5, where  $W_{baseline}$  is the initial weight). This allows synapse weights to depress to zero or to increase indefinitely under sustained firing and with the right conditions.  $D$  should always be one or less and decay back to one.  $F$  should always be one or more and decay back to one. The efficacy of the synapse at any given time is the original synaptic weight (a fixed conductance or current) multiplied by  $F$  and  $D$  (equation 2.4.5).  $F$  could be said to represent the level of calcium in the presynaptic terminal and  $D$  could represent the available quanta.

$$W \rightarrow F \cdot D \cdot W_{baseline} \quad (2.4.5)$$

2.4.1.3. *The Markram and Tsodyks model.* The second model is known as the Markram and Tsodyks model (Markram et al., 1997; Tsodyks et al., 1998). It uses four variables.  $x$ ,  $y$ , and  $z$  represent the fraction of resources available in recovered, active, and inactive states, with the resources available in the active state ( $y$ ) determining the instantaneous strength of the synapses when a spike occurs. The fourth variable,  $u$ , represents the proportion of resources that will actually be used during an event (the proportion of resources moving from  $x$  to  $y$ ). The variables update at each timestep according to equations 2.4.6 to 2.4.9. These are parametrised by  $\tau_I$  (the time constant of the post synaptic current),  $\tau_{rec}$  (the time constant for recovery from synaptic depression),  $\tau_{fac}$  (the time constant for facilitation), and  $U$  the utilization of synaptic efficacy which is considered analogous to the release probability of the synapse.

$$x \rightarrow x + \frac{z}{\tau_{rec}} \cdot dt \quad (2.4.6)$$

$$y \rightarrow y - \frac{y}{\tau_I} \cdot dt \quad (2.4.7)$$

$$z \rightarrow z + \left( \frac{y}{\tau_I} - \frac{z}{\tau_{rec}} \right) \cdot dt \quad (2.4.8)$$

$$u \rightarrow u - \frac{u}{\tau_{fac}} \cdot dt \quad (2.4.9)$$

As in the Abbott model there are also instantaneous updates that occur after a presynaptic spike. These are described in equations 2.4.10 to 2.4.12, with equation 2.4.13 describing the synaptic weight applied. This weight will either be a conductance or a current depending on the model type.

$$u \rightarrow u + U \cdot (1 - u) \quad (2.4.10)$$

$$y \rightarrow y + u \cdot x \quad (2.4.11)$$

$$x \rightarrow x - u \cdot x \quad (2.4.12)$$

$$W_{applied} \rightarrow y \cdot W_{baseline} \quad (2.4.13)$$

**2.4.1.4. Implementation.** Although variables relating to short term plasticity are notionally synapse specific, they are dependent only on the activity of the presynaptic cell. This allows us to save computational space and time by storing a single value for all synapses of a given type from each neuron.

In VERTEX, synapse types are defined on a cell type to cell type basis using a class which inherits from the synapse base class. A synapse class must provide a current to all neurons in its postsynaptic group in each iteration of the simulation loop. All variables and parameters needed to describe the state of the synapses from all neurons of one cell type to all neurons of another are stored as matrices in the synapse object. When updated with a spike, typical synapse models must be given the ID number of the neurons postsynaptic to the one that produced the spike, so that the correct currents or conductances can be added to the spike effect accumulator. This is then processed to provide a current to each of the postsynaptic neurons. More details on the implementation of the synapse models is provided in appendix E.

**2.4.2. Spike-timing dependent plasticity.** As discussed in the introduction, spike-timing dependent plasticity (STDP) is dependent on the recent activity of the pre and postsynaptic neuron. It allows Hebbian-like learning to occur, whereby synapses that contribute to the firing of a neuron are strengthened while those that do not are weakened. To the VERTEX simulator we have added a class of synapses that implements a common form of STDP. Here we describe the biology that this model seeks to represent and the implementation within VERTEX.

2.4.2.1. *Biology.* The cellular mechanisms of spike-timing dependent plasticity are specific to the synapse type. For many glutamatergic synapses the NMDA receptor and calcium signalling play a key role. The NMDA receptor is an ionotropic glutamate receptor which is normally blocked by  $Mg^{2+}$  ions preventing presynaptic glutamate release from causing an influx of ions. When the postsynaptic cell is depolarised the  $Mg^{2+}$  ions are repelled from the channel. Activation of the NMDA receptor under physiological conditions then acts a detection of presynaptic firing and postsynaptic depolarisation caused by action potentials propagating down the dendrites. The opening of the NMDA receptor without the  $Mg^{2+}$  block allows an influx of  $Ca^{2+}$  (Feldman, 2012). Large fast rises in  $Ca^{2+}$  caused by combination of the removal of  $Mg^{2+}$  and presynaptic glutamate release provoke a signalling pathway that leads to LTP, while a steady lower amplitude rise in  $Ca^{2+}$  leads to LTD (Yang et al., 1999). In the presynaptic spike followed by postsynaptic spike scenario, the  $Ca^{2+}$  influx is large because the EPSP caused by the activation of the AMPA receptors coincides with the back propagating action potential. In the postsynaptic spike followed by presynaptic spike scenario, the depolarisation caused by the back propagating action potential has already decayed significantly by the arrival of the EPSP, and so there are smaller currents produced by NMDA receptor activation, and so only modest calcium influx (Feldman, 2012).

2.4.2.2. *Model.* To model the spike timing dependent plasticity, we look only to the relative spike timing, rather than modelling the process explicitly. The logic of the model can be described as follows: For each synapse if the postsynaptic neuron fires a short time after the presynaptic neuron (indicating that the presynaptic neuron contributed to it firing) then the synapse will strengthen. If the opposite occurs - a presynaptic neuron fires shortly after the postsynaptic neuron - then the synapse will weaken (Feldman, 2012). Each synapse is specified by a pair of time windows, one for the postsynaptic neuron firing, one for the presynaptic neuron firing. These define the extent of the weight change given how much time has passed when the second spike occurs after the first one. Equations 2.4.14 and 2.4.15 describe how the trace variables  $A_{pre}$  and  $A_{post}$  are updated after a presynaptic and postsynaptic spike respectively.  $\Delta A_{pre}$  is the maximum change in synaptic weight for a pre before post spike pair, and  $\Delta A_{post}$  is the maximum change in synaptic weight for a post before pre spike pair. To

implement typical STDP rules  $\Delta A_{pre}$  would be positive and  $\Delta A_{post}$  would be negative.

$$A_{pre} \rightarrow A_{pre} + \Delta A_{pre} \quad (2.4.14)$$

$$A_{post} \rightarrow A_{post} + \Delta A_{post} \quad (2.4.15)$$

Equations 2.4.16 and 2.4.17 are applied at each time step and show how  $A_{pre}$  and  $A_{post}$  decay to zero according to their respective decay rates,  $t_{Pre}$  and  $t_{Post}$ .

$$A_{pre} \rightarrow A_{pre} + \frac{-A_{pre}}{t_{Pre}} \cdot dt \quad (2.4.16)$$

$$A_{post} \rightarrow A_{post} + \frac{-A_{post}}{t_{Post}} \cdot dt \quad (2.4.17)$$

When a postsynaptic spike occurs the synaptic weight is modified by equation 2.4.18:

$$w \rightarrow w + A_{pre} \quad (2.4.18)$$

When a presynaptic spike occurs the synaptic weight is modified by equation 2.4.19:

$$w \rightarrow w + A_{post} \quad (2.4.19)$$

**2.4.2.3. Implementation.** As VERTEX is written in an interpreted language (MATLAB), its execution speed is greatly aided by vectorised code. We have utilised the techniques described by Brette and Goodman (2011) to vectorise our implementation and keep memory usage minimal. Our implementation has two variables.  $A_{pre}$  is updated (equation 2.4.14) when a presynaptic spike occurs and describes the magnitude of the weight change that would occur if the postsynaptic neuron were to fire at any point in time.  $A_{post}$  is updated (equation 2.4.15) when a postsynaptic spike occurs and represents the magnitude of the weight change that would occur if the presynaptic neuron were to spike at any time. The rate at which each changes is typically equal but opposite with  $A_{post}$  being negative, and their magnitude specified by a single parameter.

**2.4.2.4. Delays.** When modelling STDP it is important to consider delays - between the presynaptic neuron firing and the action potential reaching the synapse (axonal delay), and between the post synaptic neuron firing and the backpropagating action

potential reaching the relevant part of the dendrite (dendritic delay) (Morrison and Diesmann, 2008). As there is no vectorised solution to introduce dendritic delays, and as the axonal delay will dominate in most scenarios (Brette and Goodman, 2011), we consider only the axonal delay. To incorporate this, we introduce a delay into the update rules for the weight change (equations 2.4.18 and 2.4.19 become 2.4.20 and 2.4.21 ), equations 2.4.14 and 2.4.15 remain the same.

$$w(t_{post}) \rightarrow w(t_{post}) + A_{pre}(t_{post} - d) \quad (2.4.20)$$

$$w(t_{pre} + d) \rightarrow w(t_{pre} + d) + A_{post}(t_{pre} + d) \quad (2.4.21)$$

Where  $t_{post}$  is the time of the postsynaptic spike and  $t_{pre}$  is the time of the presynaptic spike. To implement 2.4.20 we require access to past values of  $A_{pre}$ , and so  $A_{pre}$  becomes a two-dimensional array, so that each entry for each presynaptic neuron contains a circular array which stores a trace of  $A_{pre}$  values. This is illustrated in figure 2.13. Equation 2.4.21 cannot be vectorised over all postsynaptic neurons because the delay is inhomogeneous. Instead, we record a snapshot of activated synapses in a circular array. A buffer count points to the current location and the pre and post IDs of the activated synapse are placed into the array at  $t_{pre} + delay$ . We can then vectorise the operation over all postsynaptic neurons that are receiving a spike at each time step. As including delays requires additional resources and is not always required we incorporate it in an additional STDP\_delays class.

## 2.5. Discussion

We have added a mechanism for simulating the effects of electric field stimulation on neocortical networks created using the Virtual Electrode Recording Tool for Extracellular potentials (VERTEX). Electric fields described analytically or calculated numerically using MATLAB's partial differential equation toolbox (or an external tool that can export to MATLAB) can be incorporated into the simulation. We have looked at the effects of monopolar and uniform field stimulation on interneurons, layer 2/3 pyramidal cells and layer 5 thick tufted pyramidal cells. For uniform field stimulation we replicated the *in vitro* data of Radman et al. (2009), showing that our reduced neuron models produce similar rates of polarisation to varying strengths of uniform field stimulation. This gives us confidence in our reduced models for simulating the

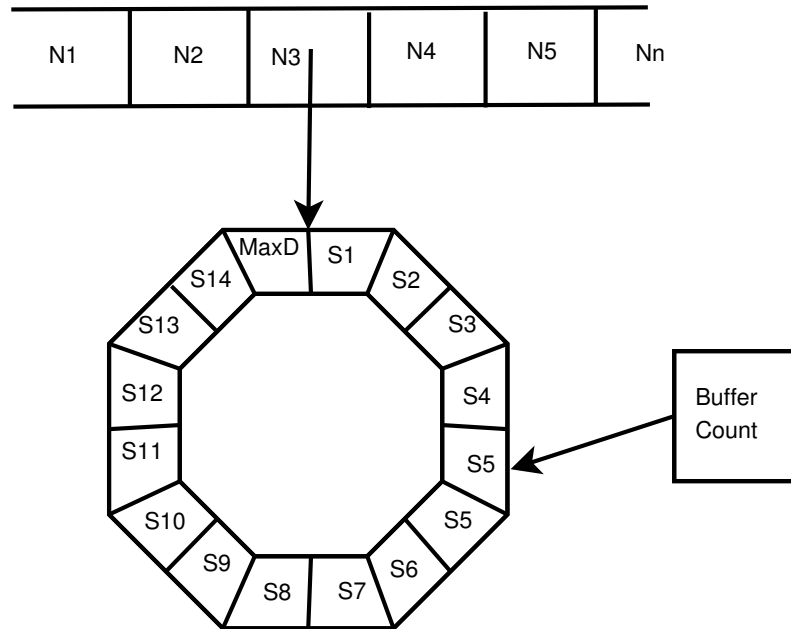


FIGURE 2.13. The data structure storing the  $A_{pre}$  variable for the STDP model with delays. The first dimension of the array has an entry for each presynaptic neuron (N1 to Nn) the entry points to a unique circular array (buffer) with an entry for each delay step (S1 to the max delay steps, specified as a parameter). This stores the value of  $A_{pre}$  for present and past time points. There is a buffer count that points to the location in the buffer that corresponds to the present.

effects of uniform electric fields *in vitro* but also for simulating non-invasive electric field stimulation. For monopolar stimulation we compared the response of a detailed model to that of reduced models with varying compartment sizes. We find that reducing the fidelity of the model introduces errors of between 5 and 10 % at the steady state but errors of up to 60 % for shorter stimulus durations. We have also evaluated the effect of using a simplified morphology in our model. This was found to introduce a significant overestimation of the response in the pyramidal cells when compared with the response in detailed reconstructions of the equivalent cells. Adjusting the dendrite diameter to better match that of the detailed model was shown to reduce the error and the dendrite diameter has been previously shown to have a significant influence on the response to electric field stimulation through its effect on the axial resistance of the cell (Yi et al., 2017). An issue with simply reducing the diameter is that this will alter the processing of synaptic inputs (Bush and Sejnowski, 1993) and LFP generation (Tomsett et al., 2015). One solution to this would be to use two models. For one model we could fit the passive properties so that it best captures the response of the detailed cell to the type of stimulation we are interested in modelling. This model could be used

to capture the effect of stimulation, while the original model would be used for processing synaptic inputs and generating the LFP. If the altered model was constrained to having the same compartments, just with alternative passive properties, then this would result in simply two sets of axial resistances, one of which would only be used for calculating the axial currents produced by stimulation (the final two expressions in equation 2.2.2). We have also added two models of synaptic plasticity: short term plasticity and spike timing dependent plasticity. The VERTEX simulator now has the infrastructure so that it can be extended to include other models of plasticity by the addition of a new synapse class that extends the STP class for plasticity dependent only on presynaptic activity or on the STDP class for plasticity dependent on both pre and postsynaptic activity. VERTEX can now be used to simulate electric field evoked potentials and incorporate the effects of synaptic plasticity, as we demonstrate in the following chapter.

# A Model Of stimulus-evoked Activity In Rat Somatosensory Cortex

## 3.1. Introduction

In this chapter we outline a model of stimulus evoked activity in rat somatosensory cortex created using the VERTEX simulator. In doing so, we illustrate how one can create and incorporate a finite element model of the electric field created by a bipolar stimulating electrode into the VERTEX simulator to produce simulations of two experimental paradigms. Much work has been done creating realistic finite element models of electric field stimulation in resected tissue (Joucla et al., 2014, 2012b) and models of transcranial stimulation in the living brain (Seo et al., 2016). This allows more complex geometries to be modelled in comparison to the analytic solution used in section 2.3 to model monopolar stimulation. We have added support to the VERTEX simulator to allow models of this nature to be easily incorporated and applied. Here we illustrate this in an example model of a bipolar stimulating electrode in a rat neocortical brain slice. We describe in detail the immediately evoked activity (directly comparing with published experimental data) as well as the synaptic dynamics that result from repetitive stimulation, both in the short term (short term plasticity) and long term (spike-timing dependent plasticity). We show how the tool may be used to aid in the interpretation of the response to stimulation by revealing the cells and currents that contribute to the initial field potential, the changes to synaptic weights induced by repetitive stimulation, and how both residual inhibition and short term plasticity both contribute to paired pulse depression.

**3.1.1. Long term potentiation and theta burst stimulation.** Long term potentiation (LTP) usually describes a stable change in the efficacy of synapses after a brief tetanic stimulation. It was first shown to occur in the hippocampus (Bliss and Lomo, 1973) but has since been observed *in vitro* and *in vivo* in a range of brain areas including the neocortex (Bliss and Lomo, 1973; Teyler and DiScenna, 1987; Tsumoto,

1990). The order and timing of input has been shown to be of critical importance when inducing LTP in a particular connection. The connection must be activated within a time window (usually around 20 ms) before the postsynaptic site has been activated. Long term depression (LTD) occurs when the connection is activated after the postsynaptic site and manifests as a decrease in synaptic efficacy. Although it does not capture all processes that lead to LTP or LTD (Clopath et al., 2010) it is thought that the spike-timing dependent plasticity rule described in chapter 2 does capture some of the conditions which lead to long term synaptic changes (Dan and Poo, 2004). The tetanic stimulation used to induce LTP varies, however theta burst stimulation (TBS) has been shown to induce LTP in hippocampus and neocortex (Walcott and Langdon, 2002). Its mechanism of action in the hippocampus has been thoroughly characterised (Larson and Munkácsy, 2016) however, in neocortex it can not be so reliably induced, and its mechanism of action is not as clear (Walcott and Langdon, 2002). We propose using a VERTEX simulation of TBS in rat neocortex as a step towards a greater understanding of this mechanism.

### **3.1.2. Paired pulse stimulation and ambiguities in the paired pulse ratio.**

Applying paired pulses of stimulation and measuring the respective responses as a function of the interval is a common technique for characterising dynamical systems (Bouteiller et al., 2014). It has often been used to study the dynamics of synapse strength, usually to quantify the effect of previous synaptic activation on the synapse strength in the short term (Zucker and Regehr, 2002; Regehr, 2012). To this end it has been applied via the electrical field stimulation (Varela et al., 1997) of populations of neurons with the output measured via the field potential response, and intracellular stimulation of a single neuron while recording from cells on which it forms synapses (Reyes et al., 1998; Beierlein, 2003). When studying the neocortex the latter has become more popular because it allows individual connections to be more precisely targeted - field stimulation targets a multitude of cell types, and field potentials relate to the postsynaptic currents but this relationship is complex (Einevoll et al., 2013). On the other hand the field potential represents the sum of currents arriving at many thousands of cells (Einevoll et al., 2013) averaging out the neuron level variance, and are easier to record *in vivo*. As well as measuring short term synaptic dynamics, paired pulse stimulation is also often applied to measure the overall strength of inhibition

present in a network (Waldbaum and Dudek, 2009; Queiroz et al., 2009; David et al., 2010; Mesgari et al., 2015). Here, the suppression of response to the test stimulus (second pulse), compared with the response to the conditioning stimulus (first pulse) acts as a proxy for the strength of inhibition in the network. In a network with stronger inhibition the residual inhibitory currents present when the second stimulus is applied will be stronger, and so reduce the recruitment. This inhibitory strength is usually loosely defined, and a number of mechanisms could influence the strength of suppression, including the efficacy of inhibitory synapses, the efficacy of excitatory synapses onto inhibitory cells, or the firing properties of inhibitory cells. The time scale of this suppression can extend to 200 ms after the first stimulation (Waldbaum and Dudek, 2009) and so will overlap with the effects of the synaptic dynamics. To properly interpret the field potential response we will have to untangle the effect of synapse dynamics from that of residual inhibition. In this chapter we aim to show that simulating a paired pulse experiment using the forward modelling approach of VERTEX can firstly give us an estimate of the source of the field potential. It can also give us an estimate of the strength of those synapses that contribute most to the field potential and the strength of the inhibitory suppression during the test stimulus. This will allow us to break down the paired pulse ratio into a component contributed by the synapse dynamics and a component contributed by the inhibitory suppression.

### 3.2. Rat Neocortical Microcircuit

We build the network used in our simulation using knowledge of the local cortical microcircuit. Local circuit connectivity can be defined in terms of the cell-type and layer specific connection probabilities. These patterns influence the nature of spontaneous and evoked activity. Several studies have sought to reveal the local circuit connectivity by using anatomical or electrophysiological measures to create a map of connectivity probabilities between cell types and layers (Binzegger et al., 2004; Thomson, 2002; Ramaswamy et al., 2015). These maps allow simulations of cortical dynamics to be embedded in an estimation of the anatomy of the cortical circuit. The implications that this measured anatomy has for the simulated dynamics can be seen in the activity within in each layer and each cell-type. It has been shown that the anatomy measured by Binzegger et al. (2004) and Thomson (2002) implies the same flow of activity through cortex as that measured *in vivo* after transient thalamic stimulation

(Potjans and Diesmann, 2014). *In vitro* results have also been replicated, with Tomsett et al. (2015) showing similarities in the properties of their model of gamma oscillations in macaque neocortex when compared with those measured in neocortical slices bathed in kainate to induce gamma oscillations.

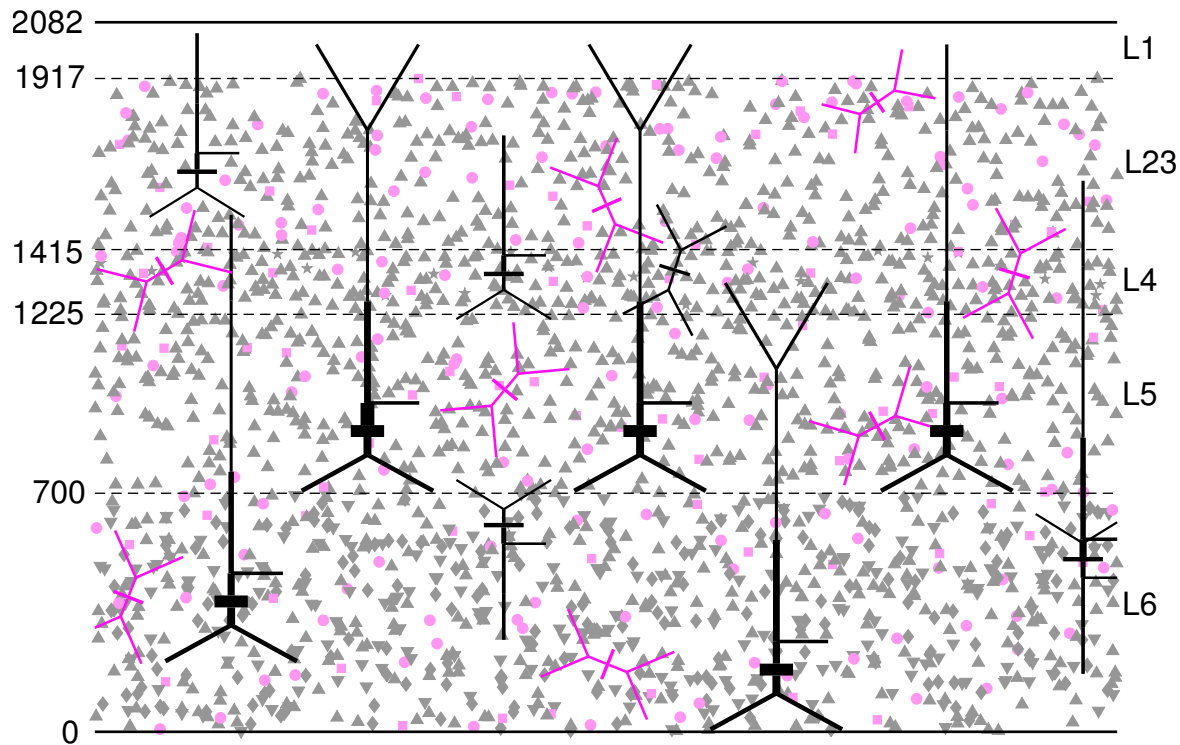


FIGURE 3.1. The structure of the neocortical slice model. The layer boundaries are shown as the dashed lines with the distance from the white matter given in  $\mu\text{m}$  on the left. The rat somatosensory cortex has 6 layers, layer 1 contains no neurons and layers 2 and 3 have been combined. The position in the  $x$  and  $z$  planes of each neuron soma is shown, pink signifies inhibitory cells, grey signifies excitatory. The triangles are various types of pyramidal cell, stars are spiny stellate cells, circles are basket cells, and squares Martinotti cells. The full geometry of a selection of cell types are also shown.

**3.2.1. Parameterising the model.** We take an approach similar to Tomsett et al. (2015), constructing a model of rat somatosensory cortex in VERTEX using the data from the the Neocortical Microcircuit Collaborative Portal (NMCP) (Ramaswamy et al., 2015). From here we adapt the neuron density, the neuron group types present and their proportions, the number of connections between the neuron groups, and their synaptic properties. We use the Markram and Tsodyks model of short term plasticity described in chapter 2 to capture the short term dynamics of the synapses. All parameters for this are taken from the NMCP, these include a mean and standard deviation for each allowing us to draw our synaptic parameters from a experimentally

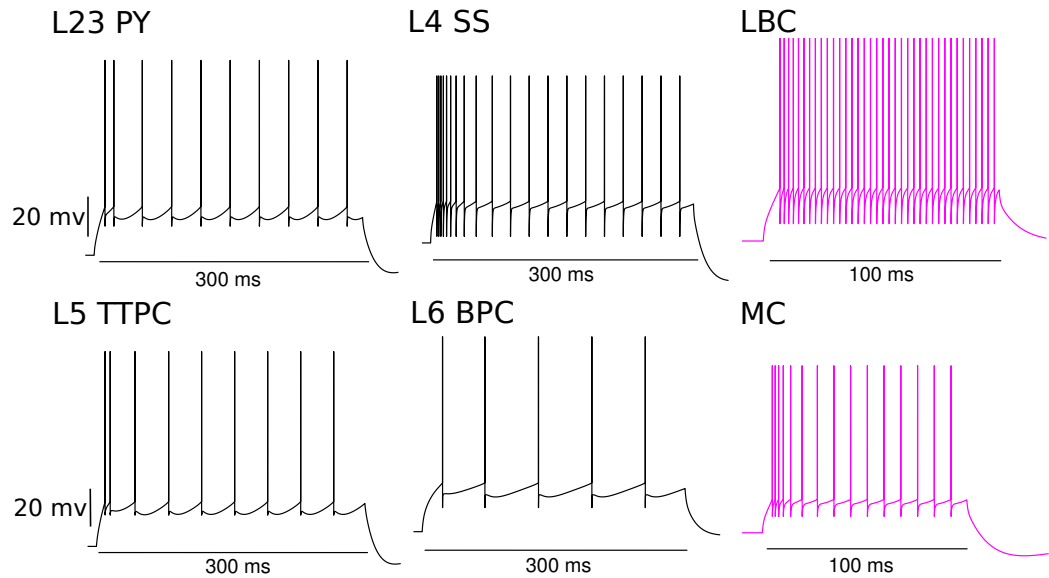


FIGURE 3.2. The response of a selection of neuron types to current injection. The amplitudes of injected current were: 500 pA for the L23 PY, 300 pA for the L4 SS, 400 for the LBC, 1000 pA for the L5 TTPC, 500 for the L6 BPC, and 400 for the MC. The adaptive exponential integrate and fire model resets at a given threshold  $V_t$ , we have extended the trace to 30 mV for illustrative purposes.

measured distribution of values. Following the approach of Markram et al. (2015) we construct a normal distribution for each synaptic parameter based on the mean and standard deviation provided. This distribution is truncated for those parameters (such as synaptic conductance and time constant) that must be positive. For each new connection formed as the network is built, a set of parameters are drawn from these distributions. The time constants used for facilitation and depression of synapses are shown in figures 3.4 and 3.5 respectively. We model a typical *in vitro* neocortical slice preparation measuring 2000  $\mu\text{m}$  horizontally, 2082  $\mu\text{m}$  vertically x 400  $\mu\text{m}$  deep. It contains layers 1 - 6 but with layer one containing no neurons and layers 2 and 3 combined. The full slice model has a density of 103730 cells per  $\text{mm}^3$  giving a total of 172773 neurons in the simulation. Figure 3.1 shows the layout of the slice, with sample geometries and the soma positions of 5 % of neurons. 29 neuron types are included, defined by their layer of location, morphology, intrinsic dynamics, and connectivity. Table 3.1 shows the proportion of each neuron type within the model. Figure 3.2 shows the response of a selection of neuron types to current injections. We can see regular-spiking pyramidal cells (L23 PY, L5 TTPC, L6 BPC), low threshold-firing Martinotti cells (MC), and fast-firing basket cells (LBC). The number of connections between neuron groups is shown in figure 3.3, we can see the strong connectivity from

layer 2/3 pyramidal cells to all cells in layers 2 to 5. We can also see that other neuron types tend to preferentially synapse onto and receive synapses from neurons in their own layer. Like Tomsett et al. (2015) and Hellwig (2000) we use a 2D Gaussian spatial profile to calculate the probability of connection with increasing distance from the presynaptic neuron in the X and Z planes. In the Y plane, the connection probability is constant. The mean and standard deviation are set using estimates of the axonal arbourisation adapted from Schnepel et al. (2015).

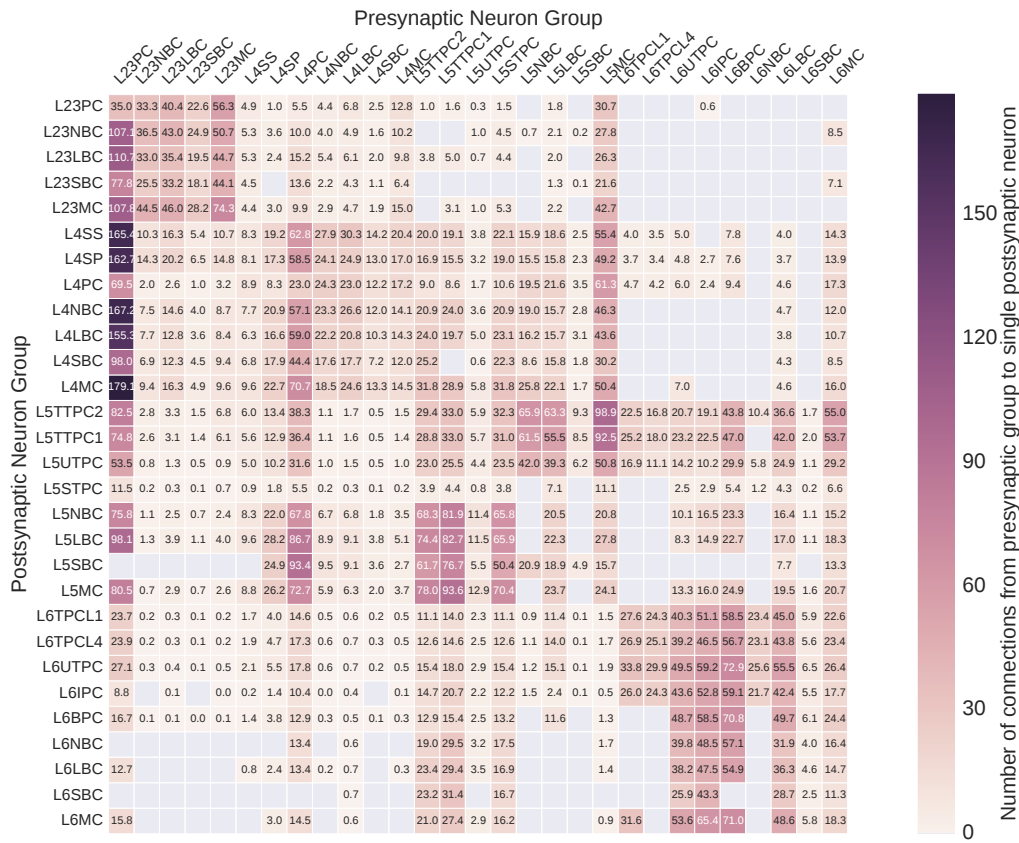


FIGURE 3.3. The expected number of connections from the population of presynaptic neurons in the presynaptic group to a single neuron in the postsynaptic group. Based on the data from Ramaswamy et al. (2015)

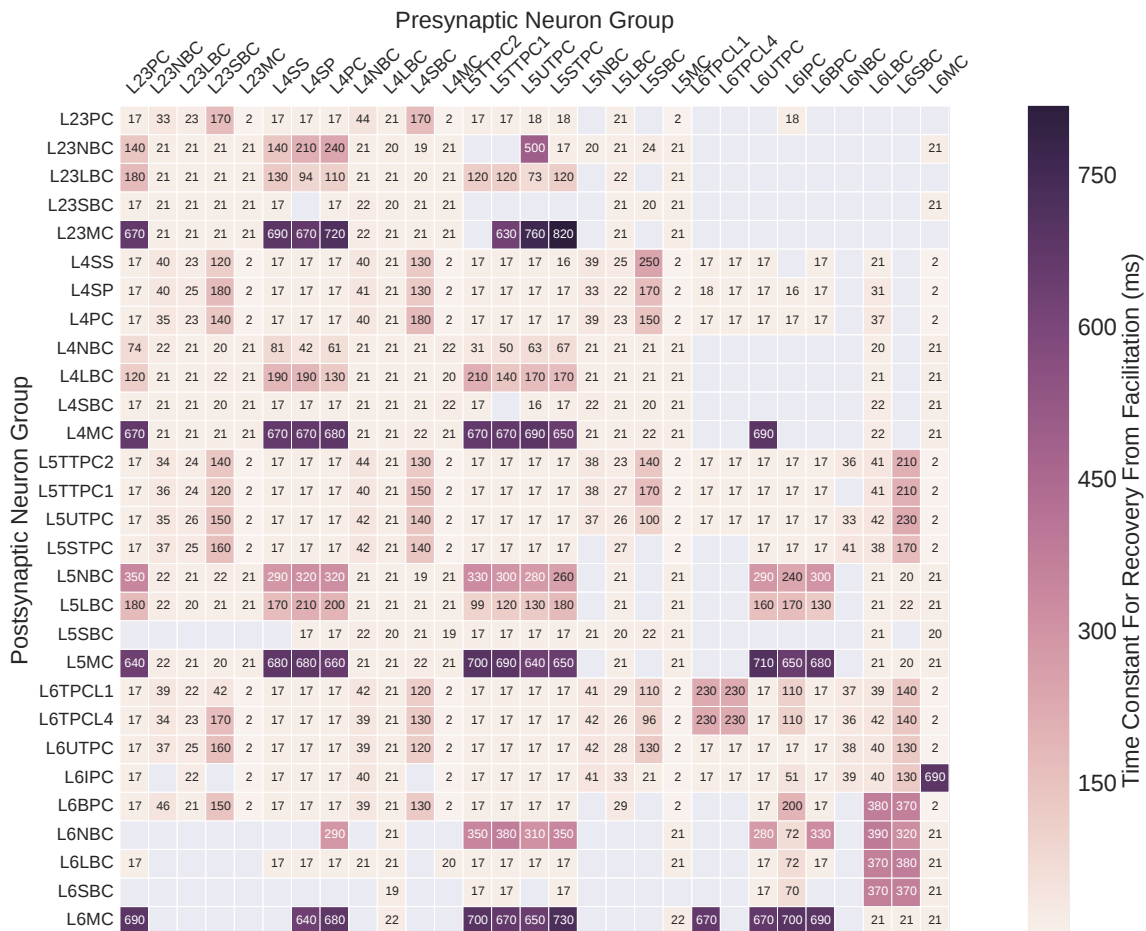


FIGURE 3.4. The time constant for facilitation of synapses between the cell types of rat somatosensory cortex. Based on the data from Ramaswamy et al. (2015)

### 3.3. Creating a finite element model of a bipolar electrode and brain slice

The modelling process requires us to specify a 3D model of the tissue and electrode, as well as their electrical properties. These include the conductivity of the tissue and the electrical potential at either electrode when the stimulation is turned on.

**3.3.1. Creating the 3D model:** Using the Blender 3D modelling tool we have created a 3D model of the tissue and extracellular medium and the electrode, seen in figure 3.6. The tissue and extracellular medium was modelled as a cuboid,  $3000 \mu\text{m} \times 2700 \mu\text{m} \times 500 \mu\text{m}$ , and the electrode as two  $40 \mu\text{m} \times 40 \mu\text{m}$  cuboidal indents into the tissue separated by a space of  $80 \mu\text{m}$ . The model of the extracellular medium extends beyond that of the tissue, in particular it extends  $100 \mu\text{m}$  deeper than the tissue would, allowing for the flow of current through the bathing solution below the tissue. This is shown in figure 3.7. We then used the MATLAB Partial Differential Equation toolbox

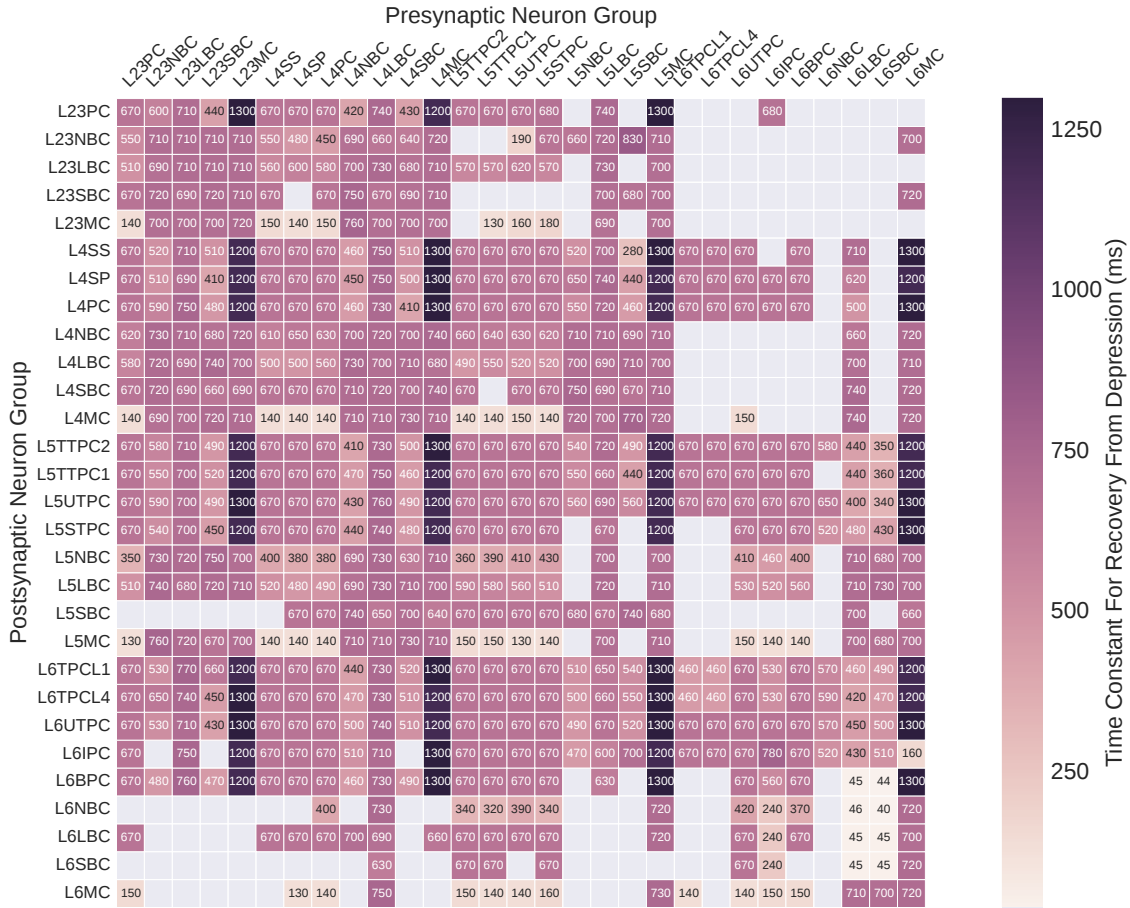


FIGURE 3.5. The time constant for depression of synapses between the cell types of rat somatosensory cortex. Based on the data from Ramaswamy et al. (2015)

(The MathWorks, Inc., Natick, Massachusetts, 2016) to calculate the electric potential across the slice as a result of applying a potential difference at the two electrodes.

**3.3.2. The volume conductor equation:** Following Joucla et al. (2012a) we model our system as a direct current between two dipoles in a conductive media. This begins with Ohm's law generalised for a field  $\sigma \vec{E} = \vec{J}$ , where  $\vec{E}$  is the electric field (a vector field),  $\vec{J}$  is the current density (a vector field), and  $\sigma$  is the conductivity (a scalar field). We then use the relationship between the electric field and the electric potential ( $V$ , a scalar field)  $\vec{E} = -\nabla V$ , and the relationship between current density and current source ( $Q$ , a scalar field)  $\nabla \cdot \vec{J} = Q$  to get the Poisson equation (equation 3.3.1) for our volume conductor equation. Using the vector calculus notation used by Feynman (1963),  $\nabla$  is the vector operator which when applied to a scalar field will produce a vector field by calculating the gradient in each dimension (e.g.  $\nabla T = (\frac{\partial T}{\partial x}, \frac{\partial T}{\partial y}, \frac{\partial T}{\partial z})$ , where  $T$  is some scalar field). The vector operator combined with the dot product is known as the divergence ( $\nabla \cdot$ ), this can be applied to a vector field to produce a scalar

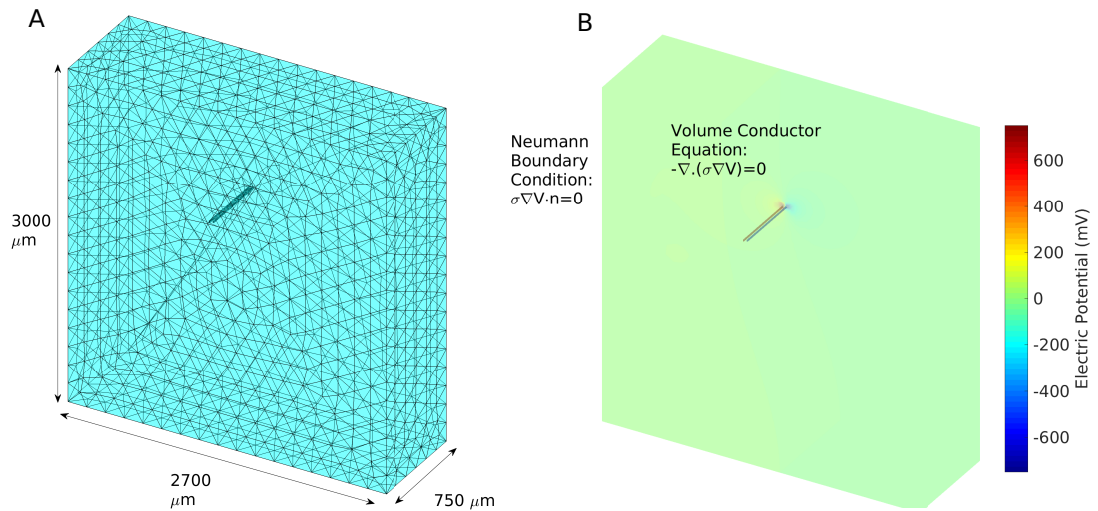


FIGURE 3.6. (A) The 3D mesh. The initial geometry was built using Blender (essentially a cuboid representing the tissue with the two cuboidal electrodes cut out). The geometry is then meshed using the PDE toolbox. (B) The potential field calculated using the PDE toolbox. The equations used for this are shown in the figure, here  $\sigma$  is the conductivity, and  $V$  is the electrical potential. The Poisson equation is used as the volume conductor equation, Neumann boundary condition (representing no current flowing) has been used for the boundary of the tissue/extracellular fluid with the air or recording chamber, here  $n$  is the outermost vector normal to the boundary. The Dirichlet boundary condition ( $V = A$ ) has been used for the electrodes. Where  $A$  is the amplitude of the stimulation in mV and will be positive at one electrode and negative at the other.

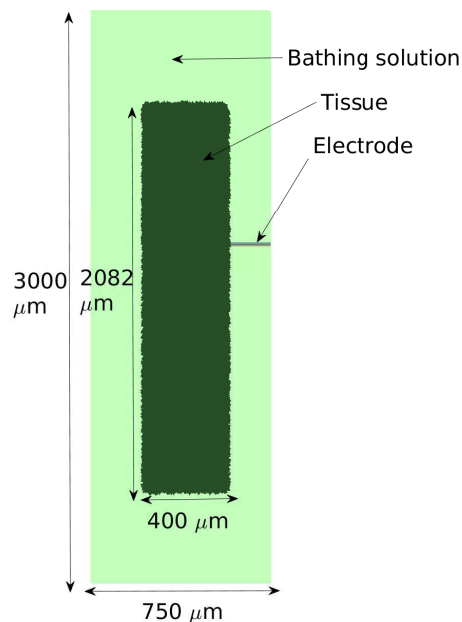


FIGURE 3.7. Shows the tissue placed within the electric field. The volume used to model the electric field encompasses the tissue and its surrounding bathing solution. The bathing solution has a conductivity in the same range as that of the grey matter and so we assume a homogeneous conductivity in the volume.

TABLE 3.1. The 29 neuron types present in the model, along with their layer, their synaptic reversal potential (RP) indicating whether they are excitatory or inhibitory, and the proportion of the model they compose.

Neuron Group	Neuron Type	Layer	RP (mV)	Proportion
L23PC	Pyramidal Cell	2/3	0	0.1849
L23NBC	Nest Basket Cell	2/3	-70	0.0084
L23LBC	Large Basket Cell	2/3	-70	0.0143
L23SBC	Small Basket Cell	2/3	-70	0.0052
L23MC	Martinotti Cell	2/3	-70	0.0105
L4SS	Spiny Stellate	4	0	0.0128
L4SP	Star Pyramid	4	0	0.0345
L4PY	Pyramidal Cell	4	0	0.0841
L4NBC	Nest Basket Cell	4	-70	0.0030
L4LBC	Large Basket Cell	4	-70	0.0038
L4SBC	Small Basket Cell	4	-70	0.0019
L4MC	Martinotti Cell	4	-70	0.0037
L5TTPC1	Thick Tufted Pyramidal Cell	5	0	0.0630
L5TTPC2	Thick Tufted Pyramidal Cell	5	0	0.0765
L5UTPC	Untufted Pyramidal Cell	5	0	0.0108
L5STPC	Slender Tufted Pyramidal Cell	5	0	0.0630
L5NBC	Nest Basket Cell	5	-70	0.0063
L5LBC	Large Basket Cell	5	-70	0.0066
L5SBC	Small Basket Cell	5	-70	0.0007
L5MC	Martinotti Cell	5	-70	0.0124
L6TPC.L1	Tufted Pyramidal To Layer 1	6	0	0.0515
L6TPC.L4	Tufted Pyramidal To Layer 4	6	0	0.0453
L6UTPC	Untufted Pyramidal Cell	6	0	0.0546
L6IPC	Inverted Pyramidal Cell	6	0	0.1094
L6BPC	Bitufted Pyramidal Cell	6	0	0.0999
L6NBC	Nest Basket Cell	6	-70	0.0062
L6LBC	Large Basket Cell	6	-70	0.0146
L6SBC	Small Basket Cell	6	-70	0.0021
L6MC	Martinotti Cell	6	-70	0.0106

field (e.g.  $\nabla \cdot \vec{H} = (\frac{\partial H_x}{\partial x} + \frac{\partial H_y}{\partial y} + \frac{\partial H_z}{\partial z})$ , where  $\vec{H}$  is some vector field). As there is no current source (other than at the boundary with the electrode) in our scenario  $Q$  is zero, giving equation 3.3.2. Estimates for the conductivity of the extracellular medium (the grey matter or cerebrospinal fluid) range from 0.1 S/m to 0.3 S/m (Joucla and Yvert, 2012; Latikka et al., 2001; Gabriel et al., 2009), we have used a value of 0.3 S/m.

$$-\nabla \cdot (\sigma \nabla V) = Q \quad (3.3.1)$$

$$-\nabla \cdot (\sigma \nabla V) = 0 \quad (3.3.2)$$

**3.3.3. The boundary conditions:** We assume that the outer edges of the model, where the slice comes into contact with the media in the recording chamber, are insulating boundaries where no current flows. These are represented by the Neumann

boundary condition (equation 3.3.3).

$$\sigma \nabla V \cdot n = 0 \quad (3.3.3)$$

Where  $\sigma$  is again the conductivity of the medium,  $n$  is the outermost vector normal to the boundary, and  $V$  is the potential.

With the volume conductor equation and boundary conditions set the electric potential within the tissue when stimulation is turned on can be calculated.

The partial differential equation (PDE) solution describing the extracellular potential throughout the tissue can then be passed into VERTEX when we specify our simulation parameters. Having received the solution VERTEX will calculate the value of the field at the midpoint of each neuron compartment ( $V_e$ , as described in chapter 2) and store these for simulation. For time dependent solutions this value will be calculated and stored for each point in its cycle at the resolution defined by the timestep of the simulation. When stimulation is turned on the extracellular potential will be incorporated into the solving of the cable equation, according to equation 2.2.2.

### 3.4. Response To Stimulation

In this section we explore the activity generated in the network as a result of stimulation using the bipolar electrode. We first look in detail at the response to a single pulse of stimulation, before moving on to look at how this stimulation can create long term changes in the network through spike-timing dependent plasticity, and how short term synaptic plasticity alters the response in the short term.

**3.4.1. Single Pulse Stimulation.** We began by investigating how our network responded to a single pulse of stimulating current delivered to layer 4. This is a common paradigm, and responses are expected in both superficial layers and deep layers (Kirkwood et al., 1993). The response to stimulation was characterised at several stages, the initial recruitment (the cells directly recruited by stimulation), the subsequent synaptic currents and the LFPs they generate, and finally the secondary recruitment (the cells recruited by these currents). We took the results of Walcott and Langdon (2002) for comparison, as they provide a detailed description of the field waveforms recorded in layer 2/3 after stimulation in layer 4, as well as descriptions of multi-unit activity. They

also provide descriptions of the waveform with the stimulus artefact subtracted so that we can see early currents important in identifying the pattern of activity invoked.

3.4.1.1. *Direct recruitment.* Figure 3.8 illustrates the direct response to stimulation for a stimulus strength of  $54 \mu A$  and pulse width of 0.5 ms. We can see strong recruitment of cells in layer 4 and 5, but minimal recruitment in layer 2/3 or 6. Cells in layer 4 are most strongly recruited with around 6 - 8 % of cells recruited. There are several parameters that can alter the recruitment, the stimulus amplitude, the pulse width or shape, and the position of the electrode. Here we have kept the electrode position constant but investigated the effects of an increasing stimulus amplitude and pulse width. Figure 3.9 shows how these parameters alter the recruitment of the excitatory and inhibitory cells in layers 2 - 4. We can see that, as we would expect, increasing the amplitude or width of the stimulus increases the proportion of cells recruited. Of note is that layer 2/3 excitatory cells do not show any significant recruitment until stimulus amplitudes of  $161 \mu A$  or higher, meaning we can exclusively target layers 4 and 5 with lower amplitude stimulus. Limiting the pathways contributing to the response to those from layers 4 and 5 simplifies the interpretation of the response potential and is more reflective of the pathways activated by in vitro experiments such as those by Walcott and Langdon (2002). For this reason we choose to use an amplitude of  $54 \mu A$  and a pulse width of 0.5ms for the subsequent simulations.

3.4.1.2. *Response LFP.* In our model the initial response measured by the local field potential is generated by the synaptic currents of those cells directly recruited by the stimulus. We can begin investigating the source of these currents by first isolating the cell types that contribute most significantly to the generation of the LFP. We can then isolate the specific synaptic currents that contribute to the transmembrane currents in these cells. To remove the stimulus artefact and other non synaptic currents from the LFP we rerun the simulations, using the spike times from the initial simulation to generate the same synaptic currents without the need for a spiking mechanism or any currents from stimulation. The LFP is generated primarily (exclusively in VERTEX) by transmembrane currents. In compartmental models such as those used in VERTEX the transmembrane currents can be calculated for each compartment. The change in membrane potential for a given compartment is calculated using equation 3.4.1, where  $C_{m,j}$  is the membrane capacitance and  $V_j$  its membrane potential.  $g_{l,j}$  is its

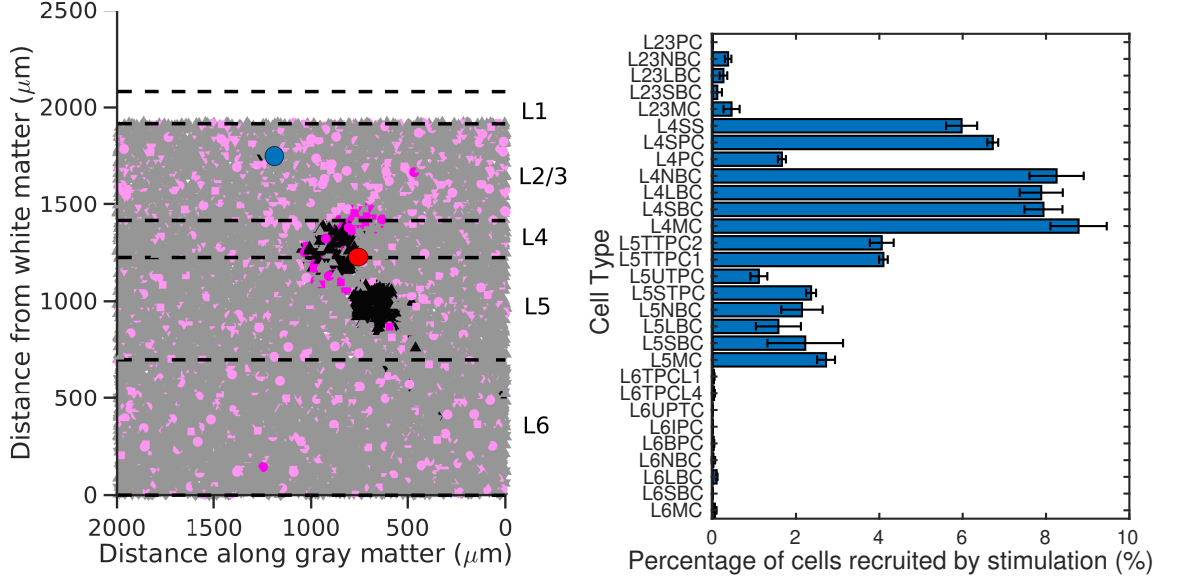


FIGURE 3.8. Shows the cells recruited directly by bipolar stimulation with a pulse amplitude of  $54 \mu A$  and a pulse width of  $0.5 \text{ ms}$ . (Left) shows an example of the location of cells directly recruited by stimulation. Grey triangles are excitatory cells that are not directly recruited, light pink circles are inhibitory cells not directly recruited. Black triangles show excitatory cells that spike during stimulus, dark pink circles show inhibitory cells that spike during stimulus. The blue circle shows the location of the recording electrode, the red circle shows the location of the stimulating electrode. (Right) shows the percentage of cells of each type that fire during stimulus. Bars show the mean, and error bars the standard deviation of 5 networks.

leak conductance,  $E_l$  its leakage potential and  $g_{l,j}(V_j - E_l)$  is the leakage current.  $\sum_{k=1}^K g_{j,k}(V_j - v_k)$  is the axial current (the current from neighbouring compartments) where  $K$  is the number of neighbouring compartments to  $j$ ,  $g_{j,k}$  is the axial conductance between  $j$  and  $k$ , and  $V_k$  is membrane potential of compartment  $k$ .  $I_{ion,j}$  are the currents from active ion channels, and  $I_{syn,j}$  the synaptic currents. As Kirchoff's law states that all transmembrane current entering and exiting a compartment must sum to zero, and current can enter a compartment only across the membrane or from neighbouring compartments we can assume that the transmembrane current is equal to the negation of the axial current. This relationship is described in equation 3.4.2, which is a rearrangement of 3.4.1. To calculate the transmembrane currents, which are then used to calculate the LFP, we use equation 3.4.3.

$$C_{m,j} \frac{dV_j}{dt} = -g_{l,j}(V_j - E_l) - \sum_{k=1}^K g_{j,k}(V_j - v_k) + I_{ion,j} + I_{syn,j} \quad (3.4.1)$$

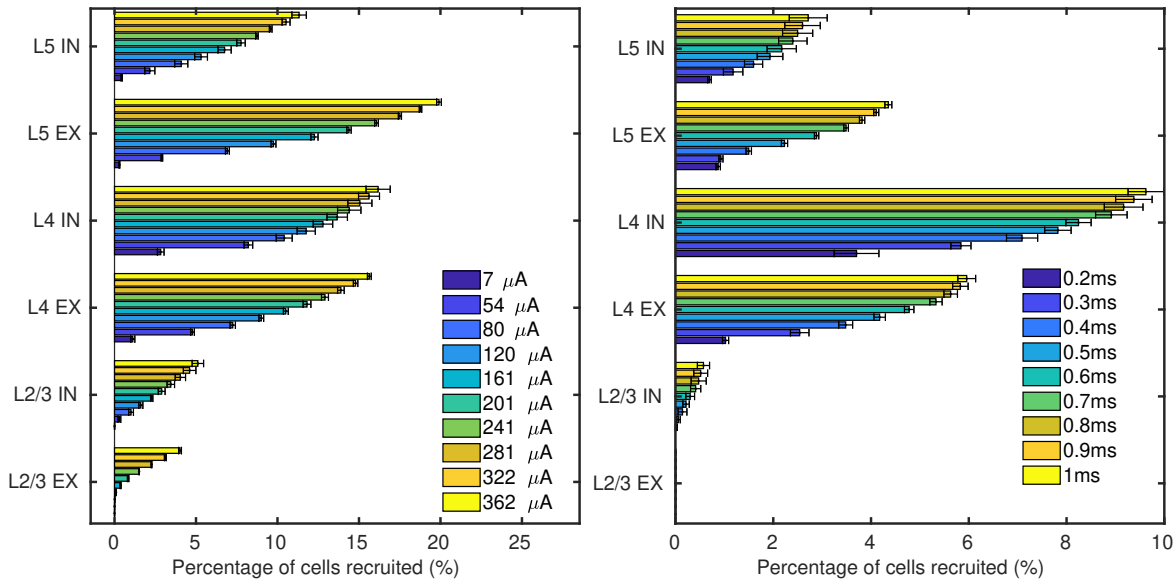


FIGURE 3.9. Increasing the stimulus amplitude (left) and pulse width (right) increases the recruitment of cell in layers 2-5. Bars show the mean percentage of each cell group recruited by stimulus, errorbars show the standard deviation of 5 networks. The colour of the bar indicates the stimulus amplitude (left) or the pulse width (right). A neuron was determined to have been recruited if it spiked during the stimulus period. The pulse width for the simulations of various amplitudes was 0.5ms, the amplitude for those testing the widths was 54  $\mu A$ .

$$\sum_{k=1}^K g_{j,k}(V_j - V_k) = -C_{m,j} \frac{dv_j}{dt} - g_{l,j}(V_j - E_l) + I_{ion,j} + I_{syn,j} \quad (3.4.2)$$

$$I_{mem,j} = -I_{ax,j} = \sum_{k=1}^K g_{j,k}(V_j - V_k) \quad (3.4.3)$$

The LFP is then calculated using the transmembrane current of each compartment as the current source and using a line current source model for dendrites and a point current source model for the soma. The potential generated by each compartment can then be combined through linear summation to produce the total LFP. As the contribution of all cells is summed to produce the total, we can calculate the contribution that each cell or group of cells makes by comparing the LFP they produce on their own with that generated by the whole network. To do this we calculate the power of the LFP generated by each group of cells on their own and combine this to get a total power. The contribution of each group is then the percentage that it makes up of this

total power (equation 3.4.4).

$$Contribution_{group} = 100 \frac{Power_{group}}{Power_{total}} \quad (3.4.4)$$

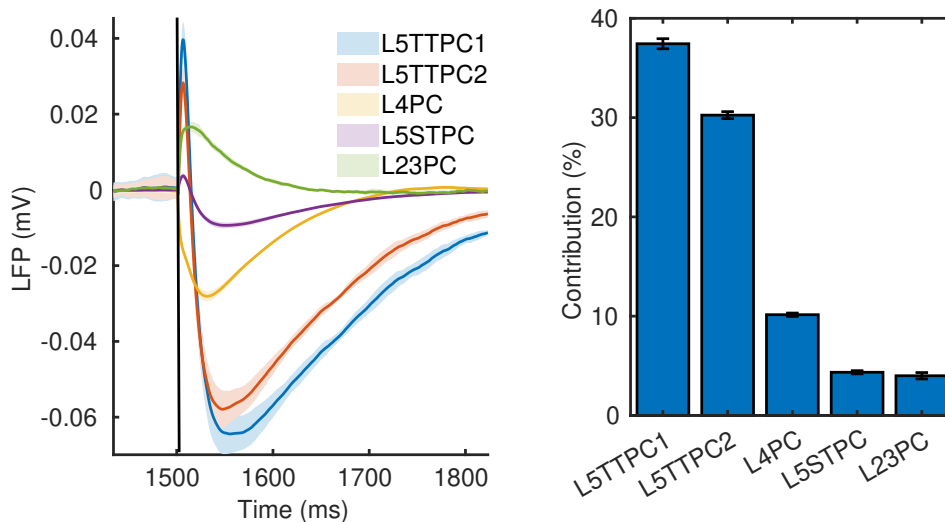


FIGURE 3.10. Shows the LFP recorded by an electrode in layer 2 and generated by the 5 cell types that contribute the most. The left panel shows the waveform of the contributed signal from each cell type, the each line shows the mean of 5 networks, the standard deviation is indicated by the shading surrounding each line. The black line at 1500ms indicates the moment of stimulation. The right panel shows the contribution of each cell type as a percentage of the entire signal.

Figure 3.10 shows the LFP recorded at an electrode in layer 2/3 (shown in figure 3.8) and generated by the stimulation described above. It has been broken down into the contributions from the 5 neuron groups that contribute the greatest. We can see that the layer 5 thick tufted pyramidal cells contribute the majority of the signal. As the LFP generated by these groups makes up the majority of the signal we will first focus on revealing the synaptic source of the currents that generate them. The L5 TTPC generated LFP has two distinct components, an early positive inflection, and then a subsequent trough. An obvious place to start would be to look at the synaptic currents arriving at L5TTPCs during the response to stimulus. Figure 3.11 A shows the presynaptic source of the largest currents arriving at the cell. Here the largest currents are calculated as those with the largest area under the trace. We can see that layer 4 and 5 pyramidal cells contribute the strongest excitatory currents while layer 5 Martinotti cells, large basket cells, and nest basket cells all contribute significant

inhibitory currents. The excitatory currents peak immediately after stimulation while the inhibitory currents peak after a slight delay. From this we can show a correlation between the peak of the excitatory current and the initial response, and the peak of the inhibitory current and the second response. However, as the LFP is determined by the spatial distribution of currents, and is generated by transmembrane currents, not just synaptic currents, we should look at the spatial distribution of currents arriving at the TTPCs as well as how these translate into transmembrane currents. In figure 3.11 B we can see the currents arriving at each compartment grouping. These are colour matched to the compartments in the illustration of a TTPC in figure 3.11 E. Here we also show the compartments on to which three classifications of cell synapse. The basket cell (BC, red circle) represent LBCs, NBCs, and SBCs, and synapse onto the soma. The Martinotti cell (MC, blue circle) represents only Martinotti cells and synapse onto the dendrites. The pyramidal cell (PC, green triangle) represents all excitatory cells and synapses onto the dendrites. The dendrites all show an initial depolarisation, this translates into a positive transmembrane current, and so a negative LFP, the compartments not receiving this depolarising current (the tuft, and the soma) respond with a negative transmembrane current as a result of axial currents from their depolarised neighbours. All transmembrane currents should cancel out across the cell (all traces in C sum to zero), but the contribution of each membrane current to the LFP is weighted by its distance to the recording electrode. In this case, currents from the soma or basal dendrites will be reduced while those from the apical dendrites or the tuft will be amplified. We can see this in figure 3.11 D , which shows the LFP contributed by each section of the cell. It is the transmembrane current inverted and weighted by the distance to the recording electrode.

The initial positive inflection of the LFP can be attributed to the transmembrane current at the tuft. These are caused by the excitatory synaptic currents arriving at the apical, oblique, and trunk dendritic compartments, which become heavily depolarised. These synaptic currents can be seen as the main peak just after 1500 ms in figure 3.11 B. The depolarisation of the apical dendrite causes a potential difference between it and the tuft, which then according to equation 3.4.3 receives a positive axial current. This positive axial current translates to the negative transmembrane current (again following from equation 3.4.3), which then results in a positive contribution to the LFP (the light

blue line in figure 3.11 D). The negative inflection in the LFP can be attributed to the positive transmembrane current at the apical dendrite (purple line in figure 3.11 D). This is caused by the strong hyperpolarising currents arriving at the soma from the synapses of the basket cells. We can see the strong inhibitory current in the dark blue trace in figure 3.11 B, and the corresponding negative transmembrane current at the soma and then the positive transmembrane current at the apical dendrite (purple trace) in panel C. The positive apical transmembrane current is again a result of the axial currents arising from a difference in membrane potential between compartments. As the currents from apical dendrites are closer to the electrode they are amplified enough to overcome the opposing contribution from the soma.

We now have a mechanistic explanation for how the excitatory potential and inhibitory potential are generated. This is particularly useful in this case, as the positive LFP is often associated with inhibitory currents because a negative current source would produce a positive LFP. This is one discrepancy between our model and the results of Walcott and Langdon (2002). In their waveforms an excitatory potential manifests as a negative deflection in the LFP. This is interpreted as an overall depolarisation of the layer 2/3 pyramidal cells which is also in contrast to our model where the layer 5 pyramidal cells contribute the majority of the signal. Other features, such as the halfwidth and latency of the excitatory potential show similarity between experiments and simulations. We summarise these in table 3.2.

Now that we have identified the excitatory potential and inhibitory potential components of the response we can observe how they are each affected by the changing stimulus parameters. Figure 3.12 shows the effect of the stimulus amplitude on the response amplitude. The threshold for producing any response was found to be around  $7 \mu A$  while the excitatory extracellular potential reaches a maximum amplitude of around  $0.8 \text{ mV}$  at an stimulus amplitude of  $200 \mu A$ . The data from Walcott and Langdon (2002) reaches an average maximum of  $5.74 \text{ mV}$  at a range of stimulus amplitudes between  $160$  and  $400 \mu A$ .

3.4.1.3. *Response activity.* Having described the number of neurons directly recruited by stimulation of a range of amplitudes, and having described the response LFP generated by this, we can now look at the response activity in terms of the post synaptic recruitment. To measure the level of postsynaptic recruitment Walcott and

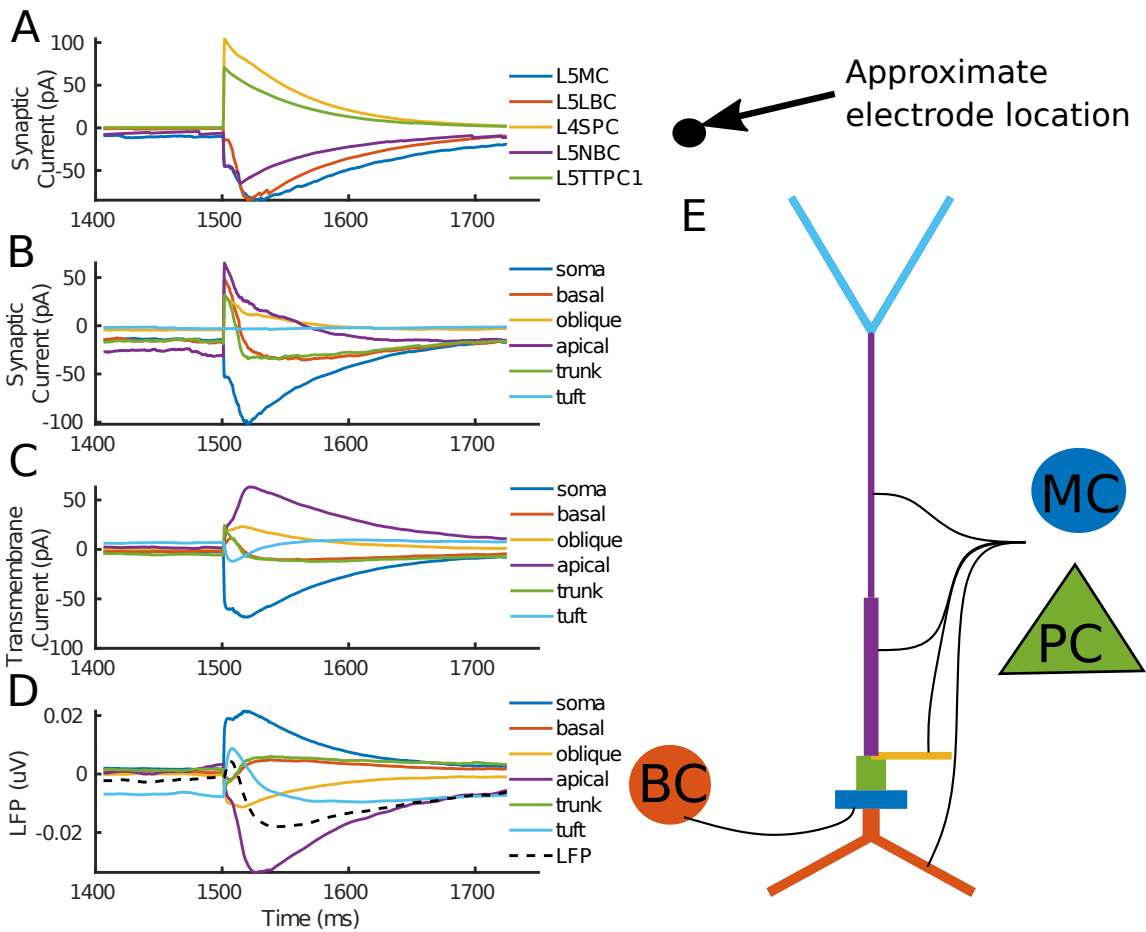


FIGURE 3.11. Shows the synaptic currents arriving at and local field potential generated by the 100 layer 5 TTPCs nearest to the recording electrode after a 54  $\mu A$ , 0.5 ms pulse of stimulation applied at time 1500 ms. Each line indicates the mean across all sampled cells. The illustration to the right shows the cell-type specific locations of synapses arriving onto the TTPC. We can see that pyramidal cells (PC) and Martinotti cells (MC) synapse at the dendrites, while the basket cells (BC) synapse at the soma. The top panel shows the synaptic currents arriving at the cell with each line corresponding to the presynaptic neuron type. We show traces for the 5 largest contributors. The second panel shows the synaptic currents but this time grouped by the compartment they arrive at. We can see that the dendrites are depolarised by the initial currents (mostly from layer 4 and 5 pyramidal cells), while the soma is hyperpolarised by the basket cells. The third panel shows the transmembrane currents for each compartment. These currents are generated in response to synaptic current in order to fulfil Kirchoff's law that the sum of all currents entering an exiting a compartment of a cell must be equal to zero. They are proportional to the difference in membrane potential between neighbouring compartments and are the source of the LFP. In the final panel we can see the LFP generated by each compartment.

TABLE 3.2. Shows the mean $\pm$ standard deviation of the latency, halfwidth and amplitude of the response in the simulation, in the literature survey done by Walcott and Langdon (2002), and in the experiments of Walcott and Langdon (2002). The stimulus parameters for the simulation were  $54 \mu A$  and  $0.5$  ms. The stimulus amplitudes used in the experiments ranged from  $8$  to  $100 \mu A$  with a mean of  $35.1 \mu A$  and standard deviation of  $21.1 \mu A$ . Those from the literature survey are described by Walcott and Langdon (2002) as similar.

	Simulation	Literature Survey	Experimental
Latency (ms)	$7.0 \pm 0.85$	$6.0 \pm 1.9$	$5.3 \pm 1.0$
Halfwidth (ms)	$6.13 \pm 0.46$	$4.5 \pm 2.2$	$4.7 \pm 1.8$
Amplitude (mV)	$0.07 \pm 0.01$	$0.64 \pm 0.38$	$0.83 \pm 0.37$

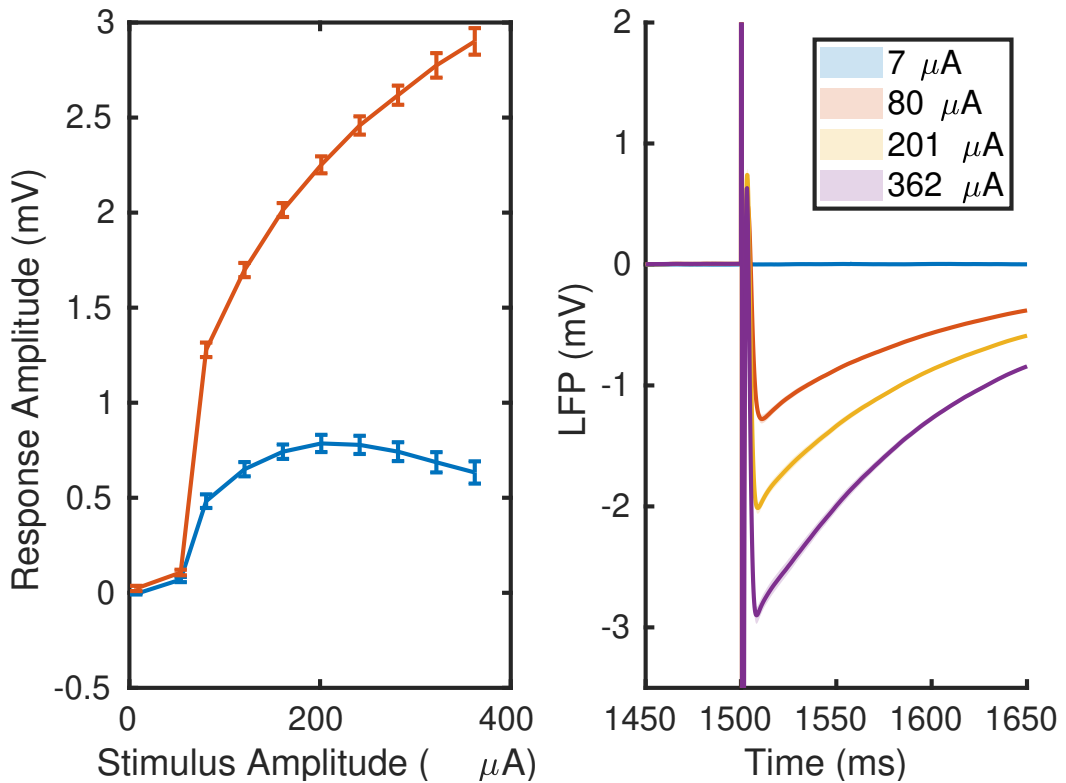


FIGURE 3.12. The amplitude of the response increases with increasing stimulus amplitude. The left panel shows the mean amplitude of the maximum of the response signal (blue) and the minimum of the response signal (red). Error bars indicate standard deviation. The maximum and minimum amplitude are calculated by taking the maximum or minimum of the signal from 2 ms after stimulation to 150 ms after stimulation. The right panel shows some example traces of the response to stimulus at  $7 \mu A$ ,  $80 \mu A$ ,  $201 \mu A$ , and  $362 \mu A$ .

Langdon (2002) performed cell attached recordings of layer 2/3 pyramidal cells within  $200 \mu m$  horizontally of the stimulating electrode. They calculate an estimate of the total recruitment within their sampling volume of 16 - 22 % of all pyramidal cells there. In our simulations we measure the total recruitment of pyramidal cells in an equivalent sampling volume spanning all of layer 2/3 vertically and  $200 \mu m$  horizontally from the

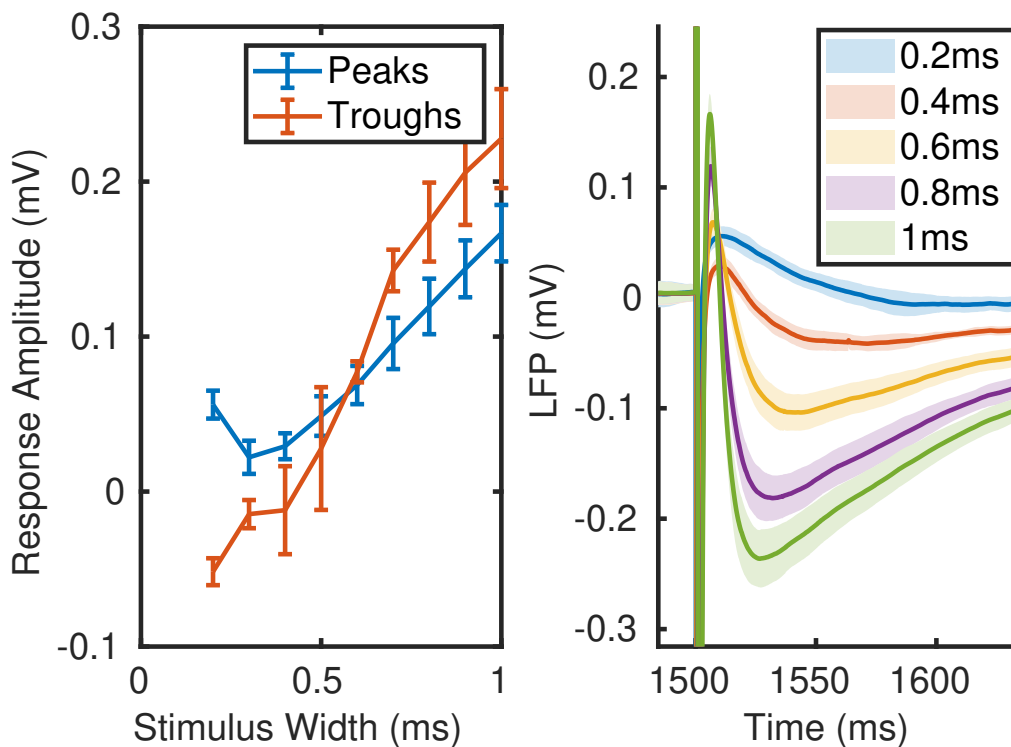


FIGURE 3.13. The response amplitude increases as the pulse width increases. The left panel shows the amplitude of the response measured both as the peak (the maximum value of the response) and the trough (the minimum value of the response). The peak is calculated as the maximum value of the trace in the time window between 1505 ms and 1515 ms. The trough is calculated as the negation minimum value of the trace between 1515 ms and 1600 ms (to achieve larger values for deeper troughs). We can see that the trend is for the amplitude to increase with the pulse width, however at 0.2ms pulse width we see a larger peak than at 0.4ms. We see a negative amplitude for the troughs at short stimulus widths, this is because they do not go below zero during the trough window. This is illustrated in the panel on the right, where we can see the response traces for stimulus widths: 0.2ms, 0.4ms, 0.6ms, 0.8ms, 1ms.

stimulating electrode. We find a significantly lower rate of recruitment, with an average of  $0.287 \pm 0.06\%$ . This corresponds with the lack of synaptic currents arriving at layer 2/3 cells during stimulation, which also results in a smaller contribution to the LFP. Given that the main connection expected to contribute to the recruitment of layer 2/3 (and generate the field potentials recorded there) comes from excitatory cells in layer 4, we considered that perhaps this connection was not strong enough in our model. Looking at figure 3.3 we can see that the number of connections between principle cells in layer 4 and layer 2/3 (4.9,1 and 5.5 connections per postsynaptic neuron) is relatively low compared with the layer 4 to layer 5 connection (6,13.4 and 38.3 connections per postsynaptic neuron). The number of connections from layer 5 principle cells to layer 2/3 is also relatively low (0.3 - 1.6 connections per postsynaptic neuron)

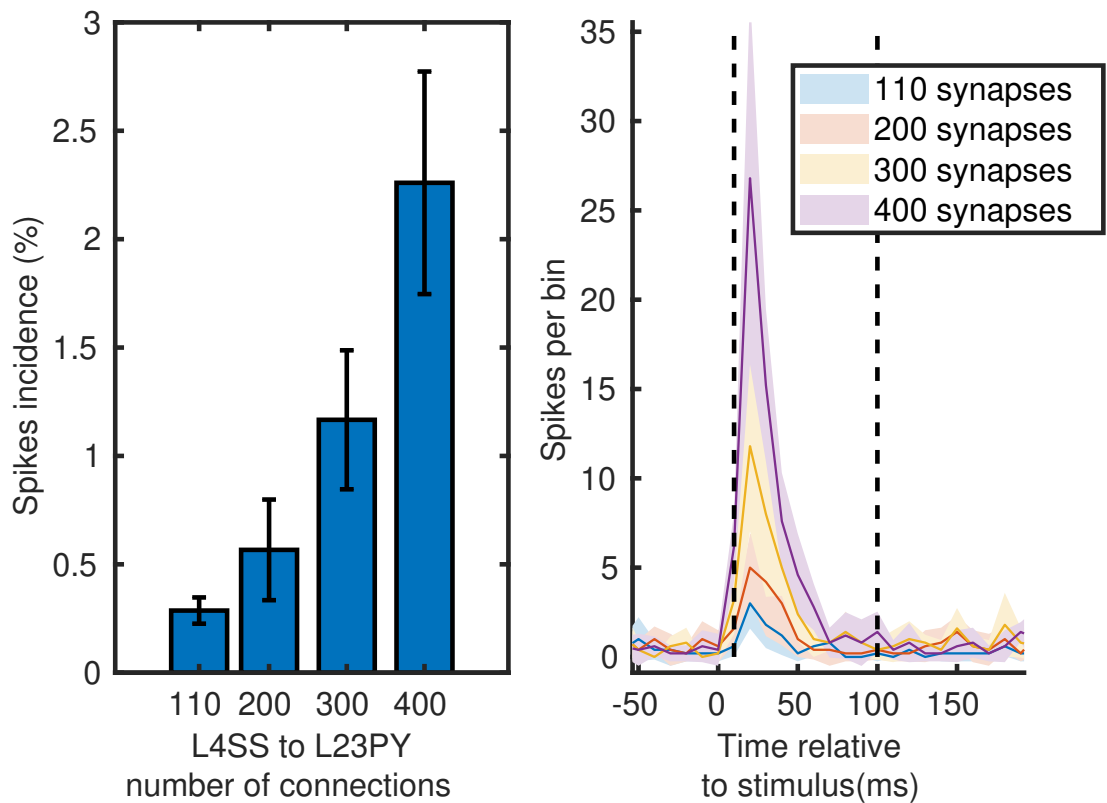
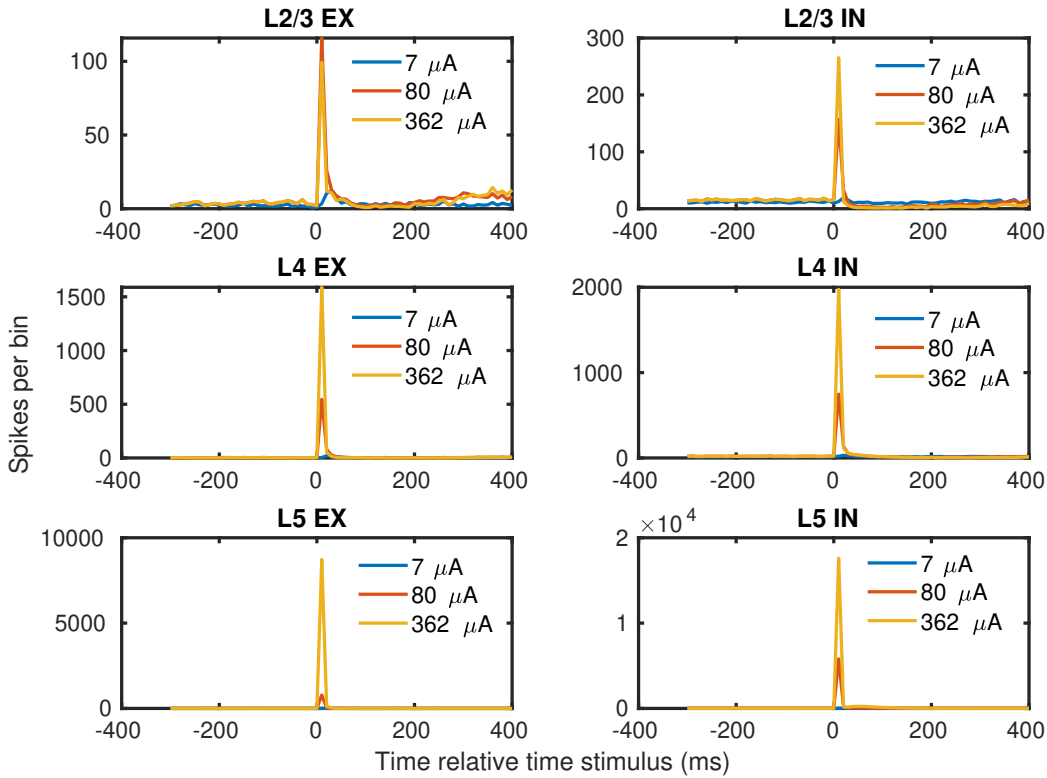


FIGURE 3.14. Increasing the number of synapses from layer 4 spiny stellate cells to layer 2/3 pyramidal cells causes significant increase in the number of spikes seen in layer 2/3. The right panel shows a peristimulus time histogram of the number of spikes per bin per network, for 5 networks. The shading around each line indicates the standard deviation of the 5 networks, and the bin size was 10 ms. The bar chart on the left shows the total spikes recorded during the window outlined by the dotted lines (100 ms post stimulus). Error bars indicate standard deviation.

compared to their recurrent connections (29.4, 33 connections per neuron). Our connectivity is based solely on data from Ramaswamy et al. (2015), so we compared the connectivity data for the layer 4 to layer 2/3 connection with other major studies of neocortical connectivity. Layer 4 principle cells are generally thought to act as a hub that distributes thalamocortical excitation to other areas of the cortex, with layer 2/3 considered the most prominently innervated (Feldmeyer, 2012). In cat neocortex it has been shown that spiny stellate cells form the largest proportion of their synapses in either layer 3 or layer 4, with all showing strong connections to layer 3 (Binzegger et al., 2004). Morphologically, their axons tend to project vertically and often terminate in layer 2/3 (Lübke and Feldmeyer, 2007). In summary, the literature on this describes layer 4 stellate cells forming numerous synapses onto layer 2/3 (Binzegger et al., 2004; Lübke and Feldmeyer, 2007; Thomson and Lamy, 2007; Feldmeyer, 2012).

## (A) Stimulus Amplitudes



## (B) Pulse Widths

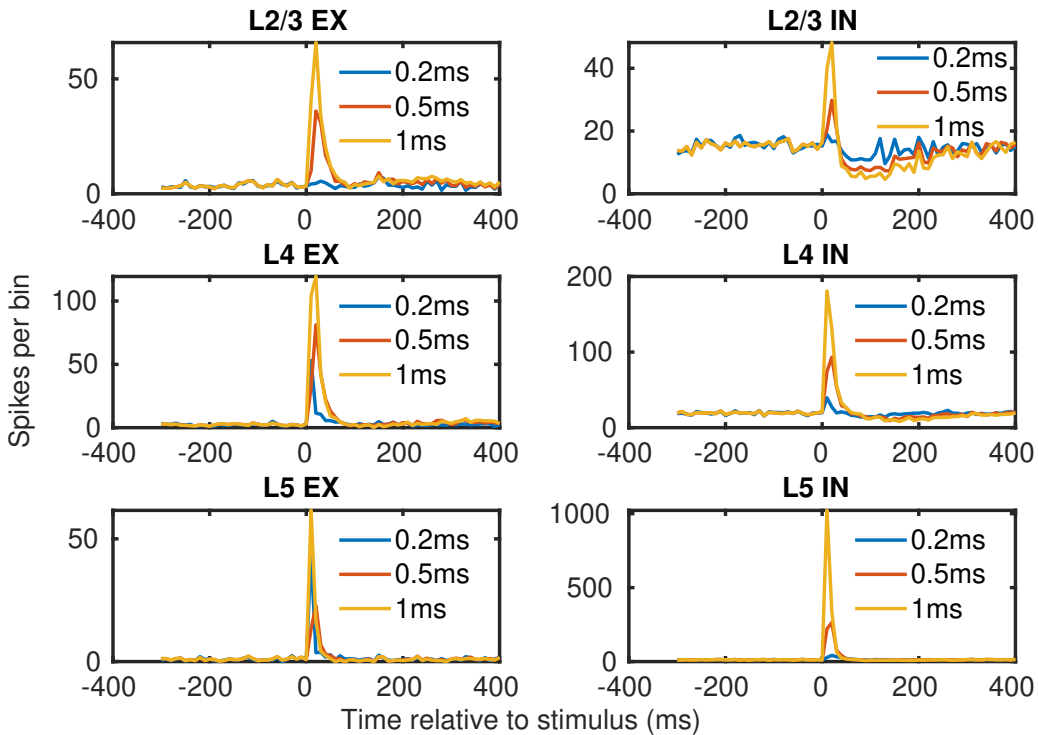


FIGURE 3.15. Shows the peri-stimulus time histogram for a range of stimulus amplitudes (A) and pulse widths (B). Cells are grouped into excitatory and inhibitory for each layer. Each trace shows the number of spikes per bin per network, where the bin size is 10 ms and we have simulated 5 networks for each stimulus amplitude. The time relative to the stimulus time is shown on the x axis. The spikes per bin for pulse widths of 0.2ms, 0.5ms and 1ms are shown.

Lübke et al. (2003) describe a convergent and divergent connectivity between L4SS and L23PC of between 300 and 400. To test the influence of this on the postsynaptic recruitment in layer 2/3 and the field potential contribution of L23PCs we tested our network with 110 (the default), 200, 300, and 400 connections from each L4SS to all L23PCs. From figure 3.14 we can see that increasing the number of connections increases the spike incidence, up to 2.3 % for 400 connections. This is still an order of magnitude short on the estimate of Walcott and Langdon (2002) of 16- 22 %. The LFP contribution is also not significantly affected. To test the effect of the stimulus parameters on the postsynaptic recruitment in each layer we use the estimate of 300 connections per postsynaptic neuron. In figure 3.15a we show the peri-stimulus time histogram of the spiking response in each layer to 7, 80, and 362  $\mu A$  stimulation (with a pulse width of 0.5ms). In figure 3.15b we show the peri-stimulus time histogram of the response in each layer to stimulation of 54  $\mu A$  with a pulse width of 0.2ms, 0.5ms and 1ms. The histograms are calculated as averages of recordings from 5 networks. Figure 3.16 summarises the spiking response seen in each layer to the range of stimulus parameters. Here we calculate a z score - the number of standard deviations the response is away from the baseline mean - to quantify the level of response. A stimulus amplitude of 54 $\mu A$  generates a significant response in all layers, stimulus amplitudes greater than this increase the response. A further consideration is the pattern of activity after the initial response. Experimentally, we tend to see a suppression of activity after the initial response. In our current simulations we have a very low baseline firing rate, and so we cannot discern any post stimulus suppression from the firing rates. However, we do see strong delayed inhibitory currents that would be expected to suppress activity, if the baseline was high enough.

**3.4.2. Theta burst stimulation.** Having described the response of our network to a single pulse of stimulation, we then wished to investigate how this stimulation, when applied repetitively, would modify the synaptic weights of the network according to the spike-timing dependent plasticity rule. We add STDP to all excitatory synapses in the network, the parameters used are described in table 3.3. Values for  $\tau_{pre}$  and  $\tau_{post}$  are based on estimates taken from Larsen et al. (2010), while the learning rate is based on that used by (Hiratani and Fukai, 2017) and is typical of rates used by others when modelling cortical networks (Song et al., 2000; Rubin et al., 2001).

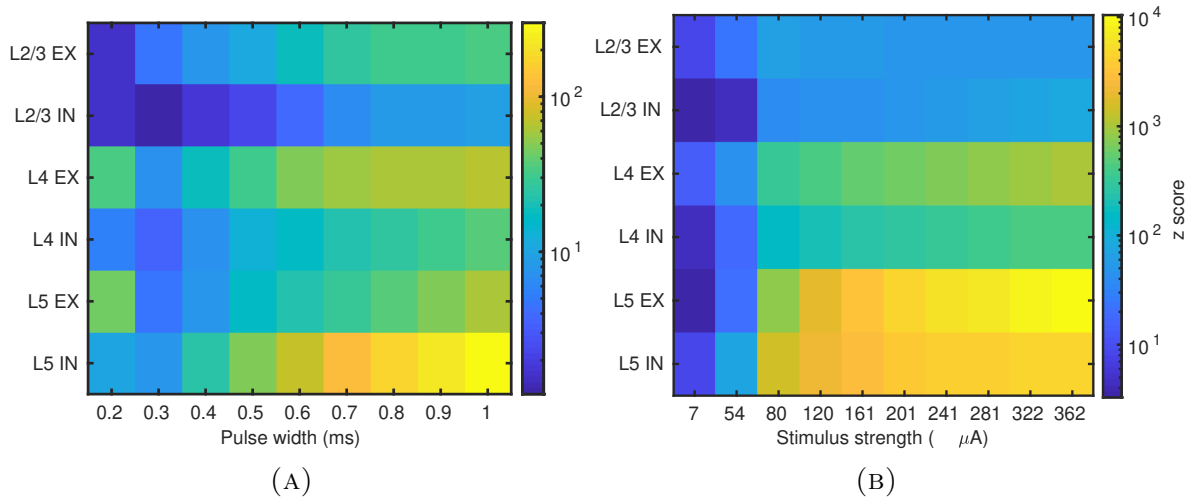


FIGURE 3.16. Shows the strength of spiking response for each of the neuron types (excitatory and inhibitory types for layer 2/3 to 5) in terms of a zscore for a range of pulse widths (A) and a range of stimulus amplitudes (B). The zscore is calculated as  $z = \frac{\text{mean}(S_r - S_b)}{\text{std}(S_b)}$  where  $S_r$  is spikes per bin during the response window (1 to 100 ms after stimulus) and  $S_b$  is the baseline spikes per bin.

TABLE 3.3. The STDP parameters and VERTEX synapse model used during the theta burst stimulation simulation.

Presynaptic Group	Synapse Type	Rate (nS)	$\tau_{pre}$ (ms)	$\tau_{post}$ (ms)
Superficial Excitatory (L2-4)	g_exp_mt_stdp	0.001	25	75
Deep Excitatory (L5-6)	g_exp_mt_stdp	0.001	25	25
Inhibitory	g_exp_mt	NA	NA	NA

We investigated the response of the unmodified network (*Default Network*), based purely on the NMCP data, the *Modified Network* (with the number of connections between L4SS and L23PC increased to 400) and the *Reduced Inhibition Network* (the same as the *Modified Network* but with the number of L5MC to L23PC connections halved). The data from Ramaswamy et al. (2015) imply a large number of connections from layer 5 Martinotti cells to layer 2/3 pyramidal cells, while others such as Naka and Adesnik (2016) describe Martinotti cells projecting to layer 2/3 but synapsing onto the apical dendrites of layer 5 pyramidal cells, without mentioning any synapses onto layer 2/3 cells. As L5MCs are strongly recruited by TBS, we hypothesised that a strong connection here is likely dampen the activity of L23PCs during TBS and therefore reduce any potentiation of the connection. We therefore reduced the strength of this connection as described above to test whether this would result in a greater potentiation of the connection. Figure 3.17 shows the activity of the *default network* under theta burst stimulation. We apply the same protocol as Walcott and Langdon (2002) with

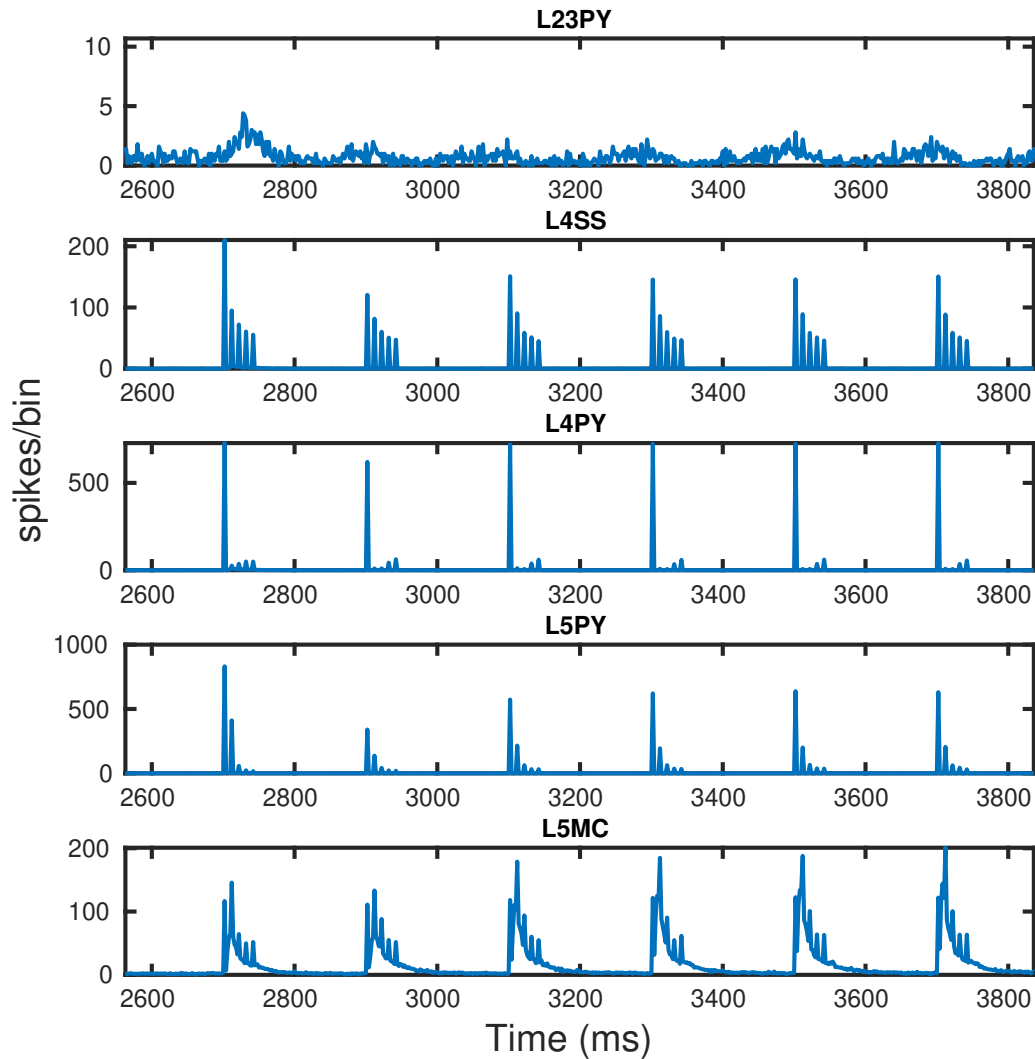


FIGURE 3.17. Shows the neural activity of L23PYs, L4SSs, L4PYs, L5TTPCs, and L5MCs, during the theta burst stimulation in the *Default network*. Each trace indicates the average spikes per bin for 5 networks. The bin size is 2 ms. We can see that the principle excitatory cells in layers 4 and 5 are actively recruited during the stimulus, while the L23PYs show a slight positive modulation during the first stimulus (0.76 standard deviations above baseline) but none during subsequent bursts (-0.03, -0.24, -0.13, -0.002, -0.11 standard deviations from baseline). MCs are strongly recruited postsynaptically.

six 100 Hz bursts at an interval of 200 ms, with a stimulating current of  $54 \mu\text{A}$  and a pulse width of 0.5 ms. Like for the single pulse, the stimulation directly recruits mainly the layer 4 and 5 pyramidal cells, which then recruit large parts of the rest of the network, in particular local interneurons. In the *default network* L23PCs show minimal recruitment either directly by the stimulus or postsynaptic recruitment. The activity of the *modified network* in layers 4 and 5 is broadly the same as for the default connectivity, while the L23PCs show stronger recruitment during the first burst, but no

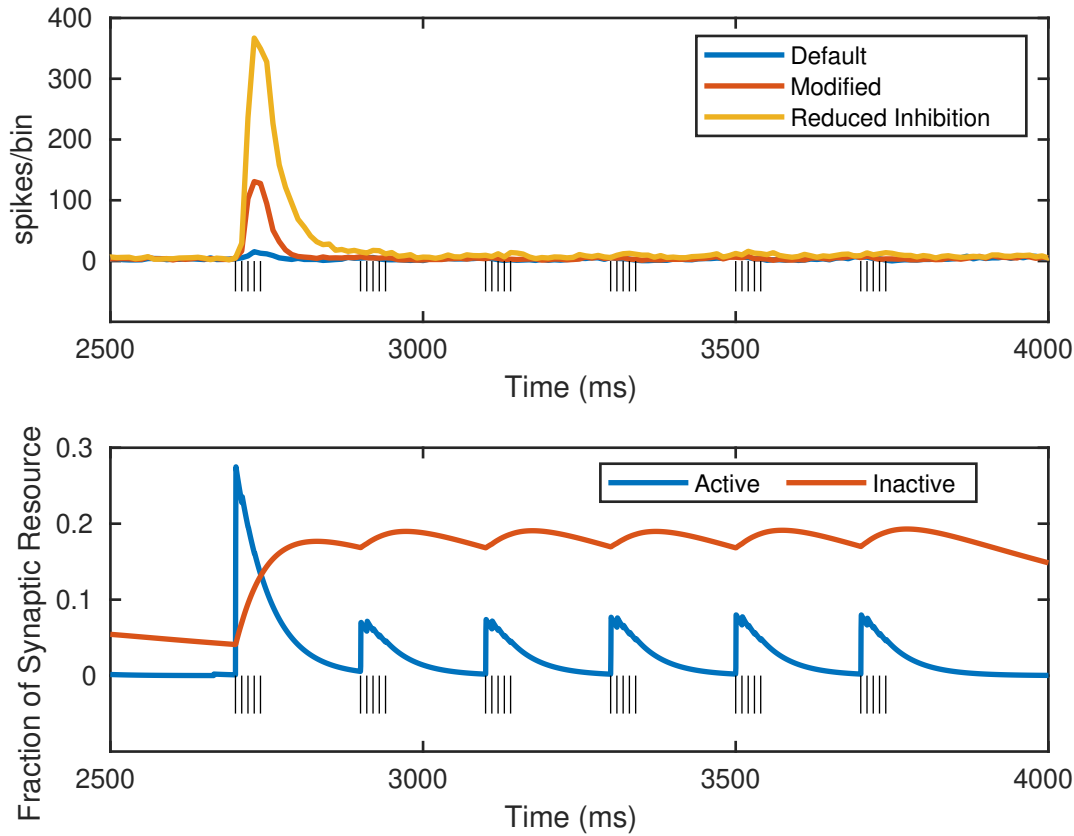


FIGURE 3.18. **Top:** Shows the per-stimulus time histogram of L23PC firing during TBS, for the three networks tested. The vertical bars below the trace indicate the timings of the stimulus. Each trace indicates the spikes per bin per simulation for 5 simulations, and with a bin size of 10 ms. The *Default* network is based on the NMCP data with no changes, the *Modified* network has the number of L4SS to L23PC connections increased to 400, and the *Reduced Inhibition* network is the same as the *Modified* network but also has the number of L5MC to L23PC connections reduced to half of that specified by the NMCP data. **Bottom:** Shows the fraction of synaptic resources in the active and inactive states on synapses between L5TTPCs and L23PCs during TBS. The active resource is currently being applied (generating current) and corresponds to the  $y$  variable in equations 2.4.7 and 2.4.11, the inactive has been applied and is currently not available to be applied (it corresponds to variable  $z$  in equations 2.4.6 and 2.4.8). There is a third state not shown here, the recovered state, of resource that is available, corresponding to the  $x$  variable in equations 2.4.6 and 2.4.12, which is why the two traces on their own do not sum to one.

recruitment during subsequent bursts. Figure 3.18 shows the activity of the L23PCs during TBS in the *default*, *modified*, and *reduced inhibition* networks. We can see that increasing the L4SS to L23PC connection numbers increases the response and that decreasing the L5MC to L23PC connection increases it further. While the initial response increases in both of the altered networks, the response to the subsequent burst

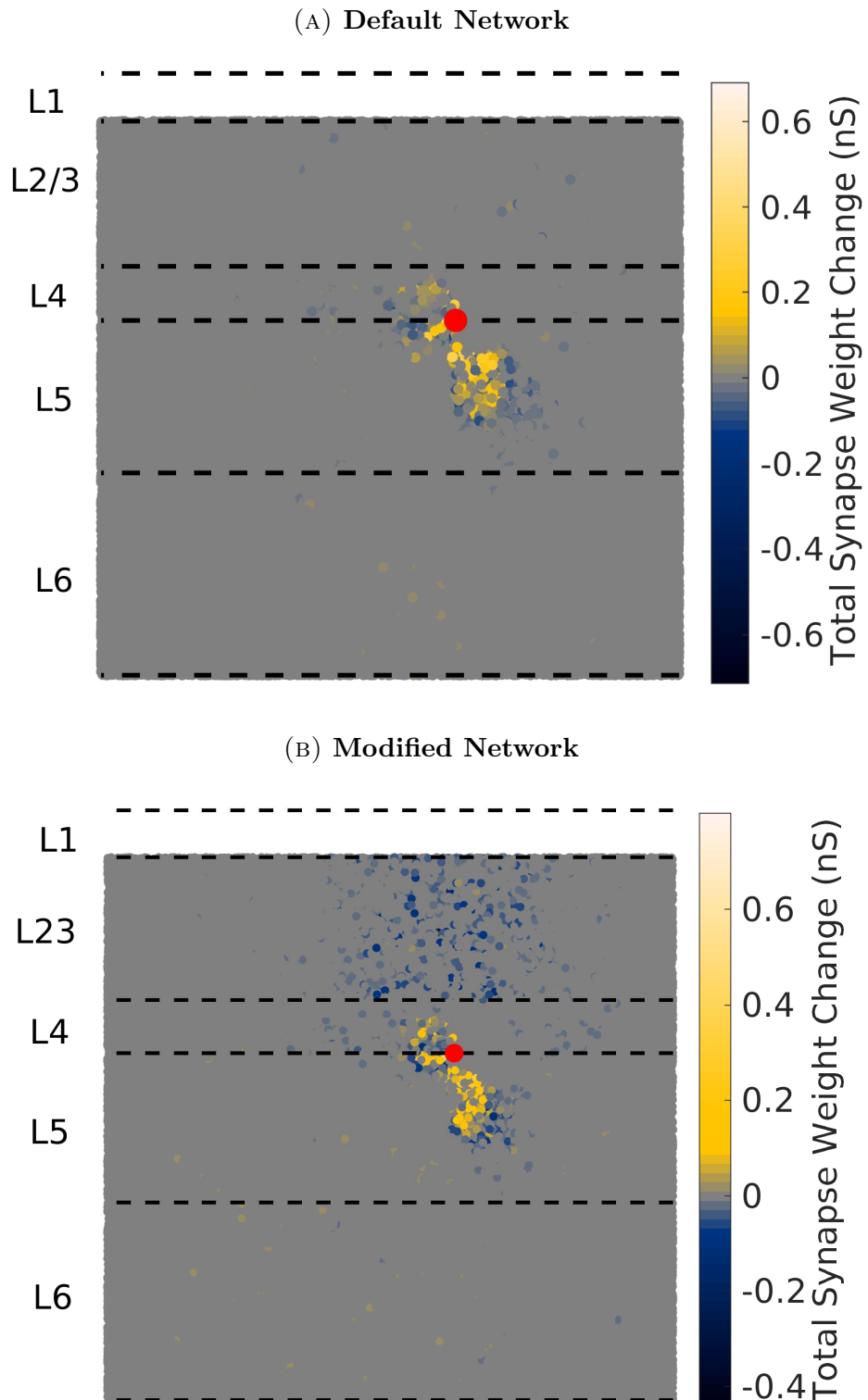


FIGURE 3.19. Shows the extent of the synaptic weight change for each neuron in a single network. The colour indicates the weight change of all of a neurons synapses, the location of the dot indicates the soma position of the cell in the X and Z plane. The default network uses the unmodified connectivity provided by the NMCP, the modified network has the same connectivity but the number of connections between L4SS and L23PC cells has been increased to 400. In the modified network we can see that as well as a potentiation of the synapses directly recruited, there is also a depression of the synapses of the L23PCs not directly recruited by stimulation.

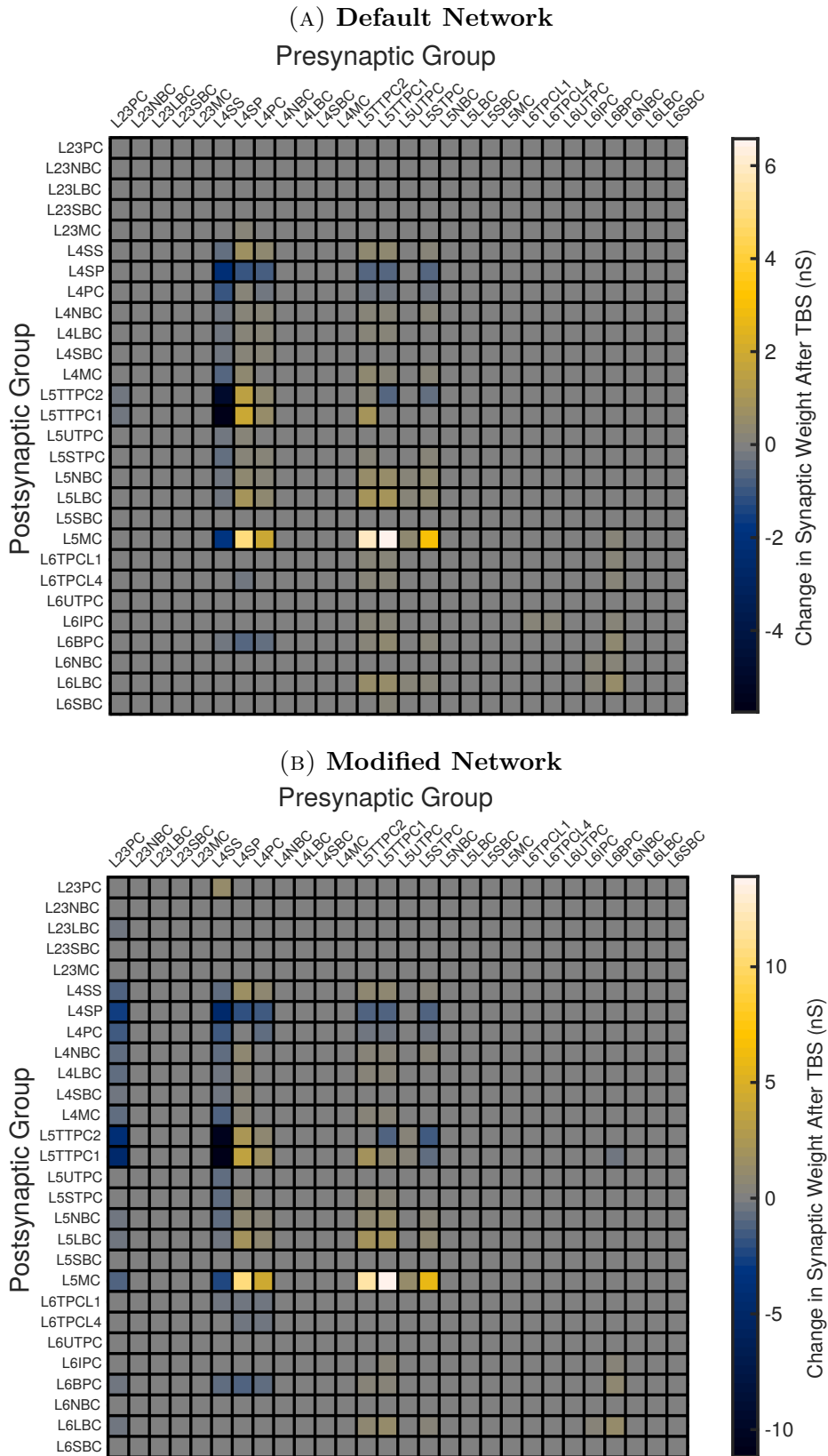


FIGURE 3.20. Shows the extent of the synaptic weight change on the connection between each neuron group. The colour of each box indicates the total weight change summed over each synapse in the connection, and averaged over 5 networks. The default network uses the unmodified connectivity provided by the NMCP, the modified network has the same connectivity but the number of connections between L4SS and L23PC cells has been increased to 400.

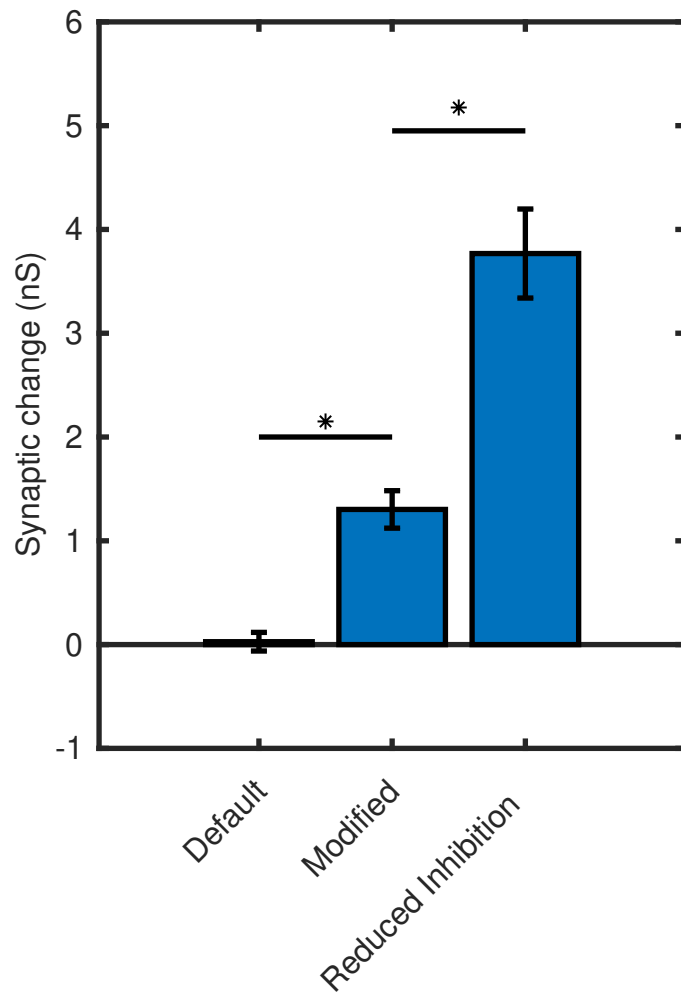


FIGURE 3.21. Shows the change in synapse strength on the L4SS to L23PC connection as a result of TBS in the default, modified, and reduced inhibition networks. Shows the mean and standard deviation of simulations run on 5 networks of each type. \* indicates  $p < 0.05$  (Student's t test).

remains suppressed. Figure 3.18 also shows the dynamics of the synaptic resource on the L4SS to L23PC connection. We can see here that during the initial TBS burst a significant proportion of the synaptic resource shifts into the inactive state, resulting in a smaller proportion moving to the active state during subsequent bursts, reducing the excitatory postsynaptic currents arriving at the L23PCs. We suggest that this synaptic depression makes a significant contribution to the suppression of the response to subsequent TBS bursts. Figure 3.19 shows the spatial extent of any weight change in the *default* and *modified* networks, with the neurons closest to the stimulation electrode those that undergo the most synaptic change. Figure 3.20 shows the weight change on each neuron group to neuron group connection for both the default and modified network. In both networks we can see here that there is a potentiation of the connection

between L4 and L5 pyramidal cells and L5 Martinotti cells. In the default network synapses to or from L23PCs show little change (which is expected as the L23PCs show little activity), but in the modified network the L23PCs show a depression of their synapse strength, particularly to the pyramidal cells in layer 4 and 5, and there is a potentiation of the connection from L4SS to L23PC. The depression follows from the pattern of activity we see in figures 3.17 and 3.18, with layers 4 and 5 active during the stimulus and layer 2/3 active after the stimulus. This results in strong postsynaptic activation before presynaptic activation on the connection from L23PC to L4PCs and L5PCs, and so LTD. We also see a moderate and significant ( $p < 0.05$ , paired t test) potentiation of the L4SS to L23PC connection in the *modified* network and in the *reduced inhibition* network. We can see in figure 3.21 that increasing the number of L4SS to L23PC connections increases the potentiation of the connection, and that decreasing the number of L5MC to L23PC connections increases this potentiation further.

**3.4.3. Paired Pulse Stimulation.** Having looked at the response of the network to a single pulse of stimulation and to theta burst stimulation we wished to perform a virtual paired pulse stimulation experiment. This experimental paradigm presents two pulses separated by an interval, known as the paired pulse interval.

When we consider the LFP produced by the network in response to the extracellular stimulation, the second response may be greater than the first (known as paired pulse facilitation) or less than (known as paired pulse depression). The ratio between first and second response is known as the paired pulse ratio, and can vary depending on the interval between the stimuli. We use the same network as that described above with the default connectivity parameters provided by Ramaswamy et al. (2015) rather than the altered network used for the long term potentiation experiment. As we can see in figures 3.4 and 3.5 the time constants for synaptic facilitation and depression (taken from Ramaswamy et al. (2015)) show the rat neocortex tends to be depressing (the time constant for depression is larger than for facilitation) with the exemption of excitatory synapses on to Martinotti cells. This cell-type specific short term plasticity is a prominent characteristic of neocortical function and is well explored *in vitro* (Reyes et al., 1998; Beierlein, 2003). Given the time constants for facilitation and depression we would expect most of the synapses in neocortex to show depression (other than for

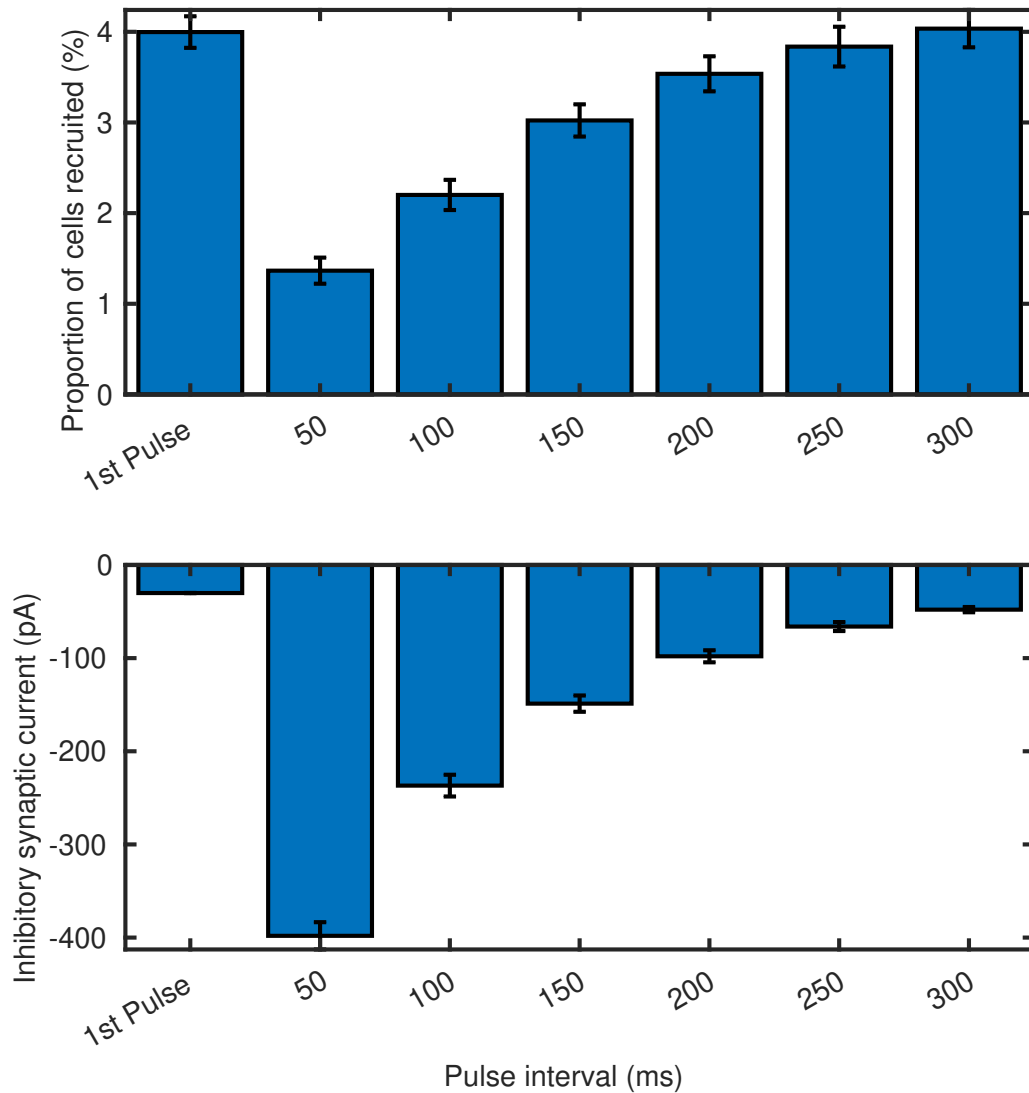


FIGURE 3.22. The proportion of cells recruited by the second stimulus increases and the mean inhibitory currents arriving at these cells decreases as we increase the interval from 50 ms to 300 ms. The top panel shows the proportion of L5TTPC cells recruited during the first pulse and then the second pulse for paired pulse intervals of 50 to 300ms. The bottom panel shows the mean inhibitory current arriving at the recruited cells at the moment of stimulation. All bars indicate the mean of 15 networks, and errorbars indicate standard deviation.

very high stimulation frequencies or very low stimulation frequencies). As a result we would expect most responses to be depressing and this is what we see in most in vitro studies (Casto-Alamancos and Connors, 1997).

However, it is also known that inhibitory currents from cells directly recruited by the stimulus or recruited by the resulting response, are still present after the initial stimulus (Margineanu and Wülfert, 2000; Leung et al., 2008; Queiroz et al., 2009). These can cause a depression of the response to the second pulse by hyperpolarising

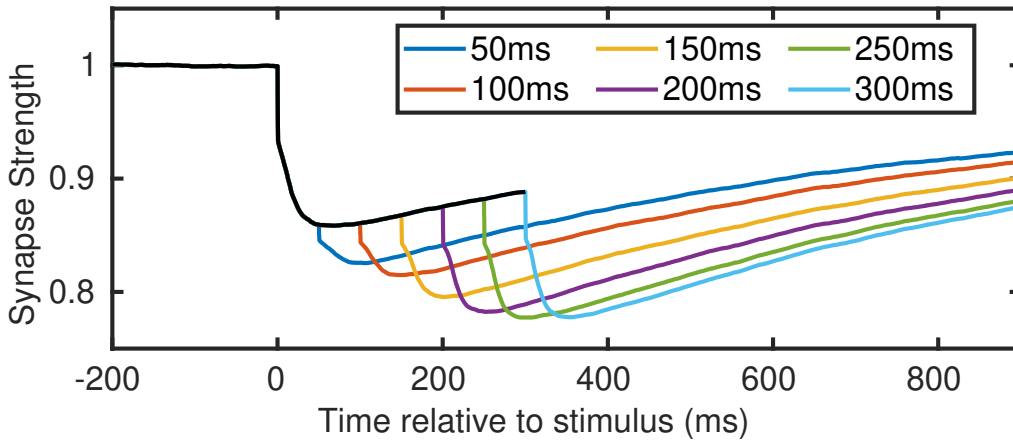


FIGURE 3.23. Shows the relative synapse strength on synapses from L5TTPCs to other L5TTPCs. The synapse strength is shown as a proportion of the baseline synapse strength, measured before any stimulus has been applied. We show the change in synapse strength in response to the first stimulus in black, and in response to the second stimulus in a range of colours corresponding to the pulse interval. All traces are the mean of the response in 15 networks.

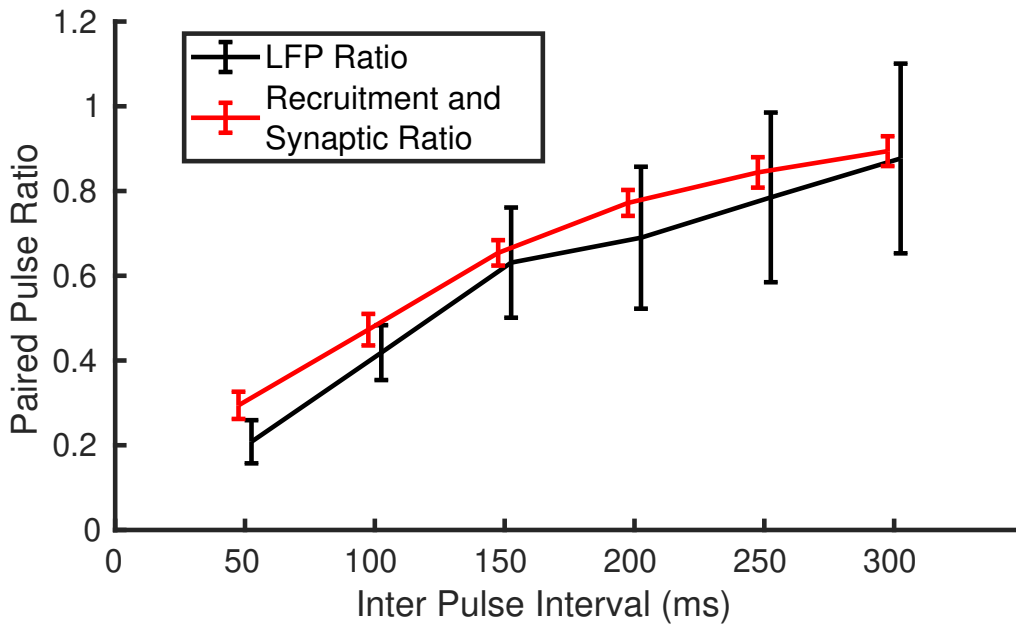


FIGURE 3.24. The paired pulse ratio measured from the amplitude of the excitatory component (as identified in figure 3.11) of the LFP is shown in black. The paired pulse ratio measured as the product of the recruitment ratio and synaptic ratio. The recruitment ratio is defined as  $rr = \frac{R_{2nd}}{R_{1st}}$  where  $R_{1st}$  is the number of L5TTPC cells recruited by the first pulse, and  $R_{2nd}$  is the number of L5TTPC cells recruited by the second pulse. The synaptic ratio is defined as  $sr = \frac{S_{2nd}}{S_{1st}}$ , where  $S_{1st}$  and  $S_{2nd}$  are the mean synapse strengths of the recruited L5TTPC cells at the time of the first pulse and second pulse. Error bars indicate the standard deviation of 15 networks. The difference between the estimate and the LFP ratio is shown in figure 3.25.

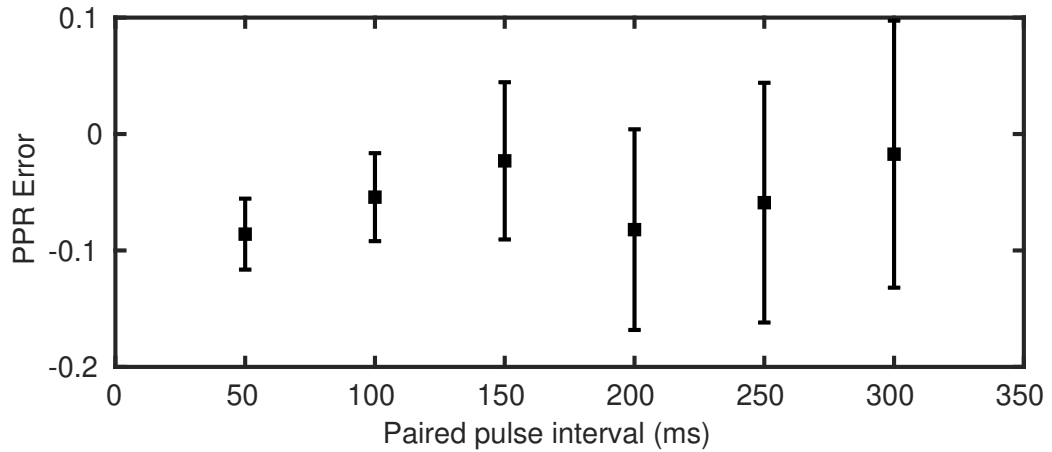


FIGURE 3.25. Shows the error and 95% confidence interval between our estimate of the PPR using the recruitment and synapse ratios and the PPR measured via the LFP.

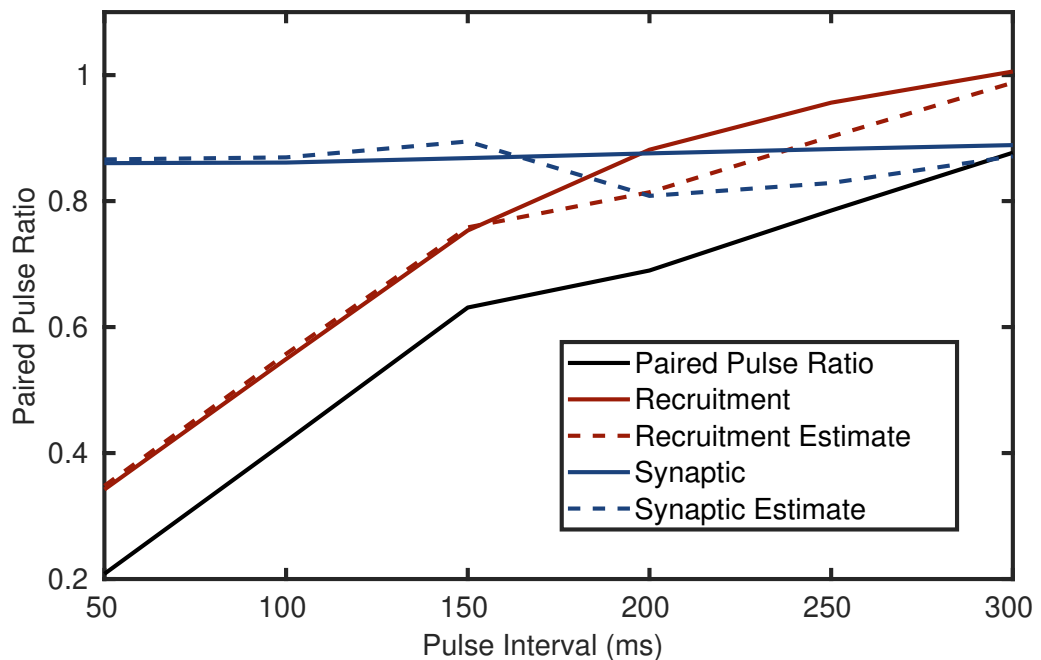


FIGURE 3.26. Shows the paired pulse ratio of the recruitment, reflecting the levels of residual inhibition, (the solid red line) and the paired pulse ratio of the synapse strength (the solid blue line). We can also see the paired pulse ratio as measured by the LFP in black. The dashed lines show the estimated recruitment ratio (red) based on the LFP ratio and the simulated synaptic ratio, and the estimated synaptic ratio based on the LFP ratio and the simulated recruitment ratio. Error bars have been omitted from this plot to avoid clutter but each point shows the mean of 15 networks, the standard deviation of the LFP measured ratio is shown in figure 3.24 and the confidence interval on the difference between the estimates and the simulated values are shown in figure 3.27.

their neighbouring cells, reducing their susceptibility to stimulation. In the experimental setting, distinguishing between these effects can only be achieved by recording

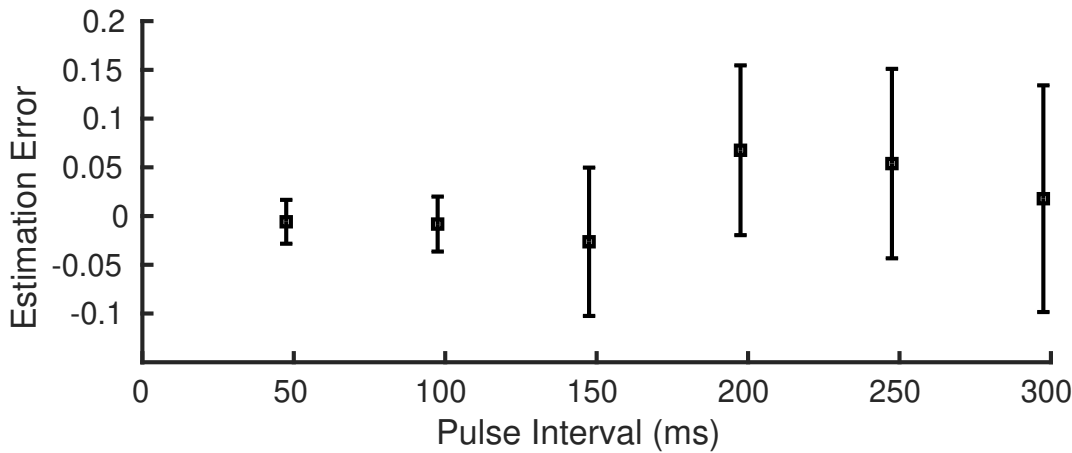


FIGURE 3.27. For each paired pulse interval we can estimate the paired pulse depression shown by the synapses given the paired pulse ratio measured from the LFP and the paired pulse ratio of the rate of recruitment. Here we show the error on that estimation and its 95% confidence interval.

postsynaptic currents intracellularly. *In silico*, we can estimate the relative contributions of the recruitment component and the synaptic component of the paired pulse ratio as measured by the field potential response. Our estimate of the residual inhibition will be based on our prediction of the recruitment of the various cell types and our knowledge of the strength and decay time of their synapses. Our prediction of the synaptic component will rest on an accurate model of short term plasticity. As L5TTPCs are the main source of the LFP and make the greatest contribution to the excitatory current they receive, we focus on the recurrent connections between L5TTPCs between them when considering the level of excitatory recruitment. Figure 3.22 shows that the proportion of L5TTPC cells recruited at 50 ms drops to around 1.5% compared with 4% during the first pulse. It takes until around 300 ms after the first pulse for the second pulse to recruit this 4 % again. We can see below (in the bottom panel of figure 3.22) that a strong residual inhibitory current contributes to this reduction in recruitment. In figure 3.23 we can see how the strength of the recurrent L5TTPC synapses weakens after the first pulse, and subsequent pulses weaken them further. The overall reduction is small (a maximum of 86 % reduction after one stimulus) but it does linger longer than the reduction in recruitment, suggesting that the effect of residual inhibition will dominate the measured PPR at shorter stimulus intervals and the short term plasticity dominate at longer intervals. We can compute a paired pulse ratio for the synaptic component and the recruitment component by taking a snapshot of the

relative synapse strength or proportion of cell recruited immediately before the delivery of the stimuli. If we assume that the post synaptic currents will be proportional to the total number of synapses activated multiplied by the total synaptic strength, then we can combine the synapse ratio and recruitment ratio to get an estimate of the PPR recorded by the LFP. In figure 3.26 we show our estimate (the product of the synaptic and recruitment ratios) compared with the paired pulse ratio measured from the amplitude of the excitatory component. Our estimate remains within 0.15 of the LFP ratio (as shown in figure 3.25) and shows a consistent underestimation of the paired pulse depression. This suggests that there is a further process contributing to the paired pulse depression, but that it contributes a relatively minor component. In figure 3.26 we show the PPR broken down into its synaptic component (solid blue), its recruitment component (solid red), and as measured by the LFP (solid black). Using our model, we can isolate the contribution of the synaptic or recruitment component by subtracting our estimate of the other component from the PPR measured in the LFP. The dashed lines in figure 3.24 show these estimates, and figure 3.27 shows the error on the estimated synaptic component.

### 3.5. Discussion

We have constructed a detailed biophysical model of the activity of rat somatosensory cortex during focal electric field stimulation. Using this, we have made predictions of the cellular source of the response potential, and from this the synaptic source. Unexpectedly, layer 5 thick tufted pyramidal cells made the largest contribution to the response potential, despite the recording electrode being placed in layer 2/3. This goes against the conventional interpretation of this field potential as being generated by synaptic currents onto layer 2/3 cells and is an indication that our model does not fully capture all the aspects of the system. We find that the currents contributing to the L5TTPC generated excitatory extracellular potential come mainly from the synapses of L5TTPCs themselves, but also L4SPCs. This follows from their susceptibility to electrical stimulation, and strong connections to the L5TTPCs (a result of the NMCP data, but also in agreement with other literature (Feldmeyer, 2012)). We found that other aspects of the NMCP data were not in agreement with the anatomical literature and limit the ability of the network to respond to stimulation in agreement with the experimental data of Walcott and Langdon (2002). The number of connections

from L4SS to L23PCs is relatively low in the NMCP data, while other studies have found it to be relatively high (Lübke and Feldmeyer, 2007), and as L4SS are one of the principle cells of layer 4 (our layer of stimulation) it is likely that any reduction in their connectivity to layer 2/3 will reduce the recruitment of the layer 2/3 cells. We found that it was necessary to increase the number of L4SS to L23PC connections to within the range described by Lübke and Feldmeyer (2007) to achieve recruitment of layer 2/3 cells after stimulation. This did not have any significant impact on the excitatory potential, however, and further work will be required to produce a response potential that matches with the experimental data. Possible areas to investigate here are the distribution of synapse locations on dendritic compartments, as well as the overall patterns of connectivity onto the L5TTPCs. To illustrate two potential use cases for this tool we constructed a simulation of theta burst stimulation (utilising the spike timing dependent plasticity described in chapter 2) and paired pulse stimulation. Theta burst stimulation is known to reliably induce LTP in the hippocampus (Larson and Munkácsy, 2016) but do so less reliably in the neocortex (Walcott and Langdon, 2002). We applied theta burst stimulation to both our default network and the modified network, as well as an additional network with a reduced number of connections from L5MCs to L23PCs. This modification was motivated by the suggestion that inhibition can impede LTP in this protocol (Walcott and Langdon, 2002; Varela et al., 1997), and the possibility that the NMCP data may be overestimating the strength of this particular connection. The NMCP data suggests a relatively strong connection between L5MCs and L23PCs (36 connections per presynaptic cell, compared with 5.4 for L5LBCs), while other literature suggests that L5MCs axons project to L2/3 but synapse onto the apical dendrites of L5TTPCs rather than L23PCs. Additionally, Walcott and Langdon (2002) have used regular artificial cerebral spinal fluid as their cutting solution, while the NMCP data (Ramaswamy et al., 2015), was measured in slices cut using a neuroprotective solution. As interneurons and their synapses are particularly sensitive to the cutting solution used (Yang et al., 2015) this could have led to greater preservation of interneurons and their connections, and so a stronger inhibitory network than would exist in the slices of Walcott and Langdon (2002). Unsurprisingly the default network did not show any potentiation of the synapses onto L23PCs because there was limited postsynaptic recruitment. In the modified networks

we do see an initial recruitment of L23PCs during the first burst, but not in subsequent bursts. This is due to the weakening of the L4SS to L23PC connection under sustained activation as a result of the short term plasticity rules. This leads to a prediction from our model that a single burst of TBS may be just as effective as the 5 bursts. The response to the initial burst is also stronger in the network with a reduced L5MC to L23PC connection leading to greater potentiation of the L4SS to L23PC connection. This indicates that the strength of the L5MC to L23PC connection and the strength of the inhibitory network in general may have a strong influence TBS induced LTP in neocortex. Through our paired pulse simulations we wished to show how VERTEX can be used to predict the contributions of residual inhibition and short term synaptic plasticity to the paired pulse ratio as measured through the excitatory field potential. We found that, in our model, they have a significant temporal overlap so that one cannot be measured without the influence of the other until the effect of the residual inhibition has worn off at around 300 ms after the initial stimulus. We have then shown how VERTEX can be used to remove the predicted effect of one process (e.g. residual inhibition) from the paired pulse ratio measured by the LFP response to get an estimate of the paired pulse ratio of the second process (e.g. synaptic depression).



## Analysis of Epileptiform Activity Recorded *in vitro*

### 4.1. Introduction

In the previous chapters we have described our additions to the VERTEX simulator as well as example simulations of stimulus evoked activity *in vitro*. As well as simulating stimulus evoked activity in physiological conditions, we are also interested in simulations of pathological conditions such as epilepsy. In this chapter we describe a simple analysis tool, created to identify and quantify epileptiform activity recorded *in vitro*.

The analysis of *in vitro* electrophysiology data is often done using either off-the-shelf commercial software or with scripts written in-house specifically for each task. Commercial software often lacks flexibility, it only provides a given set of measures and cannot be modified or built upon by the user. Only those familiar with programming and signal analysis can write their own scripts. Several open source general purpose platforms for analysing neural signals are also available (Hazan et al., 2006; Bokil et al., 2010; Lidiérth, 2009) . These provide a wide range of measures and tools for all sorts of neural signal. This flexibility however, means that they can still be daunting to use for those researchers not experienced in programming or signal processing.

This toolbox aims to provide an analysis platform specifically for extracellular potentials recorded during *in vitro* seizure-like events and late recurrent discharges. It provides a simple graphical interface for isolating events, and then processing each event to extract several measures from them. These are saved as a table of results with an entry for each event, easily readable and processed by any statistical software. Most of the measures included are well established and widely used in the identification or analysis of seizure-like events, however we also include a measure of seizure abruptness, which we believe has not been described before.

**4.1.1. Experimental models of epilepsy.** Epilepsy is a disease characterised by recurrent seizures - events of excessive and hypersynchronous activity, that can be seen on the EEG of patients (Beghi et al., 2005). Electrophysiologically similar events

can be recreated in the *in vitro* brain slice. Slices of tissue resected from patients with epilepsy have been found to show spontaneous epileptiform activity when recorded in an interface chamber. (Cunningham et al., 2012; Jones et al., 2016). Slices of tissue from healthy rodents show epileptiform activity when subject to various manipulations (Whittington et al., 1995; Trevelyan et al., 2006; Zemann et al., 2013). Manipulations usually concern a change in the ion concentrations of the bathing solution or the addition of a pharmacological agent. Removing magnesium ( $Mg^{2+}$ ) from the bathing solution is a robust method for the induction of seizure-like events in rodent tissue. Removal of the  $Mg^{2+}$  causes seizure-like events through a number of mechanisms. Firstly, it significantly increases the amplitude and duration of EPSPs by removing the block of the NMDA-receptor (Whittington et al., 1995). Secondly, removal of  $Mg^{2+}$  ions impairs inhibition by removing a substrate (Mg-ATP) required for the phosphorylation of the GABA<sub>A</sub> receptor (Stelzer et al., 1987; Whittington et al., 1995). Increasing the concentration of extracellular potassium ( $K^+$ ) is also considered ictogenic. It reduces the magnitude of the after hyperpolarisation, mediated by  $K^+$  flowing back out of the cell after the action potential has been generated. (Feng and Durand, 2006). It is often combined with lowering the concentration of  $Mg^{2+}$ , as we have done in the experiments described in chapter 5. These models rely on both an increase in excitation, and a partial weakening of inhibition to increase the likelihood of seizure-like events. Pharmacological manipulations may also increase the excitability of cells, or weaken in the effects of inhibition. 4-aminopyridine (4-AP) is a potassium channel blocker. By blocking potassium channels it prevents the rectifying currents that repolarise the cell after action potential. This keeps the cell depolarised, increasing its firing rate significantly (Perreault and Avoli, 1991). Blocking the function of GABAergic synapses also induces epileptiform activity. Gabazine, picrotoxin, and bicuculline all disrupt the function of GABAergic synapses, inducing epileptiform activity. This activity is often described as interictal discharges, and is of shorter duration than the seizure-like events induced by 4-AP or zero magnesium ACSF. This is attributed to the more complete blockade of GABAergic synapses, which have been shown necessary for more complex forms of epileptiform activity (Pitkänen et al., 2017). The tool presented here has been developed to identify and quantify the longer complex events induced by pro-convulsant ACSF solutions or 4-AP - referred to as seizure-like events (SLEs) - and

those induced by disinhibition - referred to as late recurrent discharges (LRDs). The late recurrent discharge refers to the late events induced in some models of SLEs. It is used here to refer to all short, large amplitude, spike wave events, which may or may not follow SLEs.

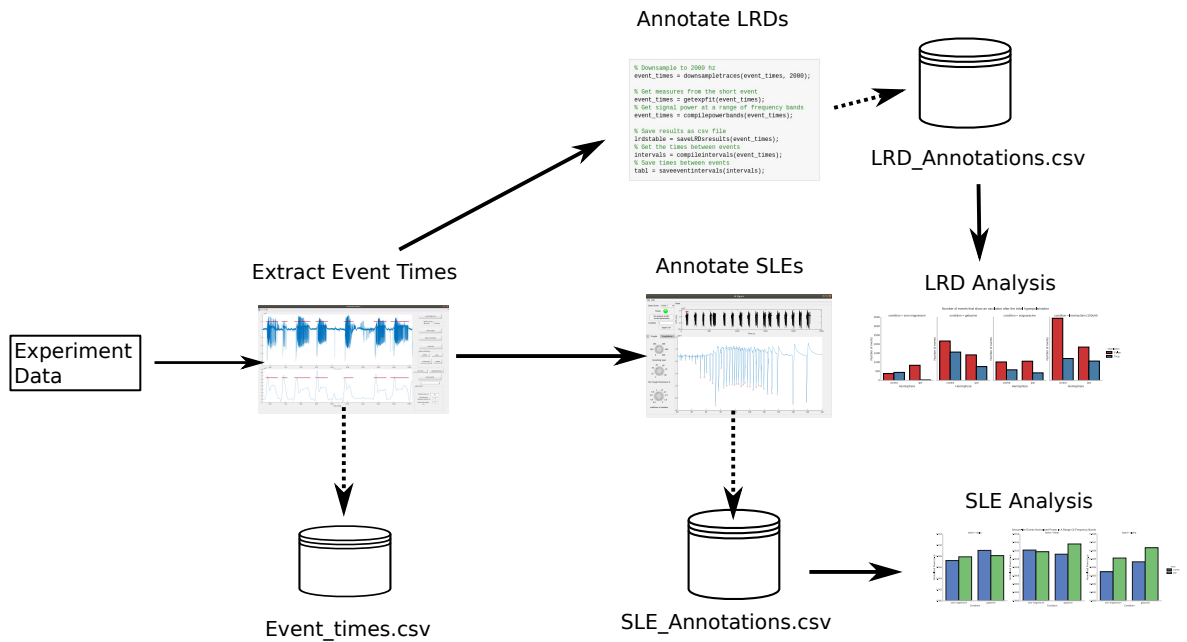


FIGURE 4.1. Schematic showing the workflow of the event isolation tool, the SLE annotation tool and the LRD analysis scripts. The full lines show inputs and next steps in the process, the dashed lines indicate the saving of data.

## 4.2. Event Isolation

One of the most arduous tasks in analysing seizure-like events or late recurrent discharges is isolating them from the rest of the trace. This has often involved manual annotation, whereby the researcher notes down the time at the beginning and end of each event, which can take some time and reduce the reproducibility of results because of individual variances in how one might annotate seizures. Automated annotation has been the solution to this, using metrics such as signal entropy or amplitude to identify seizure onset and termination. However, the variability inherent in biological data as well as artefacts and noise mean that human input is still needed for accurate results. We have taken a combined approach with an interface that allows the user to supervise the results, alter the parameters used to isolate events, select the time frame to be annotated, and remove or alter incorrectly labelled events.

**4.2.1. Isolating events:** The event isolation tool uses the power of the low frequency component of the signal as an estimate of where the seizure-like events start and stop. The process for isolating the events is described below:

If using a threshold on signal power:

- The signal is low pass filtered at 40 Hz using a 5th order Butterworth filter then segmented into a number of non-overlapping segments (the size of these is specified by the user) and the power of each segment is calculated as:

$$P = \sum_{i=n}^m S_i^2$$

Where  $n$  is the starting index of the segment and  $m$  is the ending index of the segment and  $S[i]$  is the segment at index  $i$ .

If using a threshold on the entropy:

- The signal is segmented into a number of non-overlapping segments (the size of these is specified by the user) and the Shannon entropy of each segment is calculated using MATLAB's `wentropy` function, which performs the following computation:

$$E = - \sum_{i=n}^m S_i^2 \log(S_i^2)$$

Where  $n$  is the starting index of the segment and  $m$  is the ending index of the segment and  $S[i]$  is the segment at index  $i$ . We call this the derived signal.

And then for both approaches (We refer to either the entropy or signal power as the derived signal):

- We interpolate (using MATLAB's `interp` function) the derived signal so that we have a derived signal with a sampling frequency of 200 Hz, regardless of the window size. This helps prevent the windowing of the signal from introducing inaccuracies.
- The derived signal is then displayed to the user and the user requested to select a threshold (as can be seen in the lower pane of the tool shown in figure 4.2, the red line is the selected threshold).
- The tool then takes all points of the derived signal above the threshold, it combines any that are separated by less than the minimum distance between

events parameter (default is 5 seconds), then discards any that are shorter than the minimum event length parameter (default is 10 seconds).

- The events are annotated on the trace using a red bar positioned above the trace and extending for the length of the event.

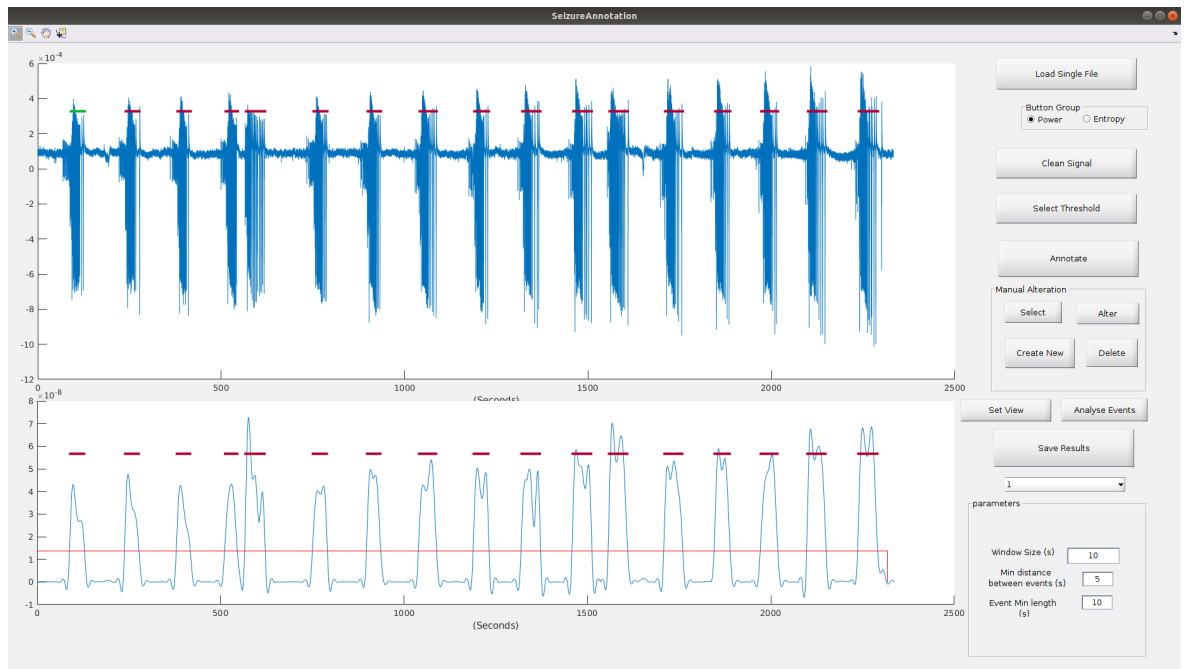


FIGURE 4.2. The graphical interface to the event isolation tool showing seizure-like events automatically isolated from the rest of the trace using the power of the low frequency component of the signal. The top trace shows the recorded SLEs, the bottom trace shows the power of the signal, the red line across the bottom trace shows the threshold power selected by the user. The maroon bars show the isolated events.

**4.2.2. Isolating late recurrent discharges.** In some *in vitro* seizure models the events may present as recurrent discharges (Pitkänen et al., 2017) that are not collated into easily identifiable longer events. These present late on in the zero magnesium model, and so in this context are known as late recurrent discharges (LRDs). Epileptiform activity described as interictal epileptiform discharges (IEDs) often shows similar characteristics, and can be identified using the same method. In analysing these we may wish to isolate each discharge individually, the tool provides some additional features for doing this. There is a parameter set especially for shorter events, with a shorter minimum event length and distance apart.

**4.2.3. Altering and saving event times.** The events are shown as the purple bars for long events and green bars for short events above the trace, the user can select any of these and either alter the start or end point of them, or delete them. The user

TABLE 4.1. The parameters used to generate the artificial traces. Shows the mean and standard deviation in parenthesis. Duration and interval were sampled from normal distribution, the frequency was constant.

Parameter	Mean (SD)
Duration	40 (5) seconds
Interval	100 (50) seconds
Frequency	1 Hz

can also add a new event by selecting the create event button and clicking where they would like it to start. Saving the event times can be done at any time by pressing the save results button. This will save the event times in a comma separated value format that can be opened using any spreadsheet software.

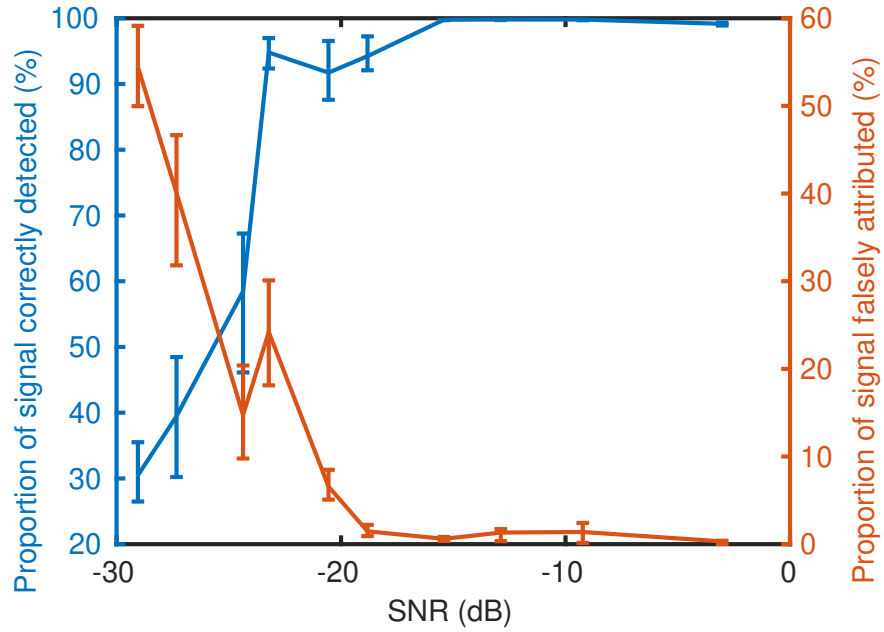
**4.2.4. The accuracy of the tool.** To evaluate the accuracy of this tool we applied it to an artificially generated dataset representing seizure-like events recorded with various levels of noise. Each artificial signal was generated by combining a number of event signals (1 Hz sine wave) separated by intervals of silence. The duration of events and intervals were randomly selected from a normal distribution, the parameters of which are described in table 4.1.

The noise was generated by randomly sampling from a normal distribution, and then scaled to the desired amplitude. The signal to noise ratio (SNR) was then calculated using the `snr` function in MATLAB. For each level of noise amplitude we generated 5 traces. We then used the tool to annotate each trace, to get a mean accuracy for each amplitude of noise. The accuracy was calculated as two measures, the amount of time wrongly assumed to be an event (as a proportion of the total amount of event time), and the proportion of the total event time correctly detected. We can see how the accuracy of the tool begins to decrease as the signal to noise ratio worsens in figure 4.3. We see similar levels of performance using both entropy and signal power and find the tool is quite robust until the SNR crosses the -20 dB threshold, at which point parts of events begin to be missed, and areas of noise mistaken for events. At lower levels of noise there is a persistent mis-attribution error using either method, indicating that the tool may be overestimating the duration of events.

### 4.3. Event Analysis

When the events have been isolated from the rest of the trace one can then extract a range of measures from them.

(A) The accuracy of the tool using signal power.



(B) The accuracy of the tool using entropy.

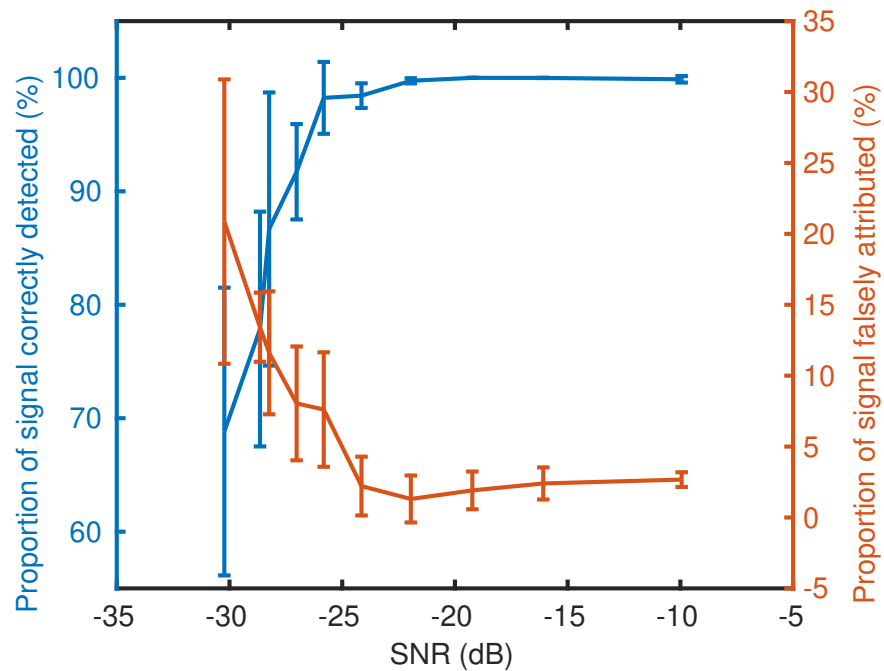


FIGURE 4.3. Higher amplitude noise results in a lower signal to noise ratio. The SNR is calculated as  $snr = 10\log_{10}\left(\frac{power(signal)}{power(noise)}\right)$ , with units in decibels (dB). As the SNR decreases, the tool begins to struggle with annotating the events. The left (blue) axis shows the proportion of the total event time in the signal correctly identified by the tool. The right (red) axis shows the amount of time misattributed to events, as a proportion of the overall event time.

**4.3.1. Automatic annotation.** From within the event isolation tool, having saved the event times of those just isolated, the user can select the Analyse Events

button. This will open the trace most recently saved for further analysis in a new window. This analysis will involve extracting several features, with each feature having its own tab on the main control panel. Table 4.2 summarises the measures taken of each event. Each tab contains some controls that allow the user to modify the parameters used for this part of the analysis. This can be useful to allow for the variance found in electrophysiological recordings. Users can also specify the experimental conditions and experiment date. If an experiment is recorded over multiple traces, then the user may specify the trace number and the offset to apply to the time course of the trace. When the user saves the analysis all measurements and parameters used for the measurements are saved in a comma separated value file. Figure 4.4 shows the interface of the event analysis tool.

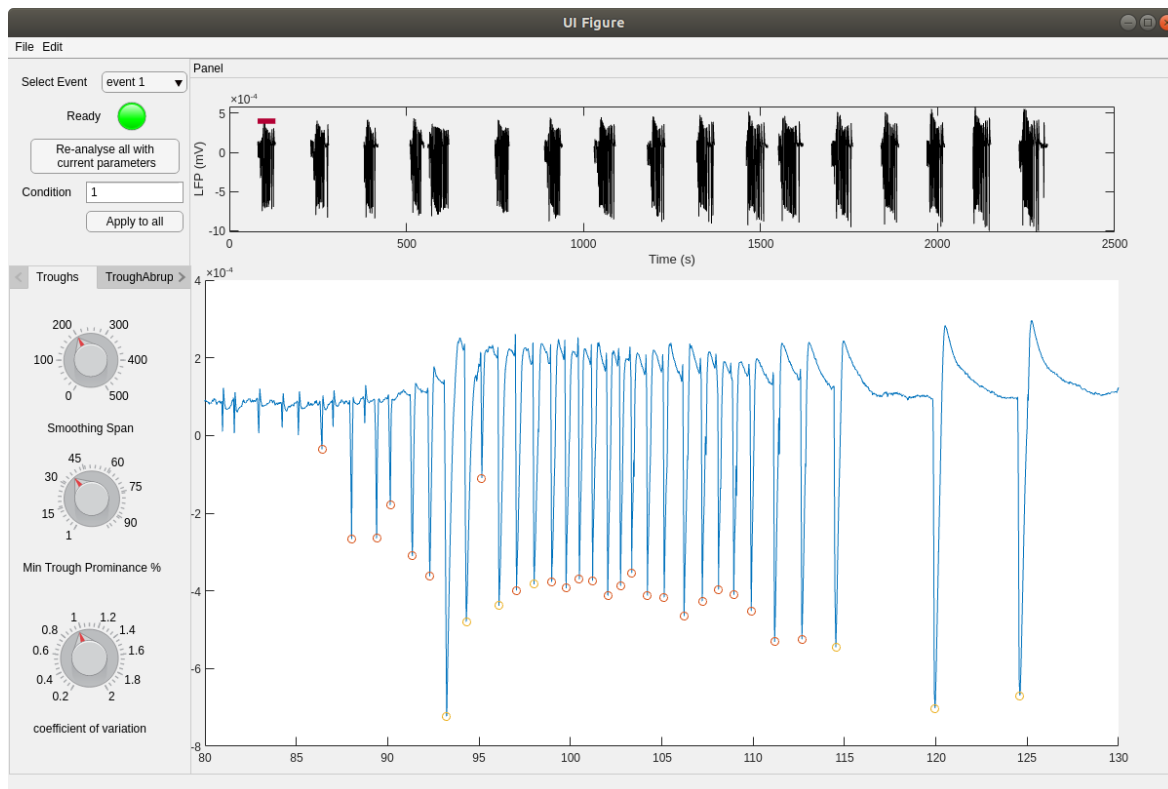


FIGURE 4.4. The tool used to do further analysis of the event signals. All isolated events are shown in the top panel, with the one currently selected highlighted by a red line above. Events can be selected from the drop down menu at the top left. The panel on the left shows the controls for the currently selected analysis. Trough identification is currently shown, the user can adjust the extent of smoothing on the signal, the minimum trough prominence, and the coefficient of variance, used in determining the troughs. The graph will update automatically as the user adjusts the dial.

### 4.3.2. Seizure-like events.

TABLE 4.2. Description of the main features currently extracted from the seizure-like event signal

<b>SLE Features</b>	<b>Explanation</b>
Number of troughs	Total number of troughs identified in the signal
Inter trough interval	Mean of the intervals between trough peak times
Trough mean width	The duration of the trough (time from when the signal drops below baseline to when it returns)
Average trough amplitude	The average of the distances from the baseline of the peak of the troughs
Max trough amplitude	The maximum of the distances from the baseline of the peak of the troughs
Trough abruptness	Steepness of logistic function fit to the troughs peaks
Trough rate	The rate of trough amplitude increase
MUA abruptness	Steepness of logistic function fit to the multi-unit activity
MUA rate	The rate of MUA increase during the event
LFP abruptness	Steepness of logistic function fit to the LFP
LFP rate	The rate of LFP increase during the event
Power in frequency bands	The normalised power of the signal in the standard range of frequency bands
Coastline	The sum of variation in the signal (Corresponds to a subjective measure of burst strength )
Intermittency	The concentration of the coastline within segments of the signal

4.3.2.1. *Trough identification.* In analysing each event, the first step is to identify the individual troughs in the LFP. The steps taken to do this are as follows:

- The signal is downsampled to a sampling frequency of 1000 Hz and then smoothed using the MATLAB smooth function (where the span parameter can be set by the user adjusting the corresponding dial).
- The MATLAB findpeaks function is then applied. The MINPEAKPROMINENCE parameter is specified by the user as a percentage of the range of the signal (minimum of signal - maximum of the signal). The MinPeakDistance parameter is fixed at 200 ms.
- From the findpeaks function we get a selection of troughs along with their heights and widths.
- Troughs with a width shorter than 50 ms classified as fine troughs (these are used for the abruptness analysis but considered separately for the other trough based metrics).
- Troughs with a width greater than 2 seconds are considered to be spreading depression like events and are not included in the analysis.

Figure 4.5 shows an example SLE with troughs identified as yellow circles and fine troughs as red circles.

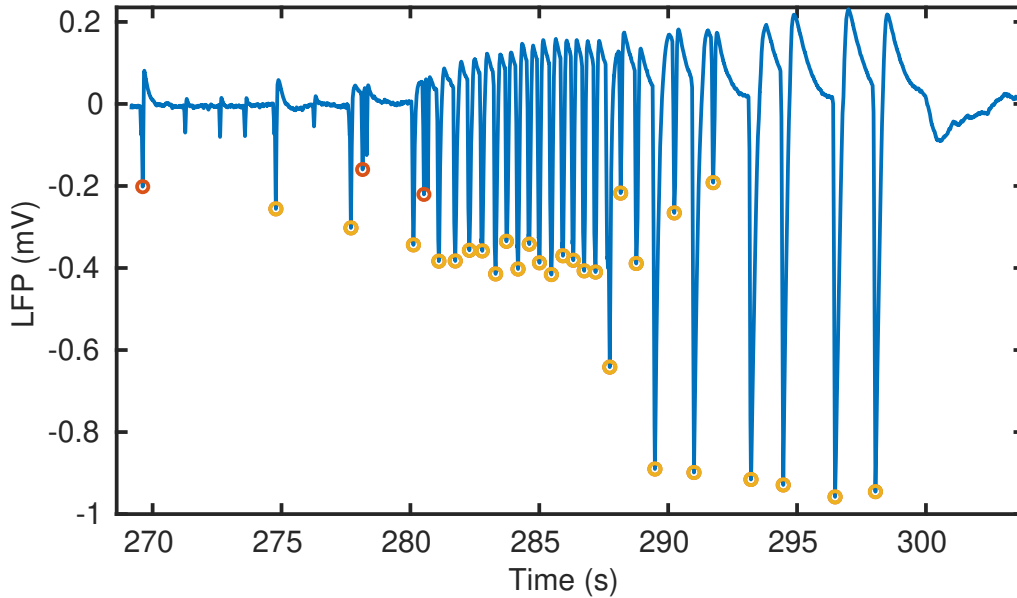


FIGURE 4.5. Shows an example SLE with troughs identified using the method outlined in this chapter. The major troughs are shown in yellow, the fine troughs shown in red.

4.3.2.2. *Calculating the coastline and intermittency.* The coastline is defined as the sum of the absolute value of the distance between subsequent data points in a signal. It can be calculated using equation 4.3.1, where  $S_i$  is the signal at point  $i$ , and  $N$  is the total number of points in the signal.

$$coastline = \sum_{i=2}^N |S_i - S_{i-1}| \quad (4.3.1)$$

We then normalise the coastline by dividing by the coastline of the baseline signal (the signal before SLEs begin). The intermittency can be calculated by sorting the absolute signal deviation ( $|S_i - S_{i-1}|$ ) in descending order before summing it. Then calculating the ratio of the sum of the first 20 % of the sorted coastline to the sum of the entire coastline. This gives a measure of how concentrated the signal is within its strongest segments. So SLEs that show strong bursts followed by silences, will show high intermittency.

4.3.2.3. *Measures of abruptness.* We compute several measures of seizure abruptness to quantify the rate at which the seizure signal reaches its maximum. This signal can either be the local field potential or the multi-unit activity. When measuring the abruptness of the local field potential, we can use either the trough peak amplitudes as

our data points, or we can bin the signal, calculate the power of the LFP during each bin, and use these as our data points. For the abruptness of the multi-unit activity this binning approach is used. We then take these data points and calculate a cumulative maximum (starting at the beginning of the event) of them. This signal is then used as the basis of our abruptness measures. Our first measure is based on the steepness of a logistic function fit to this cumulative maximum. To calculate the abruptness based on the fit of a logistic function we take the following steps:

- The signal is extended by 5 seconds at the beginning of the event to give it a baseline. The value used for the baseline of the multi-unit activity or the LFP power is its initial value, the baseline for the troughs is zero.
- To prepare the signal for fitting, it is normalised to between 0 and 1.
- We then fit the logistic function to these and use the logarithm of the k coefficient (the steepness of the fit), as the abruptness measure. Equation 4.3.2 shows the logistic function, where L is the curve's maximum value,  $e$  is the natural logarithm base, and  $x_0$  is the x value at which the curve crosses the midpoint.

$$f(x) = \frac{L}{1 + e^{-k(x-x_0)}} \quad (4.3.2)$$

A second approach to measuring the abruptness is to measure the rate of change of the cumulative maximum of the signal. We measure the mean rate of change of the cumulative maximum of the LFP or MUA over the course of the event. Equation 4.3.3 shows the calculation of this rate, where x is the cumulative maximum of the signal (either the MUA power or the LFP power) and m is the index of the maximum point of the event. This results in a measure of the rate of change of the cumulative maximum, that will have units mV/bin, where the bin is the time window specified by the user (default is 1 second). This rate can then be normalised by the maximum amplitude of the cumulative maximum (as it is for the results presented here), however the tool provides the rate before the normalisation along with the maximum amplitude of each event.

$$\Delta x = \frac{\sum_{i=1}^{i=m-1} x_{i+1} - x_i}{m} \quad (4.3.3)$$

This results in 5 measures of abruptness, three based on the steepness of the logistic function - described as *Trough Abruptness*, *LFP Abruptness*, and *MUA Abruptness* - and two based on the average rate of change - described as *LFP Rate* and *MUA Rate*.

TABLE 4.3. Shows the results of applying the three techniques used to measure the abruptness to 124 SLEs. Shows the abruptness value ( $\log(k)$ , where  $k$  is the coefficient of the logistic function), the median fitting error ( $R^2$ ), and the percentage of events that have an  $R^2$  greater than 0.95. The standard deviation (SD) is shown for the mean value, and inter quartile range (IQR) shown for the fitting error.

Measure	Mean Value ( $\pm$ SD)	Median $R^2$ ( $\pm$ IQR)	$R^2$ above 0.9
Trough Abruptness	2.05 $\pm$ 1.27	0.97 $\pm$ 0.05	92 %
MUA Abruptness	2.13 $\pm$ 1.25	0.98 $\pm$ 0.04	95 %
LFP Abruptness	1.8 $\pm$ 0.94	0.98 $\pm$ 0.03	97 %

We test our measures on a dataset of seizure-like events described in more detail in Chapter 5. The tool described above has been used to identify SLEs and then calculate the abruptness measures on them using the method just described. In figure 4.6 we show an example SLE, with its cumulative trough amplitude overlain in purple, and the logistic function shown in green. Figure 4.7 shows the example cumulative multi-unit activity and the LFP power fit to the logistic function. In table 4.3 we summarise the goodness of fit of the SLEs to the logistic function. Over the whole dataset of 154 SLEs we find that the logistic function provides a good fit, with over 90% of events having an  $r^2$  value of more than 0.9 for each of the measures, and median  $r^2$  values of 0.97, 0.98, and 0.98 for the *Trough Abruptness*, *LFP Abruptness*, and *MUA Abruptness* respectively.

**4.3.3. Correlations between SLE measures.** To test whether measures were contributing unique information we applied a pairwise correlation test across a range of the metrics calculated on the SLEs. As not all measures were normally distributed we used Spearman’s rank correlation coefficient to measure the correlation. The strength of correlation between each of the measures is shown in figure 4.8. Only correlations calculated to be statistically significant are shown (white cells have  $p > 0.05$ ). We find some expected correlations, for example the number of troughs in an event correlates with the duration of the event ( $\rho = 0.72$ ). The peak MUA amplitude also correlates strongly with the trough amplitude, again this is expected because we would expect that deeper troughs would indicate greater recruitment of cells. The abruptness measured from the LFP power (using the logistic function method) also correlates with the abruptness measured by trough amplitude ( $\rho = 0.55$ ), which is unsurprising because the power of the LFP will largely be determined by the size of the troughs. However the abruptness measured by the MUA does not have a significant correlation

with either. The LFP rate weakly correlates with the trough and LFP abruptness ( $\rho = 0.17$ ), but not with the MUA abruptness or MUA rate. The MUA rate correlates strongly with the coastline ( $\rho = 0.73$ ) and intermittancy ( $\rho = 0.77$ ), but not with any other abruptness measures. The coastline and intermittancy themselves are also very strongly correlated ( $\rho = 0.92$ ). The strong correlation here indicates that events that have a large coastline do so because they contain powerful bursts of activity rather than persistently high activity. The strong correlation between coastline and the MUA rate ( $\rho = 0.73$ ) and the MUA peak amplitude ( $\rho = 0.43$ ), indicate that it may be dominated by the MUA when this is high. The coastline is also strongly correlated with the trough amplitude ( $\rho = 0.65$ ).

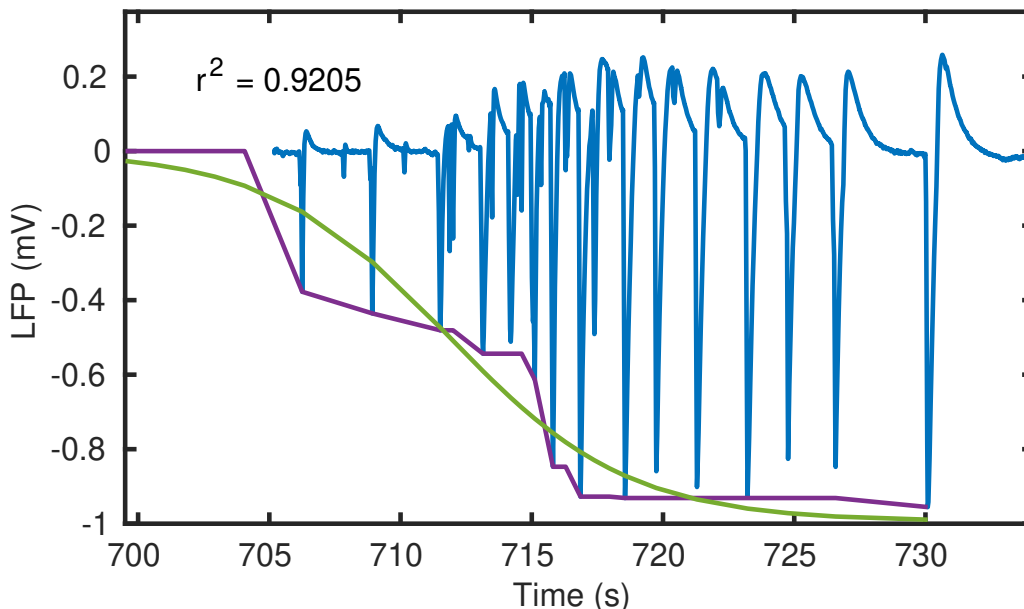


FIGURE 4.6. Shows an example SLE with the cumulative maximum of its trough amplitudes shown in purple. A baseline has been created by extending the cumulative maximum by 5 units before the first trough, where each unit is the mean inter trough interval of the event, and the baseline has a value of 0. The logistic function (defined in equation 4.3.2) has then been fitted to this, the fitted curve is shown as the green line.

**4.3.4. Quantifying Repetitive Short Events.** Late recurrent discharges (LRDs) are repetitive short events with a large amplitude. They occur late on in the zero magnesium model or with the application of gabazine (Pitkänen et al., 2017). They are characterised by an initial hyperpolarisation, which then decays back to the baseline level. This decay phase often contains an oscillating afterhyperpolarisation, which may contain up to ten troughs. Figure 4.9 illustrates an example LRD. While our analysis

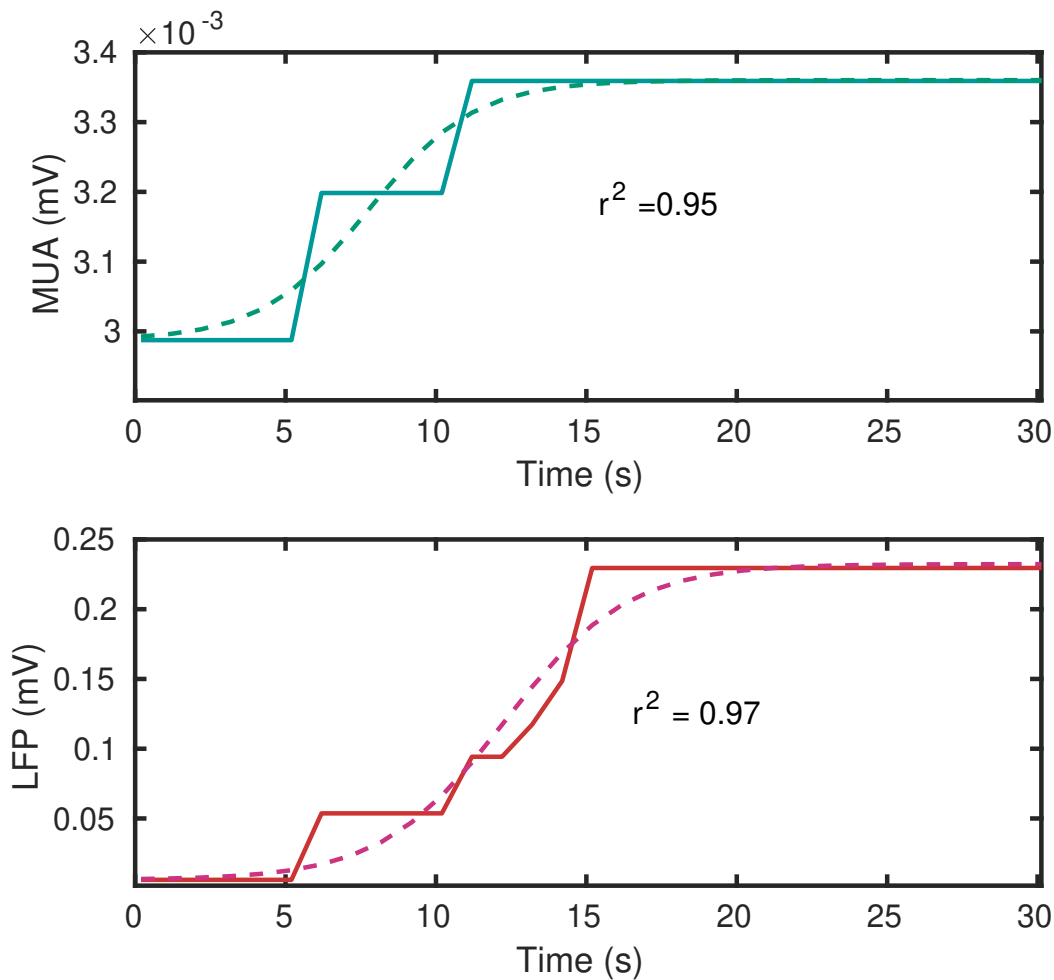


FIGURE 4.7. (Top) Shows the cumulative maximum of the multi unit activity from the example trace as the solid green line. A baseline has been created by extending the cumulative maximum by 5 units before the start of the signal, where a unit is the time window over which the MUA power is calculated. The logistic function (defined in equation 4.3.2) has then been fitted to this, the fitted curve is shown as the dashed green line. (Bottom) Shows the cumulative maximum of the LFP power as the solid red line. The baseline has been calculated in the same manner as for the MUA, the logistic function fit is shown as the dashed red line.

tool does not analyse LRDs, we provide a series of MATLAB scripts to measure the amplitude of the initial hyperpolarisation, and the amplitude of the after hyperpolarisation (the decay phase oscillation). Two measurements are taken for the initial hyperpolarisation, one taken from the raw signal and one using the smoothed signal to avoid sampling any sharp spikes (like the one seen in figure 4.9). This then allows the user to obtain a measure of the initial sharp spike if it exists, and of the slower initial hyperpolarisation. We also fit a single exponential function to the signal, between the minimum point of the initial hyperpolarisation (from the smoothed signal) to the start of the oscillation, to get a rate of decay of the signal amplitude. We can then create a

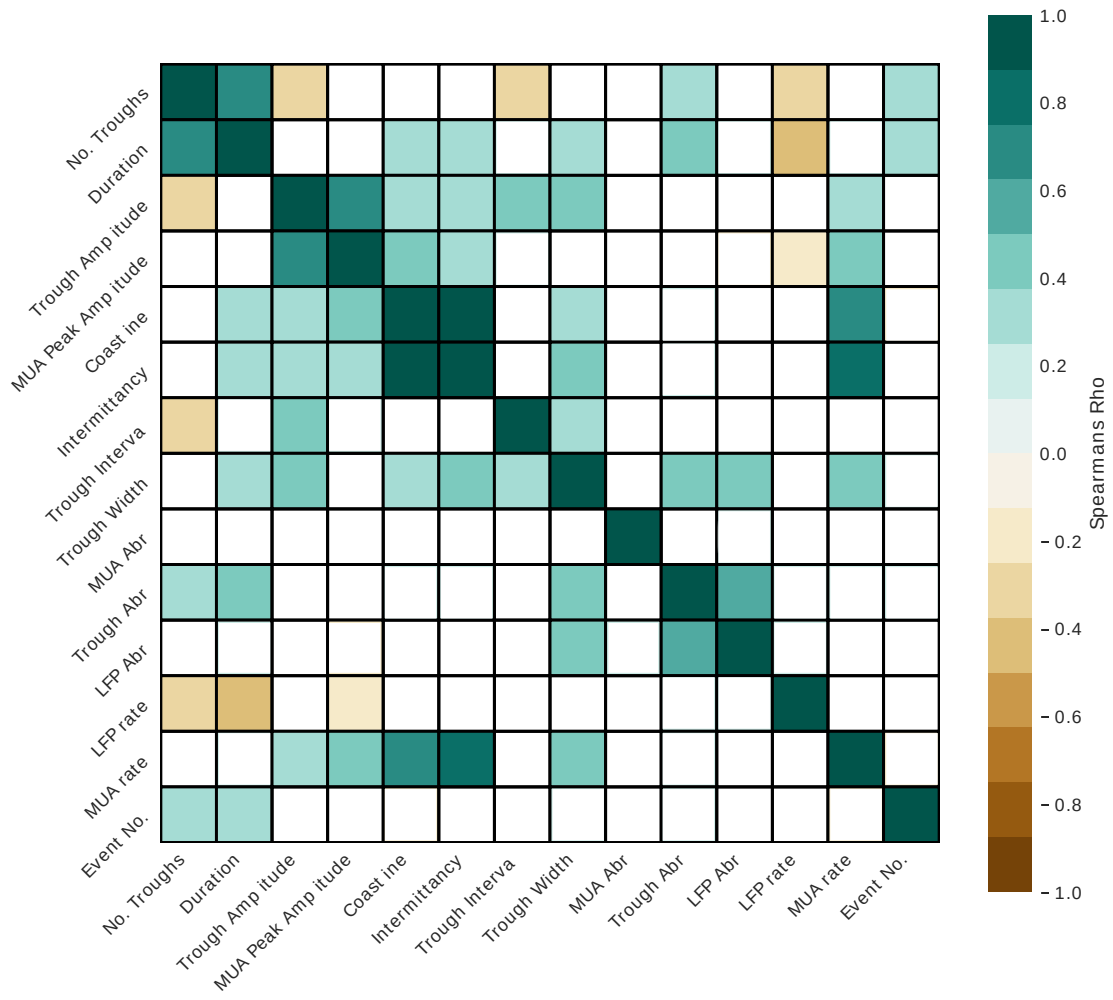


FIGURE 4.8. Shows the correlation between the major features of the events. Spearman's rank correlation coefficient has been used, as some features are not normally distributed. Only shown are correlations of statistical significance ( $p > 0.05$ ) which have been corrected through the false discovery rate correction for multiple comparisons.

residual signal by subtracting our exponential fit from the decay phase. The peaks and troughs of this residual can then be found using the Matlab findpeaks function. Their amplitude then provides a measure of the decay phase oscillation amplitude which indicates the size of currents contributing to this phase. We can also calculate the frequency of this oscillation by finding the interval between peaks.

#### 4.4. Discussion

This tool firstly provides an easy to use interface for the identification of SLEs (seizure-like events) and LRDs (late recurrent discharges) using a threshold based approach. These event times can be saved in a spreadsheet format, which serves as the input to the next part of the tool. We have found that these times can be identified with good accuracy (identifying more than 95% of the signal, and misidentifying less than

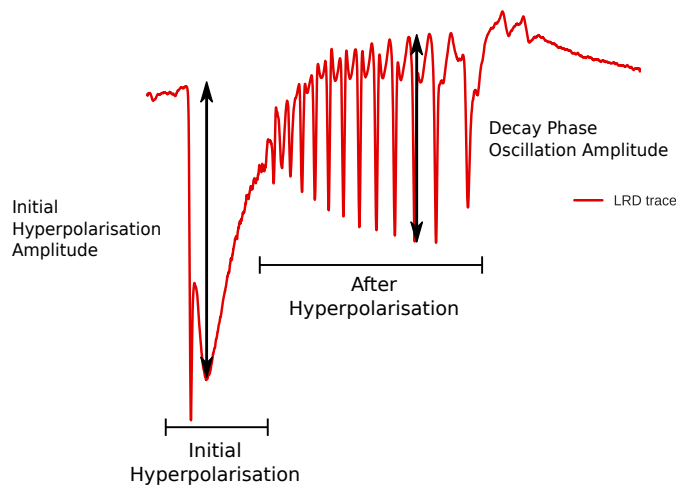


FIGURE 4.9. A late recurrent discharge, with an after hyperpolarisation oscillation. Shows the areas referred to as the initial hyperpolarisation and after hyperpolarisation and the measure referred to by their amplitude. The initial hyperpolarisation measures the amplitude of the first major trough, the amplitude of the sharp spike is measured separately as not all events show a sharp spike. The after hyperpolarisation is measured as the amplitude of the subsequent troughs.

5%) up until a signal to noise ratio of -20 dB. At low levels of noise the proportion of the signal identified approaches 100%, however, the proportion of the signal incorrectly identified remains at around 2%. This indicates that we are consistently overestimating the duration of the events, which is likely caused by the averaging approach used to construct the signal used for taking the threshold. We use an averaged signal because the oscillatory nature of SLEs leads to periods where the power or entropy will be below threshold, resulting in the segmentation of the event. Averaging using a window introduces an error because unless the window happens to fall at the event onset and offset, it will encompass time within the event and outwith the event, so if the window average is above threshold it will misidentify the portion of this window that lies outwith the event as being part of the event. To minimise this effect we have used interpolation to resample our averaged signal at 100 Hz. This does not completely remove the error because the sharp increase in the signal at event onset will not be matched by such a sharp increase in the interpolated averaged signal. Future work to remove this error should look for a windowing function that will allow a sharp onset without following the oscillation of the event. As well as event isolation, for SLEs we provide another interface from which the user can observe the annotations made on each event and adjust the parameters used. This tool extracts the heights and widths of the event

troughs, the coastline and intermittency of the event and measures the abruptness of the event. We have compared the abruptness measured using the LFP, MUA, and trough amplitude on 154 example SLEs. We found that the abruptness measured via LFP and trough amplitude have similar mean values across the all events (2.05 and 1.8 respectively), and are correlated with a Spearman's rho of 0.55. Abruptness measured by the MUA has a mean of 2.13 and does not correlate with the LFP and trough based measures. It is unsurprising that the LFP and trough based measures correlate because the size of the troughs will correlate with the power of the LFP over their sampling window. The lack of correlation between the abruptness of the MUA and LFP may be due to the spatial extent over which they sample. The MUA is a very local measure, recording the magnitude of activity within the immediate proximity of the electrode. The LFP on the other hand can measure recurrent synaptic activity reflective of the activity in the local network, but it can also measure feed-forward synaptic activity reflective of neural activity in tissue upstream of the recording electrode (Mattia et al., 2010). Distinct patterns of MUA and LFP activity during seizure onset are also well documented (Schevon et al., 2012) with LFP build up being observed before MUA build up, or LFP build up observed without any subsequent MUA build up (Wagner et al., 2015). This presence of LFP without MUA has been hypothesised to represent the attempted recruitment of the area under the electrode, with a subsequent peak in MUA representing eventual recruitment, and no subsequent MUA peak representing failed recruitment. This could be the case here, with some events possibly being quite abrupt but failing to recruit the tissue directly under the electrode and so limiting the abruptness measured there. This analysis pipeline provides a complete solution for electrophysiologists who wish to isolate and obtain an initial set of measures describing their SLEs or LRDs. It may also be easily built upon to provide any additional specific measures the user may wish. Chapter 5 shows how this tool can be used to analyse *in vitro* recordings from a chronic model of epilepsy in rat.



# An Analysis of *Ex Vivo* Recordings From A Chronic Model of Epilepsy In Rats

## 5.1. Introduction

Focal epilepsy is characterised by a region of hyper-excitability, which transiently recruits the rest of the brain into its pathological regime, causing seizures. This hyper-excitability region, known as the focus, is often identified and removed to stop seizures when pharmacological intervention does not work (Wiebe et al., 2001). Identifying the focal region however, is not a trivial task (Valentín et al., 2002). In this chapter we wished to investigate whether we could identify the focus in *ex vivo* brain slices taken from rats subject to the tetanus toxin model of chronic focal epilepsy, using either the abruptness measures described in chapter 4 or using the response to single pulse stimulation. It has been shown that single pulses of electrical stimulation, applied intracranially can identify regions of hyper-excitability in patients with focal epilepsy, with more complex responses more likely to occur in or near to the focus (Valentín et al., 2002; Nayak et al., 2014). Characterising a comparable phenomenon *in vitro* would provide a more accessible system with an output that can be readily compared to clinical data. We propose that our measures of seizure abruptness may also help to distinguish the focal region (or slice) from the non-focal. Theoretical work has linked excitable tissue to high amplitude onset patterns, while healthy tissue has been linked to lower amplitude onset patterns (Wang et al., 2017). If the focal slices in our model are more excitable then we would expect a higher amplitude onset pattern which would translate to a more abrupt onset. This chapter begins by looking at the abruptness (as well as some typical measures of seizure intensity) of seizures recorded in slices contralateral and ipsilateral to the tetanus toxin injection site. We then look at the response to single pulsed stimulation, first looking for differences in the immediate response to stimulation, and then in looking at the likelihood of more complex late responses occurring. We end the chapter by looking at simulations of stimulus evoked activity, comparable to that recorded in experiments, and simulations of epileptiform

activity which we compare with our recordings of non-evoked activity. The preparation and monitoring of the rats, the preparation of the brain slices, and the experiments recording the activity induced purely by pro-convulsant medium or pharmacological manipulation were performed by Anupam Hazra. The experiments involving stimulus evoked activity and multi-electrode array recordings were performed by the author as well as the analysis of all data presented here. The pipeline described in the previous chapter has been used for the analysis.

## 5.2. The Tetanus Toxin Model of Chronic Epilepsy

The tetanus toxin model has been used in the study of epilepsy since the early 1990s and is one of the most commonly used models of chronic focal epilepsy (Nilsen et al., 2005). Usually applied to rats, it involves the injection of the tetanus toxin directly into the neural tissue, which then causes a decrease in the function of inhibitory synapses, leading to focal and secondarily generalising seizures (Jefferys and Whittington, 1996). Although the injection causes an impairment of the inhibitory synapses, this is temporary and has been shown to reverse when the toxin is cleared from the system with seizures persisting in the animal for a long time after this. Injections into both hippocampus and neocortex have been studied, with both producing a chronic epileptic focus, but with injections to neocortex causing an epileptic condition that is more severe and that persists for longer (Nilsen et al., 2005).

**5.2.1. Mechanism of action.** Tetanus toxin (TeNT) is known to bind to Vesicle Associated Membrane Protein (VAMP) which it then breaks down. VAMP is present at synaptic terminals where it is essential for synaptic transmission (Schiavo et al., 1993). TeNT's ictogenic action is hypothesized to be a result of its selectivity for inhibitory synapses. Although it has been shown that over its active period TeNT selectively impairs inhibition, there is no conclusive agreement on the mechanism by which it does this (Ferecsko et al., 2015). One hypothesis is that greater uptake of TeNT by interneurons is a result of their higher firing rate. This is supported by the evidence that synaptic transmission is required for uptake. Another hypothesis is that it binds differentially to various VAMP isoforms. In neocortex VAMP2 has been seen to be predominantly expressed at excitatory synapses, while VAMP1 is expressed equally at both excitatory and inhibitory (Bragina et al., 2010). While in hippocampus, VAMP1

is more prevalent at inhibitory synapses (Ferecsko et al., 2015). However, there is no agreement as to whether TeNT preferentially binds to or breaks down VAMP1 more than VAMP2 (Schiavo et al., 1993; Ferecsko et al., 2015), and functionally, while it does show a preference for inhibitory synapses, excitatory synapses are also significantly impaired (Ferecsko et al., 2015).

### 5.2.2. Resected neocortical slices from rats injected with tetanus toxin.

Although the tetanus toxin model of chronic epilepsy is primarily studied *in vivo* much can be gained from *ex vivo* slices prepared from the injected rats. The slice preparation provides a reduced, more accessible system, that may be easier to interpret than the larger and more complex *in vivo* system. Carter et al. (2011) use *ex vivo* slices from the pilocarpine model of chronic epilepsy to characterise the different spontaneous recurrent epileptiform discharges found in multiple regions of the hippocampus. Serafini et al. (2016) use the *ex vivo* preparation of somatosensory cortex slices, from tetanus toxin injected rats, invoking seizure-like events by exposing the slices to zero magnesium ACSF and 4-aminopyridine. They use a high density 60 channel electrode array to sample across the cortex around the injection site, identifying patterns of seizure spread that differ between control and injected animals. They find that seizures in injected animals have higher voltages and wider spreads than in controls. In control slices several small local foci appear on the recording simultaneously, while in injected slices, one large focus appears that has a wide spread. They also compare the primary focus (ipsilateral to injection site) with the secondary focus (contralateral to injection site), with the primary focus showing larger amplitude events among other differences.

## 5.3. Experimental Setup

In the experiments described here, slices have been prepared from rats injected with tetanus toxin in the motor cortex of the right hemisphere. Eight to 20 days after the TeNT injection rats were euthanised by non-recovery general anaesthesia followed by intracardial injection of a sucrose based artificial cerebrospinal fluid (sACSF). Coronal slices are cut, with the preparation kept in oxygenated ice cold sACSF at all times. The motor cortex (M1 and M2) at Bregma 1.60 mm and interaural 10.60 mm is then isolated from subcortical structures and the neighbouring somatosensory cortex. These slices are then placed into a holding chamber with oxygenated regular ACSF for at least one

hour before being transferred to an interface recording chamber. Here they are allowed to rest for 30 minutes before being washed through with a pro-convulsant artificial cerebrospinal fluid (ACSF) containing no magnesium and elevated potassium (6mM) to induce seizure-like activity. The slice is kept like this for 1.5 hours, most slices then show spontaneous seizure-like events (SLEs) during this time. Gabazine (10 $\mu$ M) is then added to the bath. This provokes the slice to show late recurrent discharges (LRDs) usually within 15 minutes. We record the extracellular potential throughout, using a glass micropipette in layer 2/3, sampling at 5 KHz.

## 5.4. Experimental Results

The software described in chapter 4 has been used to identify and quantify the events described here. We used the automated seizure detection, counting only SLEs that persist longer than 10 seconds. The experimental results presented here concern the differences found in *in vitro* recordings from neocortical slices taken from hemispheres ipsilateral and contralateral to the tetanus toxin injection site. We first look at differences in the characteristics of SLEs produced by the pro-convulsant medium (the zero magnesium, high potassium ACSF, referred to in figures as zero magnesium) which accounts for the majority of SLEs. We then look at the LRDs provoked by the application of gabazine. Finally we look at events evoked by bipolar electric field stimulation in slices also bathed in the pro-convulsant medium.

5.4.0.1. *Statistical methods:* For each measurement we calculate a mean for each slice - two or four slices were taken from each animal (one or two from each hemisphere). We show a box plot for each measure, illustrating the distribution of slice means. In these, the midline represents the median value, the box shows the first to third quartiles, whiskers show the range of values within 1.5 of the interquartile range. All other points are shown as outliers.

**5.4.1. Interhemispheric differences in seizure-like events.** The following figures show the interhemispheric differences in the properties of seizure-like events generated after switching to the pro-convulsant medium. Figure 5.1 compares the properties of seizure-like event troughs. We find no significant difference in the number of troughs, the frequency of the troughs, or the width of the troughs between hemispheres. We do find a significant difference ( $p < 0.05$ , Student's t test) in the amplitude of the troughs.

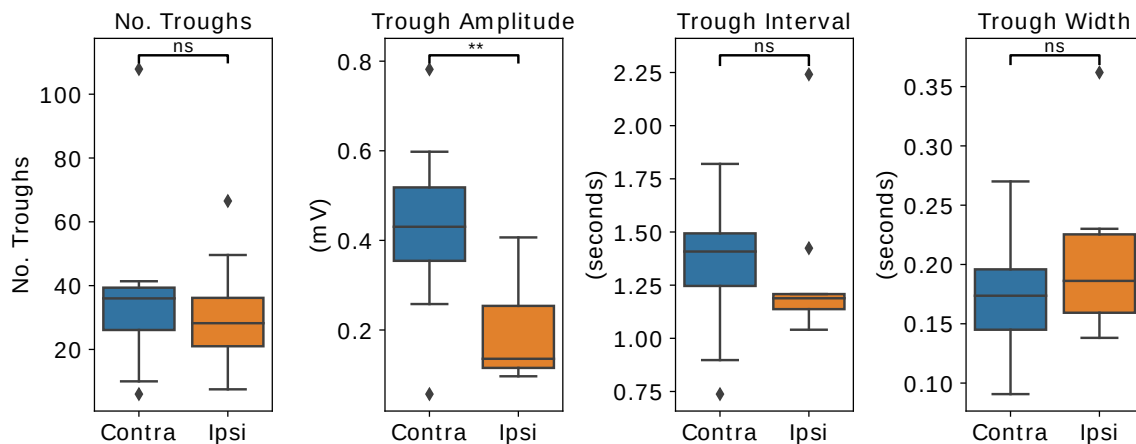


FIGURE 5.1. Shows a comparison of the trough characteristics of events contralateral (blue) and ipsilateral (orange) to the TeNT injection site. The distributions presented are based on slice averages from 11 contralateral slices and 9 ipsilateral slices. \* indicates a significant difference between the means ( $p < 0.05$ , Student's t test), \*\* indicates that it remains significant when corrected for multiple comparisons, ns indicates no significance. Boxplot midline indicates the median, and the whiskers indicate 150% of the interquartile range, with values outwith this shown as outliers.

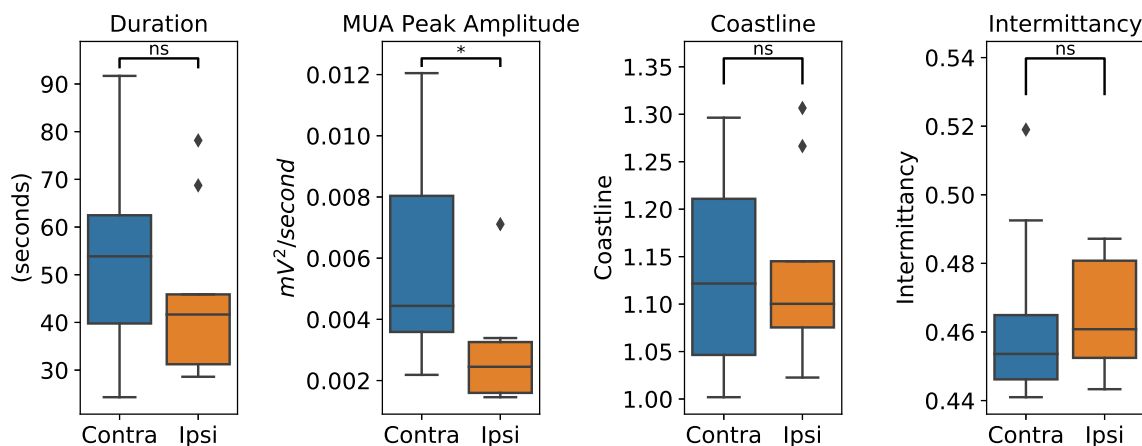


FIGURE 5.2. Shows a comparison of the duration, multi-unit activity peak amplitude, coastline, and intermittency of events contralateral (blue) and ipsilateral (orange) to the TeNT injection site. The distributions presented are based on slice averages from 11 contralateral slices and 9 ipsilateral slices. \* indicates a significant difference between the means ( $p < 0.05$ , Student's t test), \*\* indicates that it remains significant when corrected for multiple comparisons, ns indicates no significance. Boxplot midline indicates the median, and the whiskers indicate 150% of the interquartile range, with values outwith this shown as outliers.

This indicates that while events from each hemisphere evolve over a similar timescale, there are significantly larger synaptic currents at play during the troughs of the events in the contralateral slices. This is surprising, given that tetanus toxin is known to be icogenic and Serafini et al. (2016) report finding increased amplitudes in the site

ipsilateral to injection. Figure 5.2 compares the duration, multi-unit activity (MUA) peak amplitude, the coastline, and the intermittency of events in each hemisphere. We see a median duration in contralateral slices of 54 seconds and in ipsilateral slices of 42 seconds, however this difference is not significant ( $p = 0.36$ ). We do see a significant difference between the peak MUA amplitude, with contralateral slices showing a larger peak amplitude. This indicates that at the peak of the seizure there is more recruitment of local cells in contralateral slices. We find no significant difference in the coastline or intermittency between hemispheres. Figure 5.3 compares the three abruptness measures based on the logistic fit to the trough amplitudes, LFP power, and MUA power. We find no significant difference for any of these measures but the median LFP abruptness measure is higher in ipsilateral events ( $p = 0.2$ ). Figure 5.4 compares the rate at which events reach their maximum amplitude either of LFP or of MUA. We find that the ipsilateral hemisphere approaches its maximum LFP faster than that of the contralateral, but that there is no difference between how fast each approaches its maximum MUA. As there is no difference in the MUA rate or MUA abruptness measure between hemispheres it appears unlikely that the pattern of MUA build up can be used to differentiate between the area of the injection site and the area contralateral to it. The build up of the LFP may do a better job of distinguishing between regions, there is a clear difference between the LFP rates, and it is possible that with more repeats we would see a difference in the LFP abruptness measure. As they are correlated ( $\rho=0.17$ , shown in figure 4.8), it is possible that the abruptness measured by fitting the logistic function is less sensitive than that measured by the rate, but that they capture similar patterns of activity. We should also consider that the LFP rate is normalised by the maximum LFP amplitude, and so while they are reaching their maximum amplitude at different rates, the absolute rate may not be any different. We find no difference between hemispheres in the non-normalised rate, indicating that the rate of ipsilateral events is not scaled down to reflect their lower overall amplitudes as we might expect. This is despite the non-normalised rate correlating strongly ( $\rho=0.7$ ) with the event amplitude across all events, indicating that we should expect a group of events with consistently lower amplitudes to have lower rates of increase. Figure 5.5 shows the relative power of events in a range of frequency bands, we find that there is no significant difference between hemispheres for any bands.

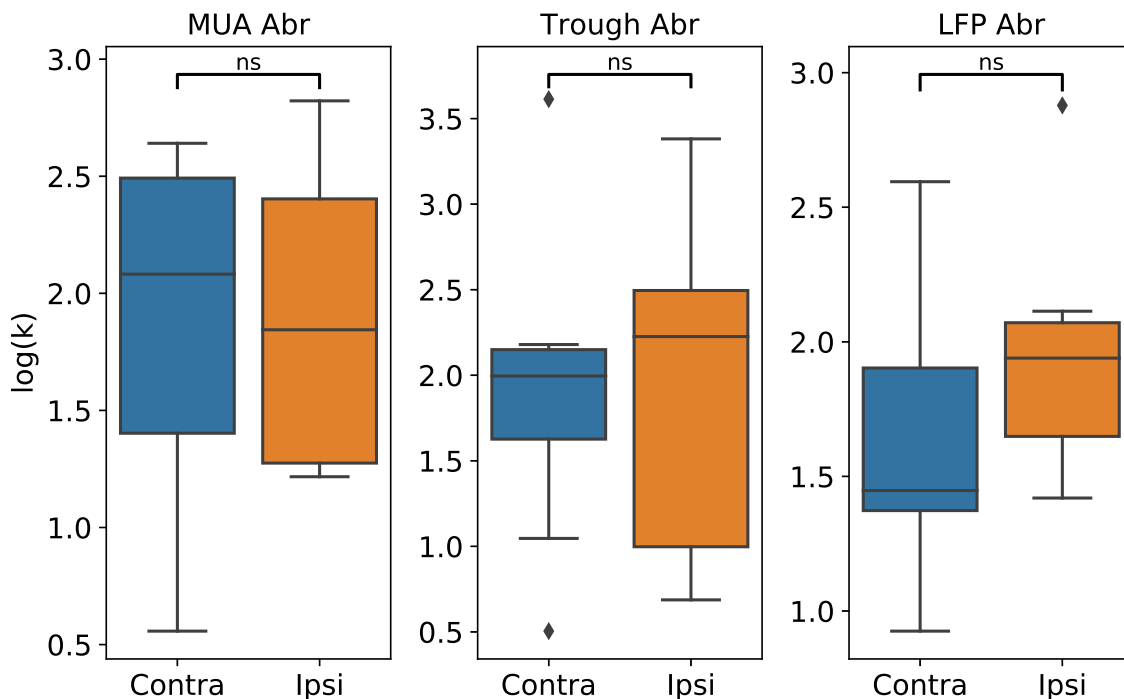


FIGURE 5.3. Shows a comparison of the abruptness measurements applied to events recorded from slices contralateral (blue) and ipsilateral (orange) to the injection site. The abruptness measure is the steepness of the logistic function fit to the build up of seizure-like activity measured in three different ways. The multi-unit activity abruptness (MUA Abr) fits the logistic function to the cumulative maximum of the multi-unit activity power, the trough abruptness (Trough Abr) fits the logistic function to the cumulative maximum of the trough amplitudes, and the LFP abruptness (LFP Abr) fits the logistic function to the power of the LFP. These measures are described in more detail in chapter 4. The distributions presented are based on slice averages from 11 contralateral slices and 9 ipsilateral slices. \* indicates a significant difference between the means ( $p < 0.05$ , Student's t test), \*\* indicates that it remains significant when corrected for multiple comparisons, ns indicates no significance. Box-plot midline indicates the median, and the whiskers indicate 150% of the interquartile range, with values outwith this shown as outliers.

5.4.1.1. *Interhemispheric differences in late recurrent discharges.* We add gabazine to the slices after one hour in the pro-convulsant ACSF. This firstly transforms the SLEs, which become shorter and sharper, before quickly becoming what many refer to as a late recurrent discharge - a short event with a relatively large amplitude initial hyperpolarisation, which is then often followed by an oscillation as the extracellular potential decays back to the baseline. By applying gabazine at  $10 \mu\text{M}$ , we nullify the inhibitory synapses, and so we can attribute interhemispheric differences to the excitatory network. Figure 5.6 shows the inter-event intervals for slices from contralateral and ipsilateral hemispheres when exposed to gabazine. We can see a significantly larger interval for events in ipsilateral slices, which implies a lower frequency of events.

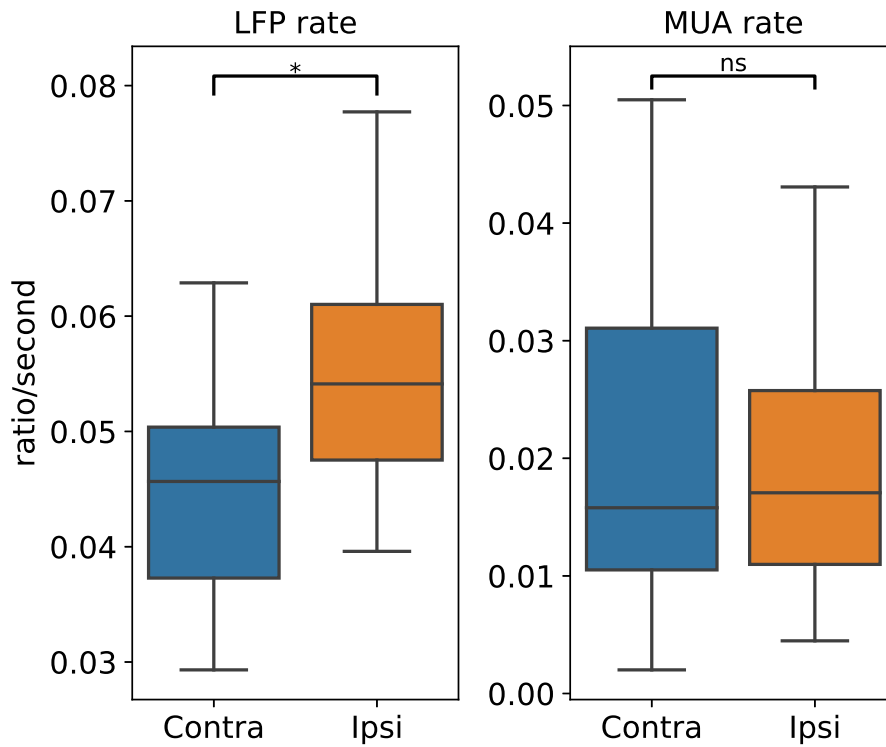


FIGURE 5.4. Shows the rate at which the event LFP and MUA approaches its maximum. This is calculated on the cumulative maximum of the signal, and then normalised by dividing by the signal maximum so that the units would be the proportion of the maximum gained per second. The calculation of the rate is described in more detail in chapter 4. \* indicates a significant difference between the means ( $p < 0.05$ , Student's t test), \*\* indicates that it remains significant when corrected for multiple comparisons, ns indicates no significance. Boxplot midline indicates the median, and the whiskers indicate 150% of the interquartile range, with values outwith this shown as outliers.

When we look at the amplitudes of LRDs we also see a significant difference, both the initial hyperpolarisation and the decay phase oscillation, contralateral events are larger. Initial hyperpolarisation amplitudes are between 0.1 and 1.2 mV and decay phase oscillations have amplitudes in the range of 0.05 to 0.5 mV.

With the inhibitory network nullified, a reduction in the frequency of events may be a result of the impaired excitatory synapse function that is seen with TeNT injections (Ferecsko et al., 2015). The difference in event amplitude could also be the result of an impaired excitatory network in ipsilateral slices.

5.4.1.2. *Correction for multiple comparisons.* As multiple comparisons have been made on various aspects of the same data - we have performed 21 tests for statistical significance in total - it is important to consider the possibility of type 1 errors as a result of apparently significant results appearing by chance. To account for this we have

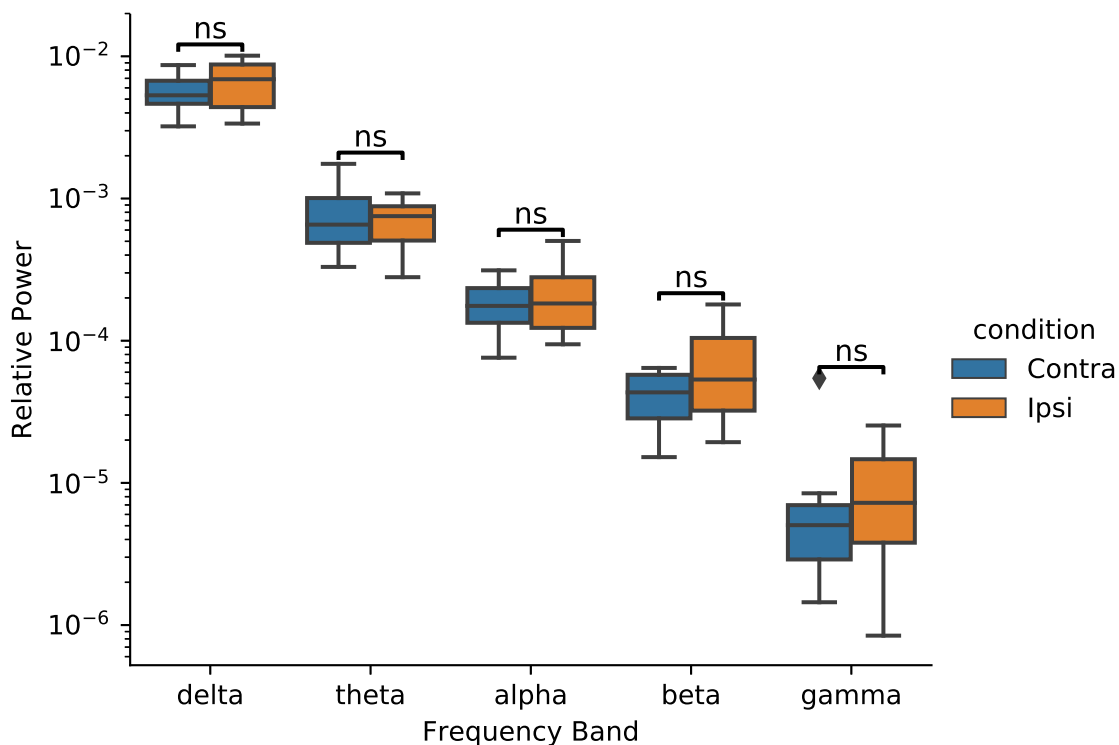


FIGURE 5.5. Shows the relative power of the various frequency bands. Showing Delta (1 - 4 Hz), Theta (4 - 8 Hz), Alpha (8 - 13 Hz), Beta (13 - 30 Hz), and Gamma (30 - 80 Hz). Boxplot midline indicates the median, and the whiskers indicate 150% of the interquartile range, with values outwith this shown as outliers, ns indicates no significance.

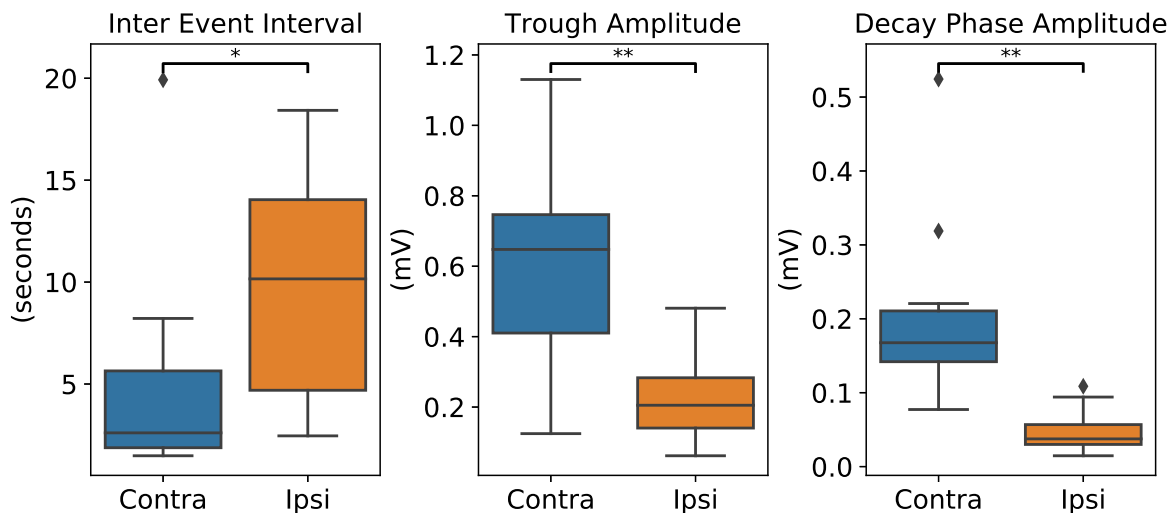


FIGURE 5.6. Shows the inter-event interval and amplitude of LRDs recorded in slices either contralateral or ipsilateral to the injection site. The trough amplitude is the amplitude of the major trough, not the initial sharp spike or the troughs that occur during the decay phase. The decay phase amplitude is the mean amplitude of the troughs identified during the decay phase. \* indicates a significant difference between the means ( $p < 0.05$ , Student's t test), \*\* indicates that it remains significant when corrected for multiple comparisons, ns indicates no significance.

TABLE 5.1. Shows the p values of measures with a statistically significant difference before multiple comparisons correction and after.

Measure	Un-corrected P	Corrected P
Trough Amplitude	0.006	0.041
MUA Amplitude	0.029	0.101
LFP Rate	0.022	0.09
LRD Interval	0.018	0.09
LRD Trough Amplitude	0.00005	0.0006
LRD Decay Phase Amplitude	0.00006	0.0006

adjusted the p-values for all measures to account for the multiple comparisons. To do this we have used the false discovery rate procedure. (Benjamini and Hochberg, 1995) The corrected p values for those measures that were found to be statistically significant before correction are shown in table 5.1. We find that after applying this correction, three of the differences found can no longer be considered statistically significant. This indicates that further experiments would be needed to show with confidence that these differences exist.

**5.4.2. Response to stimulation.** As well as testing the ability of the abruptness measures to discriminate between ipsilateral and contralateral slices we also wished to test whether the response to electric field stimulation could discriminate. We replicated the conditions used to induce the SLEs described above, while also stimulating each slice near to the recording electrode. We first compared the initial response to stimulation. This would tell us whether there was any difference in the direct recruitment between hemispheres. We then wished to look at the secondary response, in particular whether the stimulation provoked any complex epileptiform activity. As human studies have shown that the response to stimulation is more likely to be more complex when stimulating in the focus (Valentín et al., 2002) our initial hypothesis was that we would be more likely to see an epileptiform response in the ipsilateral slices. However, as we have seen the ipsilateral slices produce weaker SLEs, and less frequent LRDs, indicating a reduced functioning of the seizure generating network. We therefore hypothesised that artificial stimulation, while not compensating for any loss in seizure power, may aid in seizure initiation by synchronising a large population of pyramidal cells that struggle to reach this synchronised state as frequently as those in the contralateral slices. This would indicate that while the level of activity is lower in ipsilateral slices,

the barrier to synchronised activity spreading is not any different, or possibly reduced in ipsilateral slices.



FIGURE 5.7. Shows the two setups used for stimulating and recording the rat motor cortex slices. The multi-electrode array can be seen in layer 2/3 (left) and layer 6 (right). The bipolar stimulating electrode can also be seen.

5.4.2.1. *Methods.* As for the experiments described above, slices were placed into an interface chamber and, initially, continuously perfused with fully oxygenated regular ACSF. After 15 minutes, this solution was swapped for the pro-convulsant solution containing 6 mM  $K^+$  and 0  $Mg^{2+}$ . The slice was allowed to be perfused with this solution for 30 minutes before we began stimulation. The electric field stimulation took the form of focal stimulation applied by a bipolar electrode. We applied a 10 ms, 200  $\mu A$  monophasic pulse, with the cathode always towards the white matter. The stimulation was applied every 60 seconds. This was first delivered to layer 2/3 for 30 minutes (while we recorded the extracellular potential with a linear multi-electrode array in the same layer). We then applied the same stimulation to layer 5 of the motor cortex slices for one hour while recording below the stimulating electrode in either the lower half of layer 5 or layer 6. The recording setup can be seen in figure 5.7. In almost all slices stimulation produced an initial synaptic response measured in the LFP, in some slices the response took the form of epileptiform activity. Many slices also show spontaneous epileptiform activity. Example spontaneous and evoked epileptiform activity are shown in figure 5.11.

5.4.2.2. *Results.* The full data set includes slices from 8 injected animals and two control animals (injected with saline), with 4 slices (two from each hemisphere) taken from each animal resulting in 30 slices (in one animal we took only two slices). We first look at the immediate response to stimulation in layer 2/3, in particular at the

amplitude and decay of the response as we move away from the stimulating electrode. Here two slices from the ipsilateral hemisphere and three slices from the contralateral hemisphere did not show any response to stimulation and so were not included in the analysis. Figure 5.8 shows the averaged waveforms of the response in layer 2/3 to stimulus, we can see that the averaged waveforms are similar in response amplitude and in response width, however, there is significant variability in the response amplitude within groups. We can see this in figure 5.10 with response amplitudes ranging from 0.1 mV to 6 mV. Here we also see that the control slices have a significantly lower amplitude than those from the ipsilateral hemisphere, the larger variance in the response in contralateral slices means we do not have enough statistical power to say that there is a difference between them and controls. Figure 5.9b shows the 90 % confidence interval on the difference between response amplitudes in contralateral and ipsilateral slices. We find a mean difference of around zero and can be 90 % confident that this difference is between -1.1 and 1.1 mV. Figure 5.9a shows how the response amplitude decays with the distance from the stimulating electrode. This decay fits well to a single exponential ( $r^2 = 0.93 \pm 0.08$ ) and so we can calculate a space constant for decay for each response. We compare the distributions of this space constant for all three conditions in figure 5.10, we can see that they all overlap. In figure 5.9b we see that we can be 90 % confident that the difference between contralateral and ipsilateral is between -200 and 600  $\mu m$ . Having established that there was no difference in the immediate response to stimulation, we then wished to look at the response to stimulation after the immediate response, to determine whether any more complex secondary activity was evoked. For this analysis we looked at the recordings in layer 5. These recordings were longer (1 hour) and took place after the layer 2/3 recordings. The slices, having been in the pro-convulsant ACSF for longer were more prone to show seizure-like events and epileptiform responses to stimulation. We found that in slices from both hemispheres stimulation could evoke a response but that these responses were not reliably invoked. To quantify the likelihood of evoking an epileptiform response we counted the number of events (spontaneous and evoked) over the hour of the recording. We then classified them as either spontaneous or evoked. Only events that progressed immediately (less than one second) after the stimulation artefact and which showed no epileptiform activity before the stimulation artefact were counted as evoked. All others counted as

TABLE 5.2. Contralateral slices are more likely to show spontaneous events during the hour of stimulation and recording in layer 5. Applying the N-1 Chi-Square we find that there is a 85% chance that the proportion of slices showing spontaneous events is different between ipsilateral and contralateral slices (two tailed p value = 0.15).

	Shows Spontaneous Events	Total Number
Contralateral	10 slices	15 slices
Ipsilateral	6 slices	15 slices

TABLE 5.3. Shows the number of evoked events in each hemisphere. Applying the N-1 Chi-Square test we get a 53% chance that there is a difference in the proportion of slices that show evoked events, with a two tailed p value of 0.47.

	Shows Evoked Events	Total Number
Contralateral	9 slices	15 slices
Ipsilateral	7 slices	15 slices

spontaneous. The frequency of events (less than 25 over one hour), means that the chances of an event occurring spontaneously one second after stimulation are very low.

Not all slices produced events (either spontaneous or evoked). Of the 15 ipsilateral slices tested we found 6 that produced spontaneous events and 7 that produced evoked events. Of the 15 contralateral slices tested we found 10 produced spontaneous events and 9 produced evoked events. Of the 10 control slices tested 5 produced spontaneous events, but only 2 produced evoked events. Tables 5.2 and 5.3 summarise the number of contralateral and ipsilateral slices showing epileptiform responses and spontaneous SLEs. Tables 5.4 and 5.5 compare the number of spontaneous and evoked events in control and TeNT injected slices. To test whether the slices from the injected hemisphere were more prone to generating a complex response to stimulation we wished to measure the likelihood of an evoked event with each stimulation applied to slices that do generate evoked responses. As only two control slices produced evoked events, they have not been included in this analysis. Overall the likelihood is low with a range of ratios (events/stimulus) of between 0.01 and 0.35 (figure 5.12). We find no significant difference between hemispheres but on average the contralateral side is more likely to show an epileptiform response. We also looked at the ratio of spontaneous events to evoked events, as this may show whether the stimulus is simply evoking events that would still occur without stimulation, or whether it is generating events in tissue that would be unable to generate events on its own. Again we find no significant difference between hemispheres.

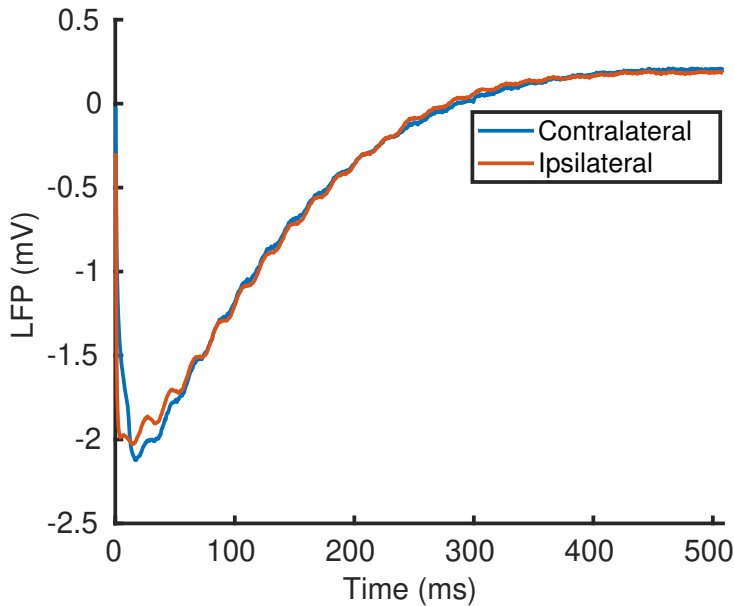


FIGURE 5.8. Shows the averaged waveforms of responses in layer 2/3 to stimulation in layer 2/3. The response shown is that recorded in the electrode closest to the stimulating electrode.

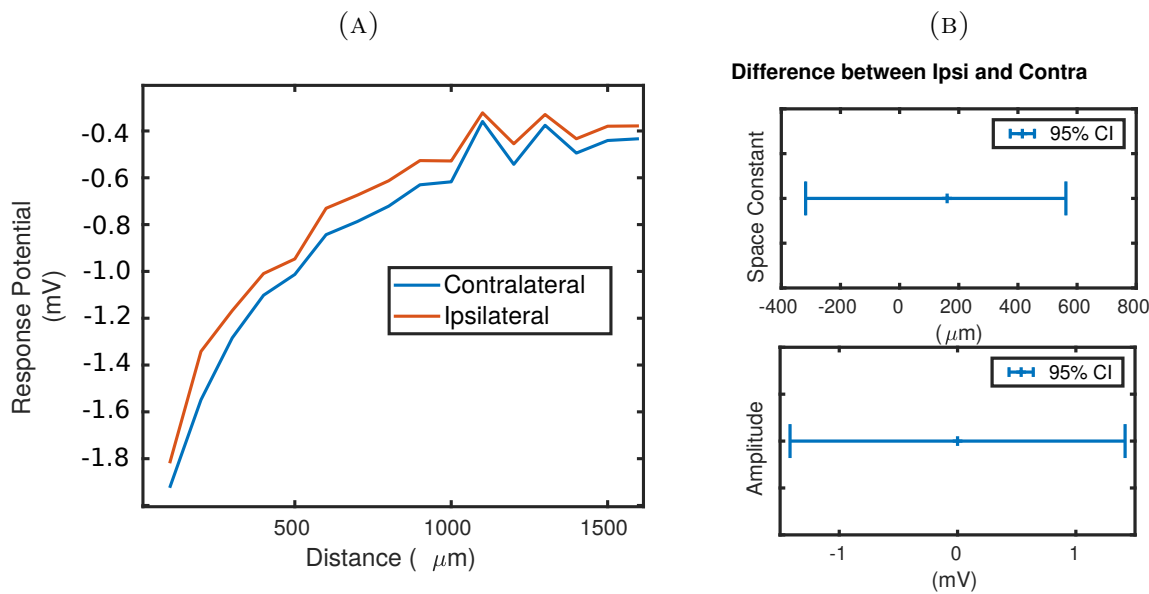


FIGURE 5.9. (A) shows how the amplitude of the averaged response potential decays as we move away from the stimulating electrode - the x axis shows the distance from the stimulating electrode. (B) Shows the 95% confidence interval on the difference between the space constant measured in the slices ipsilateral and contralateral to the injection site. Below we show the 95 % confidence interval on the difference between the amplitude of the response in slices from each hemisphere. We can be 95% confident that the absolute amplitude difference is less than 1.5 mV.

**5.4.3. Discussion and summary of experimental results.** We have analysed the seizure-like events produced by slices of rat motor cortex prepared from rats injected with tetanus toxin. Slices have been taken from the injected hemisphere (ipsilateral)

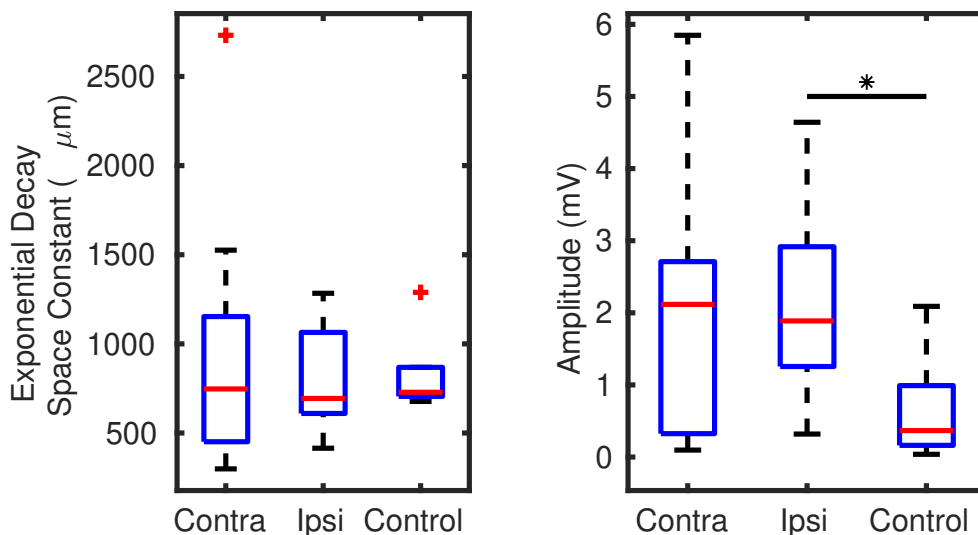


FIGURE 5.10. (Left) Shows the distribution of the spatial decay constant of the response potential in slices contralateral and ipsilateral to the injection site. (Right) Shows the amplitude of the response potential at the electrode closest to the stimulating electrode in slices contralateral and ipsilateral to the injection site.

TABLE 5.4. Shows the proportion of spontaneous SLEs found in slices from rats with TeNT injection and rats with saline injection (control). Both hemispheres have been grouped together. Applying the N-1 Chi-Square we find that there is a 14% chance that the proportion of slices showing spontaneous events is different between TeNT and control slices (two tailed p value = 0.86).

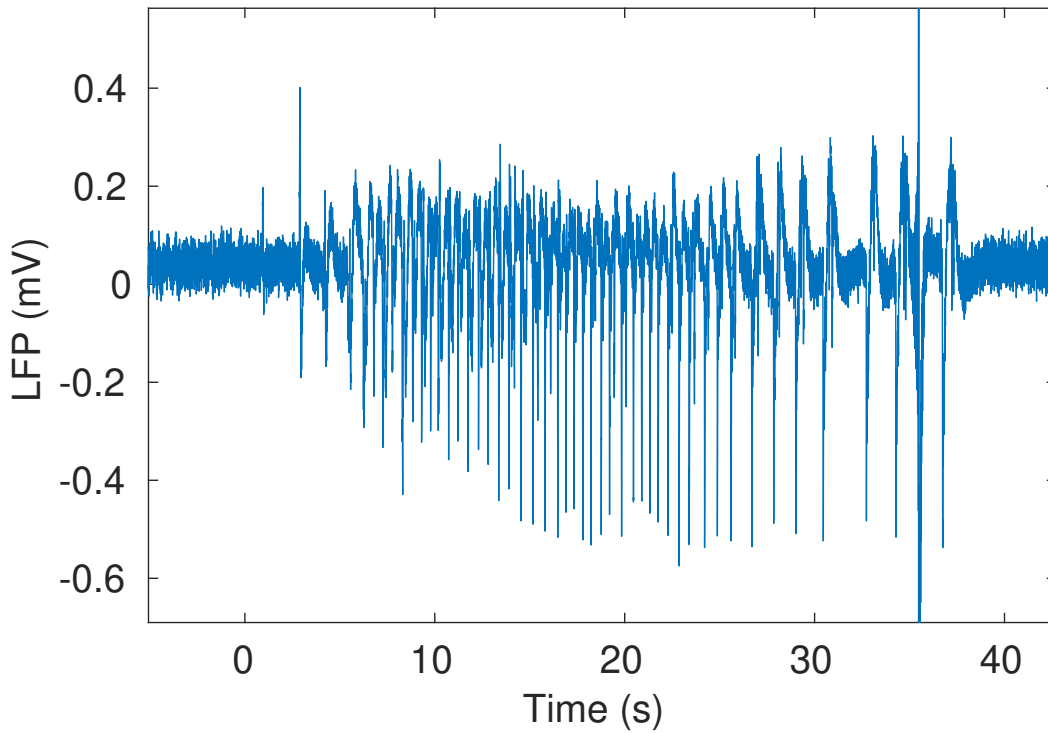
	Shows Spontaneous Events	Total Number
TeNT	16 slices	30 slices
Control	5 slices	10 slices

TABLE 5.5. Shows the proportion of evoked SLEs found in slices from rats with TeNT injection and rats with saline injection (control). Both hemispheres have been grouped together. Applying the N-1 Chi-Square we find that there is a 93% chance that the proportion of slices showing spontaneous events is different between TeNT and control slices (two tailed p value = 0.07).

	Shows Evoked Events	Total Number
TeNT	16 slices	30 slices
Control	2 slices	10 slices

where we would expect the toxin to have been present at greater concentrations and the contralateral hemisphere where due to the proximity and strong connectivity between the two regions we would expect the toxin to be present but to a lesser extent. As the slices were prepared from animals 8 to 20 weeks after injection, we would expect the primary action of the toxin to still be in effect (Ferecsko et al., 2015) and so the

(A) Spontaneous



(B) Stimulus Evoked

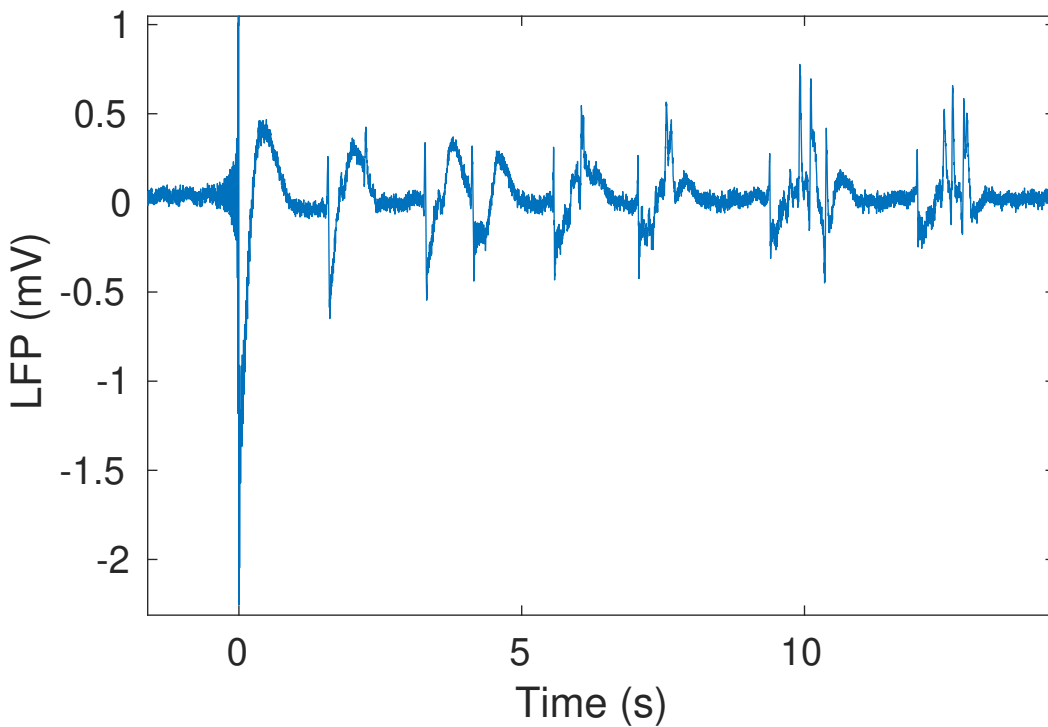


FIGURE 5.11. Shows an example of a spontaneous events (A), and an evoked event (B).

injected hemisphere to be more excitable. We compared the characteristics of the events recorded in each hemisphere and the abruptness of events in each hemisphere.

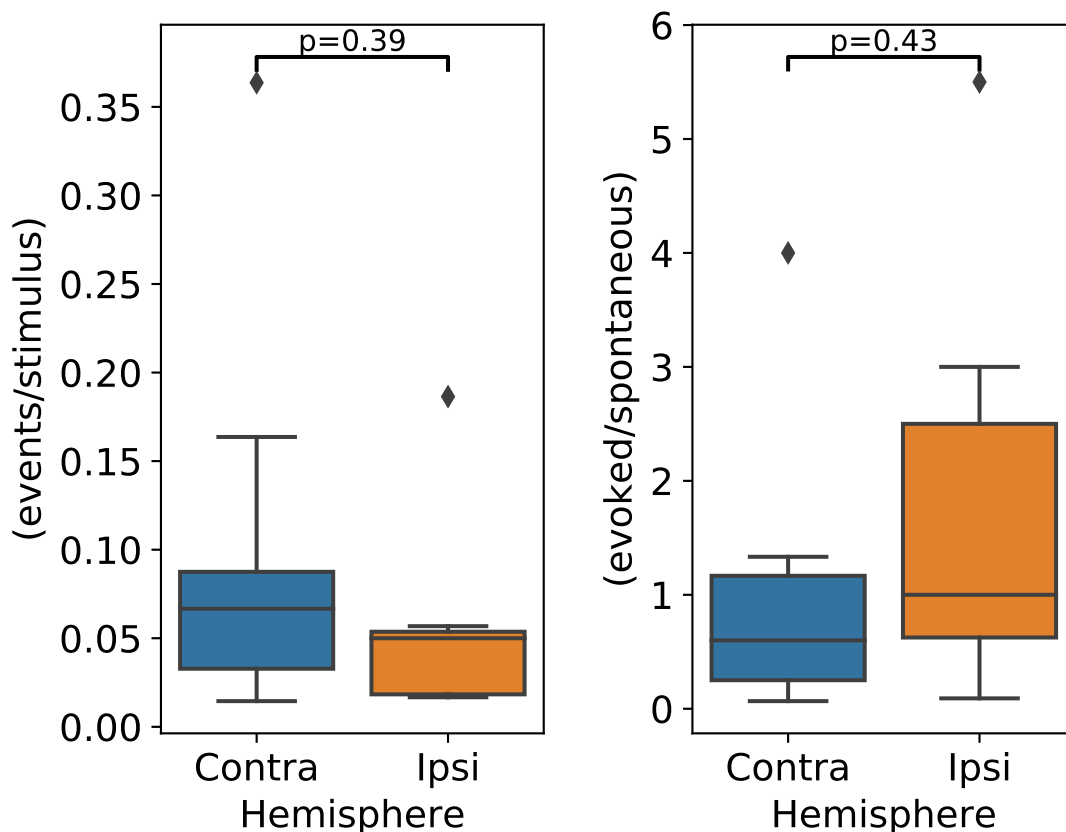


FIGURE 5.12. (Left) Shows the number of events evoked per stimulus applied. The stimulus was applied every minute of a 60 minute period. (Right) Shows the ratio of evoked events to spontaneous events.

We also compared the characteristics of events evoked by the application of the GABA<sub>A</sub> antagonist gabazine, and of events evoked by electrical stimulation.

5.4.3.1. *Lower amplitude events in ipsilateral slices.* We record lower amplitude events in the injected (ipsilateral) hemisphere. Lower amplitude events may be a consequence of the reduced EPSPs and IPSPs produced by TeNT injection (Ferecsko et al., 2015). However, lower amplitude events contrasts with the results of Serafini et al. (2016), who show events in the primary focus (ipsilateral site) to be of a greater voltage. They apply 4-AP as well as using zero magnesium ACSF to induce SLEs, and study somatosensory cortex instead of motor cortex. The different model used to induce SLEs (Perreault and Avoli, 1991) or the different network studied could contribute to this difference.

5.4.3.2. *The abruptness of events.* If we consider a slowly propagating seizure, abruptness may be related to the time constant for the failure of inhibitory restraint. Theoretically, seizure onset patterns have been linked to the dynamics of network

recruitment. In particular, a high amplitude onset has been linked with focal perturbation or permanent oscillation within an area that is surrounded by excitable tissue. Low amplitude onset is associated with focal perturbation or intrinsic oscillation when the surrounding area is less excitable (Wang et al., 2014, 2017). Serafini et al. (2016) use a large 2 dimensional multi-electrode array to record at multiple sites in their neocortical slices. They show that when slices from rats injected with TeNT are placed into pro-convulsant medium one large focus occurs recruiting all recording areas within a short time. While in slices from healthy rats, small localised foci occurred, which then coalesced slowly to form an SLE. This could indicate that the area around the injection site (ipsilateral slices) is one of increased excitability, where events spread rapidly, seen from a single electrode recording as an abrupt onset. We hoped to capture a similar phenomena here using the abruptness of seizure onset. To make this measure we tried several approaches, either fitting the logistic function to the build up of amplitude at the onset of the event, or calculating the rate of amplitude build up. The amplitude was either that of the LFP or that of the MUA. We found no difference between hemispheres for the abruptness of the MUA by either measure, but we did find a significant difference in the abruptness as measured by the rate of LFP build up. However, this difference did not survive correction for multiple comparisons and so further evidence is required to be confident in this result. The difference measured by the logistic function fit to the LFP was not statistically significant, which could indicate that the rate is a more sensitive measure.

5.4.3.3. *LRDs are larger and more frequent in contralateral slices.* Late recurrent discharges begin when gabazine has been added to the bathing solution, abolishing synaptic inhibition. In slices contralateral to injection site, the amplitude and frequency of these events is higher. This indicates that while there may be differences in the inhibitory synaptic function between contralateral and ipsilateral slices, there is also a significant difference in the function of excitatory synapses. This supports the work of (Ferecsko et al., 2015) who show that EPSPs as well as IPSPs are reduced by TeNT injection.

5.4.3.4. *The response to stimulation.* When comparing slices ipsilateral and contralateral to the TeNT injection site we did not find any differences in the immediate response amplitude to electrical stimulation, or in the decay of the response amplitude

with distance from the stimulating electrode. As the TeNT injection is expected to reduce synaptic function (Ferecsko et al., 2015) we might have expected to see a reduction in the amplitude of responses in the injected slices. That we didn't detect any difference could be down to the small sample size and large variance of the response amplitudes in both hemispheres. It could also be that the action of the TeNT on the contralateral hemisphere is great enough that any effect it does induce is present to a similar extent in either hemisphere. We do see a difference between the response amplitude in controls and in slices from TeNT injected animals (ipsilateral only). Again, this goes against the expectation that TeNT reduces synaptic function, which would reduce the amplitude of the field potential. On the other hand, TeNT may increase the overall excitability of the cortex, and so allow stimulation to recruit a greater number of cells, producing a larger field potential.

### **5.5. Simulating evoked potentials and epileptiform discharges in rat neocortex**

In the experiments described above we have induced epileptiform activity in rat neocortex using a pro-convulsant medium, and evoked responses measured in the LFP using electric field stimulation. In this section we outline two simulations produced using the VERTEX simulator that represent initial work towards producing detailed biophysical simulations of these conditions.

**5.5.1. A simulation of the response to bipolar stimulation in rat neocortex bathed in magnesium-free ACSF.** As described in chapter 1 the local field potential response to electric field stimulation can be used to infer dynamic properties of the network. However, the field potential is notoriously difficult to interpret (Herreras, 2016). Detailed simulations have been shown to aid in interpretation (Tomsett et al., 2015). Here we outline a simulation of the response to bipolar stimulation in rat neocortex bathed in magnesium-free ACSF, and compare it directly with that recorded *in vitro*. We use a similar rat neocortex model to the one outlined above but have also introduced an NMDA (N-methyl-D-aspartate) receptor-mediated current. Under physiological conditions, the contribution of this current is often ignored because it is only open when the cell is depolarised enough to push the  $Mg^{2+}$  away from the channel. When  $Mg^{2+}$  is washed out of the solution, its contribution becomes

significant. We include an additional NMDA receptor mediated conductance to reflect this. This is modelled as a single exponential with a peak conductance that is equal to that of the original synapse (effectively doubling the peak conductance of the synapse as a whole) and a decay time constant of 66 ms (Perouansky and Yaari, 1993). We have set the synaptic strength and random input currents so that the network is active but not showing any seizure-like activity, and simulate stimulation in 5 networks. In both the simulation and experiment we applied bipolar stimulation to layer 2/3, the stimulation had a duration of 10 ms and amplitude of 200  $\mu A$ . We compare the experimental and simulated field potential response at the nearest electrode in figure 5.13. The simulation captures the amplitude of the response as well as the polarity of the deflection. We quantify this in figure 5.15 where we see that the mean difference between the simulation and experiment is just above 0 mV but that the large variance of the experiment amplitudes gives us a 90 % confidence interval of between -0.5 and 0.5 mV. The simulated response also shows a second deflection around 400 ms after the stimulus has been applied, which is not present in the averaged responses from the experiments. This second deflection shows that the tissue is excitable enough that the synaptic activation of the initial activity can provoke an additional response. Figure 5.14 shows the amplitude of the response recorded by the linear multi-electrode array placed next to the stimulating electrode in layer 2/3 (figure 5.16 shows the location of the recording electrode (black circles) and stimulating electrode (red circle) in the tissue). We have already seen how the decay of the experiment response amplitude is well fit by a single exponential, this is also true for the simulation response amplitude. We find that the simulation response decays faster than that of the experiment, again we quantify this in figure 5.15 and find that the simulated response decays significantly faster. Figure 5.16 shows the neuronal response of simulated tissue to stimulation. We can see that the activity spreads strongly vertically towards the white matter, and horizontally away from the stimulation electrode. The activity in layer 2/3 is suppressed before it reaches the slice boundary, the layer 4 and layer 6 activity reaches the slice boundary nearest to the stimulating electrode. This indicates that although the slice is excitable, inhibition is intact and can suppress the response.

While this immediate response is a relatively simple scenario, accurately capturing this baseline is the first step towards simulating more complex responses to electric field

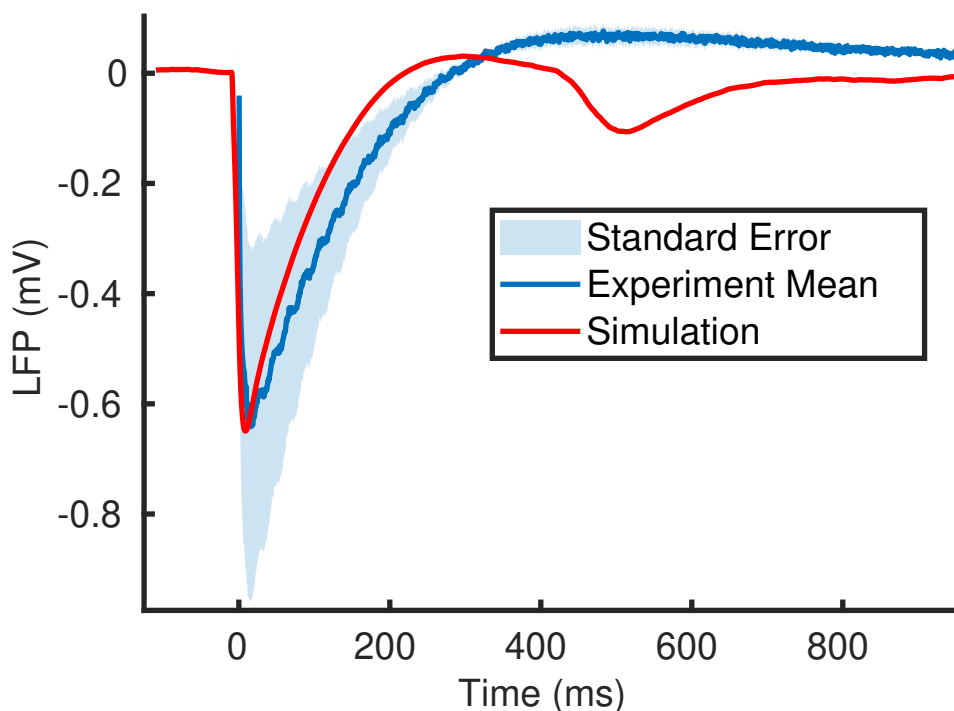


FIGURE 5.13. Comparing the response in the experiment to the response in the simulation. The stimulation was a 10 ms,  $200 \mu A$  pulse of applied to layer 2 with the recording electrode placed approximately  $200 \mu m$  away on the horizontal axis. Here we show the mean response from the experiment ( $n=6$ ), compared with the mean simulation response ( $n=5$ ). We show the standard error of the mean of the experiment in light blue, the variance of the simulation is much smaller (the mean standard deviation across the response is 0.02 mV), we have not shown this to improve the clarity of the plot.

stimulation. In particular we capture the long NMDA receptor mediated synaptic currents and their contribution to the local field potential. As this current is the primary driver for more complex evoked responses, accurate simulation of this is important when we seek to model them. This model also helps us to interpret our experimental results, as we can now say with more confidence that the LFP response represents an excitatory current mediated by the NMDA receptor. We hope to use combine this with simulations of epileptiform activity to investigate evoked epileptiform activity, and the effect of stimulation on ongoing epileptiform activity. One difference between the averaged recorded response and the simulated response is the second deflection. This arises as a result of a second recruitment of cells, as can be seen in figure 5.17. Here we can see the in the top panel the number of cells spiking peaks again during the downward phase of the second deflection. In the bottom panel of the same figure we can see that the net current arriving at the cells becomes excitatory again after around 200 ms, just

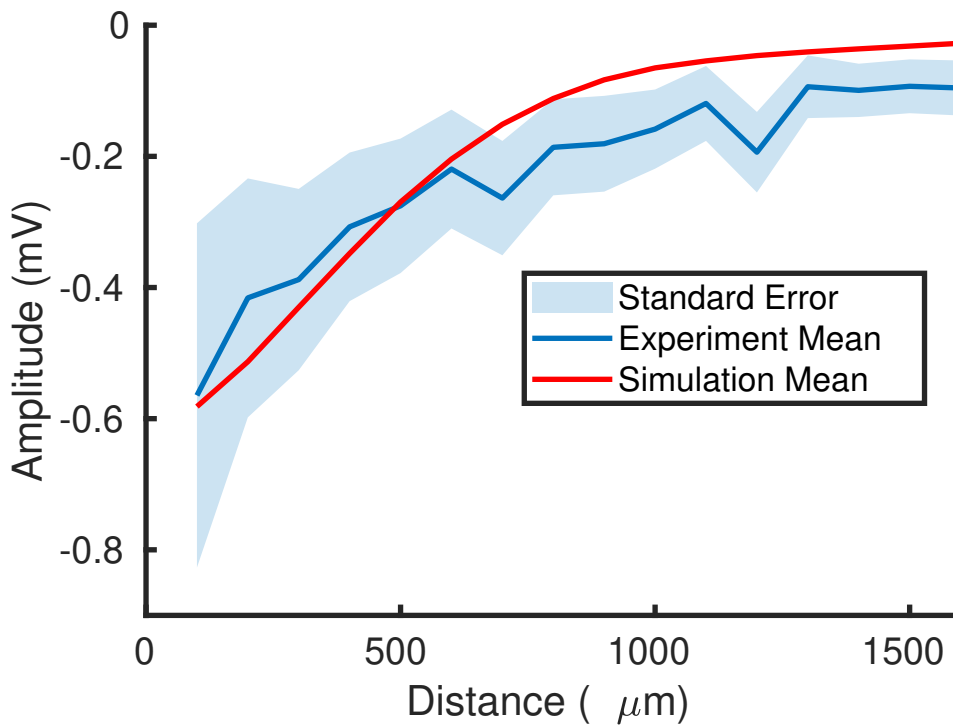


FIGURE 5.14. Shows the amplitude of the simulated and experiment response against the distance from the stimulating electrode. Again we show the standard error of the mean of the experimental data, and the mean of the simulated data.

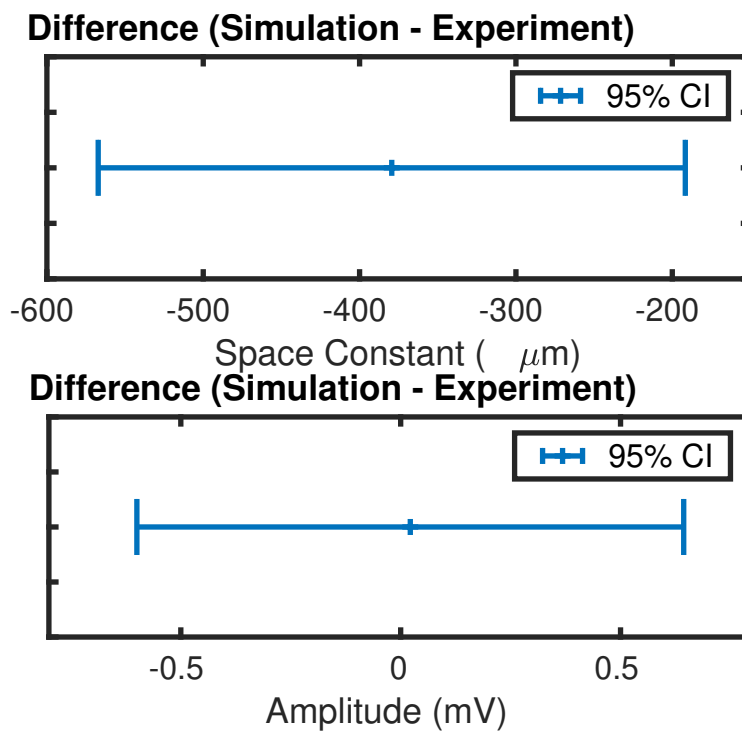


FIGURE 5.15. Shows the difference in amplitude and decay space constant between the simulated response and the experiment. The confidence interval was calculated as  $C_i = 1.960\sqrt{\frac{\sigma_e^2}{N_e} + \frac{\sigma_s^2}{N_s}}$ , where  $\sigma_e$  and  $N_e$  are the variance and number of samples of the experimental result and  $\sigma_s$  and  $N_s$  are the variance and number of samples of the simulated result.

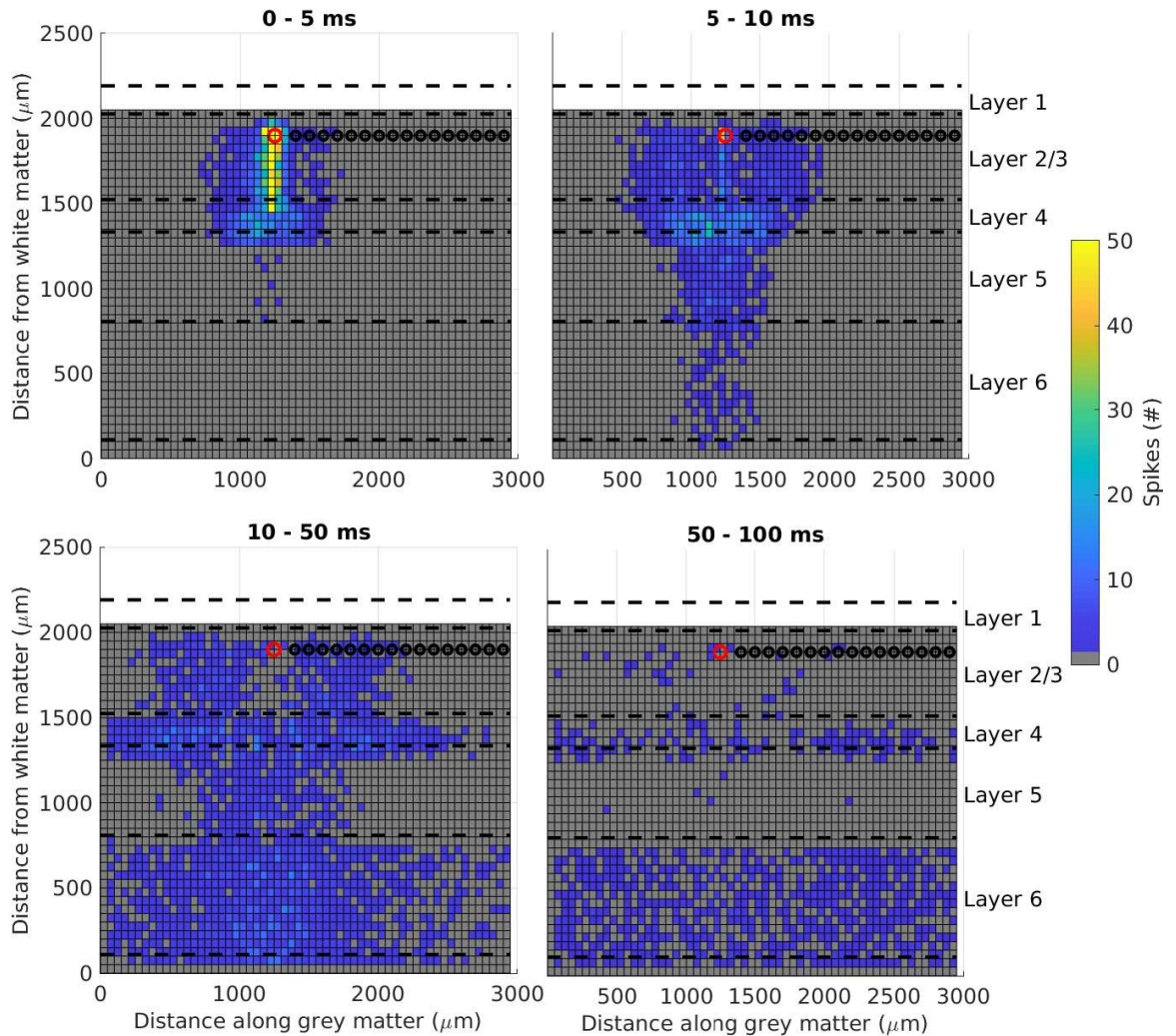


FIGURE 5.16. Shows the neuronal response of the tissue to stimulation. Here, each box represents a square of tissue ( $50 \times 50 \mu\text{m}$ ) and the colour shows the mean number of spikes generated by the 5 networks, within this box over the time course specified above the plot. If fewer than 1 spikes occurs during the time period then the cell is coloured grey, otherwise the colour reflects the number of spikes that occur. The number of spikes per box is saturated at 50, the only squares to show more than 50 spikes are the 4 directly under the stimulating electrode in the time interval of 0 - 5 ms.

as the activity begins to build again. This come about because the inhibitory current has decayed faster than the excitatory, and so although it dominated initially after the stimulus (suppressing the activity) it has decayed sufficiently that by 200 ms after the stimulus the net current becomes excitatory again. Although we do not see this secondary deflection in the averaged response, it is present in some individual traces. Figure 5.18 shows an example typical of one of these traces. Here we see a second deflection around 1500 ms after the stimulus. These second deflections are rare (5 out of the 10 control slices show them at least once, their occurrence rate in those that do

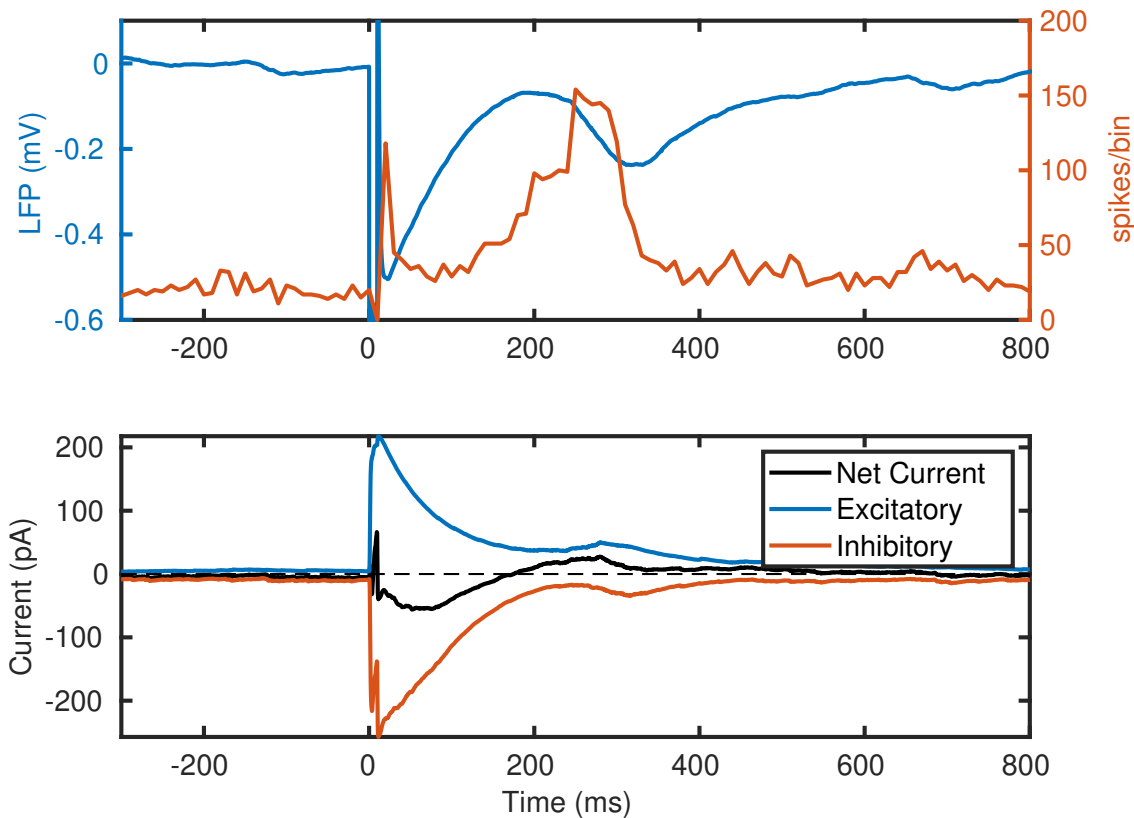


FIGURE 5.17. **Top:** Shows the LFP recorded in layer 2/3 (blue trace) and the peri-stimulus time histogram of layer 2/3 pyramidal cells. The spikes that occur while the stimulus is applied have not been included to emphasise the spiking activity seen in immediately after the stimulus. **Bottom:** Shows the currents arriving at layer 2/3 pyramidal cells (the average of the 100 cells nearest to the stimulating electrode). We can see that the net current becomes excitatory at around 200 ms, just as the secondary spiking response begins in the top panel.

is 14 %). The delay between stimulus and second deflection shown in figure 5.18 is typical of the data set where we see an average delay between stimulus applied and the second deflection of 1467 ms with a standard deviation of 702 ms.

**5.5.2. A model of epileptiform activity.** Most models of epileptiform activity involve a breakdown in the balance of excitation and inhibition. Even in *in vitro* models such as the zero magnesium model, this breakdown occurs through multiple mechanisms and across a wide range of timescales (Jirsa et al., 2014). Very slow processes such as the fluctuations in extracellular potassium (Fröhlich et al., 2008) and calcium (DeLorenzo et al., 2005) concentration, or the availability of ATP and regulation of energy (Wei et al., 2014) in the tissue, are thought to play a role in the frequency of events and the long term build up in excitability needed for an event to occur. Short term plasticity has been suggested as a mechanism for ictogenesis at a shorter time

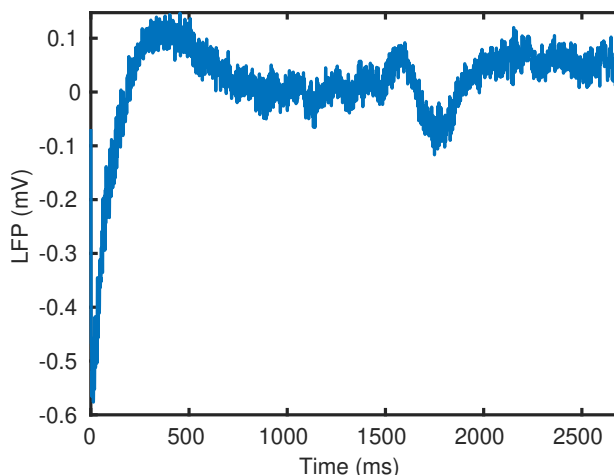


FIGURE 5.18. Shows a response to stimulation that includes a second deflection. Five out of the 10 control slices show a second deflection in at least one response. When considering only those slices that do show a second deflection, the proportion of responses showing a second deflection is 14 % with a standard deviation of 5 %. The average delay between stimulus applied and the second deflection is 1467 ms with a standard deviation of 702 ms.

scale (Staley, 2015). As it fluctuates over seconds, it fits well with the time scale for the initial build up of activity that culminates with the paroxysmal depolarising shift. Here we describe a simulation of the field potential of epileptiform discharges in rat neocortex. We use the model described in chapter 3, simulating a slice of tissue in three dimensions, with realistic neuron density, 4 layers (layers 1-6, with 2 and 3 combined and 1 containing no cells), and 29 different cell types. Values for the time constants for facilitation and depression (also shown in chapter 3) are experimentally measured and taken from Ramaswamy et al. (2015). However, in contrast to the model described in chapter 3 we use the Abbott model (Abbott and Regehr, 2004) as this provides a simpler and easier to interpret description of synaptic depression. We induce activity by increasing the strength of excitatory synapses and/or increasing the rate at which inhibitory synapses depress. Figure 5.19 shows our exploration of these two parameters. We find that to evoke events when the rate of inhibitory synaptic depression is a 50% (synapses are reduced to 50% of their value after each spike) we must increase the strength of excitation to 250% of its original value. If we increase the rate of synapse depression to 40%, then we find we can evoke events with an excitatory synapse strength of 225%. The resulting network generates spontaneous discharges of synchronous activity at a frequency of 1 Hz. The LFP generated by these events, recorded in layer 2/3, is shown in figure 5.20A. We can also see the firing rates of

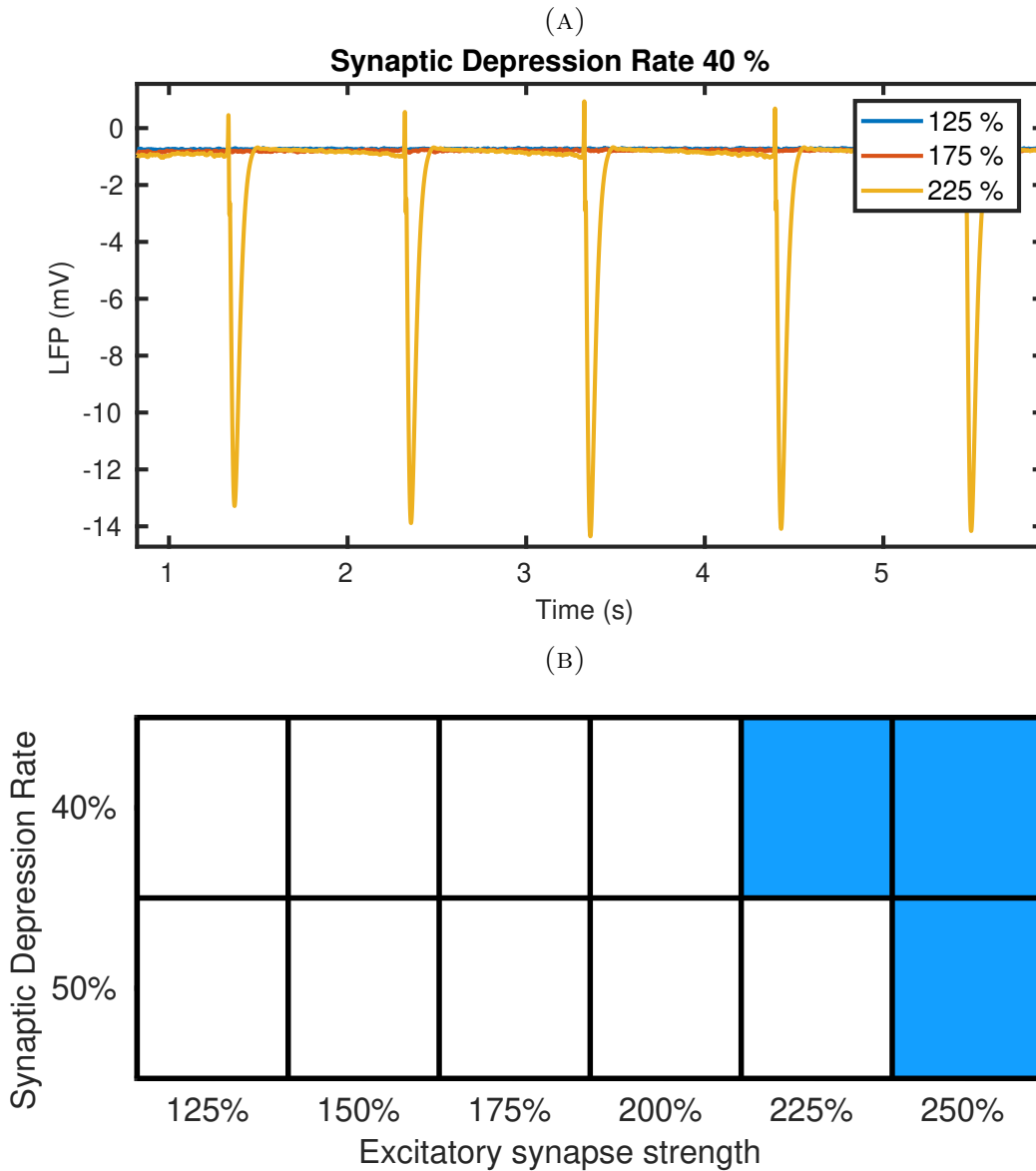


FIGURE 5.19. We increase the synapse strength in increments of 25% until the model begins to generate epileptiform activity, indicated by the blue patches in (B). We do this for networks with an inhibitory synaptic depression rate of 40% and 50%. We find that increasing the rate at which the inhibitory synapses depression, decreases the threshold excitatory synapse strength required to illicit activity. (A) shows example LFP traces of activity with synapse strengths of 125%, 175% and 225% and the inhibitory synaptic depression rate at 40%.

L5 pyramidal cells and interneurons during each event and the build up to the event. The firing rates of both cell types build gradually before the event, but rapidly increase during the initiation of the event (the downswing of the LFP). Their firing rate reduces substantially for around 50 to 100 ms, before recovering and beginning to build again. The build up of activity is caused by the recovery of strong recurrent excitation which is initially held back by feedback inhibition from basket cells and Martinotti cells.

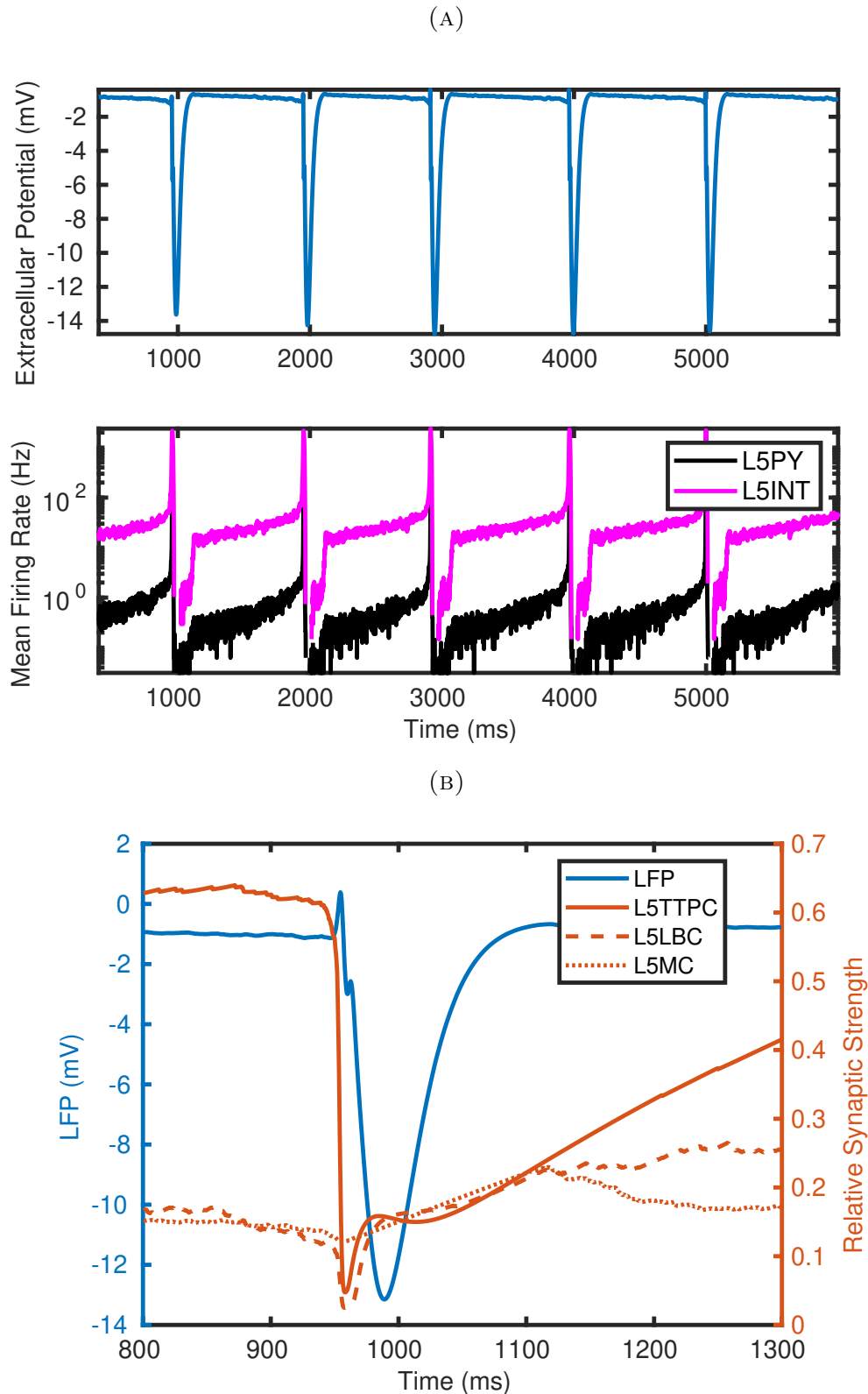


FIGURE 5.20. (A) Shows the firing rate and LFP of the events. (B) Shows the relative synapse strengths (fraction of full synapse strength) of layer 5 pyramidal cells, basket cells, and Martinotti cells, during a simulated epileptiform discharge. We can see that in the run up to the event the basket cell synapse strength is decreasing and inhibitory synapses are more depressed than the excitatory. During the event all synapses decrease in strength but there is a dramatic decrease in excitatory synapses strength bringing it into line with the inhibitory synapses. As we leave the event the excitatory synapse strength begins to diverge from the inhibitory strength again.

The eventual failure and subsequent spike in activity is caused by a failure of the inhibitory synapses, which under the short term plasticity rules used, gradually weaken as the firing rates of their cells increase. This time course of inhibitory synapse strengths can be seen in figure 5.20. The lower firing rates of the pyramidal cells ensure that they maintain synaptic efficacy for longer than the interneurons, only weakening significantly during the spike itself. As excitatory synapses onto Martinotti cells tend to facilitate, when the network is undergoing excessive excitation they will receive stronger excitatory drive (compared to baseline) than basket cells therefore reaching a higher normal firing rate. This may then depresses their synapses even further, leading them to lose efficacy completely, allowing the dendritic excitation to dominate, causing the synchronous activity.

5.5.2.1. *Comparison with experimental data.* To investigate the similarity between our simulated events and events recorded *in vitro* we compare them with the troughs of a particular subset of events recorded in TeNT injected slices. As our model does not show the full evolution of epileptiform activity expected of a seizure-like event, we looked for similar events within the experiment recordings. We found that in some slices activity occasionally transitioned to spike wave discharges without the high frequency activity typically seen at the start of events in the zero magnesium model *in vitro* (Trevelyan et al., 2007). We therefore chose these for comparison, because as regular and repetitive events, they could be directly compared with the simulated results.

Figure 5.21 compares the experimental recordings with the simulated. We find that the simulated events repeat on a similar timescale to those in experiments, but are much sharper events - they have a much shorter trough width and a much larger peak amplitude. We also find that the experiment traces tend to show an after-polarisation peak in the LFP after the main trough. This forms part of the wave of the spike-wave discharge, and so it would traditionally be interpreted as being caused by currents re-polarising the cells after their extensive depolarisation during the main spike, and as occurring during a time of neuronal silence. In our simulations, this period of neuronal silence appears to be confined mostly to the main trough. It may be that in the experiment, this re-polarising phase occurs later and lasts for longer causing the peak we see after the main trough. In the simulated discharges we also see an initial sharp peak before the main trough. In our model this initial peak comes from

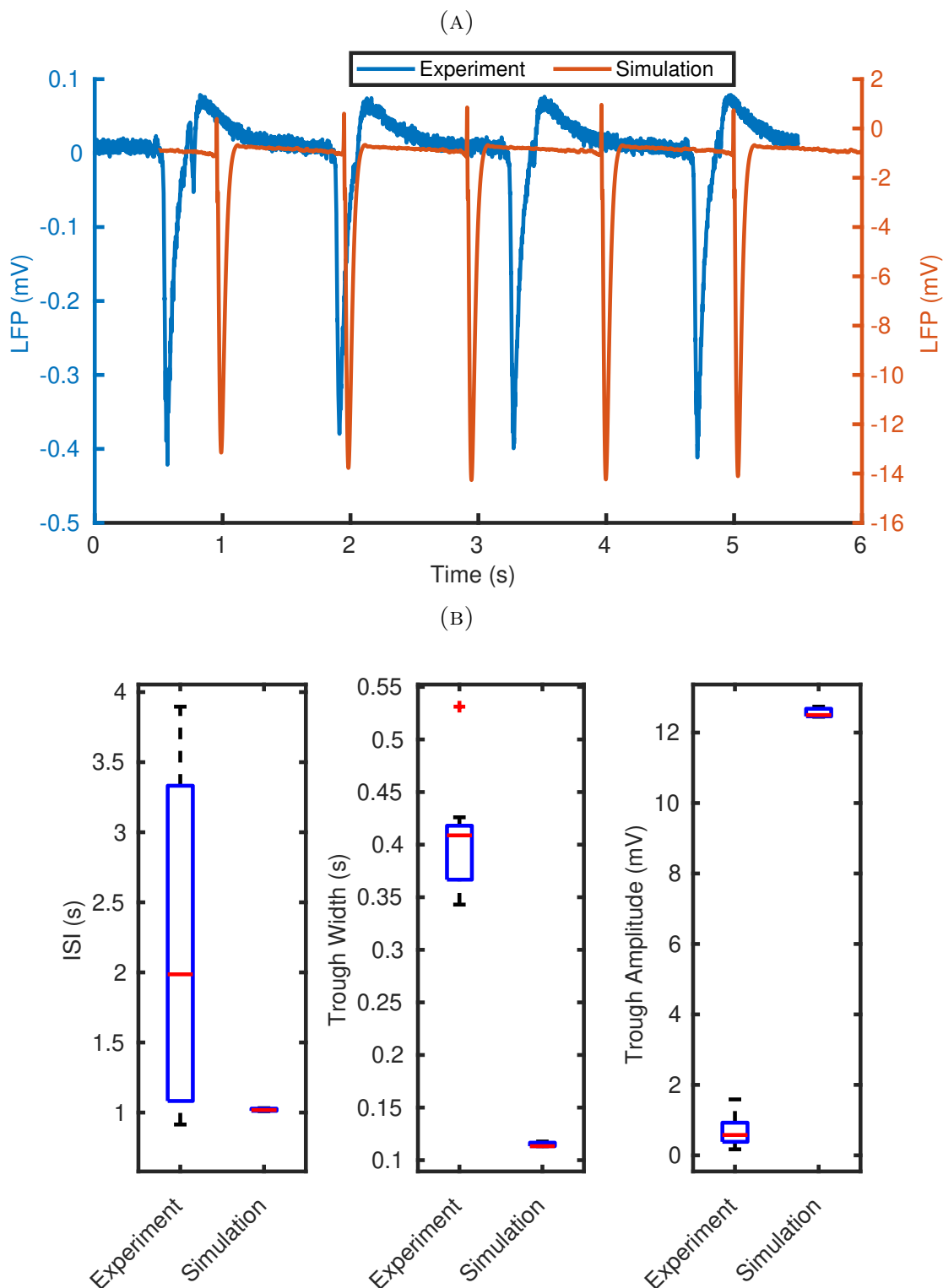


FIGURE 5.21. Comparing simulated epileptiform discharges with those recorded in experiments. (A) Shows an example trace of epileptiform discharges recorded in the *in vitro* model described above. We overlay the simulated events in red (note the separate scale on the right). (B) Compares the interspike interval, the trough width, and the trough amplitude, of simulated activity with that recorded in 8 slices of the *in vitro* model. Events were not full seizure-like events that display an evolution of activity, but were rather events that manifest as repetitive spike wave discharges that begin and end gradually. These events were identified in recording from the TeNT injected animals described above, the data described here is from both ipsilateral and contralateral slices.

the initial barrage of excessive excitatory currents arriving at layer 5/6 pyramidal cells (figure 5.22) with the positive inflection a result of strong depolarising currents arriving at the apical dendrite causing negative transmembrane current at the tuft which is the closest compartment to the electrode (a mechanism similar to that described in chapter 3, figure 3.11). This initial inflection is not present in many of the traces examined (including that shown in figure 5.21) but is present in a subset (an example is given in figure 5.23), indicating that this can occur *in vitro* under specific conditions and possibly depending on electrode location (in our simulation the initial peak is no longer present when the recording electrode is moved to the bottom of layer 2/3, 1500  $\mu\text{m}$  from the white matter). A final discrepancy between our model and the data is an occasional notch that appears on the rising phase of the trough in experimental recordings. This notch indicates that the experiment discharge may be generating more prolonged activity (perhaps in a subset of cells) than the simulated discharge.

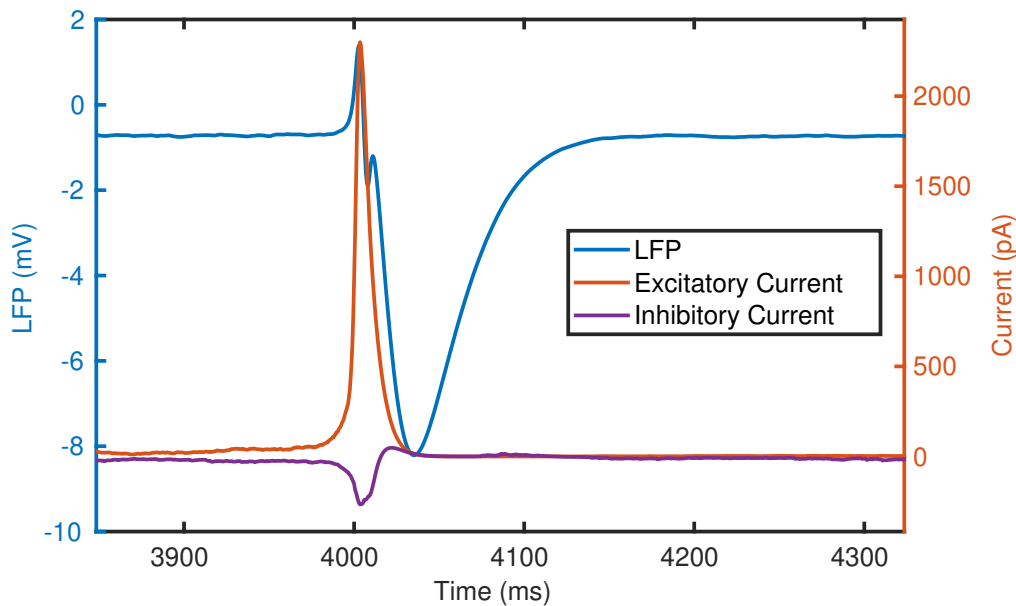


FIGURE 5.22. Shows the local field potential (blue trace) during a simulated epileptiform discharge, along with the excitatory and inhibitory currents arriving at layer 5 pyramidal cells (the mean recorded from 100 cells). We can see that the main excitatory barrage coincides with the initial peak in the LFP. The inhibitory current briefly becomes positive (and so excitatory), this is possible because synapses are conductance based, and so if the membrane potential of the compartment onto which they synapse polarises beyond their reversal potential they will provide an depolarising current.

**5.5.3. Discussion of simulations.** Although our model of an epileptiform discharge does not produce an LFP timecourse that resembles that of a full ictal discharge,

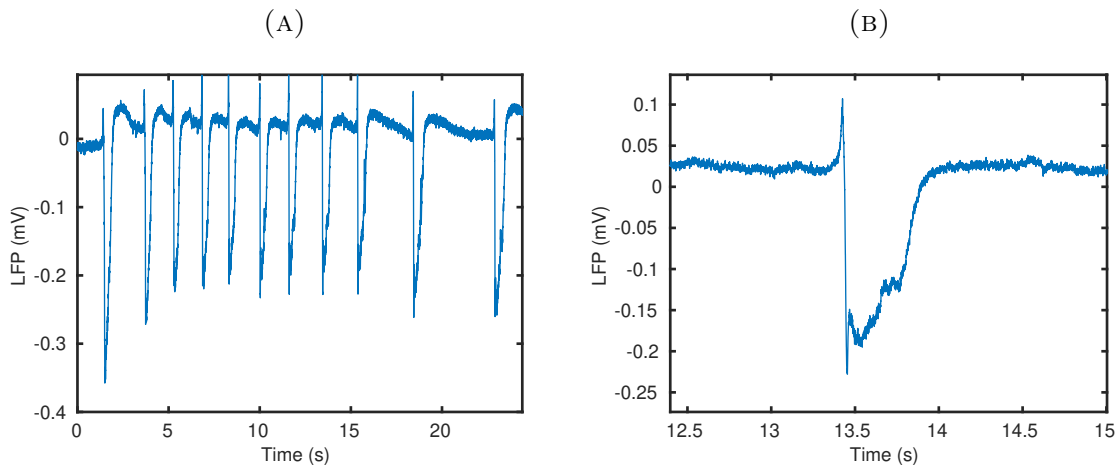


FIGURE 5.23. Shows an example epileptiform discharge recorded *in vitro* which shows an initial peak before the main trough. (A) Shows a sequence of discharges. (B) Shows a single discharge.

it does resemble some epileptiform activity seen *in vitro*. Interictal epileptiform discharges (IEDs) are often recorded in the EEG of epilepsy patients during periods between seizures. They are short events, described as a spike and wave discharge, that do not cause the symptoms associated with a full ictal event (seizure) (de Curtis et al., 2012). A spectrum of events with similar morphologies are also recorded in many *in vitro* preparations that mimic epileptic activity (Zelmann et al., 2013). Although the mechanisms of initiation and the currents that contribute to the LFP may be very different to those involved in the interictal events of patients, these are often still described as IEDs. The morphology (spike and wave) and timecourse (200 ms events at 1 Hz) of the events in our model are similar to some events described as IEDs in these *in vitro* models.

From our model we can also say that, according to our current knowledge of the neocortical microcircuit in rats, the power of the excitatory circuit is such that it can drive the inhibitory population to the extent that they lose synaptic efficacy, before the excitatory cells lose theirs, resulting in the synchronised activity seen in the spike. This gives a timescale and more specific description to the role that may be played by short term synaptic plasticity in the generation of epileptiform discharges. A major discrepancy between the activity seen in our model and that seen in *in vitro* models is the amplitude of the spike. The large amplitude reflects the fact that during the peak of activity in our model all cells are recruited (the set difference between all cells and cells recruited in the 30 ms of the event peak is zero in all simulations). This is in sharp contrast to what is seen in *in vitro* seizure models, where events manifest as

the synchronous activity of a subset of neurons (Feldt Muldoon et al., 2013). This clustering of neuronal activity is likely down to the heterogeneous nature the tissue, in particular patterns of local connectivity which can result in clusters of spatially localised and highly connected cells, and of hub cells (Bui et al., 2015). In our model, while synaptic properties for each neuron are selected from a distribution, the overall number of connections between neurons is fixed and so does not allow the formation of hub neurons, or for clusters of cells to form particularly strong connectivity. One possible consequence of this is that when we push the model towards epileptiform activity by increasing the synaptic weight, we have an all or nothing scenario, where excitation overcomes inhibition across all of the tissue at once or it does not. Introducing heterogeneity into the model may allow for inhibition to break down in spatially localised clusters of cells, while leaving other cells out of the event, producing a far lower field potential more similar to those seen *in vitro*.

We have also simulated the LFP generated by bipolar stimulation in layer 2/3 of rat neocortex when magnesium has been removed from the ACSF. We find that by including an additional NMDA receptor mediated current we can reproduce the amplitude of the response recorded *in vitro*. This highlights the role of these currents in the generation of the local field potential measured in the equivalent setting *in vitro*. Simulating the response to stimulation in this manner can also help to parameterise the model, as we have a well controlled and directly comparable output. So for example, by ensuring that the amplitude of the response to stimulation matches with that recorded *in vitro* we could be more confident that we are not overestimating or underestimating the strength of NMDA receptor mediated currents in the generation of seizure-like events. This approach compliments the approach of taking our parameters from the experimental literature and can compensate for the variability found there and for the effect of the particular conditions of the experiments we are trying to replicate (e.g. temperature, strain of animal). Future work should also look to apply stimulation to the model of an epileptiform discharge with the aim of investigating whether electrical stimulation could suppress events by disrupting the slow breakdown in inhibitory synapse strength in the run up to the event. Multi-channel asynchronous stimulation (Desai et al., 2016) may be a promising approach to investigate.

## Discussion and Outlook

Electric field stimulation has a wide range of applications in neuroscience research and in the treatment of neurological disorders. For many of these applications, accurate prediction of the immediate or long term effects of stimulation using computational modelling could aid in the design of experiments or interpretation of results. Applied focally to neural tissue, such as an *in vitro* brain slice preparation, electric field stimulation can directly evoke action potentials in nearby cells. Previous work has established the theory of how extracellular electric field stimulation generates action potentials in individual neurons (Rall, 1962; Tranchina and Nicholson, 1977; Rattay, 1986, 1989, 1998, 1999; Joucla et al., 2014; Yi et al., 2017). Electric field stimulation can temporarily alter the membrane potential of neurons, directly causing them to generate action potentials. The response to stimulation (measured in the LFP) can reveal properties of the network. Applying specific patterns of stimulation can modify the synaptic connections between cells, with many of the pioneering studies of synaptic plasticity using electric field stimulation (Bliss and Lomo, 1973; Ito et al., 1982).

However, current simulation frameworks are not suited to modelling these evoked local field potentials. This thesis contributes an addition to the VERTEX simulator, allowing one to easily model the response to electric field stimulation in neocortical networks generating intrinsic dynamics. These networks can consist of multiple cortical layers, with accurate cell and synapse properties. This allows simulations to be embedded in a network generated using our current knowledge of the neocortical microcircuit (Ramaswamy et al., 2015).

### 6.1. Contributions

#### 6.1.1. Interpreting field potential responses to electric field stimulation.

The VERTEX simulator can compute an accurate local field potential (LFP) from the dynamics of the neural compartments (Tomsett et al., 2015). As the LFP is relatively easy to record in the *in vitro* setting, this facilitates direct comparison between experiment and simulation, allowing a tighter coupling of theory and experiment. Many

experiments that make use of electric field stimulation, record the response as an LFP. However, the notorious difficulty in interpreting the LFP (Herreras, 2016) requires the evoked potential to be either well characterised or for the researcher to justify their interpretation using knowledge of the underlying circuit (Einevoll et al., 2013).

VERTEX has already been shown to aid in the interpretation of intrinsic dynamics of neocortex (Tomsett et al., 2015), we have extended it to allow interpretation of evoked potentials, as well as changes in evoked potentials as a result of synaptic plasticity. We have illustrated this by simulating the response to bipolar stimulation in the rat neocortex. We first looked at the initial synaptic response and have compared the response characteristics to that recorded *in vitro* in previous described work (Walcott and Langdon, 2002), and in our own experiments with slices bathed in pro-convulsant media. Additionally, we have provided an explanation of the individual synaptic currents which contribute to these recorded potentials.

**6.1.2. Predicting the effects of electric field stimulation on large scale dynamic networks.** As well interpreting the initial response, we have also simulated the response to multiple stimulations, in networks with dynamic synapses. We have added short term plasticity and spike-timing dependent plasticity to the VERTEX simulator. This allows us to simulate stimulus evoked changes to the network. These changes can be combined with the changes seen in the simulated evoked response to aid in interpreting the changes in synaptic properties seen through changes in the experimentally recorded evoked response. We show this in a simulation of paired pulse stimulation, where we can attribute the reduced amplitude of subsequent responses to a combination of the reduced synaptic efficacy due to the depression of the synapse, and reduced neuronal recruitment caused by the inhibitory currents evoked by the first stimulation. In this scenario, by simulating the short term synaptic dynamics (and parameterising our synapse model using experimentally measured values) we can make a prediction of the relative contributions of these components. This has applications in interpreting experiments that use the field potential response to paired pulse stimulation as a measure of the synaptic properties of the network (Wilson et al., 1998; Tamura et al., 2011). Building a model such as this allows one to more easily keep track of, and check the consistency of, the assumptions made in the interpretation. In particular, the assumptions involved in the interpretation of the response LFP.

**6.1.3. Validating maps of neocortical microcircuits:** The construction of maps of the neocortical microcircuit is an ongoing field of study (Thomson, 2002; Binzegger et al., 2004; Potjans and Diesmann, 2014; Ramaswamy et al., 2015; Markram et al., 2015). Constructing accurate maps is seen as a vital step towards facilitating *in silico* research in a variety of areas of neocortex research. From understanding the information processing abilities of healthy neocortex, to understanding its role in various neurological disorders. Validation of these maps must be done in the specific context of their use. We have found that to replicate the response to stimulation applied *in vitro* in a particular study (Walcott and Langdon, 2002), we needed to modify the network generated with data from the Neocortical Microcircuit Collaborative Portal (Ramaswamy et al., 2015). This does not necessarily invalidate the map, differences in cortical region, preparation methods, and animal age, as well as unknown sources of variability mean that further experimental work would be required for validation. However, simulations built using VERTEX could aid in validation of microcircuit maps. Its ease of use and more directly comparable recording outputs (LFP) and stimulating inputs (electric field stimulation), may make constructing comparison simulations more appealing to experimentalists.

## 6.2. Current limitations and avenues for future research

**6.2.1. The effect of electric fields on axons.** Our neuron models contain only dendrites and soma, without explicitly modelling the axon. In VERTEX the propagation of the action potential is modelled as a delay in the arrival of the spike at the postsynaptic cell. This allows for a more efficient simulation as simulating the propagation of the action potential would be computationally costly. However, stimulating the white matter (axon tracts) is a common stimulation paradigm, and exclusively axonal stimulation in the grey matter has been shown to produce significant responses (Rattay, 1986; Nowak and Bullier, 1998). For white matter stimulation it is a more consistent paradigm, and so previous detailed theoretical and experimental studies can provide an accurate estimation of the spike trains to given levels of stimuli. However, for grey matter stimulation, the contribution of electric field evoked action potentials generated exclusively in the axons is a factor lacking in our simulations. In particular, the intracortical microstimulation technique has been shown by number of studies to induce its effect through the activation of axon terminals. For example Boychuk et al.

(2015) show that a pharmacological block of synaptic transmission reduces the spiking response to stimulation by 85%, indicating that synaptic currents induced via the activation of local axon terminals may have a significant role. Similarly Histed et al. (2009) also indicate that axonal recruitment contributes significantly to the response to stimulation in layer 2/3. These results are also corroborated by work that indicates that axons have a lower threshold for excitation (Rattay and Wenger, 2010), and are more likely to be the site of action potential initiation as a result of extracellular stimulation (Stuart et al. (1997)). It is therefore likely that, particularly at close to threshold levels of stimulation, a simulation without axons may overestimate the current required to induce a response.

**6.2.1.1. Implementing axons in VERTEX.** Future development of the simulator should involve the addition of explicitly modelled axonal compartments. This should build on the work of Aberra et al. (2018) who have constructed a set of axonal morphological models for rat neocortex, that have been validated in the context of electrical stimulation. Incorporating large and detailed axonal models will have a significant computational cost, limiting the volume of tissue that be modelled. A possible solution to this can be to take advantage of the short duration over which most stimulation is applied, by only including the axon model during stimulation. As an action potential in the axon will propagate both ways, if an action potential is generated in the axon, this can be processed in the same way as it would if it had been generated in the soma.

**6.2.2. More accurate models of plasticity.** The plasticity models currently implemented for the VERTEX simulator represent only two of the established models for short term plasticity and one of the established models for spike-timing dependent plasticity. While these are useful for some applications, other plasticity models have been suggested that may be more valid biologically, or for modelling particular scenarios. For example, the implemented model of STP contains only a single component for facilitation and depression, allowing only a single time constant for the decay of each. Adding a second depression component to this model has been shown to produce a better fit to experimental data (Varela et al., 1997). There are also alternatives to the implemented model of STDP, many of which may be more biologically plausible. We implement classical Hebbian STDP with exponential decays but STDP has been

shown to depend on many factors other than spike-timing. The spike-timing component forms just one part of the plasticity process along with pre and postsynaptic firing rates and dendritic depolarisation (Feldman, 2012). Models based on the instantaneous and averaged membrane potential of the postsynaptic cell and spike-timing of the presynaptic cell better capture this multifaceted plasticity and have been shown to produce connectivity patterns that better reflect those seen in cortex (Clopath et al., 2010). Models of this nature may also be useful in predicting electric field induced enhancement of plasticity, particularly that induced by transcranial stimulation devices (Fritsch et al., 2010), as these devices often produce subthreshold effects to induce or augment NMDA-receptor mediated plasticity. Adding models such as that described by Clopath et al. (2010) to the VERTEX simulator would be relatively straightforward and should form part of the continued development of VERTEX.

**6.2.3. Extending to model human or mouse tissue.** In this thesis we have described a VERTEX model of rat neocortex, in previous work Tomsett et al. (2015) described a model of macaque neocortex. While rat is a common model animal for *in vitro* and *in vivo* electrophysiology, models of mouse or human tissue would increase the scope of the tool. As a model animal, the mouse is commonly used when gene alterations are required. This has made its use in neuroscience research into epilepsy (Buckmaster et al., 2002; Chu et al., 2010) and the functional consequences of synaptic plasticity (Bostrom et al., 2015), routine. Although of a different nature to the maps describing the rat microcircuit (Ramaswamy et al., 2015), there are sufficient resources describing the mouse neocortex to construct a suitable VERTEX model (O'Connor et al., 2009; Belgard et al., 2011; Cocas et al., 2016). In particular the Allen brain atlas contains significant resources on the cells of the mouse neocortex (Sunkin et al., 2013). Building a human neocortex model is also desirable. Tissue resected from patients is also increasingly being used in epilepsy research. Constructing a model of human neocortex will aid in the interpretation of local field potentials recorded from these *ex vivo* slices. It will also serve to aid in predicting the effects of non-invasive stimulation in humans, explored further in the following section. Data on human neocortical circuits is less extensive than that on rat and mouse. However, there significant overlap in cell types between mammals, including rodents and humans (Nieuwenhuys et al., 2007). Data on the additional cells types found in humans - such as the von Economo neurons

(Semendeferi et al., 2010), and the variations in layer thicknesses and cell densities, can be combined with the cell-type specific connectivity of the rat to produce an approximation of the human neocortex.

**6.2.4. Modifying neuronal circuits with brain stimulation.** We have shown an initial simulation of the modification of a neocortical network using theta burst stimulation in the *in vitro* setting. There is the potential to use a similar approach to model the therapeutic modification of neural circuits in humans using transcranial electric field stimulation techniques such as transcranial direct current stimulation (tDCS) or transcranial magnetic stimulation (TMS). Non-invasive brain stimulation has shown promise or been suggested for the treatment of diseases such as depression (Nitsche et al., 2009), tinnitus (Rabau et al., 2017), epilepsy (Theodore, 2003), stroke (Hong et al., 2017), and general improvement in cognition (Chrysikou et al., 2017). The therapeutic effects are often attributed to mechanisms of plasticity, particularly NMDA-receptor/ $\text{Ca}^{2+}$  mediated synaptic plasticity (Fritsch et al., 2010). Much work has gone into building accurate predictions of the distribution of current and associated electric field produced by these stimulation devices (Kim et al., 2009; Krieg et al., 2015). However, interpretation of its effects are often limited to single neuron models (Yi et al., 2015; Seo et al., 2016), or abstract models that do not include neuron morphologies and so miss morphology specific, or location specific effects of the induced fields Esser et al. (2005). Simulations of these effects using VERTEX would be at the level of the neocortical microcircuit, and could take into account the morphology and location of cell types, the ongoing dynamics of the network, and realistic synaptic plasticity rules.

**6.2.5. A full biophysical model of ictal activity.** We have described epileptiform activity generated by our rat neocortical model with short term plasticity. In this model the network is in a chronically hyperexcitable state due to a large increase in the strength of excitatory synapses. The network restrains activity until the activity dependent depression of inhibitory synapses causes them to lose efficacy and recurrent excitatory activity takes hold, resulting in the rapid recruitment of most of the network in a synchronised discharge. Although previously described computational models of epileptiform activity have included short term plasticity (Hall and Kuhlmann, 2013),

ours is a novel contribution in that it includes the full detail of a reconstructed neocortical slice, with realistic spiking dynamics and short term plasticity time constants. It also focuses on the cell type specific synaptic dynamics involved in the initiation of the event, and the contributions to the LFP generated.

The extent to which this mechanism interacts with other mechanisms suspected to contribute to the failure of inhibition during epileptiform activity, as well as the possible roles they would play in extending this model of a single spike into a full ictal event, should be the subject of future research.

Mechanisms of interest could include the depolarisation block of interneurons (Kim and Nykamp, 2017) and the changing reversal potential of GABA as a result of chloride loading (Alfonsa et al., 2015), both influenced by slow fluctuations in  $K^+$  concentration. Depolarisation block occurs when neurons receive overwhelming excitatory drive. We illustrate this in a NEURON simulation of a single pyramidal cell receiving a large excitatory current (figure 6.1). Instead of increasing its firing rate linearly with increasing input, a typical real neuron initially increases rapidly but then decreases rapidly after the input begins to overwhelm the cell. The AdEx model currently used in VERTEX does not capture the depolarisation block. The Hodgkin-Huxley type equations do, but so too do the Morris-Lecar equations, a more reduced model that can be fitted to model the spiking properties of most types of neurons (Meijer et al., 2015; Kim and Nykamp, 2017). Applying this to model inhibitory neurons may be sufficient for studying its role in seizure initiation, while the role of depolarisation block of excitatory neurons may be involved in seizure termination.

**6.2.6. Controlling epileptiform activity with stimulation.** Future applications of a full ictal model in VERTEX could include testing stimulation paradigms for potential in controlling seizures. Closed loop stimulation (where measurements of ongoing activity are used to inform the timing and intensity of stimulation) have shown promise in controlling seizures (Nelson et al., 2011; Belluscio and Mao, 2016). As VERTEX allows explicit modelling of the means of recording, stimulation, and dynamics, it provides an ideal environment for the testing of such devices.

**6.2.7. Measuring the properties of epileptic networks with stimulation.** Electrical stimulation has also shown promise in measuring the properties of epileptic

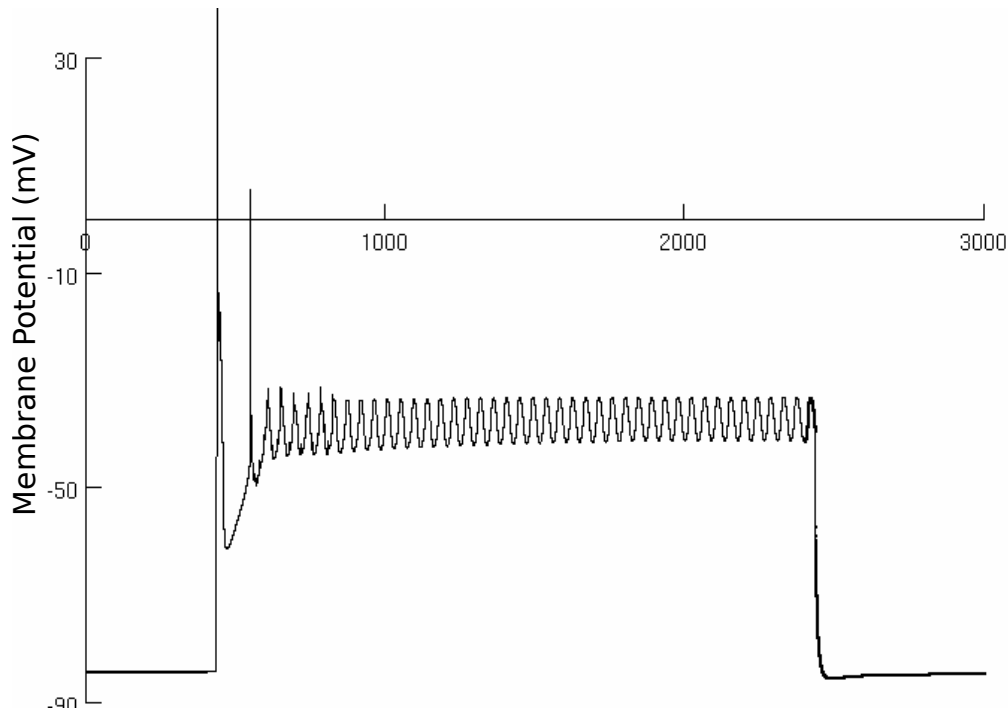


FIGURE 6.1. Depolarisation block induced by injection of a large excitatory current into a pyramidal cell. Modelled using Hodgkin Huxley like equations in the NEURON simulator.

networks, particularly dynamic properties. Measuring changes in the state of the network during a seizure may help uncover the changes in network function that allow seizures to take hold and to persist. Queiroz et al. (2009) take this approach in their analysis of spontaneous seizures recorded in the rat hippocampus *in vivo*. They show how the response to paired pulse stimulation varies throughout the seizure, and find that the depression of the second pulse decreases as the seizure progresses, indicating that the inhibitory neurons have become less effective. The direct interpretation of this change to the depression of evoked local field potentials, would be aided by building a comparable simulation in VERTEX. This would allow a direct link to be drawn between the mechanisms thought to be involved in the progression of a seizure, and the measured response.

## APPENDIX A

### Adding Electric Field Stimulation to a VERTEX Simulation

In this chapter we will describe how to add a stimulating electrode to a VERTEX simulation. We will simulate bipolar stimulation to an isolated slice of layers 1 and 2/3 in rat neocortex. Our slice will be  $1500\mu\text{m} \times 600\mu\text{m} \times 400\mu\text{m}$ .

#### A.1. Creating the 3D model in Blender

To build the 3D mesh of the slice and tissue we will use the Blender 3D modelling tool. We have chosen this because it is easy to use, free, open source, and can export the mesh as an STL (STereoLithography) file, which can be read by the MATLAB PDE toolbox. To download Blender visit their website (<https://www.blender.org/>).

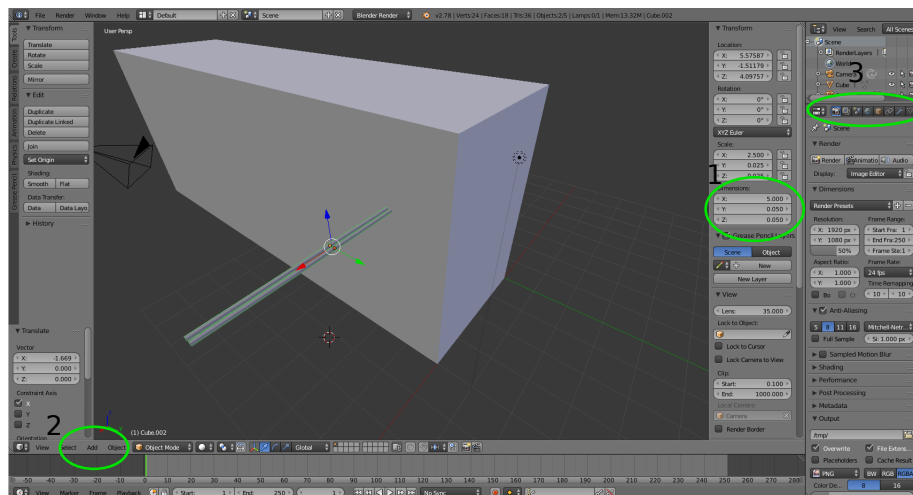


FIGURE A.1. Shows the Blender environment. The location of the tools required at each step are circled in green and numbered.

When you open Blender there is usually a cube, we will resize this to the dimensions of our slice. Press `n` to bring up the dimension controls (circle 1). Change the dimensions to 4, 15, 6 (X, Y, Z). We will scale the mesh up when we export. Move the cuboid so that its far right corner is at the origin, this will ensure that it is in the correct location when we import into MATLAB. We then need to create the electrode, from the Add menu (circle 2) at the bottom right of the panel, select cube. This will add an additional cube to the scene. Resize this to 5, 0.05, 0.05, and duplicate it (`Ctrl + C`, `Ctrl + V`). Move the second electrode prong slightly to one side of the other

and join them (select both with Cntrl + right click, the Cntrl +J). Place the electrode about half way in to the slice. As the boundary conditions in the PDE model are

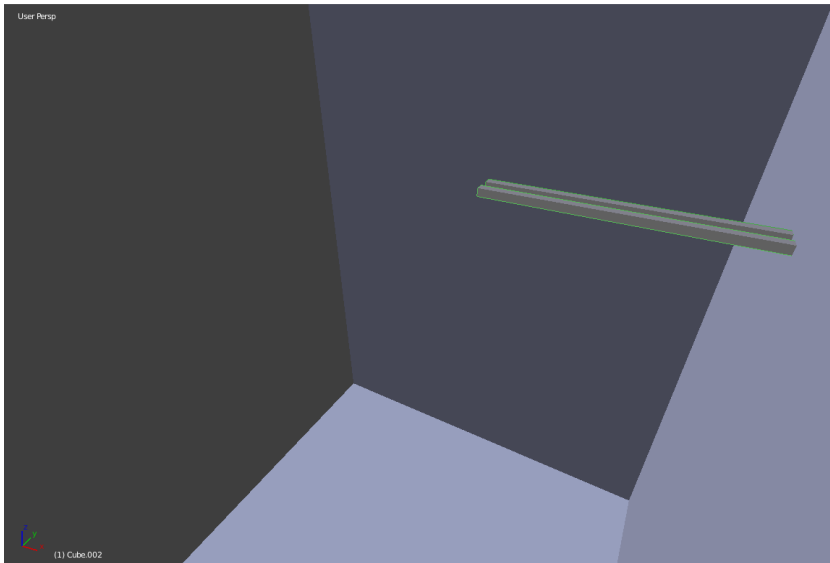


FIGURE A.2. Shows the electrode placed into the slice.

applied at the faces of a single box (more complicated setups are possible but this is the easiest way for two charged conductors in a homogeneous conductive media). We then wish to cut out the shape of the electrode from the tissue. To do this, select the tissue cuboid, then select the spanner on the toolbar to the top right. Then select the

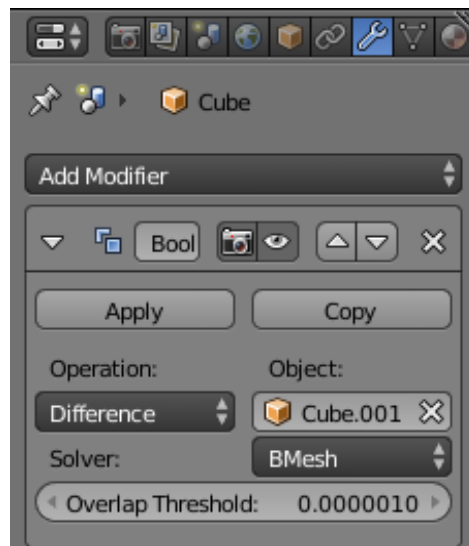


FIGURE A.3.

Add modifier button, then add a boolean difference modifier, selecting the electrode (probably Cube.001) as the modifier (figure A.3), then click Apply. We then wish to export, select the tissue cube, select file → export → Stl. This will bring up the export dialogue, enter the filename for your export file, then in the panel at the bottom left, select selection only, and scale by 100 % (figure A.4).



FIGURE A.4. Exporting the STL file.

## A.2. Calculating the electric field

With our 3D model saved as an STL file, we can now import it into the PDE toolbox and apply the conditions to calculate the electric field and electric potential. This involves assigning boundary conditions to each of the faces of the imported geometry. As the PDE toolbox does this in an unpredictable fashion, one must load in the geometry and assign the conditions manually for each geometry. The volume conductor equation used is implicit in the coefficients that we provide.

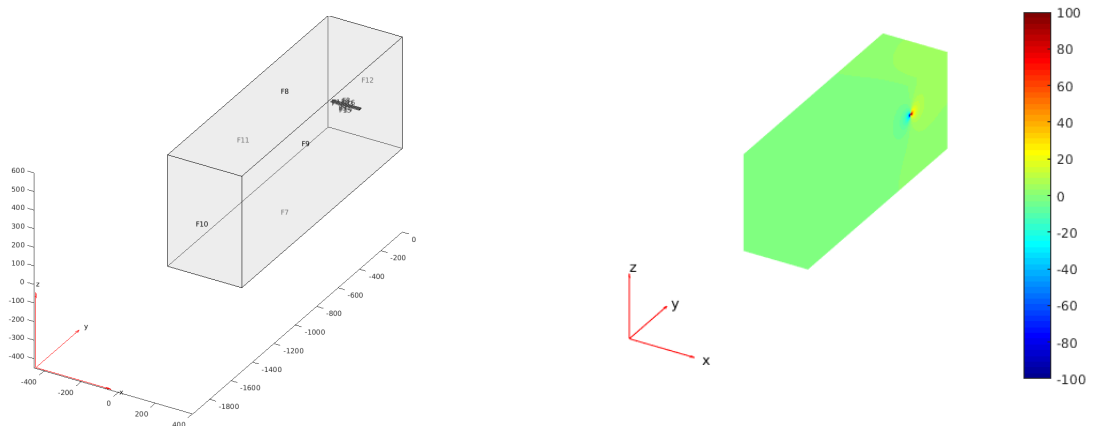


FIGURE A.5. The mesh and electric potential calculated.

```

%% Load the geometry as an stl file.
geometryloc = '~/Dropbox/layer23.stl';
model = createpde;
%load the file
importGeometry(model,geometryloc);

%plot the geometry with
figure(1)
pdeplot(model,'FaceLabels', 'on','FaceAlpha',0.3)

%% Apply the boundary conditions and specify the coefficients.
%insulating boundary - edge of the tissue
applyBoundaryCondition(model,'face',7:12,'g',0.0,'q',0.0);
%conductive boundary - tissue/electrode interface
%positive electrode
applyBoundaryCondition(model,'face',[2,3,14,1,16],'h',1.0,'r',1000);
%negative electrode
applyBoundaryCondition(model,'face',[4,13,5,6,15],'h',1.0,'r',-1000);

%conductivity of brain tissue is around 0.3 S m^-1
%As vertex is in units of micrometers c --> 0.3/1000000
specifyCoefficients(model,'m',0, 'd',0, 'c',0.3/1e6, 'a',0, 'f',0);

%% Generate mesh and calculate the electric potential across the tissue.
generateMesh(model);

result = solvepde(model);

figure(2)
pdeplot3D(model,'ColorMapData', result.NodalSolution);

```

FIGURE A.6. The above code will import the geometry and plot it, the specific face numbers may need to be altered for the specific geometry. Then apply the boundary conditions and coefficients to produce the electric field.

### A.3. Running the simulation

We can run the stimulation a simplified layer 2/3 model. The MATLAB code to do this is in figure A.7. To do this we first load the geometry and model the field using the code from figure A.6. We then set the stimulation on and off times, then call `tutorial_2_g`, a typical script for running a VERTEX simulation.

```

%load and build pde model (calls the code in figure A.6)
loadgeometryandapplyconditions
%Assign the StationaryResult object representing the field to the
%TissueParameters.
TissueParams.StimulationField = result;
%Set the stimulation on and off times.
TissueParams.StimulationOn = [500 900];
TissueParams.StimulationOff = [502 902];
%%
%Run the tutorial as normal
tutorial_2_g

```

FIGURE A.7. Code for calling the first script to load the geometry and create the electric field model. Then we assign the stimulation on and off times. Then we call the tutorial 2 file. This is a typical tutorial to run a simple network simulation in VERTEX.

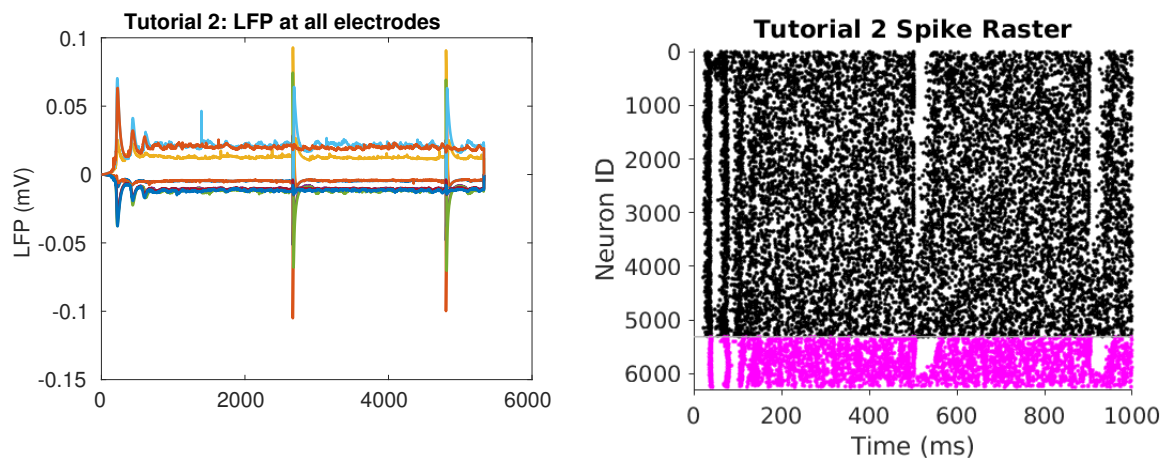


FIGURE A.8. The result of stimulation on the tutorial 2 output.



## APPENDIX B

### Adding Synaptic Plasticity to a VERTEX Simulation

To show how to add synaptic plasticity to a VERTEX simulation, we will take the tutorial\_2.g program used above and show how to convert it to have short term plasticity or spike-timing dependent plasticity.

#### B.1. Adding short term plasticity

To add short term plasticity, a rate of facilitation and depression must be specified, each between 0 and 1. Here we specify 0.5 for both. We also must specify a time constant for the decay of the effect of the facilitation or depression.

```
%The connection parameters for synapses from pyramidal cells to pyramidal
%cells
ConnectionParams(1).numConnectionsToAllFromOne{1} = 1700;

%Here we specify the synapse type, g_stp is the type for exponential
%conductance based synapses with short term plasticity.
%g_exp is for the same synapses without plasticity.
ConnectionParams(1).synapseType{1} = 'g_stp';
%Specify the target compartments of the synapses
ConnectionParams(1).targetCompartments{1} = [NeuronParams(1).basalID, ...
                                             NeuronParams(1).apicalID];
ConnectionParams(1).weights{1} = 0.05; %The baseline synaptic weight
ConnectionParams(1).tau{1} = 1;% The time constant for the decay

%Here we specify the parameters for the plasticity,
%facilitation is a unitless parameter that
%indicates the rate at which facilitation occurs. It should be a value
%between 0 and 1, at 0 there will be no facilitation at 1 strong
%facilitation. The depression value should also be between 1 and
%greater than 0 with 1
%being no depression and small values being strong depression.
%Depressing
ConnectionParams(1).facilitation{1} = 0.5;
ConnectionParams(1).depression{1} = 0.5;
% The time constants for facilitation and depression, a longer time
% constant indicates that the effect will persist for longer.
ConnectionParams(1).tD{1} = 670;
ConnectionParams(1).tF{1} = 17;
```

FIGURE B.1. Shows the code required to specify a synaptic connection between two neuron groups (here connections from one group to itself) with short term synaptic plasticity.

## B.2. Adding spike-timing dependent plasticity

Here we need add a time constant for Apre and Apost, as well as maximum and minimum weights, and a rate that applies both to increases in weight and decreases.

```
ConnectionParams(1).numConnectionsToAllFromOne{2} = 600;
ConnectionParams(1).synapseType{2} = 'g_stdp';
ConnectionParams(1).targetCompartments{2} = NeuronParams(2).dendritesID;
ConnectionParams(1).weights{2} = 0.1;
ConnectionParams(1).tau{2} = 1;
ConnectionParams(1).rate{2} = 0.001;
ConnectionParams(1).tPre{2} = 2;
ConnectionParams(1).tPost{2} = 10;
ConnectionParams(1).wmin{2} = 0;
ConnectionParams(1).wmax{2} = 100;
```

FIGURE B.2. Shows the code required to add spike-timing dependent plasticity to a synaptic connection.

## APPENDIX C

### Simulating the effect of an electric field

We incorporate the effect of the electric field when calculating the axial currents (the current flowing from compartment to compartment). The effect is incorporated as an additional axial current, proportional to the difference in extracellular potential between compartments. This follows from the theory described by Rall (1962) and Rattay (1999). The equation describing the membrane potential change caused by the electric field (and any endogenous differences in membrane potential between compartments) at any compartment  $n$ , is reproduced below (equation C.0.1).

$$\begin{aligned} \frac{dV_n}{dt} = & [I_{ion} + \frac{V_{n-1} - V_n}{R_{n-1}/2 + R_n/2} + \frac{V_{n+1} - V_n}{R_{n+1}/2 + R_n/2} \dots \\ & + \frac{Ve_{n-1} - Ve_n}{R_{n-1}/2 + R_n/2} + \frac{Ve_{n+1} - Ve_n}{R_{n+1}/2 + R_n/2}] / C_{m,n} \end{aligned} \quad (\text{C.0.1})$$

In VERTEX, we incorporate this as an additional set in the calculation of axial currents, performed in the abstract `Neuron_Model` class, from which other types of neuron model - adaptive exponential integrate and fire, Morris-Lecar, etc, inherit. Below is the code used to calculate the axial currents contributed by differences in extracellular potential across compartments. This corresponds to the second part of equation C.0.1 -  $\frac{Ve_{n-1} - Ve_n}{R_{n-1}/2 + R_n/2} + \frac{Ve_{n+1} - Ve_n}{R_{n+1}/2 + R_n/2}$  the first part of the equation  $\frac{V_{n-1} - V_n}{R_{n-1}/2 + R_n/2} + \frac{V_{n+1} - V_n}{R_{n+1}/2 + R_n/2}$  has already been added to `L_ax`. The ionic current `I_ion` is incorporated into the membrane potential separately, as is the capacitance term.

```

if NM.incorporate_vext
    %tree children is max number of children (neighbours) a node can have
    %so vectorised over all compartments for each connecting neighbour
    for iTree = 1:NM.treeChildren
        %Additional Axial current caused by
        %temporary v_ext change is proportional to the difference between the
        %external potential in adjacent compartments
        NM.I_ax(:, N.adjCompart{iTree}(1, :)) = ...
            NM.I_ax(:, N.adjCompart{iTree}(1, :)) + ...
            bsxfun(@times, N.g_ax{iTree}, ...
                (NM.v_ext(:, N.adjCompart{iTree}(1, :)) - ...
                 NM.v_ext(:, N.adjCompart{iTree}(2, :)))));
    end
end
end

```

FIGURE C.1. Code for incorporating external potentials. `NM` is the `Neuron_Model` object, `incorporate_vext` is a boolean, set to 1 when the stimulation is to be incorporated, `v_ext` is the extracellular potential at each compartment location of each neuron in the group, `treeChildren` is the maximum number of neighbours a compartment can have, `I_ax` is the axial current, which will contribute to the membrane potential change of each compartment when it is next integrated. `N` is an object containing invariant parameters for a neuron type, `adjCompart` contains the IDs of adjacent compartments of each compartment, `g_ax` is the conductance between compartments. The computation is vectorised across all neurons in the group and across compartments. We loop through the possible neighbouring compartments to calculate the additional axial current contributed by the extracellular potential.

## APPENDIX D

### **The Adaptive Exponential Integrate And Fire Model**

The adaptive exponential integrate and fire (AdEx) model (Brette and Gerstner, 2005) is the main model used by the VERTEX simulator. In the table here we show the parameters used to generate a range of neuronal dynamics. These parameters are taken from Naud et al. (2008). We show the neuronal dynamics in figure D.1.

TABLE D.1. Show the parameters used to generate a range of neuronal dynamics with the AdEx model.

Type	C (pF)	gL (nS)	EL (mV)	VT (mV)	Delta T (mV)	a (nS)	tau w (ms)	b (pA)	Vr (mV)	I (pA)
Tonic Spiking	200	10	-70	-50	2	2	30	0	-58	500
Adaptation	200	12	-70	-50	2	2	300	60	-58	500
Initial Burst	130	18	-58	-50	2	4	150	120	-50	400
Regular Bursting	200	10	-58	-50	2	2	120	100	-46	210
Delayed Accelerating	200	12	-70	-50	2	-10	300	0	-58	300
Irregular Spiking	100	12	-60	-50	2	-11	130	30	-48	160

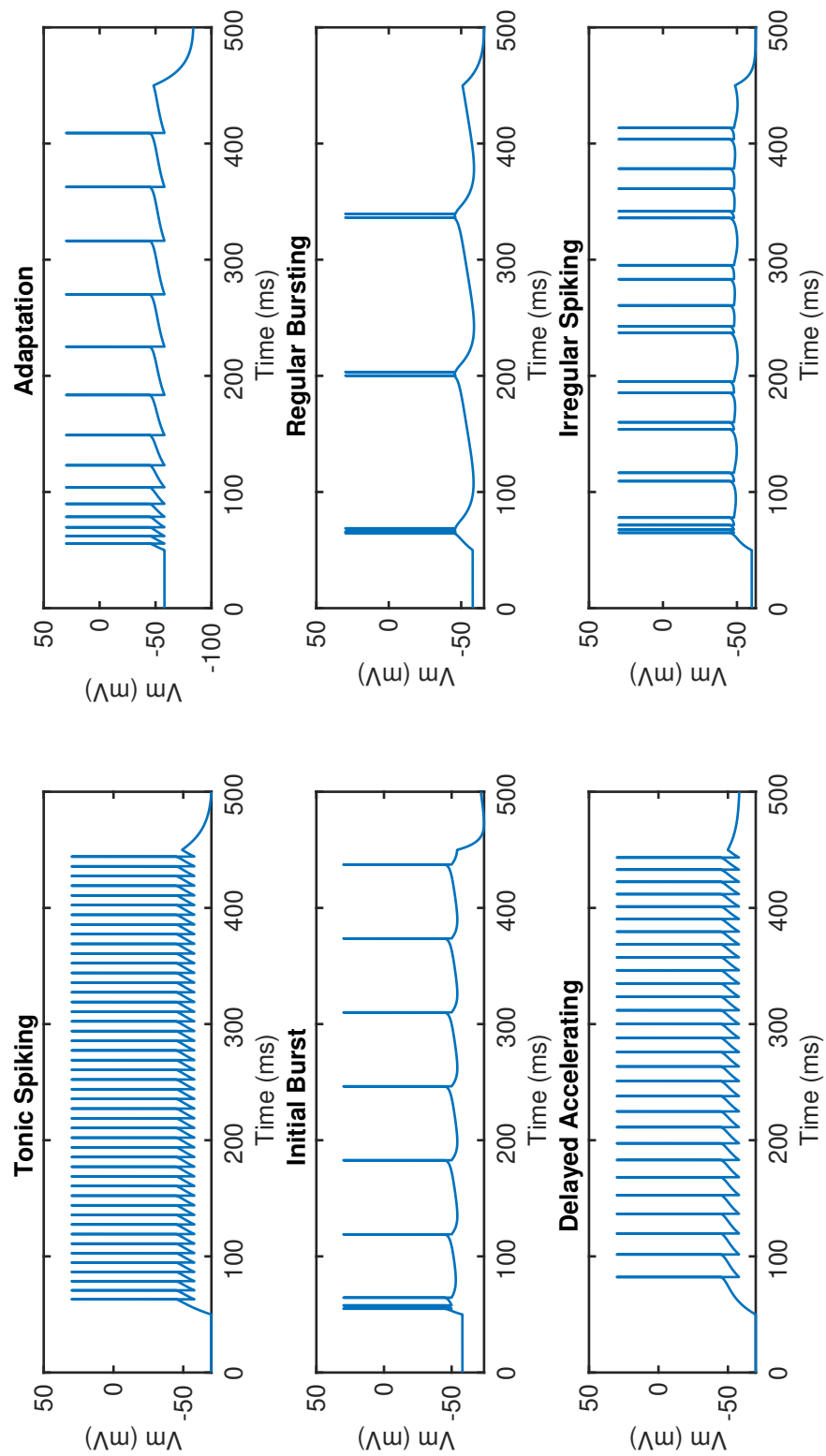


FIGURE D.1. Shows the neuronal dynamics of a VERTEX AdEx neuron with the parameters described in table D.1.



## Implementation of the Synapse Models and Spike Processing

VERTEX is built using MATLAB, and makes use of the object-orientated and parallel programming support it provides. The core VERTEX program has been described previously (Tomsett et al., 2015), the changes made to VERTEX for this release comprise the addition of a mechanism to incorporate an extracellular stimulating field, and various forms of synaptic plasticity. This section will describe the various data structures used to store the properties and variables of the synapses and neurons, as well as the methods used to update the synaptic variables and weights during the main simulation loop.

### E.1. Class hierarchy:

Neuron and synapse types are described using inheritance to avoid the duplication of functionality. The abstract `NeuronModel` class describes the functionality provided by all multi-compartment neurons. It contains the membrane potential, external potential, and axial current (the currents that flow between compartments as a result of the difference between their membrane potentials) properties, as well as the functionality required to integrate these. The integration of equation 2.2.2 is included as an additional step during the calculation of the axial currents and is performed at each time step when the stimulation is turned on. It is part of the core functionality of the abstract `Neuron` class. Classes with specific mechanisms then inherit from this, e.g. the `NeuronModel_passive` class provides a simple wrapper on top to allow a neuron with no active channels. The `NeuronModel_adex` adds the adaptive exponential integrate and fire mechanism to the soma, allowing the cell to generate action potentials. Here each instance of a class would represent a group of neurons in the same layer and of the same type. This allows us to utilise MATLAB's vectorised operations when updating variables so that for example: the membrane potential variable (`v_m`) holds the membrane potentials of all neurons in this group as a matrix. This also allows us to utilise the object oriented design advantages without the overhead that would come from storing each neuron or synapse as its own object. The integration of the axial

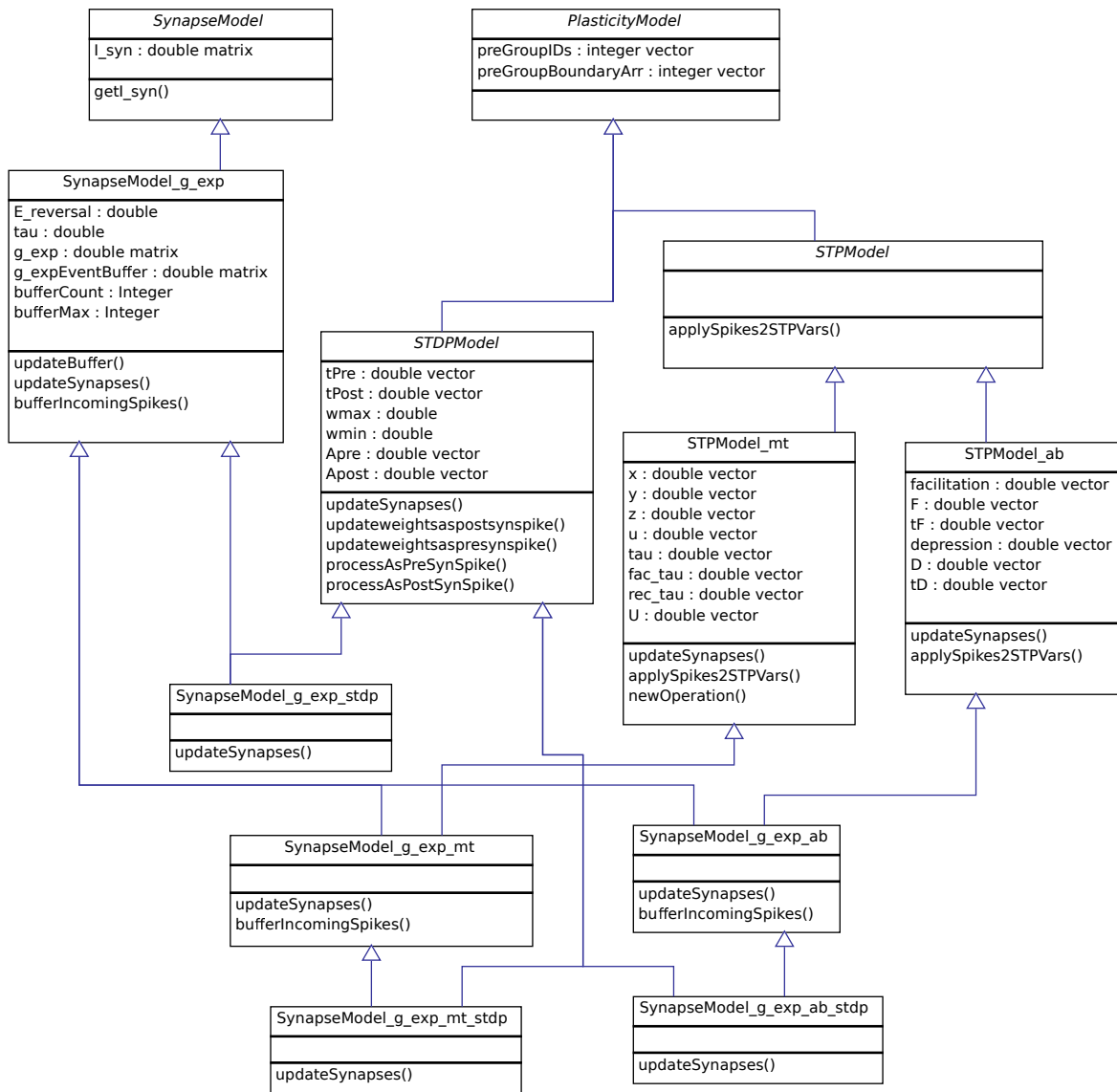


FIGURE E.1. Using multiple inheritance to represent multiple types of synapse. The hierarchy of classes representing single exponential conductance based synapses, with and without spike timing dependant plasticity and short term plasticity. Other base synapse models (current based exponential, alpha, etc) are not shown here but fit in exactly as the `SynapseModel_g_exp` does.

current involves a loop over all possible neighbouring compartments with an operation vectorised for each compartment. The class hierarchy relevant to conductance based exponential synapses (`SynapseModel_g_exp`) is shown in figure E.1. Here, we have used multiple inheritance to allow us to efficiently define many combinations of synapse types. Synapse models have a base synapse type (defining how the synapse operates without plasticity, e.g. `g_exp` will be a conductance based exponential synapse), it can then also have short term plasticity (ab for the Abbott model or mt for the Markram and Tsodyks), spike timing dependent plasticity (stdp), or both. The plasticity models are defined as separate classes from which the synapse model can inherit from.

## E.2. Data structures for synapse variables:

Synapse models are required to provide a current to be applied to each neuron in the postsynaptic group. As such they store variables relevant to this calculation as vectors with an entry for each postsynaptic neuron. As STP model variables are dependent on the presynaptic firing we store these as vectors with an entry for each presynaptic neuron. This allows operations to be vectorised over all presynaptic neurons. In the STDP model  $A_{pre}$  is a vector with an entry for each presynaptic neuron, and  $A_{post}$  with an entry for each post synaptic cell, operations on these can be vectorised over all pre and post synaptic neurons respectively. Weight updates (equations 2.4.18 and 2.4.19) can also be vectorised across either the postsynaptic or presynaptic neurons.



## Inhibitory Synapse Location and the Propagation of Activity

### F.1. Introduction

Many clinical and experimental manifestations of epilepsy show alterations in particular microcircuit motifs which are thought to contribute to the increased propensity for seizures to occur (Paz and Huguenard, 2015). One such motif is the feedforward and feedback inhibition provided by parvalbumin-positive fast spiking interneurons. This subclass of interneuron provides inhibition exclusively to the perisomatic region of pyramidal cells. This is in contrast to somatostatin positive interneurons which target more distal areas of the dendritic tree. The aim of this work is to investigate how the location of inhibitory synaptic input on the post-synaptic cell affects the ability of a neuronal network to restrain the spread of activity.

### F.2. Methods

We used the Virtual Electrode Recording Tool for EXtracellular potentials (VERTEx) Tomsett et al. (2015), a Matlab tool, to simulate a network of 5000 multi-compartmental adaptive exponential integrate and fire neurons. Our simulation contained:

- Excitatory (81.6% of total) and inhibitory populations (18.4% of total).
- Conductance based synapses.
- Excitatory and recurrent inhibitory synapses were located on the dendrites.
- Inhibitory synapses were located either at the soma or the dendrites of the post-synaptic excitatory neurons.
- A current injection of 800 pAs for 10 ms to a spatially defined subset of the excitatory population provided a seizure-like event.

Figure F.1 shows the activity after activity has been initiated by the brief current injection.

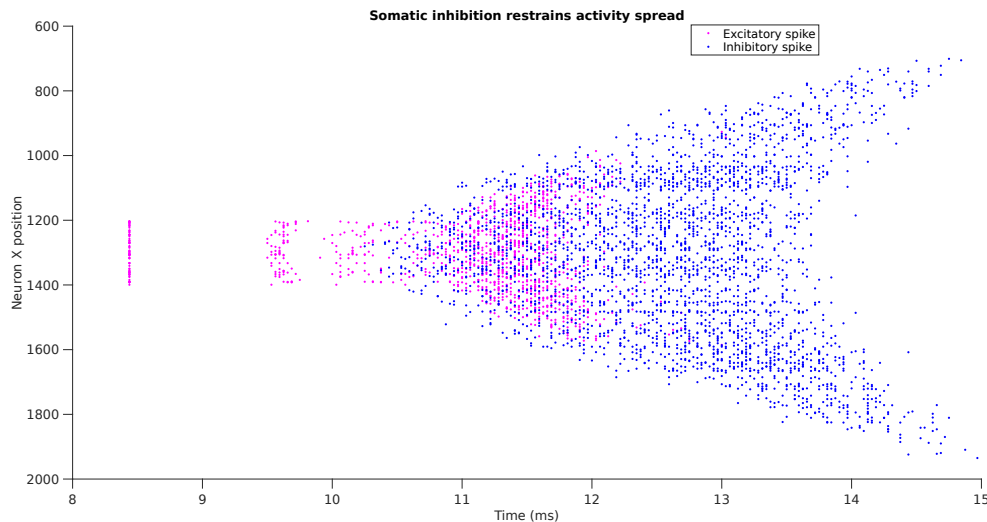


FIGURE F.1. Spatially arranged spike raster after stimulation of subset of neurons. Magenta dots indicate an excitatory neuron firing, blue dots represent an inhibitory neuron firing. This figure illustrates the simulations we performed, a seizure focus is created in the centre of network by applying current injection. If this, and recurrent excitatory connections, are strong enough then activity will begin to spread. Depending on the network this activity may or may not be restrained by inhibition. In this case it is restrained by strong somatic inhibition.

### F.3. The Firing Rate Of A Single Neuron

Previous results have shown the different effects of inhibition when applied at the soma or dendrites (Pouille et al., 2013). We reproduced these by presenting our excitatory neuron with increasingly large depolarising inputs at the dendrites and hyperpolarising input at either the soma or dendrites. This is shown in figure F.2.

### F.4. Somatic Inhibition Provides a More Powerful Restraint

We produced simulations with a range of excitatory and inhibitory synapse strengths. We found that somatic inhibition better restrains the spread of activity, allowing a higher ratio of excitatory to inhibitory synapse strength before activity propagates to the edge of our network. This is shown in Figure F.3.

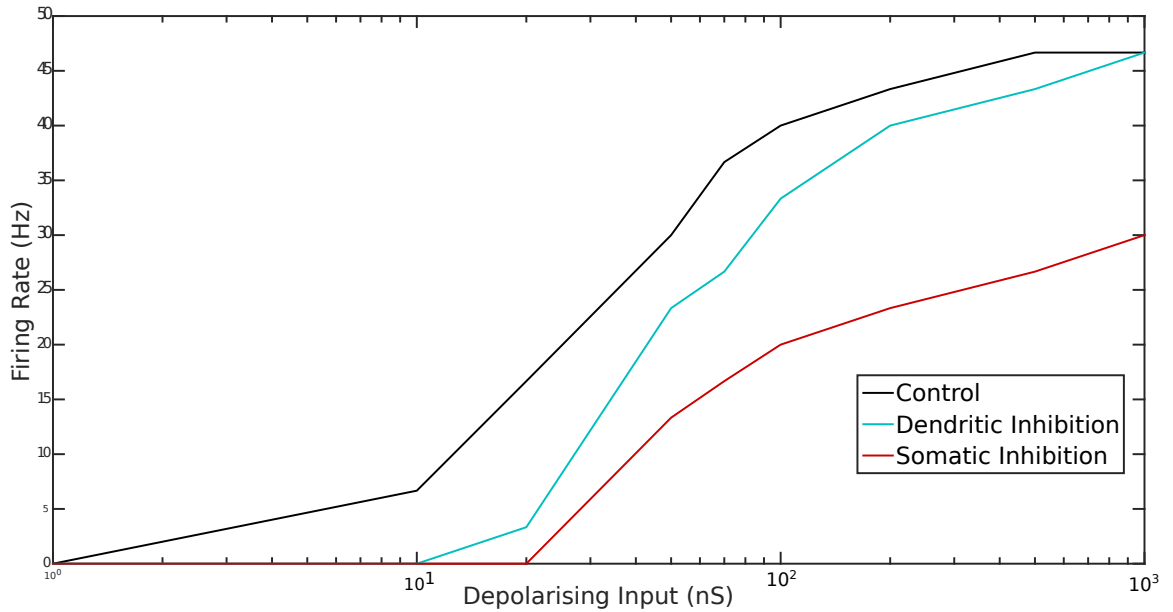


FIGURE F.2. The firing rate of the neuron increases most rapidly without inhibition, less rapidly with dendritic inhibition and less rapidly still when somatic inhibition is present. With dendritic inhibition the same maximum firing rate is still achievable, but somatic inhibition reduces this by a half.

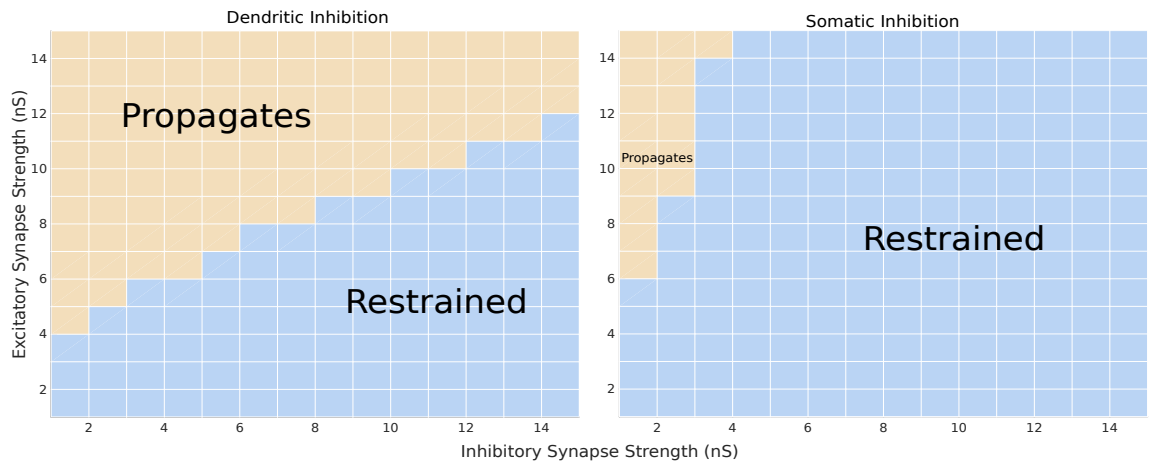


FIGURE F.3. In networks with somatic inhibition, far higher excitatory synapse strength to inhibitory synapse strength is required to propagate activity.



## References

- Abbott, L. F., Regehr, W. G., 2004. Synaptic computation. *Nature* 431 (7010), 796–803.
- Aberra, A., Peterchev, A., Grill, W., 2018. Biophysically realistic neuron models for simulation of cortical stimulation. *Journal of Neural Engineering* 15 (6).
- Alfonsa, H., Merricks, X. E. M., Codadu, N. K., Cunningham, M. O., Deisseroth, K., Racca, C., Trevelyan, X. A. J., 2015. The Contribution of Raised Intraneuronal Chloride to Epileptic Network Activity. *Journal of Neuroscience* 35 (20), 7715–7726.
- ANSYS, 2017. ANSYS® Academic Research Mechanical, Release 18.1.
- Beghi, E., Berg, A., Carpio, A., Forsgren, L., Hesdorffer, D. C., Hauser, W. A., Malmgren, K., Shinnar, S., Temkin, N., Thurman, D., Tomson, T., oct 2005. Comment on epileptic seizures and epilepsy: definitions proposed by the International League Against Epilepsy (ILAE) and the International Bureau for Epilepsy (IBE). *Epilepsia* 46 (10), 1698–9; author reply 1701–2.  
URL <http://www.ncbi.nlm.nih.gov/pubmed/16190948>
- Beierlein, M., 2003. Two Dynamically Distinct Inhibitory Networks in Layer 4 of the Neocortex. *Journal of Neurophysiology* 90 (5), 2987–3000.  
URL <http://jn.physiology.org/cgi/doi/10.1152/jn.00283.2003>
- Belgard, T. G., Marques, A. C., Oliver, P. L., Abaan, H. O., Sirey, T. M., Hoerder-Suabedissen, A., García-Moreno, F., Molnár, Z., Margulies, E. H., Ponting, C. P., 2011. A transcriptomic atlas of mouse neocortical layers. *Neuron* 71 (4), 605–616.
- Belluscio, M., Mao, D., 2016. Closed-Loop Control of Epilepsy by Transcranial Electrical Stimulation. *Science* 337 (6095), 735–737.
- Benjamini, Y., Hochberg, Y., 1995. Controlling the False Discovery Rate: A Practical and Powerful Approach to Multiple Testing. *Journal of the Royal Statistical Society, Series B.* 61 (1), 1–15.
- Binzegger, T., Douglas, R. J., Martin, K. a. C., sep 2004. A quantitative map of the circuit of cat primary visual cortex. *The Journal of neuroscience : the official journal of the Society for Neuroscience* 24 (39), 8441–53.  
URL <http://www.ncbi.nlm.nih.gov/pubmed/15456817>

- Bliss, T. V. P., Cooke, S. F., 2011. Long-term potentiation and long-term depression: a clinical perspective. *Clinics (São Paulo, Brazil)* 66 Suppl 1, 3–17.
- Bliss, T. V. P., Lomo, T., 1973. Long-lasting potentiation of synaptic transmission in the dentate area of the anaesthetized rabbit following stimulation of the perforant path. *Journal of physiology* 232, 331–356.
- Bokil, H., Andrews, P., Kulkarni, J. E., Mehta, S., Mitra, P. P., 2010. Chronux: A platform for analyzing neural signals. *Journal of Neuroscience Methods* 192 (1), 146–151.
- Bostrom, C. A., Majaess, N. M., Morch, K., White, E., Eadie, B. D., Christie, B. R., 2015. Rescue of NMDAR-dependent synaptic plasticity in *Fmr1* knock-out mice. *Cerebral Cortex* 25 (1), 271–279.
- Bouteiller, J.-m. C., Allam, S. L., Greget, R., Ambert, N., Hu, E. Y., Baudry, M., Berger, T. W., 2014. Paired-pulse stimulation at glutamatergic synapses - pre- and postsynaptic components. In: *Annual International Conference of the IEEE Engineering in Medicine and Biology Society*. No. October 2010.
- Boychuk, J. A., Brown, A. R., Hussin, A. T., Teskey, G. C., Pittman, Q. J., 2015. Intracortical Microstimulation (ICMS) Activates Motor Cortex Layer 5 Pyramidal Neurons Mainly Transsynaptically. *Brain Stimulation* 8 (4), 742–750.  
URL <http://dx.doi.org/10.1016/j.brs.2015.03.003>
- Bragina, L., Giovedì, S., Barbaresi, P., 2010. Heterogeneity of Glutamatergic and Gabaergic Release Machinery in Cerebral Cortex: Analysis of Synaptogyrin Vesicle-Associated Membrane Protein, and Syntaxin. *Neuroscience* 165 (3), 934–943.  
URL <http://dx.doi.org/10.1016/j.neuroscience.2009.11.009>
- Brette, R., Gerstner, W., 2005. Adaptive exponential integrate-and-fire model as an effective description of neuronal activity. *Journal of neurophysiology* 94 (5), 3637–42.
- Brette, R., Goodman, D. F. M., 2011. Vectorized algorithms for spiking neural network simulation. *Neural Computation* 23 (6), 1503 – 1535.
- Brody, M., Korngreen, A., 2013. Simulating the effects of short-term synaptic plasticity on postsynaptic dynamics in the globus pallidus. *Frontiers in systems neuroscience* 7 (August), 40.
- Buckmaster, P. S., Otero-Corchón, V., Rubinstein, M., Low, M. J., 2002. Heightened seizure severity in somatostatin knockout mice. *Epilepsy Research* 48 (1-2), 43–56.
- Bui, A., Kim, H. K., Maroso, M., Soltesz, I., 2015. Microcircuits in epilepsy: Heterogeneity And Hub Cells In Network Synchronization. *Cold Spring Harbor Perspectives in Medicine*

- 5 (11), 1–13.
- Burkitt, A. N., 2006. A review of the integrate-and-fire neuron model : I . Homogeneous synaptic input. *Biological cybernetics* 95, 1–19.
- Bush, P. C., Sejnowski, T. J., 1993. Reduced compartmental models of neocortical pyramidal cells. *Journal of Neuroscience Methods* 46 (2), 159–166.
- Carter, D. S., Deshpande, L. S., Raffiq, A., Sombati, S., DeLorenzo, R. J., 2011. Characterization of Spontaneous Recurrent Epileptiform Discharges in Hippocampal-Entorhinal Cortical Slices Prepared from Chronic Epileptic Animals. *Seizure* 20 (3), 218–224.
- Castel-Branco, M. M., Alves, G. L., Figueiredo, I. V., Falcão, a. C., Caramona, M. M., 2009. The maximal electroshock seizure (MES) model in the preclinical assessment of potential new antiepileptic drugs. *Methods and findings in experimental and clinical pharmacology* 31 (2), 101–106.
- Casto-Alamancos, M. A., Connors, B. W., 1997. Distinct forms of short-term plasticity at excitatory synapses of hippocampus and neocortex. *Proceedings of the National Academy of Sciences of the United States of America* 94 (April), 4161–4166.
- Chagnac-Amitai, Y., Connors, B. W., 1989. Horizontal spread of synchronized activity in neocortex and its control by GABA-mediated inhibition. *Journal of neurophysiology* 61 (4), 747–758.
- Chrysikou, E. G., Berryhill, M. E., Bikson, M., Coslett, H. B., 2017. Editorial : Revisiting the Effectiveness of Transcranial Direct Current Brain Stimulation for Cognition : Evidence , Challenges , and Open Questions. *Frontier in Human Neuroscience* 11 (September), 10–12.
- Chu, Y., Jin, X., Parada, I., Pesic, A., Stevens, B., Barres, B., Prince, D. A., 2010. Enhanced synaptic connectivity and epilepsy in C1q knockout mice. *Proceedings of the National Academy of Sciences* 107 (17), 7975–7980.  
URL <http://www.pnas.org/lookup/doi/10.1073/pnas.0913449107>
- Clopath, C., Büsing, L., Vasilaki, E., Gerstner, W., 2010. Connectivity reflects coding: a model of voltage-based STDP with homeostasis. *Nature Neuroscience* 13 (3), 334–352.
- Cocas, L. A., Fernandez, G., Barch, M., Doll, J., Zamora Diaz, I., Pleasure, S. J., 2016. Cell Type-Specific Circuit Mapping Reveals the Presynaptic Connectivity of Developing Cortical Circuits. *Journal of Neuroscience* 36 (11), 3378–3390.  
URL <http://www.jneurosci.org/cgi/doi/10.1523/JNEUROSCI.0375-15.2016>
- Coombes, S., 2006. Neural fields. *Scholarpedia* 1 (6), 1373.

- Costa, M. S., Weigenand, A., Ngo, H.-v. V., 2016. A Thalamocortical Neural Mass Model of the EEG during NREM Sleep and Its Response to Auditory Stimulation. *PLoS Computational Biology* 12 (9), 1–20.
- Cunningham, M. O., Roopun, A., Schofield, I. S., Whittaker, R. G., Duncan, R., Russell, A., Jenkins, A., Nicholson, C., Whittington, M. A., Traub, R. D., 2012. Glissandi : transient fast electrocorticographic oscillations of steadily increasing frequency , explained by temporally increasing gap junction conductance. *Epilepsia* 53 (7), 1205–1214.
- Dan, Y., Poo, M.-M., sep 2004. Spike timing-dependent plasticity of neural circuits. *Neuron* 44 (1), 23–30.  
URL <http://www.ncbi.nlm.nih.gov/pubmed/15450157>
- David, O., Bastin, J., Chabardes, S., Minotti, L., Kahane, P., 2010. Studying network mechanisms using intracranial stimulation in epileptic patients. *Frontiers in systems neuroscience* 4 (October), 1–10.
- de Curtis, M., Jefferys, J. G. R., Avoli, M., 2012. Interictal Epileptiform Discharges in Partial Epilepsy: Complex Neurobiological Mechanisms Based on Experimental and Clinical Evidence. *Jasper’s Basic Mechanisms of the Epilepsies*, 1–24.
- DeLorenzo, R., Sun, D., Deshpande, L., 2005. Cellular mechanisms underlying acquired epilepsy: the calcium hypothesis of the induction and maintainance of epilepsy. *Pharmacology & therapeutics* 105 (3), 1–69.  
URL <http://www.sciencedirect.com/science/article/pii/S0163725804001743>
- Desai, S. A., Rolston, J. D., McCracken, C. E., Potter, S. M., Gross, R. E., 2016. Asynchronous Distributed Multielectrode Microstimulation Reduces Seizures in the Dorsal Tetanus Toxin Model of Temporal Lobe Epilepsy. *Brain Stimulation* 9 (1), 86–100.  
URL <http://dx.doi.org/10.1016/j.brs.2015.08.008>
- Diehl, P. U., Cook, M., 2015. Unsupervised learning of digit recognition using spike-timing-dependent plasticity. *Frontiers in computational neuroscience* 9 (August), 1–9.
- Einevoll, G. T., Kayser, C., Logothetis, N. K., Panzeri, S., 2013. Modelling and analysis of local field potentials for studying the function of cortical circuits. *Nature reviews. Neuroscience* 14 (11), 770–785.  
URL <http://dx.doi.org/10.1038/nrn3599>
- Ellender, T. J., Raimondo, J. V., Irkle, A., Lamsa, K. P., Akerman, C. J., 2014. Excitatory Effects of Parvalbumin-Expressing Interneurons Maintain Hippocampal Epileptiform Activity via Synchronous Afterdischarges. *Neurobiology of Disease* 34 (46), 15208–15222.

- Esser, S. K., Esser, S. K., Hill, S. L., Hill, S. L., Tononi, G., Tononi, G., 2005. Modeling the Effects of Transcranial Magnetic Stimulation on Cortical Circuits. *Journal of Neurophysiology*, 622–639.
- Feldman, D. E., aug 2012. The spike-timing dependence of plasticity. *Neuron* 75 (4), 556–71.
- Feldmeyer, D., 2012. Excitatory neuronal connectivity in the barrel cortex. *Frontiers in neuroanatomy* 6 (July), 1–22.
- Feldt Muldoon, S., Soltesz, I., Cossart, R., 2013. Spatially clustered neuronal assemblies comprise the microstructure of synchrony in chronically epileptic networks. *Proceedings of the National Academy of Sciences* 110 (9), 3567–3572.
- Feng, Z., Durand, D. M., 2006. Effects of Potassium Concentration on Firing Patterns of Low-Calcium Epileptiform Activity in Anesthetized Rat Hippocampus : Inducing of Persistent Spike Activity. *Epilepsia* 47 (4), 727–736.
- Ferecsko, A. S., Jiruska, P., Foss, L., Powell, A. D., Chang, W.-C., Sik, A., Jefferys, J. G. R., 2015. Structural and functional substrates of tetanus toxin in an animal model of temporal lobe epilepsy. *Brain Struct Funct* 220 (2), 1013–1029.
- Feynman, R. P., 1963. *The Feynman Lectures on Physics*.
- Fitzgerald, P. B., Benitez, J., Daskalakis, Z. J., Brown, T. L., Kulkarni, J., 2006. A Randomized, Controlled Trial of Sequential Bilateral Repetitive Transcranial Magnetic Stimulation for Treatment-Resistant Depression. *American Journal of Psychiatry* 163 (January), 88–94.
- Friedrich, P., Vella, M., Gulyás, A. I., Freund, T. F., Káli, S., jan 2014. A flexible, interactive software tool for fitting the parameters of neuronal models. *Frontiers in neuroinformatics* 8 (July), 63.
- Fritsch, B., Reis, J., Martinowich, K., Schambra, H. M., Ji, Y., Cohen, L. G., 2010. Direct Current Stimulation Promotes BDNF-Dependent Synaptic Plasticity : Potential Implications for Motor Learning. *Neuron* 66 (2), 198–204.  
URL <http://dx.doi.org/10.1016/j.neuron.2010.03.035>
- Fröhlich, F., Bazhenov, M., Iragui-Madoz, V., Sejnowski, T., 2008. Potassium dynamics in the epileptic cortex: new insights on an old topic. *The Neuroscientist* 14 (5), 422–33.
- Gabriel, C., Peyman, A., Grant, E., 2009. Electrical conductivity of tissue at frequencies below 1 MHz. *Physics in Medicine & Biology* 54 (16).
- Gerstner, W., Brette, R., 2009. Adaptive exponential integrate-and-fire model. *Scholarpedia* 4(6) (8427).
- Gerstner, W., Kistler, W. M., Naud, R., Paninski, L., 2014. *Neuronal Dynamics*.

- Gewaltig, M.-O., Diesmann, M., 2007. NEST (NEural Simulation Tool). *Scholarpedia* 2 (4).
- Goodfellow, M., Schindler, K., Baier, G., 2012. Self-organised transients in a neural mass model of epileptogenic tissue dynamics. *NeuroImage* 59 (3), 2644–2660.  
URL <http://dx.doi.org/10.1016/j.neuroimage.2011.08.060>
- Goodman, D. F. M., Brette, R., Carnevale, N. T., Ekeberg, Ö., 2009. The Brian simulator. *Frontiers in Neuroscience* 3 (2), 192–197.
- Gurney, K., 1997. *Introduction to neural networks*.
- Hagemann, G., Hoeller, M., Bruehl, C., Lutzenburg, M., Witte, O. W., 1999. Effects of tetanus toxin on functional inhibition after injection in separate cortical areas in rat. *Brain Research* 818, 127–134.
- Hall, D., Kuhlmann, L., jan 2013. Mechanisms of seizure propagation in 2-dimensional centre-surround recurrent networks. *PloS one* 8 (8), e71369.
- Hazan, L., Zugaro, M., Buzsáki, G., sep 2006. Klusters, NeuroScope, NDManager: A free software suite for neurophysiological data processing and visualization. *Journal of Neuroscience Methods* 155 (2), 207–216.  
URL <http://linkinghub.elsevier.com/retrieve/pii/S0165027006000410>
- Hebb, D., 1949. *The Organization of Behavior*.
- Hecht-nielsen, R., 1989. Theory of the Backpropagation Neural Network. In: *International Joint Conference on Neural Networks*. pp. 593–605.
- Hellwig, B., 2000. A quantitative analysis of the local connectivity between pyramidal neurons in layers 2/3 of the rat visual cortex. *Biological cybernetics* 82 (2), 111–121.
- Hennig, M. H., 2013. Theoretical models of synaptic short term plasticity. *Frontiers in computational neuroscience* 7 (April), 45.
- Herreras, O., 2016. Local Field Potentials : Myths and Misunderstandings. *Frontier in Neural Circuits* 10 (December), 1–16.
- Hines, M., Carnevale, N., 1997. The NEURON simulation environment. *Neural Computation* 9 (6), 1179–1209.
- Hines, M., Carnevale, N., 2000. Expanding NEURON's Repertoire of Mechanisms with NMODL. *Neural Computation* 12, 995:1007.
- Hiratani, N., Fukai, T., 2017. Detailed Dendritic Excitatory/Inhibitory Balance through Heterosynaptic Spike-Timing-Dependent Plasticity. *The Journal of Neuroscience* 37 (50), 12106–12122.

- Histed, M. H., Bonin, V., Reid, R. C., 2009. Direct Activation of Sparse, Distributed Populations of Cortical Neurons by Electrical Microstimulation. *Neuron* 63 (4), 508–522.  
URL <http://dx.doi.org/10.1016/j.neuron.2009.07.016>
- Hodgkin, A. L., Huxley, A. F., 1952. A Quantitative Description of Membrane Current and its Application to Conduction and Excitation in Nerve. *Journal of Physiology* 117, 500–544.
- Hong, X., Lu, Z. K., Teh, I., Nasrallah, F. A., Teo, W. P., Ang, K. K., Phua, K. S., Guan, C., Chew, E., Chuang, K.-h., 2017. Brain plasticity following MI-BCI training combined with tDCS in a randomized trial in chronic subcortical stroke subjects : a preliminary study. *Scientific Reports* (May), 1–12.  
URL <http://dx.doi.org/10.1038/s41598-017-08928-5>
- Huerta, P. T., Volpe, B. T., 2009. Transcranial magnetic stimulation, synaptic plasticity and network oscillations. *Journal of NeuroEngineering and Rehabilitation* 6 (1), 7.
- Ito, M., Sakurai, M., Tongroach, P., 1982. Climbing Figure Induced Depression of Both Mossy Fibre Responsiveness and Glutamate Sensitivity of Cerebellar Purkinje Cells. *J. Physiol.* 324, 113–134.
- Jefferys, J. G. R., Whittington, M. A., 1996. Review of the role of inhibitory neurons in chronic epileptic foci induced by intracerebral tetanus toxin. *Epilepsy Research* 26 (1), 59–66.
- Jirsa, V. K., Stacey, W. C., Quilichini, P. P., Ivanov, A. I., Bernard, C., aug 2014. On the nature of seizure dynamics. *Brain* 137 (8), 2210–2230.
- Jones, R. S. G., Brito, A., Whittaker, R. G., Woodhall, G. L., Cunningham, M. O., 2016. Human brain slices for epilepsy research : Pitfalls , solutions and future challenges. *Journal of Neuroscience Methods* 260, 221–232.  
URL <http://dx.doi.org/10.1016/j.jneumeth.2015.09.021>
- Joucla, S., Branchereau, P., Cattaert, D., Yvert, B., 2012a. Extracellular neural microstimulation may activate much larger regions than expected by simulations: A combined experimental and modeling study. *PLoS ONE* 7 (8).
- Joucla, S., Rousseau, L., Yvert, B., 2012b. Focalizing electrical neural stimulation with penetrating microelectrode arrays: A modeling study. *Journal of Neuroscience Methods* 209 (1), 250–254.  
URL <http://dx.doi.org/10.1016/j.jneumeth.2012.05.006>
- Joucla, S., Yvert, B., 2009. The "mirror" estimate: An intuitive predictor of membrane polarization during extracellular stimulation. *Biophysical Journal* 96 (9), 3495–3508.

- Joucla, S., Yvert, B., 2012. Modeling extracellular electrical neural stimulation: From basic understanding to MEA-based applications. *Journal of Physiology Paris* 106 (3-4), 146–158.
- Joucla, S., Yvert, B., Glière, A., Yvert, B., 2014. Current approaches to model extracellular electrical neural microstimulation. *Frontiers in neuroscience* 8 (February), 1–12.
- Kahn, R. S., 2007. Efficacy of Slow Repetitive Transcranial Magnetic Stimulation in the Treatment of Resistant Auditory Hallucinations in Schizophrenia: A Meta-Analysis. *Journal of Clinical Psychiatry* 68 (3), 417–422.
- Kim, C. M., Nykamp, D. Q., 2017. The influence of depolarization block on seizure-like activity in networks of excitatory and inhibitory neurons. *Journal of computational neuroscience* 43, 65–79.
- Kim, T.-s., Generations, A., Head, H.-r. F. E., 2009. Realistic Simulation of Transcranial Direct Current Stimulation via 3-D High-resolution Finite Element Analysis: Effect of Tissue Anisotropy. In: 31st Annual International Conference of the IEEE EMBS. pp. 638–641.
- Kirkwood, A., Dudek, S., Gold, J., Aizenman, C., Bear, M., jun 1993. Common forms of synaptic plasticity in the hippocampus and neocortex in vitro. *Science* 260 (5113), 1518–1521.
- Koch, U. R., Mußhoff, U., Pannek, H. W., Ebner, A., Wolf, P., Speckmann, E. J., Köhling, R., 2005. Intrinsic excitability, synaptic potentials, and short-term plasticity in human epileptic neocortex. *Journal of Neuroscience Research* 80 (5), 715–726.
- Krieg, T. D., Salinas, F. S., Narayana, S., Fox, P. T., Mogul, D. J., 2015. Computational and experimental analysis of TMS-induced electric field vectors critical to neuronal activation. *Journal of Neural Engineering* 12.
- Kriegstein, A. R., Dichter, M. A., 1983. Morphological Classification of Rat Cortical Neurons in Cell Culture. *Journal of Neuroscience* 3 (8), 1634–1647.
- Larsen, R. S., Rao, D., Manis, P. B., Philpot, B. D., 2010. STDP in the developing sensory neocortex. *Frontiers in Synaptic Neuroscience* 2 (JUN), 1–11.
- Larson, J., Munkácsy, E., 2016. Theta-Burst LTP. *Brain Research* 1621, 38–50.
- Latikka, J., Kuurne, T., Hannu, E., 2001. Conductivity of living intracranial tissues. *Physics in Medicine & Biology* 46 (6).
- Leung, L. S., Peloquin, P., Canning, K. J., 2008. Paired-pulse depression of excitatory postsynaptic current sinks in hippocampal CA1 in vivo. *Hippocampus* 18 (10), 1008–1020.

- Lidierth, M., 2009. sigTOOL : A MATLAB-based environment for sharing laboratory-developed software to analyze biological signals. *Journal of Neuroscience Methods* 178, 188–196.
- London, M., Schreibman, A., Häusser, M., Larkum, M. E., Segev, I., 2002. The information efficacy of a synapse. *Nature neuroscience* 5 (4), 332 – 340.
- Lou, X., Scheuss, V., Schneggenburger, R., 2005. Allosteric modulation of the presynaptic  $\text{Ca}^{2+}$  sensor for vesicle fusion. *Nature* 435 (May), 497–501.
- Lübke, J., Feldmeyer, D., 2007. Excitatory signal flow and connectivity in a cortical column : focus on barrel cortex. *Brain Struct Funct* 212, 3–17.
- Lübke, J., Roth, A., Feldmeyer, D., Sakmann, B., Freiburg, A. I. D. A.-l.-u., 2003. Morphometric Analysis of the Columnar Innervation Domain of Neurons Connecting Layer 4 and Layer 2 / 3 of Juvenile Rat Barrel Cortex. *Cerebral cortex* 13 (10), 1051–1063.
- Margineanu, D. G., Wülfert, E., 2000. Differential paired-pulse effects of gabazine and bicuculline in rat hippocampal CA3 area. *Brain Research Bulletin* 51 (1), 69–74.
- Markram, H., Gerstner, W., Sjöström, P. J., 2011. A history of spike-timing-dependent plasticity. *Frontiers in Synaptic Neuroscience* 3 (AUG), 1–24.
- Markram, H., Lu, J., Frotscher, M., Sakmann, B., 1997. Regulation of Synaptic Efficacy by Coincidence of Postsynaptic APs and EPSPs. *Science* 275 (January), 213–216.
- Markram, H., Muller, E., Ramaswamy, S., Reimann, M. W., Abdellah, M., Sanchez, C. A., Ailamaki, A., Alonso-Nanclares, L., Antille, N., Arsever, S., Kahou, G. A. A., Berger, T. K., Bilgili, A., Buncic, N., Chalimourda, A., Chindemi, G., Courcol, J.-D., Delalondre, F., Delattre, V., Druckmann, S., Dumusc, R., Dynes, J., Eilemann, S., Gal, E., Gevaert, M. E., Ghobril, J.-P., Gidon, A., Graham, J. W., Gupta, A., Haenel, V., Hay, E., Heinis, T., Hernando, J. B., Hines, M., Kanari, L., Keller, D., Kenyon, J., Khazen, G., Kim, Y., King, J. G., Kisvarday, Z., Kumbhar, P., Lasserre, S., Le Bé, J.-V., Magalhães, B. R., Merchán-Pérez, A., Meystre, J., Morrice, B. R., Muller, J., Muñoz-Céspedes, A., Muralidhar, S., Muthurasa, K., Nachbaur, D., Newton, T. H., Nolte, M., Ovcharenko, A., Palacios, J., Pastor, L., Perin, R., Ranjan, R., Riachi, I., Rodríguez, J.-R., Riquelme, J. L., Rössert, C., Sfyarakis, K., Shi, Y., Shillcock, J. C., Silberberg, G., Silva, R., Tauheed, F., Telefont, M., Toledo-Rodriguez, M., Tränkler, T., Van Geit, W., Díaz, J. V., Walker, R., Wang, Y., Zaninetta, S. M., DeFelipe, J., Hill, S. L., Segev, I., Schürmann, F., oct 2015. Reconstruction and Simulation of Neocortical Microcircuitry. *Cell* 163 (2), 456–492.
- URL <http://linkinghub.elsevier.com/retrieve/pii/S0092867415011915>

- Mattia, M., Ferraina, S., Del Giudice, P., 2010. Dissociated multi-unit activity and local field potentials: A theory inspired analysis of a motor decision task. *NeuroImage* 52 (3), 812–823.  
URL <http://dx.doi.org/10.1016/j.neuroimage.2010.01.063>
- Mcculloch, W. S., Pitts, W., 1943. A logical calculus nervous activity. *Bulletin of Mathematical Biology* 52 (1), 99–115.
- Meijer, H. G. E., Eissa, T. L., Kiewiet, B., Neuman, J. F., Schevon, C. A., Emerson, R. G., Goodman, R. R., McKhann, G. M., Marcuccilli, C. J., Tryba, A. K., Cowan, J. D., van Gils, S. A., van Drongelen, W., 2015. Modeling Focal Epileptic Activity in the WilsonCowan Model with Depolarization Block. *The Journal of Mathematical Neuroscience* 5 (1), 7.
- Mesgari, M., Ghaffarian, N., Ghadiri, M. K., Sadeghian, H., Speckmann, E., Stummer, W., Gorji, A., 2015. Altered Inhibition In The Hippocampal Neural Networks After Spreading Depression. *Neuroscience* 304, 190–197.  
URL <http://dx.doi.org/10.1016/j.neuroscience.2015.07.035>
- Mochida, S., Few, A. P., Scheuer, T., Catterall, W. A., 2008. Report Regulation of Presynaptic CaV 2.1 Channels by Ca 2+ Sensor Proteins Mediates Short-Term Synaptic Plasticity. *Neuron* 57 (2), 210–216.
- Moore, C. I., Carlen, M., Knoblich, U., Cardin, J. A., 2010. Neocortical Interneurons : From Diversity, Strength. *Cell* 142 (2), 189–193.
- Morrison, A., Diesmann, M., 2008. Phenomenological models of synaptic plasticity based on spike timing. *Biological Cybernetics* 98, 459–478.
- Naka, A., Adesnik, H., 2016. Inhibitory Circuits in Cortical Layer 5. *Frontiers in Neural Circuits* 10 (May), 1–16.  
URL <http://journal.frontiersin.org/article/10.3389/fncir.2016.00035>
- Naud, R., Marcille, N., Clopath, C., Gerstner, W., 2008. Firing patterns in the adaptive exponential integrate-and-fire model. *Biological Cybernetics* 99 (4-5), 335–347.
- Nayak, D., Valentín, A., Selway, R. P., Alarcón, G., 2014. Clinical Neurophysiology Can single pulse electrical stimulation provoke responses similar to spontaneous interictal epileptiform discharges ? *Clinical Neurophysiology* 125 (7), 1306–1311.  
URL <http://dx.doi.org/10.1016/j.clinph.2013.11.019>
- Nelson, T. S., Suhr, C. L., Freestone, D. R., Lai, A., Halliday, A. M. Y. J., Mclean, K. J., Burkitt, A. N., Cook, M. J., 2011. Closed-Loop Seizure Control with Very High Frequency

- Electrical Stimulation at Seizure Onset in the GAERS Mode of Absence Epilepsy. *International Journal of Neural Systems* 21 (2), 163–173.
- Nieuwenhuys, R., Voogd, J., van Huijzen, C., 2007. *The Human Central Nervous System: A Synopsis and Atlas*.
- Nilsen, K. E., Walker, M. C., Cock, H. R., 2005. Characterization of the tetanus toxin model of refractory focal neocortical epilepsy in the rat. *Epilepsia* 46 (2), 179–187.
- Nitsche, M. A., Boggio, P. S., Fregni, F., Pascual-leone, A., 2009. Treatment of depression with transcranial direct current stimulation ( tDCS ): A Review. *Experimental Neurology* 219 (1), 14–19.  
URL <http://dx.doi.org/10.1016/j.expneurol.2009.03.038>
- Nowak, L. G., Bullier, J., 1998. Axons, but not cell bodies, are activated by electrical stimulation in cortical gray matter. *Experimental Brain Research* 118, 489–500.
- O'Connor, D. H., Huber, D., Svoboda, K., 2009. Reverse engineering the mouse brain. *Nature* 461 (7266), 923–929.  
URL <http://www.nature.com/doi/10.1038/nature08539>
- Paz, J. T., Huguenard, J. R., 2015. Microcircuits and their interactions in epilepsy : is the focus out of focus ? *Nature Neuroscience* 18 (3), 351–359.
- Perouansky, B. Y. M., Yaari, Y., 1993. Kinetic properties of NMDA Receptor-Mediated Synaptic Currents in Rat Hippocampal Pyramidal Cells Versus Interneurones. *Journal of Physiology* 465, 223–244.
- Perreault, P., Avoli, M., 1991. Physiology and Pharmacology of Epileptiform Activity Induced by 4-Aminopyridine in Rat Hippocampal Slices. *Journal of Neurophysiology* 65 (4), 771–785.
- Pinto, D. J., Patrick, S. L., Huang, W. C., Connors, B. W., 2005. Initiation, propagation, and termination of epileptiform activity in rodent neocortex in vitro involve distinct mechanisms. *The Journal of neuroscience : the official journal of the Society for Neuroscience* 25 (36), 8131–8140.
- Pitkänen, A., Schwartzkroin, P., Moshé, S., 2017. *Models of Seizures and Epilepsy*, 2nd Edition.
- Potjans, T. C., Diesmann, M., 2014. The cell-type specific cortical microcircuit: relating structure and activity in a full-scale spiking network model. *Cerebral cortex (New York, N.Y. : 1991)* 24 (3), 785–806.

- Pouille, F., Watkinson, O., Scanziani, M., Trevelyan, A. J., 2013. The contribution of synaptic location to inhibitory gain control in pyramidal cells. *Physiological Reports* 1 (5), n/a–n/a.
- Pryor, R. W., 2009. *Multiphysics Modeling Using COMSOL: A First Principles Approach*.
- Queiroz, C. M., Gorter, J. A., Lopes, F. H., Wadman, W. J., 2009. Dynamics of Evoked Local Field Potentials in the Hippocampus of Epileptic Rats With Spontaneous Seizures. *Journal of neurophysiology* 101 (3), 1588–1597.
- Rabau, S., Shekhawat, G. S., Abozeria, M., Griep, D., 2017. Comparison of the Long-Term Effect of Positioning the Cathode in tDCS in Tinnitus Patients. *Frontier in Aging Neuroscience* 9 (July), 1–8.
- Radman, T., Ramos, R. L., Brumberg, J. C., Bikson, M., 2009. Role of cortical cell type and morphology in subthreshold and suprathreshold uniform electric field stimulation in vitro. *Brain Stimulation* 2 (4), 215–228.e3.  
URL <http://dx.doi.org/10.1016/j.brs.2009.03.007>
- Rall, W., 1962. Electrophysiology of a Dendritic Neuron Model. *Biophysical Journal* 2 (2), 145–167.
- Ramaswamy, S., Courcol, J.-D., Abdellah, M., Adaszewski, S. R., Antille, N., Arsever, S., Atenekeng, G., Bilgili, A., Brukau, Y., Chalimourda, A., Chindemi, G., Delalondre, F., Dumusc, R., Eilemann, S., Gevaert, M. E., Gleeson, P., Graham, J. W., Hernando, J. B., Kanari, L., Katkov, Y., Keller, D., King, J. G., Ranjan, R., Reimann, M. W., Rössert, C., Shi, Y., Shillcock, J. C., Telefont, M., Van Geit, W., Villafranca Diaz, J., Walker, R., Wang, Y., Zaninetta, S. M., DeFelipe, J., Hill, S. L., Muller, J., Segev, I., Schürmann, F., Muller, E. B., Markram, H., 2015. The neocortical microcircuit collaboration portal: a resource for rat somatosensory cortex. *Frontiers in neural circuits* 9 (October), 44.
- Rattay, F., 1986. Analysis of Models for External Stimulation of Axons. *IEEE Transactions on Biomedical Engineering BME-33* (10), 974–977.
- Rattay, F., 1989. Analysis of Models for Extracellular Fiber Stimulation. *IEEE Transactions on Biomedical Engineering* 36 (7), 676–682.
- Rattay, F., jun 1998. Analysis of the electrical excitation of CNS neurons. *IEEE Transactions on Biomedical Engineering* 45 (6), 766–772.  
URL <http://www.ncbi.nlm.nih.gov/pubmed/9609941><http://ieeexplore.ieee.org/document/678611/>
- Rattay, F., 1999. The basic mechanism for the electrical stimulation of the nervous system. *Neuroscience* 89 (2), 335–346.

- Rattay, F., Wenger, C., 2010. Which elements of the mammalian central nervous system are excited by low current stimulation with microelectrodes? *Neuroscience* 170 (2), 399–407.
- Regehr, W. G., 2012. Short-term presynaptic plasticity. *Cold Spring Harbor Perspectives in Biology* 4 (7), 1–19.
- Reyes, A., Lujan, R., Rozov, A., Burnashev, N., Somogyi, P., Sakmann, B., 1998. Target-cell-specific facilitation and depression in neocortical circuits. *Nat. Neurosci.* 1 (4), 279–285.
- Rotenberg, A., Hyunji, E., Takeoka, M., Tormos, J. M., Schachter, S. C., Pascual-leone, A., 2009. Epilepsy & Behavior Repetitive transcranial magnetic stimulation in the treatment of epilepsy partialis continua. *Epilepsy and Behavior* 14 (1), 253–257.  
URL <http://dx.doi.org/10.1016/j.yebeh.2008.09.007>
- Rubin, J., Lee, D. D., Sompolinsky, H., 2001. Equilibrium Properties of Temporally Asymmetric Hebbian Plasticity. *Physical Review Letters* 86 (2), 364–367.
- Sanger, T. D., 1989. Optimal Unsupervised Learning in a Single-Layer Linear Feedforward Neural Network. *Neural Networks* 2, 459–473.
- Schevon, C. A., Weiss, S. A., McKhann, G., Goodman, R. R., Yuste, R., Emerson, R. G., Trevelyan, A. J., 2012. Evidence of an inhibitory restraint of seizure activity in humans. *Nature Communications* 3, 1011–1060.  
URL <http://dx.doi.org/10.1038/ncomms2056>
- Schiavo, G., Shone, C. C., Rossetto, O., Alexander, F. C. G., Montecuccos, C., 1993. Botulinum Neurotoxin Serotype. *The Journal of biological chemistry* 268 (June), 11516–11519.
- Schnepel, P., Kumar, A., Zohar, M., Aertsen, A., Boucsein, C., 2015. Physiology and Impact of Horizontal Connections in Rat Neocortex. *Cerebral Cortex* 25 (10), 3818–3835.
- Sciamanna, G., Ponterio, G., Mandolesi, G., Bonsi, P., Pisani, A., 2015. Optogenetic stimulation reveals distinct modulatory properties of thalamostriatal vs corticostriatal glutamatergic inputs to fast-spiking interneurons. *Nature Publishing Group* (June), 1–15.  
URL <http://dx.doi.org/10.1038/srep16742>
- Semendeferi, K., Erwin, J. M., Park, S., Goubert, V., Hof, P. R., 2010. The von Economo neurons in frontoinsular and anterior cingulate cortex in great apes and humans. *Brain Struct Funct* 214, 495–517.
- Seo, H., Schaworonkow, N., Jun, S. C., Triesch, J., 2016. A multi-scale computational model of the effects of TMS on motor cortex. *F1000Research* 5 (May), 1945.  
URL <https://f1000research.com/articles/5-1945/v1>

- Serafini, R., Dettloff, S., Loeb, J. A., 2016. Neocortical Slices from Adult Chronic Epileptic Rats Exhibit Discharges of Higher Voltages and Broader Spread. *Neuroscience* 322, 509–524.  
URL <http://www.ncbi.nlm.nih.gov/pubmed/26892299>
- Song, S., Miller, K. D., Abbott, L. F., 2000. Competitive Hebbian learning through spike-timing-dependent synaptic plasticity. *Nature Neuroscience* 3 (9), 919–926.
- Staley, K., 2015. Molecular mechanisms of epilepsy. *Nature Neuroscience* 18 (3), 367–372.
- Stelzer, A., Kay, A. R., Wong, R. K. S., 1987. GABAA-Receptor Function in Hippocampal Cells Is Maintained by Phosphorylation Factors. *Science* 241 (4863), 5–8.
- Stuart, G., Spruston, N., Sakmann, B., Häusser, M., 1997. Action potential initiation and backpropagation in neurons of the mammalian CNS. *Trends in Neurosciences* 20 (3), 125–131.
- Sunkin, S. M., Ng, L., Lau, C., Dolbeare, T., Gilbert, T. L., Thompson, C. L., Hawrylycz, M., Dang, C., 2013. Allen Brain Atlas : an integrated spatio-temporal portal for exploring the central nervous system. *Nucleic Acids Research* 41 (November 2012), 996 – 1008.
- Tamura, R., Nishida, H., Eifuku, S., Nagao, K., Fushiki, H., Watanabe, Y., 2011. Short-Term Synaptic Plasticity in the Dentate Gyrus of Monkeys. *PLoS ONE* 6 (5), 1–8.
- Tergau, F., Naumann, U., Paulus, W., Steinhoff, B. J., 1999. Low-frequency repetitive transcranial magnetic stimulation improves intractable epilepsy. *The Lancet* 353 (June), 2209.
- Teyler, T. J., DiScenna, P., 1987. Long-term potentiation. *Annu Rev Neurosci* 10, 131–161.
- The MathWorks, Inc., Natick, Massachusetts, U. S., 2016. MATLAB and Partial Differential Equation Toolbox Release 2016b.
- Theodore, W. H., 2003. Transcranial Magnetic Stimulaion in Epilepsy. *Epilepsy currents / American Epilepsy Society* 3 (6), 191–197.
- Thomson, A., Lamy, C., 2007. Functional maps of neocortical local circuitry. *Frontiers in neuroscience* 1 (1).  
URL <http://www.ncbi.nlm.nih.gov/pmc/articles/PMC2518047/>
- Thomson, A. M., sep 2002. Synaptic Connections and Small Circuits Involving Excitatory and Inhibitory Neurons in Layers 2-5 of Adult Rat and Cat Neocortex: Triple Intracellular Recordings and Biocytin Labelling In Vitro. *Cerebral Cortex* 12 (9), 936–953.  
URL <http://www.cercor.oupjournals.org/cgi/doi/10.1093/cercor/12.9.936>
- Tomsett, R. J., Ainsworth, M., Thiele, A., Sanayei, M., Chen, X., Gieselmann, M. A., Whittington, M. A., Cunningham, M. O., Kaiser, M., may 2015. Virtual Electrode Recording

- Tool for EXtracellular potentials (VERTEX): comparing multi-electrode recordings from simulated and biological mammalian cortical tissue. *Brain Struct Funct* 220 (4), 2333–2353.  
URL <http://dx.doi.org/10.1007/s00429-014-0793-x>
- Tranchina, D., Nicholsont, C., 1977. A Model for the Polarization of Neurons By Extrinsically Applied Electric Fields. *Biophysical Journal* 50 (6), 1139–1156.  
URL [http://dx.doi.org/10.1016/S0006-3495\(86\)83558-5](http://dx.doi.org/10.1016/S0006-3495(86)83558-5)
- Trevelyan, A. J., 2016. Do Cortical Circuits Need Protecting from Themselves ? *Trends in Neurosciences* 39 (8), 502–511.  
URL <http://dx.doi.org/10.1016/j.tins.2016.06.002>
- Trevelyan, A. J., Baldeweg, T., van Drongelen, W., Yuste, R., Whittington, M., dec 2007. The source of afterdischarge activity in neocortical tonic-clonic epilepsy. *The Journal of neuroscience : the official journal of the Society for Neuroscience* 27 (49), 13513–9.  
URL <http://www.ncbi.nlm.nih.gov/pubmed/18057209>
- Trevelyan, A. J., Sussillo, D., Watson, B. O., Yuste, R., nov 2006. Modular propagation of epileptiform activity: evidence for an inhibitory veto in neocortex. *The Journal of neuroscience : the official journal of the Society for Neuroscience* 26 (48), 12447–55.  
URL <http://www.ncbi.nlm.nih.gov/pubmed/17135406>
- Tsodyks, M., Pawelzik, K., Markram, H., 1998. Neural networks with dynamic synapses. *Neural computation* 10 (4), 821–835.  
URL <http://www.mitpressjournals.org/doi/abs/10.1162/089976698300017502{#}.VUL593W1Gko>
- Tsumoto, T., 1990. Long-Term Potentiation and Depression in the Cerebral Neocortex. *Japanese Journal of Physiology* (40), 573–593.
- Valentín, A., Alarcón, G., Honavar, M., Seoane, J. J. G., Selway, R. P., Polkey, C. E., Binnie, C. D., Hispano, P., 2005. Single pulse electrical stimulation for identification of structural abnormalities and prediction of seizure outcome after epilepsy surgery : a prospective study. *Lancet Neurology* 4 (November).
- Valentín, A., Anderson, M., Alarcón, G., Seoane, J. J. G., Selway, R., Binnie, C. D., Polkey, C. E., 2002. Responses to single pulse electrical stimulation identify epileptogenesis in the human brain in vivo. *Brain : a journal of neurology* 125 (Pt 8), 1709–1718.
- Varela, J. A., Sen, K., Gibson, J., Fost, J., Abbott, L. F., Nelson, S. B., 1997. A Quantitative Description of Short-Term Plasticity at Excitatory Synapses in Layer 2/3 of Rat Primary Visual Cortex. *Journal of Neuroscience* 17 (20).

- Wagner, F. B., Eskandar, E. N., Cosgrove, G. R., Madsen, J. R., Blum, A. S., Potter, N. S., Hochberg, L. R., Cash, S. S., Truccolo, W., 2015. Microscale spatiotemporal dynamics during neocortical propagation of human focal seizures. *NeuroImage* 122, 114–130.  
URL <http://dx.doi.org/10.1016/j.neuroimage.2015.08.019>
- Walcott, E., Langdon, R., jul 2002. Synaptically driven spikes and long-term potentiation in neocortical layer 2/3. *Neuroscience* 112 (4), 815–826.  
URL <http://linkinghub.elsevier.com/retrieve/pii/S0306452202001318>
- Waldbaum, S., Dudek, F. E., 2009. Single and repetitive paired-pulse suppression : A parametric analysis and assessment of usefulness in epilepsy research. *Epilepsia* 50 (4), 904–916.
- Wang, Y., Goodfellow, M., Taylor, P. N., Baier, G., 2014. Dynamic mechanisms of neocortical focal seizure onset. *PLoS computational biology* 10 (8), e1003787.
- Wang, Y., Markram, H., Goodman, P. H., Berger, T. K., Ma, J., Goldman-Rakic, P. S., 2006. Heterogeneity in the pyramidal network of the medial prefrontal cortex. *Nature Neuroscience* 9 (4), 534–542.  
URL <http://www.nature.com/doi/10.1038/nn1670>
- Wang, Y., Trevelyan, A. J., Valentin, A., Alarcon, G., Taylor, N., Kaiser, M., 2017. Mechanisms underlying different onset patterns of focal seizures. *PLoS Computational Biology* 13 (5), 1–22.
- Wei, Y., Ullah, G., Ingram, J., Schiff, S. J., 2014. Oxygen and seizure dynamics : II . Computational modeling. *J Neurophysiol* 112, 213–223.
- Whittington, M. A., Traub, R. D., Jefferys, J. G. R., 1995. Erosion of inhibition contributes to the progression of low magnesium bursts in rat hippocampal slices. *Journal of Physiology* 486 (3), 723–734.
- Wiebe, S., Blume, W. T., Girvin, J. P., Eliasziw, M., 2001. A Randomized, Controlled Trial of Surgery for Temporal-Lobe Epilepsy. *New England Journal of Medicine* 345 (5), 311–318.
- Wilson, C. L., Khan, S. U., Jr, J. E., Isokawa, M., Babb, T. L., 1998. Paired pulse suppression and facilitation in human epileptogenic hippocampal formation. *Epilepsy Research* 31, 211–230.
- Wilson, H. R., Cowan, J. D., 1973. A mathematical theory of the functional dynamics of cortical and thalamic nervous tissue. *Kybernetik* 13 (2), 55–80.
- Yang, J.-M., Geng, H.-Y., Li, Y., Li, X.-M., Li, K.-X., Pan, G., 2015. Preserving GABAergic interneurons in acute brain slices of mice using the N-methyl-D-glucamine-based artificial cerebrospinal fluid method. *Neuroscience Bulletin* 31 (2), 265–270.

- Yang, S.-n., Tang, Y.-g., Zucker, R. S., 1999. Selective Induction of LTP and LTD by Postsynaptic  $[Ca^{2+}]_i$  Elevation. *Journal of Neurophysiology* 81 (2), 781–787.
- Yi, G., Wang, J., Tsang, K. M., Wei, X., Deng, B., Han, C., 2015. Spike-frequency adaptation of a two-compartment neuron modulated by extracellular electric fields. *Biological Cybernetics* 109 (3), 287–306.
- Yi, G.-S., Wang, J., Deng, B., Wei, X.-L., 2017. Morphology controls how hippocampal CA1 pyramidal neuron responds to uniform electric fields: a biophysical modeling study. *Scientific Reports* 7 (1), 3210.  
URL <http://www.nature.com/articles/s41598-017-03547-6>
- Zelmann, R., Mari, F., Jacobs, J., Zijlmans, M., Dubeau, F., Gotman, J., 2013. Antiepileptic drugs abolish ictal but not interictal epileptiform discharges in vitro. *Clinical Neurophysiology* 123 (3), 106–116.
- Zucker, R. S., Regehr, W. G., 2002. Short-Term Synaptic Plasticity. *Annu. Rev. Physiol.* 2002. 64, 355–405.